Modelling soot production in fire applications

Antoine Bouffard

Aix*Marseille université
Socialement engagée

NNT : 2023AIXM0439

THÈSE DE DOCTORAT

Soutenue à Aix-Marseille Université
le 8 décembre 2023 par

Antoine BOUFFARD

Modelling soot production in fire applications

Discipline
Sciences pour l'ingénieur

Spécialité
Énergétique

École doctorale
Sciences pour l'Ingénieur : Mécanique, Physique, Micro et Nano-électronique/ED 353

Laboratoire/Partenaires de recherche
Aix-Marseille Université - IUSTI UMR 7343
EDF R&D - Lab Chatou

Composition du jury

Fengshan LIU National Research Council, Canada	Rapporteur
Denis VEYNANTE CentraleSupélec	Rapporteur
Frédéric ANDRE Université de Lille	Examinateur
Yi WANG FM Global, USA	Examinateur
John HEWSON Sandia National Laboratories, USA	Examinateur
Olivier VAUQUELIN Aix-Marseille Université	Président du jury
Jean-Louis CONSALVI Aix-Marseille Université	Directeur de thèse
Fatiha NMIRA EDF R&D, Chatou	Co-directrice de thèse

IUSTI LABORATOIRE AIX MARSEILLE UNIVERSITÉ CNRS

EDF

Affidavit

I, undersigned, Antoine Bouffard, hereby declare that the work presented in this manuscript is my own work, carried out under the scientific supervision of Jean-Louis Consalvi and Fatiha Nmira, in accordance with the principles of honesty, integrity and responsibility inherent to the research mission. The research work and the writing of this manuscript have been carried out in compliance with both the french national charter for Research Integrity and the Aix-Marseille University charter on the fight against plagiarism.

This work has not been submitted previously either in this country or in another country in the same or in a similar version to any other examination body.

Chatou, 4th September 2023

Résumé

Ce travail de thèse étudie la modélisation de la production de suie dans des flammes contrôlées par les forces de flottabilité caractéristiques des incendies. Deux principales difficultés existent : (i) la chimie associée à la suie est lente ce qui nécessite un traitement spécifique et (ii) les interactions chimie/suie/rayonnement/turbulence sont un problème complexe qui requière une attention particulière. La combustion est modélisée par un modèle de flammelettes laminaires non-adiabatiques. Le modèle RCFSK est utilisé pour les propriétés radiatives des gaz rayonnants et de suie.
Dans un premier temps, la production de suie est décrite par un modèle à deux équations semi-empirique basé sur l'acétylène/benzène comme précurseur de la suie pour simuler trois feux à l'échelle du laboratoire d'éthylène bien documentés brûlant dans l'air et dans des conditions sous-oxygénées dans un cadre de simulations aux grandes échelles (SGE). L'interaction production de suie/turbulence a été traitée par une fonction de densité de probabilité filtrée présumée prenant en compte la nature spatiale intermittente de la suie et le fort couplage entre les quantités de suie et les espèces oxydantes en raison de l'oxydation rapide de la suie. Les prédictions du modèle reproduisent fidèlement la structure des flammes, la dynamique de production de suie et les pertes radiatives. Les résultats mettent en évidence que, d'une part, la suie et les gaz rayonnants contribuent similairement aux pertes radiatives pour la flamme brûlant dans l'air et que la contribution des gaz rayonnants devient de plus en plus dominante avec la réduction de l'oxygène en raison d'une diminution de la fraction volumique de suie (FVS) et que, d'autre part, négliger la corrélation entre les quantités de suie et la fraction de mélange conduit à une surestimation systématique de l'oxydation de la suie et entraîne une sous-estimation importante du pic de la fraction volumique de suie.
Deuxièmement, les scénarios d'incendie impliquent souvent des carburants plus complexes comme l'essence, le diesel, le kérosène, ... Ces carburants contiennent des aromatiques et par voie de fait le modèle basé sur l'acétylène/benzène n'est plus adapté. Pour pallier ce problème de manière pratique, un modèle basé sur le pyrène comme précurseur de la suie a été développé et évalué sur des flammes de diffusion laminaires de type à « co-courant » mettant en jeu des combustibles brûlant sous oxygène normal et réduit. Les résultats obtenus sont en accord quantitatif avec les données expérimentales dans le cadre de flammes d'éthylène en termes de température, de FVS, et de taille de particules primaires. Le modèle a ensuite été appliqué avec le même jeu de paramètres à des mélanges plus complexes de n-heptane/iso-octane/toluène. Le modèle capture assez bien la production de suie dans les mélanges de n-heptane/toluène et iso-octane/toluène. Néanmoins, le modèle prédit l'initiation de la formation de suies de manière significativement plus précoce que les expériences. De plus, la production de suie est nettement sous-estimée pour le n-heptane et l'iso-octane purs.
Finalement, une analyse chimique a été réalisée pour mettre en évidence l'origine de ces écarts et a révélé qu'un hydrocarbure aromatique polycyclique (HAP) plus gros que le pyrène, à savoir l'anthanthrene, est mieux adapté. Les simulations réalisées en adoptant l'anthanthrene comme précurseur de la suie se sont avérées meilleures que celles réalisées avec le pyrène, conduisant à des prévisions satisfaisantes pour tous les mélanges.

Mots clés : production de suie, interaction production de suie/turbulence, HAP, combustibles gazeux et liquides.

Abstract

This Phd thesis investigates the modeling of soot production for purely buoyant fire plumes. Two main difficulties exist: i) Soot production is characterized by a slow chemistry which requires a specific treatment and ii) the interactions between chemistry/soot production/radiation/turbulence is a complex problem that necessitates a particular attention. The combustion model is based on the enthalpy defect flamelet model. The RCFSK model is used for the radiative properties of the radiatively participating gaseous products and soot.

First, an acetylene/benzene-based soot production model is used to simulate three well-documented lab-scale ethylene buoyant diffusion flames burning under air and reduced oxygenated conditions in the framework of large eddy simulations (LES). The soot production/turbulence interaction (STI) is modeled by a presumed filtered density function (FDF) which considers the spatial intermittent nature of soot and the strong coupling between soot quantities and oxidative species due to the fast oxidation process. Model predictions reproduce with fidelity the flame structure, the soot production dynamics and the radiative loss for the three flames. Model results show that soot and radiating gas have a similar contribution to radiation for the flame burning in air and the contribution of radiating gas becomes increasingly dominant with decreasing oxygen due to a reduction in soot volume fraction (SVF) throughout the overall flames. Model predictions show that neglecting the coupling between soot quantities and mixture fraction overestimates substantially soot oxidation, resulting in significantly lower soot production and radiative loss.

Second, fire scenario may involve more complex fuels such as gasoline, diesel, kerosene, ... As these fuels contain aromatics, the acetylene/benzene based model is no longer well suited. To overcome this problem in a practical way, a model based on four-ring pyrene was developed and evaluated on extensive laminar coflow diffusion flames burning under normal and reduced oxygen. The model predictions are in quantitative agreement with experimental data for ethylene flames in terms of temperature, SVF and primary particles diameters. The model has been then applied with the same set of parameters to more complex mixtures of n-heptane/iso-octane/toluene, which constitute the primary reference fuels for gasoline surrogates. The model captures rather well the soot production in n-heptane/toluene and iso-octane/toluene blends. However, the model predicts the onset of soot formation significantly earlier compared to the experiments. In addition, soot production is significantly underpredicted for pure n-heptane and iso-octane.

Finally, a chemical analysis was performed to highlight the origin of these discrepancies and has revealed that a polycyclic aromatic hydrocarbon (PAH) larger than pyrene, namely anthanthrene, is better suited. Simulations performed by using anthanthrene as soot precursor were found to improve those performed with pyrene, leading to satisfactory predictions for all the n-heptane/iso-octane/toluene blends.

Keywords : soot production, subgrid-scale soot production/turbulence interaction, PAH, gaseous and liquid fuels.

Résumé de la thèse en français

Électricité De France (EDF), en tant qu'exploitant, est responsable de la sûreté des centrales nucléaires et définit les moyens et l'organisation mis en place, conformément aux textes réglementaires. L'incendie est le risque potentiel d'agression interne le plus élevé. Outre la sécurité de son personnel et le bon fonctionnement de ses installations, EDF possède un intérêt économique (lié à la perte de matériels et à l'immobilisation du moyen de production) à diminuer le risque incendie en assurant un niveau de sûreté élevé sans recourir à des moyens de défense contre l'incendie sur-dimensionnés. La démonstration de l'efficacité de la sûreté incendie à l'aide d'outils numériques est en croissance puisqu'elle permet de défendre certaines dispositions plus adaptées aux situations de terrain.

Les outils de simulation numérique développés par la direction Recherche et Développement d'EDF (EDF R&D) participent depuis plusieurs années aux réponses apportées par EDF. Aujourd'hui, le code de référence incendie à EDF est le code *MAGIC*, code bi-zones reposant sur l'hypothèse de stratification des gaz chauds au-dessus d'une couche de gaz frais. Ce type de modélisation présente l'avantage d'un coût de calcul faible et répond à la majorité des besoins industriels. Cependant, elle n'est pas en mesure de capturer tous les processus de l'incendie, de plus, elle devient moins pertinente en l'absence de stratification. D'où la nécessité d'une modélisation plus détaillée.

La modélisation des incendies est un problème multi-physique complexe impliquant des écoulements contrôlés par la flottabilité, la turbulence induite par la flottabilité, la combustion turbulente, la production de suie, le rayonnement thermique, ainsi que la dégradation thermique de la matière condensée. Un défi supplémentaire apparaît pour les incendies en milieux sous-ventilés, qui sont très fréquent dans le parc nucléaire, et/ou sous l'action d'agents d'extinction dans la mesure où ces conditions conduisent à des extinctions partielles ou totales de la flamme.

Le feu de nappe est un scénario canonique dans la science des incendies car il contient l'ensemble des processus mis en jeu dans la phase de croissance. Il se produit lorsqu'un liquide inflammable, tel que l'essence, forme une flaque sur le sol ou dans un récipient et s'enflamme. Le combustible en phase gazeuse, alimentant la flamme, provient de la décomposition thermique ou de la vaporisation du combustible condensé sous l'effet de la rétroaction thermique de la flamme par transfert de chaleur convectif et/ou radiatif. Ce processus auto-entretenu contrôle la puissance de flamme, et par voie de fait, le développement du feu ainsi que ses interactions avec l'environnement, Karlsson and Quintiere (1999).

Le rayonnement thermique joue un rôle primordial. D'une part, la rétroaction radiative sur le combustible condensé prévaut sur la convection pour des nappes de diamètre supérieur à 20-30 cm, de Ris (1979). D'autre part, il s'agit du mode de trans-

fert dominant de la flamme dans la plupart des applications. La contribution de la suie à ce rayonnement thermique prévaut généralement sur celle des gaz dans les feux réels, de Ris (1979). En conséquence, la modélisation de la production de suie et de la radiation associée est fondamentale pour prédire la propagation du feu.

L'objectif de cette thèse est d'étendre à des combustibles produisant de la suie le modèle numérique de simulation des grandes structures turbulentes (SGE) dédié à la simulation de panaches de feux bien ventilés et sous-ventilés, et contrôlés par les forces de flottabilité, développé au sein du code de calcul *Code_Saturne* (EDF R&D (2023)) pour des combustibles ne produisant pas de suie, (Ma (2020)). Ce modèle s'appuie sur un nouveau solveur à densité variable à bas nombre de Mach d'ordre deux pour lequel des modèles de sous-maille à l'état de l'art ont été spécifiquement développés pour la turbulence, la combustion et la radiation, incluant le modèle de flammelettes stationnaires non-adiabatiques pour la combustion, le modèle de flammelettes/variable de progression pour la combustion avec extinction et le modèle RCFSK pour les propriétés radiatives. Ce modèle numérique s'est montré capable de reproduire avec une grande fidélité les structures dynamiques et radiatives des panaches de feu non lumineux, tant dans des configurations bien ventilées que sous-ventilées, cela sans ajuster aucun paramètre du modèle.

La modélisation de la production de suie dans les applications liées aux incendies présente deux difficultés principales :

- Une première difficulté est liée à la **production de suie** qui est caractérisée par une chimie lente, ce qui rend impossible l'établissement préalable de quantités de suie dans une bibliothèque de flammelettes. Un modèle de production de suie est donc nécessaire et, bien que les processus de production de suie ne soient pas entièrement compris, Martin et al. (2022), leur modélisation ont connu des avancées significatives au cours des vingt dernières années grâce au développement de modèles détaillés basés sur les HAP (hydrocarbures aromatiques polycycliques), Liu et al. (2022). Cependant, ces modèles ont été principalement appliqués aux carburants gazeux, tels que l'éthylène, et un nombre limité d'études a été rapporté pour les carburants liquides ou solides rencontrés dans les problèmes d'incendie. Un objectif de cette étude est de progressivement tendre vers des carburants liquides.
- Une deuxième difficulté a trait aux **interactions entre la chimie, la production de suie, le rayonnement et la turbulence**, constituant un problème complexe qui nécessite le développement de modèles spécifiques à l'échelle sous-maille, Liu et al. (2022). Des modèles de type RANS/PDF transporté ont été développés par le passé à EDF R&D (Burot (2017)), mais leur extension aux applications LES dans les incendies peut être trop coûteuse en termes de calculs. Il est donc nécessaire d'obtenir un compromis entre précision et efficacité de calcul, ce qui est un objectif de cette étude.

La suie est un sous-produit de la combustion incomplète présent dans les régions riches en carburant, constituées de particules presque sphériques appelées particules primaires (10-50 nm) qui s'agrègent pour former des agrégats fractals (30-200 nm). Les HAP sont les précurseurs de la suie et jouent un rôle majeur dans la formation et la croissance de la suie. Ils se composent de cycles aromatiques (A_i fait référence à un

HAP avec i cycles), et il convient de faire une distinction entre eux et les composés aliphatiques, qui ont une structure à chaîne ouverte. Pour les composés aliphatiques, il est nécessaire de former d'abord du benzène (A_1) pour initier la formation de HAP et de la suie, tandis que pour les flammes alimentées en composés aromatiques, la formation et la croissance des HAP au-delà du benzène deviennent l'étape limitante du processus global de formation de suie, Martin et al. (2022). Dans le domaine de la combustion et de l'incendie, trois types de modèles ont principalement été considérés :

- **Les modèles détaillés à HAP**, qui impliquent (i) un mécanisme cinétique détaillé incluant la formation et la croissance des HAP, (ii) une description détaillée du mécanisme de formation de la suie décrivant la nucléation des particules à partir des HAP, leur croissance par condensation des HAP et par mécanisme HACA, l'oxydation par OH et O_2, et (iii) un modèle pour suivre la dynamique des particules.
- **Les modèles basés sur** C_2H_2, qui adoptent une description simplifiée de la formation de la suie en supposant que les concentrations en HAP sont reliés aux espèces plus légères telles que l'acétylène, C_2H_2, ou le benzène, A_1, à l'origine de leur formation. Ces modèles sont généralement couplés à une formulation à deux équations pour la dynamique des suies, Lindstedt (1994).
- **Les modèles basés sur le point de fumée laminaire**, qui s'appuient sur la longueur de flamme au point de fumée qui caractérise la propension d'un carburant donné à former de la suie.

Les difficultés liées au mélange turbulent et aux interactions turbulence/chimie/-production de suie sont principalement régies par la très faible diffusivité de la suie, c'est-à-dire qu'elle est transportée de manière différentielle par rapport aux espèces gazeuses, et par la chimie lente de la suie (et des HAP) qui se déroule sur des échelles de temps significativement plus longues que celles des processus de combustion typiques. Les principales conséquences sont les suivantes : (i) la suie est confinée dans des structures très fines, avec un comportement spatialement et temporellement intermittent du champ de suie, (ii) la suie (et aussi les HAP) ne peuvent pas être paramétrisées par la fraction de mélange et le taux de dissipation scalaire, (iii) la diffusion différentielle régit la dérive de la suie dans l'espace de la fraction massique et détermine la proximité de la suie avec la flamme, ce qui influence à son tour les taux de réaction de la suie et les émissions radiatives, (iv) la concentration locale de HAP est très sensible au taux de dissipation scalaire, la croissance des HAP et de la suie étant favorisée dans les régions de faible taux de dissipation et inhibée dans les régions de taux de dissipation élevé. De plus, il a été constaté que la suie est rapidement oxydée à proximité de la surface stœchiométrique et que des fuites de suie à travers la flamme se produisent en raison d'extinctions locales.

Le modèle SGE peut décrire la nature temporellement intermittente de la suie, Mueller and Pitsch (2012), Yang et al. (2019). Cependant, les processus de formation et d'oxydation de la suie se produisent à l'échelle sous-maille, non résolues, et leur interaction avec la turbulence doit être modélisée indépendamment du traitement du champ d'écoulement. Les taux de production de suie, $\dot{\omega}_s(\phi_g, \phi_s)$, dépendent des quantités liées à la phase gazeuse, ϕ_g, et des quantités liées à la suie, ϕ_s. Dans le cadre du modèle de flammelettes stationnaires non-adiabatiques, la phase gazeuse est décrite par

la fraction de mélange, Z, le taux de dissipation scalaire, χ, et le paramètre de non-adiabaticité, X_R tel que $\phi_g = \{Z, \chi, X_R\}$. La dynamique de la suie est modélisée avec une formulation à deux ou trois équations, les particules de suie sont alors décrites par la fraction massique de suie, Y_s, le nombre densité d'agrégats, N_s, et le nombre densité de particules primaires, N_{ps}, tel que $\phi_s = \{Y_s, N_s\}$ ou $\phi_s = \{Y_s, N_s, N_{ps}\}$. La dépendance des taux de production de suie avec ces grandeurs est telle que leurs valeurs filtrées, $\overline{\dot{\omega}}_s$, ne peuvent pas être directement reliées aux valeurs filtrées de ϕ_g et ϕ_s :

$$\overline{\dot{\omega}}_s(\mathbf{x}, t) = \overline{\rho} \iint \frac{\dot{\omega}_s(\phi_g, \phi_s)}{\rho(\phi_g)} \widetilde{P}(\phi_g, \phi_s) d\phi_g d\phi_s \neq \dot{\omega}_s(\widetilde{\phi}_g, \widetilde{\phi}_s)$$

où la notation $\widetilde{\phi}$ fait référence à la valeur filtrée pondérée par la masse de ϕ. $\widetilde{P}$ représente la fonction de densité de probabilité filtrée jointe (FDF). Comme discuté précédemment, la chimie des HAP et de la suie est plus lente que celle de la combustion. De plus, les particules de suie ne se diffusent pas comme les espèces en phase gazeuse. On s'attend alors à ce que les quantités de la phase gazeuse et les quantités de suie soient statistiquement indépendantes, ce qui conduit à $\widetilde{P}(\phi_g, \phi_s) = \widetilde{P}(\phi_g) \times \widetilde{P}(\phi_s)$. Cependant, cette formulation dite "non corrélée" s'est avérée sous-estimer de manière significative la fraction volumique de suie mesurée, Yang et al. (2019). Ces écarts sont dus à une surestimation importante de l'oxydation de la suie. L'oxydation rapide implique qu'il y a peu de chevauchement entre les espèces oxydantes et les profils de suie dans l'espace de fraction de mélange, ce qui suggère une coexistence limitée des oxydants et de la suie. Par conséquent, les quantités de suie sont fortement corrélées avec les espèces oxydantes et la formulation "non corrélés" précédente n'est pas valable. Dans le présent travail, la FDF jointe est ré-exprimée tel que $\widetilde{P}(\phi_g, \phi_s) = \widetilde{P}(\phi_s|\phi_g) \times \widetilde{P}(\phi_g)$. L'expression de la FDF de la phase gazeuse, $\widetilde{P}(\phi_g)$, est supposée en assumant l'hypothèse d'indépendance statistique entre les quantités de la phase gazeuse et en utilisant une β-distribution et des δ-distribution pour les FDF marginales de Z, χ et X_R, respectivement. La FDF de la suie conditionnée, $\widetilde{P}(\phi_s|\phi_g)$, est construite de sorte (i) à prendre en compte le caractère spatialement intermittent de la suie, et (ii) à limiter la superposition entre la suie et les espèces oxydantes, Yang et al. (2019) :

$$\widetilde{P}(\phi_s|\phi_g) = \left[\omega\delta(\phi_s) + (1-\omega)\delta(\phi_s - \phi_s^*)\right] H(Z - Z_s)$$

La production de suie a dans un premier temps été modélisée par un modèle basé sur l'acétylène, C_2H_2 et le benzène, A_1, Lindstedt (1994), validé pour les combustibles C_1-C_3. La radiation des gaz et de celle issue de la suie ont été prises en compte. Une attention particulière a été portée au traitement de l'interaction entre la radiation et la turbulence (IRT), à savoir, le terme d'absorption de sous-maille de la IRT a été négligé alors que le terme d'émission est modélisé avec l'approche de la FDF présumée. Trois flammes de diffusion d'éthylène, contrôlées par la flottabilité, à l'échelle laboratoire, bien documentées et brûlant dans des conditions d'air et de sous-ventilation, ont été simulées. Les prédictions du modèle reproduisent fidèlement la structure de la flamme, la dynamique de production de suie et la perte radiative. Les résultats du modèle montrent que la suie et les gaz rayonnants contribuent de manière similaire à la radiation pour la flamme brûlant dans l'air, et que la contribution des gaz

rayonnants devient de plus en plus dominante avec la réduction d'oxygène en raison d'une diminution de la fraction volumique de suie (FVS) dans les flammes. De plus, ces investigations confirment que l'inclusion de la corrélation entre les grandeurs de la suie et la fraction de mélange est essentielle, car l'ignorer a conduit à une sous-estimation importante de la FVS. Dans cette SGE, où plus de 80% de la variance de la température est résolue, négliger l'émission de sous-maille de la IRT a également un impact significatif en causant une surestimation de la FVS moyenne et de son écart quadratique moyen par un facteur de deux. D'autre part, l'approximation de la suie grise est valide pour ces flammes à l'échelle du laboratoire caractérisées par des épaisseurs optiques modérées, et l'utilisation d'un modèle WSGG non gris couplé à l'approximation de la suie grise représente une alternative aux modèles FSK.

Les applications dans l'incendie impliquent des combustibles contenant des aromatiques, or le modèle de production de suie de Lindstedt basé sur l'acétylène/benzène est limité aux combustibles non aromatiques en raison de sa formulation, ce qui l'empêche d'être étendu vers des combustibles complexes. En présence d'aromatiques, l'alternative naturelle semble être les modèles détaillés basés sur les HAP, un second modèle de production de suie a donc été développé. Il considère le pyrène (A_4) comme précurseur de la suie et adopte une description détaillée de la formation et de la croissance de la suie en utilisant une formulation à trois équations pour sa dynamique. Afin de s'affranchir des difficultés et des couplages liés à la turbulence, le modèle a été développé et vérifié sur des flammes de diffusion laminaires de type "coflow" bien documentées brûlant dans des conditions normales et réduites en oxygène avec un combustible simple pour commencer, à savoir l'éthylène. Dans ces flammes, l'oxydant et le combustible sont simultanément N_2-dilués de sorte que la réduction en oxygène est le seul responsable de la baisse en suie résultante. Les prédictions se sont montrés en accord raisonnable avec les données expérimentales en termes de température, de FVS, et de taille de particules primaires. De plus, il parvient à capturer l'influence de la réduction en oxygène et permet d'appréhender les différents processus de la suie dans la flamme. L'analyse des processus de production de suie montre que les processus de condensation et de croissance de surface jouent des rôles comparables dans la croissance de la suie.

Le modèle basé sur le pyrène a ensuite été étendu aux carburants de substitution à l'essence en simulant des flammes de diffusion laminaire de type "coflow" alimentées par des mélanges de n-heptane, d'iso-octane et de toluène. Le modèle basé sur le pyrène capture le pic de FVS et la FVS intégrée dans les mélanges n-heptane/toluène et iso-octane/toluène représentatifs de l'essence. Le modèle à pyrène se montre ainsi adéquate pour des applications ingénieries sur des mélanges n-heptane/iso-octane/toluène. Cependant, il sous-estime considérablement la production de suie pour le n-heptane pur et l'iso-octane pur, et prédit un début de production de suie significativement plus précoce lors de l'ajout de toluène. Une étude poussée a été effectuée pour mieux comprendre ces écarts du modèle à pyrène avec l'expérience et pour élaborer une stratégie d'amélioration. D'abord, une étude de sensibilité a montré que le modèle est largement insensible à une variation de ses paramètres et que l'origine de la sous-estimation est due à un manque de précurseur prédit. Ensuite, l'analyse chimique des réactions de formation du pyrène révèlent (i) que l'addition du toluène augmente la contribution de deux réactions qui déplacent le pyrène en amont, expliquant ainsi la précocité de la suie, et (ii) des incertitudes liées à la chimie

des HAP et à l'influence du toluène sur ces derniers. Ces deux points suggèrent que le choix du HAP précurseur doit être adapté a priori au mécanisme et aux combustibles. D'une part, le pyrène ne convient pas pour le n-heptane et l'iso-octane pur avec le mécanisme cinétique utilisé car il ne permet pas une production de suie massique suffisante. D'autre part, la présence du toluène oriente le choix du précurseur vers les HAP larges car ce dernier contribue à la formation de HAP de taille intermédiaire (de A_1 à A_4). Le précurseur HAP se doit de refléter les caractéristiques de la suie pour l'ensemble des combustibles ciblés, cela se traduisent par les deux propriétés suivantes : (i) le HAP doit se former ni trop tard ni trop tôt par rapport à la suie, (ii) la concentration du HAP prédite doit être suffisamment élevée pour permettre une prédiction massique de suie d'une amplitude raisonnable. Suivant ces principes, un HAP plus grand que le pyrène appelé anthanthrène (A_6), a été trouvé et a permis de fournir un accord plus quantitatif pour l'ensemble des flammes. L'analyse des processus de production de suie montre que la condensation des HAP contribue en majorité au processus de croissance des particules pour l'ensemble des mélanges de n-heptane, d'iso-octane et de toluène, ce qui marque un tournant par rapport à l'éthylène.

Ce travail représente ainsi un pas supplémentaire vers les applications incendies en proposant des solutions aux deux difficultés principales associées à la modélisation de la production de suie, notamment pour des combustibles complexes.

List of publications and conference participations

1) List of publications conducted within the framework of the thesis work :

1. F. Nmira, A. Bouffard, J.-L. Consalvi, and Y. Wang. Large-eddy simulation of lab-scale ethylene buoyant diffusion flames : Effects of subgrid turbulence/soot production interaction and radiation models. Proceedings of the Combustion Institute, 39(3) :3959–3968, 2023. https ://doi.org/10.1016/j.proci.2022.07.004.
2. F. Nmira, A. Bouffard, J. L. Consalvi. Flamelet/transported PDF simulations of ethylene/air jet turbulent non-premixed flame using a three-equation PAH-based soot production model. Combustion Theory and Modelling. 27(6) :820-851, 2023. https ://doi.org/10.1080/13647830.2023.2224755.
3. A. Bouffard, F. Nmira, S. Thion, J-L. Consalvi. On the mechanisms affecting soot production in oxygen-depleted buoyant flames. Fire Safety Journal. 141 :103958, 2023. https ://doi.org/10.1016/j.firesaf.2023.103958

2) Conference and summer school participations during the thesis period :

1. 3ème École des Sciences des Incendies et Applications École thématique du CNRS, May 30 to June 3, 2022, La Londe-les-Maures (France)
2. 39th International Symposium on Combustion, 24-29 July 2022, Vancouver (Canada)
3. 12th Mediterranean Combustion Symposium, 23-26 January 2023, Luxor (Egypte)
4. 12th FM Global Open Source CFD Fire Modeling Workshop, 4-5 April 2023, Norwood (USA)
5. 14th International Symposium on Fire Safety Science, 22-27 October 2023, Tsukuba (Japan)

Acknowledgements

Je remercie chaleureusement Fatiha Nmira et Jean-Louis Consalvi pour leur encadrement formidable et pour m'avoir inclus dans leur travail de recherche, à tous points de vue passionnant. Merci pour m'avoir donner l'opportunité de m'enrichir à la fois scientifiquement et humainement durant ces trois années. Votre soutien et votre rigueur m'ont permis de donner le meilleur de moi-même et de repousser mes limites.

Merci à Olivier Vauquelin d'être mon président de jury, à Fengshan Liu, Denis Veynante d'avoir accepté de rapporter ma thèse, et à Frédéric André, Yi Wang et John Hewson d'avoir accepté de participer au jury.

Cette thèse s'est déroulée au sein du département MFEE d'EDF. Je tiens, à ce titre, à remercier particulièrement la cheffe de groupe I8D, Christelle Raynaud pour son management admirable et les membres du groupe I8D. J'ai une pensée pour mes camarades thésards : Guillaume, Lianfa, Federico, Ali, Manon, Roger, ... Cette thèse s'est également déroulée en collaboration avec l'IUSTI d'Aix-Marseille Université, je tiens à remercier Alain pour son accueil lors du séjour à l'IUSTI.

Je tiens à remercier ma famille, mes parents pour leur soutien, qui n'a jamais fait défaut.

Table des matières

Table des figures

Liste des tableaux

Nomenclature

$(\langle\cdot\rangle)$ Average operator
$(\bar{\cdot})$ Reynolds-filter operator
$(\tilde{\cdot})$ Favre-filter operator
$[PAH]$ Molar concentration of PAH mol/m^{-3}
$\chi_{C_{(s)}-H}$ Number density of radical sites on the soot surface, sites/m^2
$\chi_{C^{\bullet}_{(s)}}$ Number of saturated sites per particle surface, sites/m^2
$\dot{\omega}^{N_s}_{coag}$ Soot particle coagulation rate, part/m^3/s
$\dot{\omega}^{N_s}_{nuc}$ Soot particle nucleation rate, part/m^3/s
$\dot{\omega}^{Y_s}_{cond}$ Soot condensation rate, $kg/m^3/s$
$\dot{\omega}^{Y_s}_{nuc}$ Soot mass nucleation rate, $kg/m^3/s$
$\dot{\omega}^{Y_s}_{ox,O_2}$ Soot oxidation rate by O_2, $kg/m^3/s$
$\dot{\omega}^{Y_s}_{ox,OH}$ Soot oxidation rate by OH, $kg/m^3/s$
$\dot{\omega}^{Y_s}_{sg}$ Soot surface growth rate, $kg/m^3/s$
γ_{nuc} Collision efficiency of nucleation
ρ_s Soot density, kg/m^3
φ_{OH} Collision efficiency for OH oxidation
$\widetilde{Z^2}$ Second moment of the mixture fraction
A Pre-exponential factor, $cm^3/mol/s$
a Strain rate, $1/s$, or coefficient of the β-distribution
A_s Soot specific surface area, m^2/m^3
b Coefficient of the β-distribution
C_A Coagulation rate constant
C_I Constant associated with the DEDM
$C_{(s)}-H$ Saturated carbon site
$C^{\bullet}_{(s)}$ Dehydrogenated carbon site
$C_{p\alpha}$ Heat capacity of species α, J/K
D_c Fractal aggregate collision diameter, m
D_f Fractal dimension
d_s Soot particle diameter, m
D_t Subgrid-scale turbulent diffusivity, m^2/s

D_α Molecular diffusivity of species α, m^2/s

$d_{p,crit}$ Critical primary particle diameter, m

D_{PAH} Molecular diffusivity of the PAH m^2/s

d_{PAH} Collision diameter of the PAH, Å

D_{th} Thermal diffusivity, m^2/s

E Activation energy, $kcal/mol$

f_{vs} Soot volume fraction

g_i Gravitational acceleration in the j^{th} direction, m/s^2

h Total enthalpy, J/kg

h_{ad} Adiabatic enthalpy, J/kg

$h^0_{f,\alpha}$ Formation enthalpy of species α, J/kg

I_i Radiative intensity, W/m^2

$I_{b\eta}$ Spectral blackbody intensity, W/m^2

I_b Blackbody intensity, W/m^2

k_B Boltzmann constant, $k_B = 1.38 \cdot 10^{-23}\ J/K$

M_c Carbon molecular weight, kg

m_c Mass of carbon atom, $12 \times AMU$, $AMU = 1.67 \cdot 10^{-24}$, kg

m_{PAH} Mass of the PAH, kg

N_s Soot aggregate number density or Soot number density, part/kg

N_{av} Avogadro number, 1/mol

$N_{C,min}$ Number of carbon atoms in a soot nuclei

$N_{c,PAH}$ Number of carbon atoms in the PAH

N_{ps} Primary soot number density, part/kg

p Total pressure, Pa

P_{OH} Partial pressure of OH, Pa

R Gas constant, $J/K/mol$

T Temperature, K

T_b Planck temperature, K

u_i Velocity in the i-th direction, m/s

u_{th} Thermophoresis velocity of soot particles, m/s

V_Z Subgrid-scale mixture fraction variance

W_i Molar mass of species i, kg/m^3

W_s Molar mass of soot, kg/m^3

x_i Molar fraction of the species i

X_R Enthalpy defect, J/kg

Y_s Soot mass fraction

$Y_{-r,int}$ Radially integrated species mass fraction

Y_α Species α mass fraction

Y_{PAH} Mass fraction of the PAH

Z Mixture fraction

Greek symbols

β Beta distribution

χ Scalar dissipation rate, $1/s$

χ_{st} Scalar dissipation rate at the stoichiometric, $1/s$

Δ Grid filter width, mm

δ Constant for the SLF model or delta-distribution

η Wave-number, $1/cm$

κ_i Non-grey absorption coefficient of gas, $1/cm$

κ_η Spectral absorption coefficient of gas, $1/cm$

$\kappa_{s,\eta}$ Spectral absorption coefficient of soot, $1/cm$

λ Heat conductivity, $W/m/K$

μ Dynamic viscosity, $kg/m/s$

ρ Density, kg/m^3

ρ_s Soot density, kg/m^3

σ Stefan-Boltzmann constant, $W/m^2/K^4$

ξ Adjusted constant for the active site conservation/depletion concept

Acronyms

AFM Atomic force microscope

AMU Unified atomic mass unit (amu), $1.67 \times 10^{-24}\ kg$

CDSM Chemical discrete sectional method

DEDM Dynamic eddy diffusivity model

DNS Direct numerical simulation

DOM Discrete ordinate method

DSM Discrete sectional method

DSM Dynamic Smagorinski model

FDF Filtered density function

FS Full-Spectrum

FVM Finite volume method

HRR Heat release rate, kW

LBL Line-by-line method

LES Large-Eddy-Simulation

LII Laser induced incandescence

LMMS Laser microprobe mass spectrometry

LST Lagrangian soot tracking

MC Monte-Carlo

MoM Method of moments

NB Narrow Band

OTA Optically-thin approximation

OTFA Optically thin fluctuation approximation
PAH Polycyclic aromatic hydrocarbon
PBE Population balance equation
PDF Probability density function
PSD Particle size distribution
RANS Reynolds averaged Navier-Stokes equations
RCFSK Rank-Correlated Full-Spectrum k-distribution
RSR Resonantly stabilised radicals
RTE Radiative Transfer Equation
SGS Subgrid-scale
SLF Steady laminar flamelet model or Extended non-adiabatic flamelet model
STI Soot production/turbulence interaction
TCI Turbulence/chemistry interaction
TPDF Transported PDF
TPRF Toluene primary reference fuel
TRI Turbulence/radiation interaction

Dimensionless numbers

Da Damköhler number, diffusion time over chemical time
Fr Froude number, kinetic energy over gravitational potential energy
Le Lewis number, thermal diffusion over molecular diffusion
Re Reynolds number, inertial forces over viscous forces

1 Introduction

Table of contents

1.1 Context

Electricité de France (EDF), as an operator, is responsible for the safety of the nuclear power plants and defines, in agreement with the regulation, the means and the organisation implemented to ensure that its facilities do not present risks for the public and the environment.

Unwanted fires in nuclear plants is the most important risk for internal damage. Besides the safety of its staff and the operation of its facilities, EDF has an economical interest, related to the loss of material and immobilization, to reduce the fire risk by ensuring a high level of safety without using oversized fire-fighting means. The need for demonstration of the efficiency of fire safety with numerical models, thanks to the improvement of knowledge and computational resources, is increasing. Addressing these issues, with their complex economic and environmental implications, requires a better understanding of the fundamental physics of fire spreading and the development of reliable methods for modelling and analyzing fire safety systems.

The modelling tools developed by EDF R&D have been used for several years to answer questions relative to fire safety. Today, the two-zone code MAGIC is used as reference. It is based on the assumption of a stratification of the hot gases above the fresh gases and can provide rapid answers due to its low computational cost. Although this approach is efficient, it is not able to capture all the processes of the fire phenomena. In addition, it becomes less relevant in absence of stratification. The utilization of

a large eddy simulation (LES) based CFD model of fire spread in nuclear plants is a natural way to circumvent these limitations.

1.2 Pool fire : a canonical fire configuration

Pool fires are one of the most frequently encountered types of fires in both industrial and domestic settings. They occur when a flammable liquid, such as gasoline or oil, ignites and forms a pool on the ground or in a container. Pool fires are especially relevant because they contain most of the coupled physical processes involved in fire problems : buoyancy-controlled flows, buoyancy-induced turbulence, turbulent combustion, soot generation, gaseous and soot radiation, and burning rate. Pool fires also provide a well-controlled configuration representative of more complex fire scenarios. They are thus a canonical configuration in fire science, Brown et al. (2018).

The gas-phase combustible, supplying the flame, derives from the thermal decomposition of condensed combustible under the heat feedback of the flame by convective or radiative heat transfer. This self-sustained process controls the flame heat release rate, and inherently, the development of the fire and the interaction with its environment. These released gaseous species are then transported away in the buoyancy-driven regime by convection/diffusion to the reaction zone.

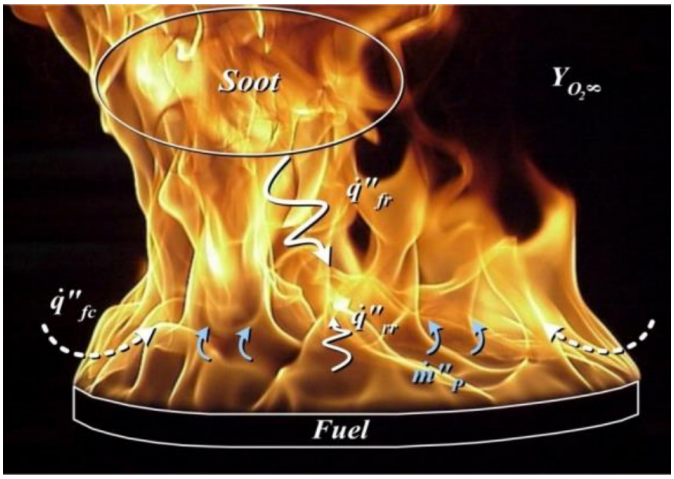

Figure 1.1 – Phenomenological illustration of a pool fire.

Figure 1.1 illustrates this canonical diffusion flame configuration. The term "diffusion (or non-premixed) flame" implies that fuel and oxidizer are not initially premixed, their mixing occurring prior to combustion. The flow evolves within the buoyancy-driven regime with the fuel injection velocity being significantly lower than the velocity induced by the gravitational acceleration, g. The Froude number, $Fr = u_{\text{inj}}^2/gL$ is typically in the order of 10^{-2}-10^{-6}, Cox (1995), where u_{inj} is the fuel inlet injection

velocity and L the characteristic length of the pool fire, typically the flame length or the pool diameter. The purely-buoyant nature of the flow leads to the formation and the growth of non-dissipative non-linear laminar instabilities near the edge of the pan that develop to become energy containing turbulent structures, Tieszen and Gritzo (2008). These structures develop periodically to form energy containing large-scale toroidal vortices that govern the flow pattern, the air entrainment as well as the mixing and combustion processes. In a figurative sense, these vortices act like a pump, drawing in fresh air behind them and supplying the necessary oxygen to the flame. When these vortices are released at the top of the flame, they cause a disruption, and a new vortex forms at the base of the flame. The frequency of this sequence, known as the flame puffing, is inversely proportional to the square root of the diameter of the fire. As discussed by Tieszen et al. (2004) and Tieszen and Gritzo (2008), these instabilities are initially non-dissipative and the associated mixing cannot be captured by conventional subgrid-scale turbulence models that are dissipative in nature. The near field flow is thus rather complex. It exhibits a rapid transition from laminar to fully turbulent regime in the few first inlet diameters and a puffing motion characterized by a repetitive shedding of these coherent vortices, Cetegen and Ahmed (1993).

Thermal radiation of gaseous combustion products (CO_2 ,H_2O, CO, and some hydrocarbons) and soot play a strong role in the growth and spread of fires. It is the dominant mode of heat transfer in most applications and soot radiation usually prevails in real fires, de Ris (1979). The gasification of the condensed fuel is the result of convective and radiative fluxes transferred from the flame to the fuel, as depicted in Figure 1.1. The radiative flux contribution increases with the fire size and the fuel sooting propensity, Ditch et al. (2013). More specifically, radiation feedback prevails over convection for pool diameter larger than 20-30 cm, de Ris (1979). The lab-scale experiments of Hamins et al. (1994), involving pool fires with a diameter of approximately 30 cm, showed that radiation accounts for 55%, 80%, and 96% of the heat transferred to the surfaces of methanol, heptane, and toluene pools, respectively. These results illustrate the importance of soot in this heat transfer, the sooting propensity of toluene being higher than that of heptane, that is in turn higher than that of methanol. Consequently, the modelling of soot production and the related radiation is fundamental to predict the fire growth.

The flow structure described earlier forms the fire plume, it is typically divided into three regions : the continuous flame region, the intermittent flame region, and the smoke plume, McCaffrey (1979). Fires in nuclear plants often occur in confined environment, which alters the fire plume. In a confined environment, during the fire growth phase, the smoke plume impacts the ceiling and forms a stream of hot gases. This stream of hot gases then encounters the side walls, expanding the layer of hot gases below the ceiling. The size, temperature, and vitiation of this layer continuously increase due to the supply from the smoke plume. As a result, the heat transfer from the hot layer and the adjacent walls to the fire source adds to that coming from the flame, thereby increasing the flame heat release rate, Karlsson and Quintiere (1999). In the case of highly confined environments, the air fueling the flame quickly becomes

heavily vitiated, leading to localized phenomena of extinction and/or re-ignition. Gaseous combustibles, carbon monoxide, and soot escape then from the fire and are released into the surroundings. This can lead to a change in the fire behavior, particularly a movement of the fuel load throughout the enclosure, including potential re-ignitions near openings if the unburnt gaseous fuel mixes with air and encounters points of sufficient heat. Flames may no longer be located close to the fuel source but rather where the stoichiometric ratio between fuel and oxygen is met. These are referred to as "ghost flames", Bertin et al. (2002). This has motivated experiments involving fire plumes in well-controlled oxygen-reduced atmospheres (Santo and Tamanini (1981), Santo and Delichatsios (1984), White et al. (2015), White et al. (2017), Zeng and Wang (2017), Zeng et al. (2019), Xiong et al. (2021)). These experiments revealed that the first effects of reducing X_{O_2} is to decrease the soot concentration and the associated radiative heat transfer while combustion remains almost complete over a wide range of oxidizer dilutions before decreasing rapidly at the onset of global extinction (White et al. (2017), Zeng et al. (2019)). Specific exhaustive experiments were undertaken at FM Global to investigate the effects of reducing oxygen below normal air level on soot production and corresponding radiative heat transfer in 15 cm diameter ethylene buoyant flames (Zeng et al. (2019), Ren et al. (2019), Xiong et al. (2021)). In these experiments, the oxygen was reduced down to to 15.8%, a level far above that of about 12% where local extinction appears, and detailed measurements of temperature statistics, soot volume fraction statistics and radiative outputs were reported.

1.3 Motivations

The previous literature survey on pool fires highlights the importance of soot radiation in fire growth. The objective of this PhD thesis is then to extend the Large-Eddy-Simulation numerical model dedicated to the simulation of well-ventilated and under-ventilated purely buoyant fire plumes, developed for non-sooting fuels (Ma (2020)), to sooting fuels. This model relies on a new second-order low-Mach number variable-density flow solver and state-of-the art subgrid-scale turbulence, combustion and radiation models were specifically developed, including the non-adiabatic SLF (steady laminar flamelet) model, the FPV (flamelet/ progress variable) model and the RCFSK (rank correlated full spectrum k-distribution) model for the radiative property. This numerical model was found capable to reproduce with high fidelity the dynamic and radiative structures of non-luminous fire plumes in both ventilated and under-ventilated configurations without adjusting any model parameters. All these developments were implemented into code_saturne, the in-house code of EDF R&D (2023).

The modelling of soot production in fire applications introduces two main difficulties:

1. Soot production is characterized by a slow chemistry and, as such, soot quanti-

ties cannot be tabulated *a priori* in a flamelet library. A soot production model is then required and, although soot-related production processes are not fully understood, Martin et al. (2022), the modelling of soot production has known significant progress over the last twenty years with the development of very detailed PAH-based soot production models Liu et al. (2022). However, these models were mainly applied to gaseous fuels, such as ethylene, and a limited number of studies was reported for liquid or solid fuels encountered in fire problems. The choice of an appropriate soot production model for such applications rises then interrogation and requires further investigations.

2. The interactions between chemistry/soot production/radiation/turbulence is a complex problem that requires the development of specific subgrid-scale models, Liu et al. (2022). Specific RANS/transported PDF modelling have been developed in the past at EDF R&D (Burot (2017)), but their extension to LES fire applications may be not computationally affordable. A compromise between accuracy and computational efficiency has then to be obtained, which is an objective of the present work.

The next section presents a detailed literature survey on these two problems with the objective to justify the modelling strategy adopted in this study.

1.4 Literature survey

1.4.1 Soot production modelling

1.4.1.1 Generalities on soot particles

Soot particles are a byproduct of incomplete fuel rich combustion. They consist mainly of carbon, with smaller amounts of other elements such as hydrogen up to 10% per mole, oxygen to a lesser extent and trace amounts of various contaminants. Figure 1.2 shows transmission electron microscopy (TEM) views of soot particles at different stage of evolution in an ethylene, C_2H_4, flame burning at atmospheric pressure. This figure shows that soot particles are made of nearly spherical primary particles (10-50 nm) aggregated together to form fractal aggregates (30-200 nm). The number of primary particles per aggregate can be up to a few hundreds, Köylü and Faeth (1992).

In the annals of history, soot served as pigment that was used in cave paintings by prehistoric humans, Curtis (2007), Gradziński et al. (2007). The oldest known tattoos, belonging to a Tyrolean iceman, were etched with soot, Pabst et al. (2009). In the same vein, the soot deposits trapped in concretions witness the human occupations of caves and rock shelters in prehistoric times, offering valuable insights with high temporal resolution up to six months, Vandevelde et al. (2018). More recently in time, soot particles emitted by human activities pose serious concerns regarding their impact on health, atmospheric pollution and global warming. Soot particles list among the

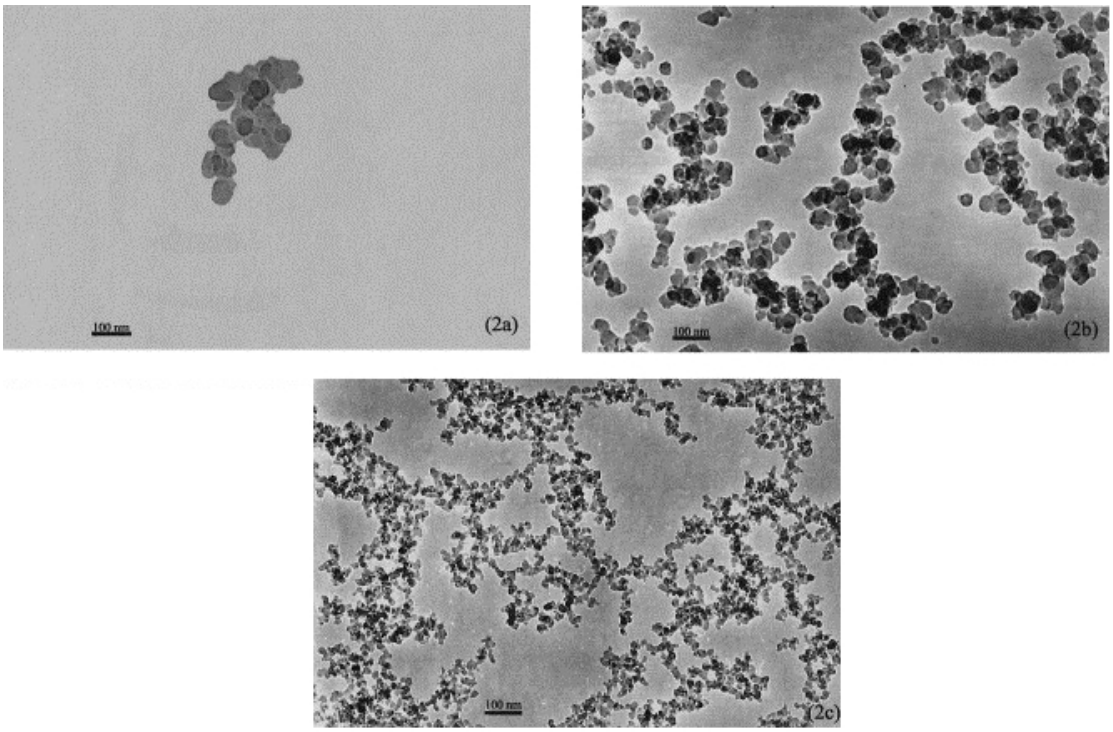

Figure 1.2 – TEM views of soot aggregates along the axis of a C_2H_4 laminar coflow diffusion flame burning in air at atmospheric pressure : (2a) near start of soot formation, (2b) near the maximum soot concentration, (2c) near the end of soot oxidization, Xu et al. (2003).

particulate matter, PM 2.5, U.S. Environmental Protection Agency (2023), and can cause lung dysfunctions and cardiovascular diseases, Donaldson et al. (2005). Soot particles also contribute to global warming and climate change as it absorbs solar radiation, influences cloud processes, and alters the melting of snow and ice cover, Jacobson (2002), Bond et al. (2013). In an industrial approach, carbon blacks, which are similar to soot particles but purer and structurally different, are synthesized and utilized for various applications. They serve as a reinforcing agent in rubber and a black pigment in inks, coatings, and plastics, Watson and Valberg (2001). Conversely, in industries such as automotive and aviation, efforts are undertaken to minimize the unintentional generation of soot particles due to their detrimental effects. Indeed, soot can lead to harmful carbon deposits in engines and the formation of hot spots, along with increased combustor wall temperatures caused by soot radiation, Dagaut and Cathonnet (2006), not to mention that the engine soot emission must adhere to very strict environmental regulations.

1.4.1.2 Physical and chemical processes in soot formation

— **Background.** Soot production occurs over a range of conditions characterized by carbon-to-oxygen ratio (C/O) higher than about 0.6, Martin et al. (2022). Soot is then produced on the fuel side of the reaction zone in non-premixed flames, and for temperatures from ~ 1350 K to ~ 2000 K, Martin et al. (2022). The thresholds on temperature suggest that, on one hand, the soot formation processes require sufficiently high temperatures to be activated and, on the other hand, higher temperatures could suppress soot formation through fragmentation of soot precursors. Polycyclic aromatic hydrocarbons (PAHs), that consist of benzene rings (A_i refers to a PAH with i rings), play a major role in soot formation and a distinction has to be made between them and aliphatics, which have open-chain structure. For aliphatics, it is necessary to form first benzene (A_1) to initiate PAH and soot formation, whereas for flames fueled with aromatics, formation and growth of PAHs beyond benzene become the rate-limiting step in the overall soot formation process, Martin et al. (2022).

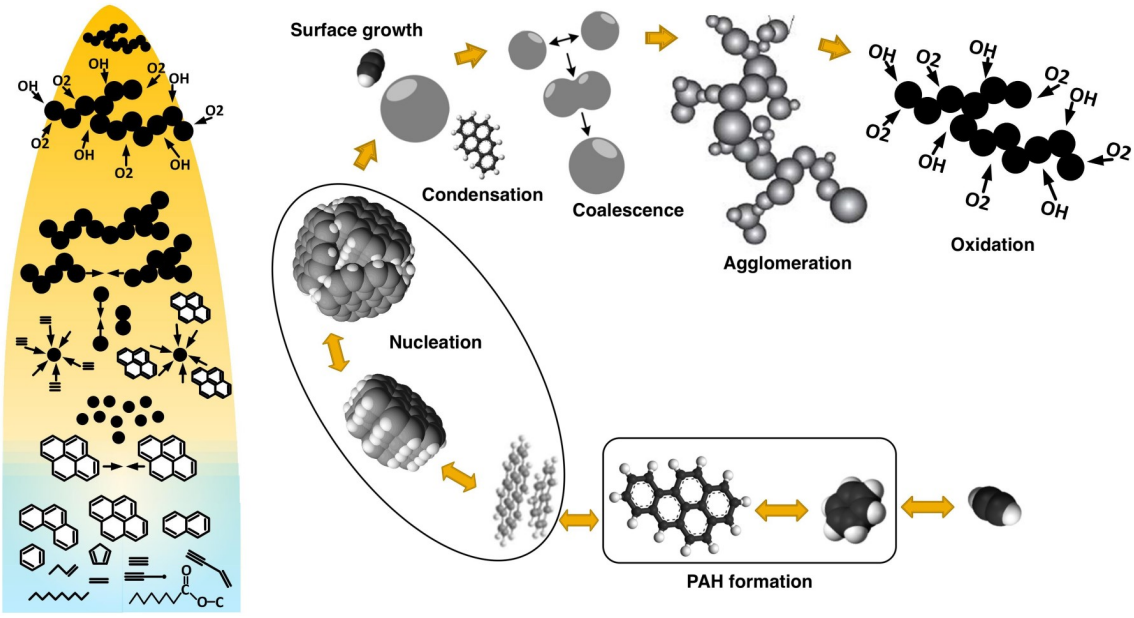

Figure 1.3 – Schematic description of the soot evolution, annotated after extraction from Thomson Lab (2016).

The main chemical and physical processes involved in soot formation in flames fueled with aliphatics include : (i) fuel pyrolysis and formation of radicals and intermediate hydrocarbon species, (ii) formation of benzene, (iii) formation and growth of PAHs, (iv) formation of incipient soot particles through coagulation and dimerization of PAHs (nucleation), (v) formation of primary soot particles through coalescence, coagulation, and surface growth (via C_2H_2-addition and PAH-condensation) of incipient soot particles, (vi) formation of fractal-like soot

aggregates through agglomeration of primary soot particles, and finally, (vii) oxidation and oxidation-induced fragmentation of soot aggregates. These processes are schematically illustrated in Figure 1.3. For soot formation in aromatic fuels, such as toluene, step (ii) will be bypassed.

— **PAH.** The accumulating body of experimental and theoretical proofs has established a scientific consensus on PAHs as the molecular precursors of soot particles. PAHs have already been associated with soot formation many decades ago by Rummel and Veh (1941), who suggested that moderately large PAH molecules react to form soot. Since then, a substantial number of research studies have shed light on PAH chemical formation and the transition from gas-phased PAH molecules to condensed phase carbonaceous particles, though unresolved questions and uncertainties remain Martin et al. (2022). Indeed, PAH species are challenging to investigate, one significant reason is their low concentrations in flames. PAH peak concentrations decrease exponentially for increasingly larger PAHs (Wang and Chung (2019)) as shown by Vincitore and Senkan (1998), who obtained that the mole fraction for the two-ring naphthalene and four-ring pyrene dropped to 10^{-5} and 10^{-6}, respectively, when the benzene mole fraction started at 10^{-4}, in a typical ethane counterflow diffusion flame.

In the last few decades, experimental techniques have provided insights on the nature of PAH precursors owing to the gradual progress of experimental methods. Most of the experimental data available on soot precursors compositions stems from mass spectrometry and optical/spectroscopic studies. Siegmann et al. (1995) carried out a time-of-flight mass spectrometry combined with laser two-photon ionization to investigate the PAH composition of the combustion gases in methane laminar diffusion flames. PAHs with 6-38 C-atoms were found with the highest peak corresponding to two-ring PAHs. Consistently, PAHs with 16-32 C-atoms (202–472 amu) were measured by Dobbins et al. (1998) who carried out a laser microprobe mass spectrometry (LMMS) on soot samples in the centerline of an ethene diffusion flames. Though these two techniques demonstrate that the surrounding gas and soot particle compositions can be correlated, the highest PAH peaks in soot samples were obtained for PAHs with 20 to 22 C-atoms, which conveys that small PAHs may play a minor role in the soot inception process. The more recent study of Sabbah et al. (2021) is in agreement with previous works. These authors analyzed nascent soot particles at 8 mm above the burner using two-step laser desorption laser ionization mass spectrometry and observed that just-nucleated soot are composed of PAHs of medium sizes from 18 to 40 C-atoms (200-700 amu) with 36 C-atoms on average. This is illustrated in Figure 1.4. PAHs containing up to 90 C-atoms were also detected.

Öktem et al. (2005) determined the chemical composition of soot using PIAMS technique that allows both aliphatic and aromatic compounds to be studied simultaneously. The technique detected the presence of aliphatic hydrocarbon chains 2-10 C-atoms as well as aromatics species with 6-membered and

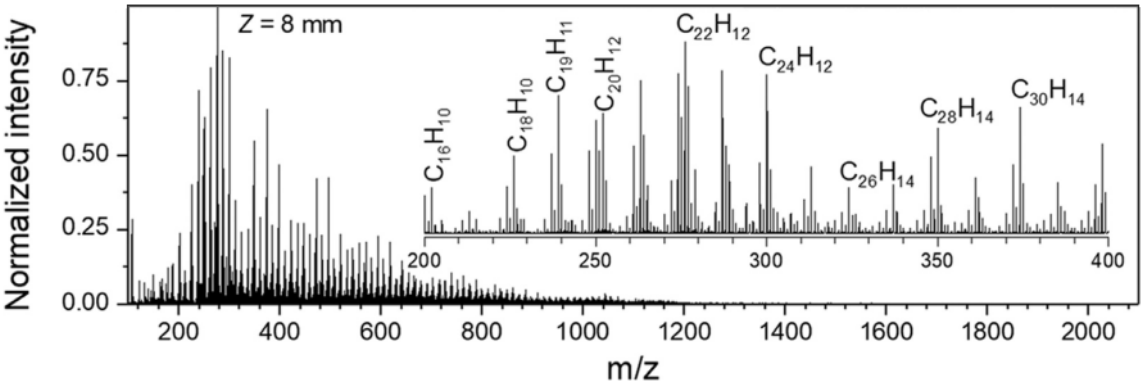

Figure 1.4 – Mass spectra of soot particles, sampled in a ethylene/air laminar premixed flame, extracted from Sabbah et al. (2021).

5-membered rings with a total of carbon atoms in the range of 16-25 for the highest peaks. The presence of aliphatic compounds was also confirmed by Cain et al. (2010) who carried out an infrared spectrometer coupled to a microscope (micro-FTIR).

Nascent soot particles seems to be composed of a wide variety of moderately large PAHs with mostly 16-40 C-atoms. However, mass spectrometry analysis provides only global information on the chemical/structural configuration which compels experimenters to interpret the molecular configuration. Mass spectrometry peaks are mostly interpreted as belonging to the most thermodynamically stable isomers defined by the Stein and Fahr grid, called stabilomers (see Figure 1.5 for examples of stabilomers). However, mass spectrometry peaks may not correspond entirely to stabilomers. Johansson et al. (2017) conducted an aerosol mass spectrometry coupled with tunable vacuum ultraviolet radiation for photoionization and compared the ion-signal response at 202 amu with pure pyrene, they obtained a departure which proved that other isomers of pyrene contributed to the 202 amu peak. Theoretical methods can be employed to determine the isomeric configuration but as the mass of molecules considered gets significant, their configuration interpretation become more uncertain.

The recent development of atomic force microscopy (AFM) permits a more detailed observation of the composition of nascent soot particles. Schulz et al. (2019) and Commodo et al. (2019) employed high-resolution AFM on soot samples of a laminar premixed ethylene/air flame above the burner to obtain direct imaging of the building blocks of the initial soot particles. The number of carbons ranges from 14 to 60 (200 to 700 amu) with a large number of molecules with 24–30 C-atoms (300–400 amu), in consistence with previous experimental works. Figure 1.6 illustrates some of the AFM images with their respective skeletal formula. Molecule M1, M5 and coronene in Figures 1.6 are isomers with 7 rings and AFM enables the distinction of the different structural configuration and

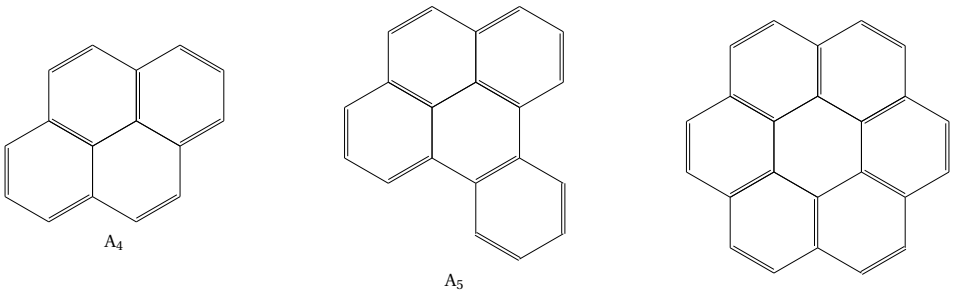

Figure 1.5 – A few examples of PAH stabilomers : A_4 pyrene ($C_{16}H_{10}$), A_5 Benzo(e)pyrene ($C_{20}H_{12}$), A_7 coronene ($C_{24}H_{12}$).

the presence of 5-membered rings. In addition, Schulz et al. (2019) provided experimental evidence of the presence of aromatics molecules linked by aliphatic chains (AALH) and aromatics with an aliphatic branch e.g molecule M2 and M6. Overall, AFM results stress out even more the variety and complexity of PAH structural configurations and the PAH large molecular size range. A quantitative census of all the PAHs encountered in typical flames is yet to be achieved.

The variety and complexity of PAHs is the primary hindrance in developing inception models based on PAHs, since any kinetic mechanism needs to consider the multitude of PAH molecules that are present. Moreover, the number of reaction pathways involved in forming PAHs grows exponentially with their sizes, Wang and Chung (2019). Wang (2011) even points out that it is uncertain whether the number of pathways to PAHs in real-fuel combustion can be treated as finite, given the large variability in fuel composition.

The most well-known and the keystone PAH growth pathway is the hydrogen-abstraction-C_2H_2-addition mechanism (HACA) proposed by Frenklach et al. (1985) which stands for the repetitive sequence of two primary steps : (i) activation of an aromatic molecule by H abstraction, (ii) followed by the carbon addition to the formed radical. The carbon is often assumed to be C_2H_2, as it is one of the most abundant and relevant species. However, the HACA mechanism exhibits a kinetic reversibility which opens the HACA sequence up to competition from other reaction pathways, Wang (2011). What's more, the HACA sequence alone underpredicts the concentration of PAHs in flames, Raj et al. (2012).

Many other mechanisms have been proposed for PAH growth that involve molecules such as CH_x, C_2H_x, C_3H_x, C_4H_x (Liu et al. (2015), Shukla et al. (2010), Georganta et al. (2017), Porfiriev et al. (2020), Landera et al. (2011), Kislov et al. (2013), Zhang et al. (2016), Wei et al. (2017), Tokmakov and Lin (2004), Lifshitz et al. (2008), Raj et al. (2014), Park et al. (2007), Tokmakov et al. (2005), Park et al. (2006), Richter and Howard (2000), Liu et al. (2019)). Moreover, resonantly stabilised radicals (RSR) such as propargyl, substituted propargyl, cyclopentadienyl, benzyl and indenyl radicals are important growth agents (e.g Sinha and Raj (2016)).

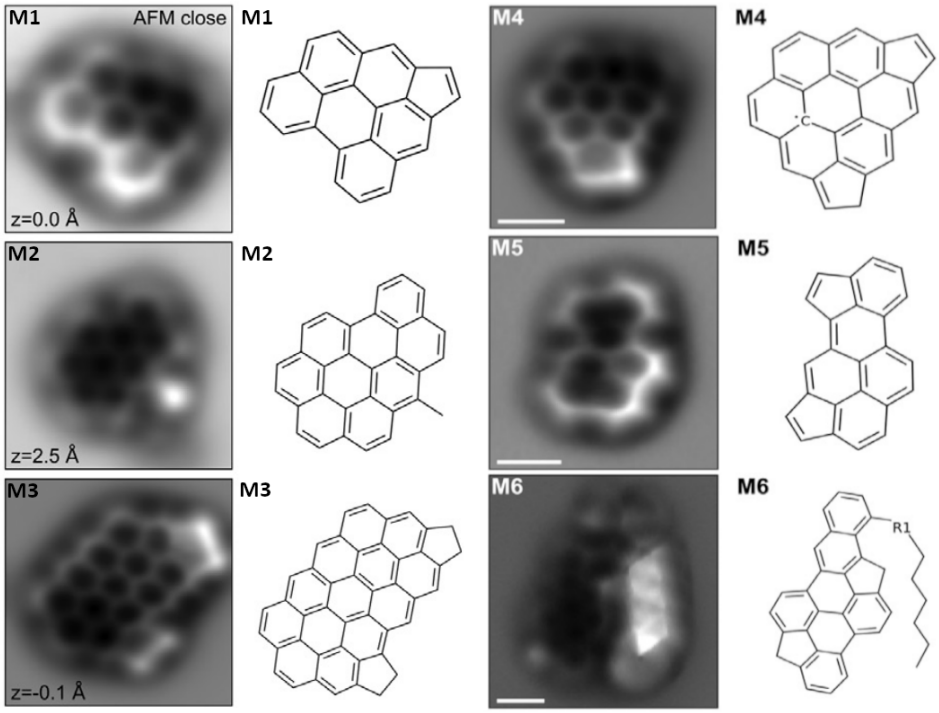

Figure 1.6 – AFM images and chemical structure of some representative PAH molecules extracted from Schulz et al. (2019). Raw formula are M1 ($C_{24}H_{12}$), M2 ($C_{31}H_{16}$), M3 ($C_{44}H_{20}$), M4 ($C_{28}H_{13}$), M5 ($C_{24}H_{12}$). Scale bars are 5 Å.

In essence, there exists many different pathways to PAH growth and many remain to be discovered. The relative importance of each individual pathway depends on fuel molecular structures as well as flame environments, Wang and Chung (2019). A significant number of these reactions are proposed only as global reactions and may contain uncertainties regarding their kinetic and thermodynamic data. As no better alternative is available, rate constants are often (i) assumed or fitted to match experiments, (ii) extrapolated from allegedly similar reactions, (iii) or obtained from chemical theories. To complicate matters, quantitative experimental data on PAHs are scarce, especially for PAHs beyond pyrene A_4, and are mostly qualitative. This scarcity hinders the validation of PAH mechanisms on an extensive range of flame configuration and perpetuates uncertainties.

— **Nucleation.** plays a bottleneck role in the subsequent growth of soot particles though it contributes negligibly to the mass of soot particles. This is because inception soot particles provide the initial soot surface for heterogeneous surface reactions and PAH condensation. The majority of PAH based soot inception models used in flame modelling assumes that incipient soot particles are formed as a result of physical dimerization of moderately sized PAHs. Soot inception

due to irreversible dimerization or coagulation of two PAH molecules through collision and sticking is assumed to proceed as :

$$\text{PAH} + \text{PAH} \rightarrow \text{dimer} \rightarrow \text{soot} \tag{1.1}$$

Dimers are considered incipient soot particles that provide initial surface for subsequent growth and oxidation through surface reactions and PAH absorption. Frenklach and Wang (1994) and Blanquart and Pitsch (2009a) provided the general expression for the formation rate of dimers of two PAHs of any size based on the gas kinetic theory. In the particular case of homogeneous dimerization by two identical PAH molecules, the soot inception rate is calculated as :

$$S_{incep} = 2.2\gamma\sqrt{\frac{4\pi k_B T}{C_{mass} N_{C,PAH}}} d_{PAH}^2 A_v^2 [\text{PAH}]^2 \tag{1.2}$$

where γ is the sticking efficiency to account for the short lifetime of dimers Blanquart and Pitsch (2009a), 2.2 is the van der Waals enhancement factor, k_B is the Boltzmann constant, C_{mass} is the mass of a carbon atom, $N_{C,PAH}$ is the number of carbon atoms in the PAH molecule, d_{PAH} is the average diameter of PAH molecule and is estimated as $d_{PAH} = d_A\sqrt{2N_{C,PAH}/3}$ with $d_A = 1.395\sqrt{3}$ Å being the size of a single aromatic ring, Frenklach and Wang (1994), and $[PAH]$ indicates the molar concentration of the PAH species involved. Pyrene has been the most widely assumed PAH species for soot inception through physical dimerization after the studies of Frenklach and Wang (1994) and Appel et al. (2000).

— **Surface growth/oxidation.**
H-abstraction Carbon addition (HACA). Acetylene, C_2H_2, and H atom are the most abundant intermediary species of combustion. Frenklach et al. (1985), Frenklach et al. (1986), Frenklach and Harris (1987) were the first to consider acetylene as a building block of PAH growth and H atom as the driving force. Frenklach and Wang (1994) proposed an analogy between PAH growth and soot surface growth. The proposed chemical mechanism is similar to the HACA mechanism, it also consists of an activation step follow by carbon addition, typically acetylene:

$$R_1 : \quad C_{(s)} - H + H \rightleftharpoons C_{(s)}^{\bullet} + H_2 \tag{1.3}$$
$$R_2 : \quad C_{(s)} - H + OH \rightleftharpoons C_{(s)}^{\bullet} + H_2O \tag{1.4}$$
$$R_3 : \quad C_{(s)}^{\bullet} + H \rightarrow C_{(s)} - H \tag{1.5}$$
$$R_4 : \quad C_{(s)}^{\bullet} + C_2H_2 \rightarrow C_{(s)} - H + H \tag{1.6}$$

Here, the activation site is a fictitious hydrogen site at the soot surface, $C_{(s)}$, that is activated by H-abstraction through reactions R_1-R_3 with a possible deactiva-

tion. Mass is then added to the soot particle via R_4 and growth is obtain with the successive sequences of the HACA mechanism. A variant carbon addition mechanism has also been proposed by Wang et al. (1996) that preserves the activated site in R_4 and other activation species by Hwang and Chung (2001) have been suggested.

Condensation. PAH species condensate on the soot surface, thereby increasing the soot particle mass. PAH species with a higher number of carbons have a higher success rate of condensation, Blanquart (2008), but there is also no consensus on what PAHs contribute to surface growth through adsorption.

Oxidation. Soot particles mass loss due the chemical action of oxidizers such as hydroxyl radical, OH, and oxygen, O_2 and O. OH is responsible for most of soot particle oxidation, Smooke et al. (1999). Soot oxidation may also lead to the fragmentation of particles if oxidation impact the inner bonds of particles, oxidizer species being rather small in size, Echavarria et al. (2011). Oxidation is temperature dependent and, as such, when the temperature decreases below a certain threshold, soot oxidation reactions are frozen. Soot particles are then called "cold soot".

— **Coagulation.** Soot particles are fractal-like aggregates as a result of coagulation. The term "coagulation" encompasses two modes of particle-particle interaction, when two particles collide :

- Coalescence : They merge, forming a bigger spherical particle,
- Agglomeration : They stick together while keeping they own initial form.

In both regime, the soot mass is preserved but the number density of particles is decreased.

1.4.1.3 Soot production modelling

Soot production models are generally decomposed into three categories, Kennedy (1997) : i) the detailed PAH-based models that incorporate all the physico-chemical processes described in the previous section, ii) the semi-empirical models that simplify these processes, and iii) the empirical models that are based on correlations with experimental data. In the recent literature on combustion and fire research, detailed and semi-empirical models were mainly considered, Liu et al. (2022). The objective of this section is to review these models to highlight their weaknesses and strengths in view of application to LES of fire applications (see Table 1.2).

— **Detailed models** : Detailed models involve: i) a gas-phase chemical mechanism that predicts the concentrations of chemical species involved in combustion and the soot precursors up to PAHs, ii) a soot kinetic model that incorporates all the processes of soot formation and growth as presented in the previous section : inception of soot from PAHs, surface growth through PAH condensation and

HACA mechanism, and oxidation by O_2 and OH, and, iii) a particle dynamics model that describes the evolution of the soot morphology. In this latter stage, the number density function (NDF) is introduced and the population balance equation (PBE) governing the NDF is solved either by using stochastic-based Monte-Carlo methods (e.g. Mitchell and Frenklach (1998), Balthasar and Kraft (2003)), moment-based methods (e.g.Frenklach and Harris (1987), Frenklach (2002), Marchisio and Fox (2005), Blanquart and Pitsch (2009a), Salenbauch et al. (2015), Mueller et al. (2009a)), or sectional methods (e.g. Netzell et al. (2007), Rodrigues et al. (2018), Dworkin et al. (2011b), Lindstedt and Waldheim (2013)). The two and three-equation soot models introduced in this thesis belong to the moment methods. These models were applied with success to the modelling of soot production in laminar and turbulent diffusion flames, Liu et al. (2022). However, the predictions of PAH-based models are strongly dependent on the chemical mechanisms mainly due to the uncertainty on the PAH growth sequences, Yang et al. (2019). These uncertainties are expected to increase with the complexity of the fuel considered. This is illustrated by the study of Kruse et al. (2019a) who investigated experimentally and numerically soot formation in laminar counterflow diffusion flames burning ethylene and three typical gasoline surrogate components, namely n-heptane, iso-octane, and toluene. Simulations were performed with two different detailed chemical kinetic mechanisms, detailed chemical soot models, and the hybrid method of moments as well as a discrete sectional method to describe soot dynamics. The models were found capable of predicting the soot volume fraction of the ethylene flames with remarkable accuracy, whereas for the gasoline surrogate components, the overall soot volume fractions were found overpredicted by at least one order of magnitude for all tested models. Another difficulties for the modelling purpose is that, as soot, PAH species are characterized by a slow chemistry and cannot be directly tabulated in flamelet library. A transport equation has then to be considered, Mueller et al. (2011), Xuan and Blanquart (2014), Xuan and Blanquart (2015), Jain and Xuan (2019).

— **C_2H_2-based models** : The main idea behind these semi-empirical models is that soot nucleation and growth can be simplified by assuming that PAH concentrations are directly related to lighter species, such as acetylene and sometimes benzene, at the origin of their formation, Lindstedt (1994), Schiener and Lindstedt (2019). This soot kinetic is generally coupled to a two-equation formulation for the soot dynamics, Lindstedt (1994), and the soot inception and surface growth are modelled by the following irreversible and first-order reactions, respectively :

$$C_2H_2 \rightarrow 2C(s) + H_2 \tag{1.7}$$

$$C_2H_2 + nC(s) \rightarrow (n+2)C(s) + H_2 \tag{1.8}$$

where C(s) denotes solid carbon. Oxidation by OH and O_2 is generally taken into account, Liu et al. (2022). These models were found to be able to predict soot volume fraction within a factor of two of measurements in laminar and turbulent diffusion flames fueled with gaseous fuels of different sooting propensities, Nmira et al. (2015) and Consalvi and Nmira (2016). The main drawback is that, due to their inherent formulation, they cannot be extended to complex fuels containing aromatics, such as gasoline or jet fuels.

— **Smoke point-based models** : In the field of fire research, a type of soot production models have been developed based on the concept of laminar smoke-point, Lautenberger et al. (2005), Beji et al. (2008). They are based on the smoke point length, L_{sp}, that represents the length of a candle-like flame as it starts to emit soot from its tip, Ris et al. (2000). The smoke point length is a metric to characterize the sooting propensity of a given fuel. The shorter the smoke point length, the greater the sooting tendency of the fuel to emit soot. Table 1.1 summarizes the smoke points of some fuels of interest for the present study.

	Methane	Ethylene	N-heptane	Iso-octane	Toluene
L_{sp} (cm)	29.0	10.6	12.3	11.0	0.6

Table 1.1 – Laminar smoke point length of methane, CH_4, ethylene, C_2H_4, n-heptane, C_7H_{16}, iso-octane, C_8H_{18}, and toluene, C_7H_8, extracted from Tewarson (1986)

The smoke-point mechanism is related to a radiation-induced extinction process. An increase in flame length enhances the residence time and, in turn, the soot formation and induced-radiative loss which reduces the flame temperature at the tip. As L_{sp} is reached, the flame temperature is reduced to a level where soot oxidation is frozen and soot escapes from the flame. Experimental observations show that the smoke point is reached for radiative loss in the order of 30% of the heat release rate, this level being roughly independent of the fuel. Based on this observation and a scaling analysis, it can be demonstrated that the soot mass formation rate is inversely proportional to L_{sp}, Ris et al. (2000). The idea behind the smoke-point-based soot production model was then to fit soot formation rates for a reference fuel, typically ethylene, based on experiments and to extend it to other fuels by using the previously-mentioned scaling, Lautenberger et al. (2005), Beji et al. (2008). This approach was successfully applied to moderately sooting gaseous fuels, Nmira et al. (2015). Chatterjee et al. (2015) and Chen et al. (2014) also employed it on pure n-heptane and toluene liquids. However, to the author's best knowledge, no attempt was reported to use such model for liquid mixtures or solid fuels. In addition, the soot production rate was derived as a function of only mixture fraction and temperature and ignores the dependency on soot-related properties, such as soot particle size and soot surface area. A consequence is that these soot models, with the current formulation, does not

incorporate the physics of the soot growth and oxidation processes that are known to be strongly related to these properties, Liu et al. (2022).

Table 1.2 summarizes the main advantages of the previously described soot models. It appears that the alternative smoke-point based models are not sufficiently well-designed on their current form and should be revisited to incorporate the basic physic of soot formation and oxidation processes. On the other hand, our experience (Nmira et al. (2015), Consalvi and Nmira (2016)) shows that the semi-empirical acetylene-based model are good candidate for applications as long as non-aromatic fuels are considered. For aromatic fuels, PAH-based soot production models seem to be the default choice although they increase the complexity of the model formulation and suffer from uncertainties, especially regarding the growth of PAH. How are these models able to describe soot production in fuel of different complexity, ranging from ethylene to surrogates of gasoline, is one of the question of this thesis.

Model	Advantages	Disadvantages
Detailed PAH-based	• Contains all the processes • Mature for gaseous fuels	• Sensitive to the chemical mechanism • Increasing uncertainties with fuel complexity • Specific transport model for PAH
C_2H_2-based	• Accurate for gaseous fuels • Ease of implementation within the flamelet framework	• Invalid for aromatic fuels
Smoke-point based	• Simple to implement • Cost-effective • No need of gas-phase mechanism	• Not accurate for weakly-sooting fuels • Does not capture the physics of soot growth and oxidation • Only applied to pure fuels

Table 1.2 – Advantages and disadvantages of detailed PAH-based and semi-empirical soot production models for fire applications.

1.4.2 Turbulence-soot interaction

The modelling of soot production in turbulent flames introduces additional difficulties related to turbulent mixing and turbulence/chemistry/soot production interactions.

The simultaneous developments of, on one hand, Direct Numerical Simulation (DNS) of canonical scenarios (e.g. Lignell et al. (2007), Bisetti et al. (2012), Attili et al. (2014), Attili et al. (2015)) and, on the other hand, temporally and spatially resolved soot measurement techniques (e.g. Lee et al. (2009), Mahmoud et al. (2015), Park et al. (2017), Kruse et al. (2019b)), have greatly contributed to the understanding of how turbulence and soot production processes interact. These interactions were found to be mainly governed by the very low diffusivity of soot, i.e., it is transported differentially compared to gaseous species, and by the slow soot (and also PAH) chemistry that results in time scales significantly longer than those of typical combustion processes. The main consequences are that : (i) soot is confined to very thin structures with the soot field exhibiting a high spatially and temporally intermittent behaviour, (ii) soot (and also PAHs) cannot be parameterized by local mixture fraction and scalar dissipation rate, (iii) the differential diffusion governs the drift of soot in the mixture fraction space and determines the proximity of the soot to the flame which, in turn, influences soot reaction rates and radiative emission, (iv) the local concentration of PAHs is very sensitive to scalar dissipation rate with PAH and soot growth being favoured in regions of low dissipation rate and inhibited in regions of high dissipation rate. In addition, it was found that soot is rapidly oxidized in the vicinity of the stoichiometric surface and soot leakage across the flame occurs due to local extinction events, Attili et al. (2015).

Contrary to RANS, LES can describe the temporal intermittent nature of soot, Mueller and Pitsch (2012), Yang et al. (2019). However, the soot formation/oxidation processes occur at the unresolved sub-grid scales and their interaction with turbulence must be modelled irrespective of the treatment of the flow field. The soot production rates, $\dot{\omega}_s(\phi_g, \phi_s)$, depend on gas-phase related quantities, ϕ_g, and soot-related quantities, ϕ_s, such as soot mass fraction, number density, and particle size. $\dot{\omega}_s(\phi_g, \phi_s)$ are functions of ϕ_g and ϕ_s, such as its Reynolds-averaged value in RANS, $\langle\dot{\omega}_s\rangle$, or its filtered value in LES, $\langle\dot{\omega}_s\rangle_\Delta$, cannot be directly related to mean or filtered values of ϕ_g and ϕ_s:

$$\langle\dot{\omega}_s(\mathbf{x},t)\rangle = \langle\rho\rangle \iint \frac{\dot{\omega}_s(\phi_g,\phi_s)}{\rho(\phi_g)} \widetilde{P}(\phi_g,\phi_s)\,d\phi_g\,d\phi_s \neq \dot{\omega}_s(\widetilde{\phi}_g,\widetilde{\phi}_s) \tag{1.9}$$

$$\langle\dot{\omega}_s(\mathbf{x},t)\rangle_\Delta = \langle\rho\rangle_\Delta \iint \frac{\dot{\omega}_s(\phi_g,\phi_s)}{\rho(\phi_g)} \widehat{P}_\Delta(\phi_g,\phi_s)\,d\phi_g\,d\phi_s \neq \dot{\omega}_s(\widehat{\phi}_g,\widehat{\phi}_s) \tag{1.10}$$

where the notations $\widetilde{\phi}$ and $\widehat{\phi}$ refer to density-weighted mean and filtered values of ϕ, respectively. Δ represents the LES filter width. $\widetilde{P}$ and $\widehat{P}_\Delta$ represent the joint density-weighted PDF and FDF, respectively. As discussed previously, the PAH and soot chemistry is slow as compared to the combustion chemistry. In addition, soot particles do not diffuse as gas-phase species. It is then expected that gas-phase quantities and soot quantities are statistically independent, leading to $\widetilde{P}(\phi_g,\phi_s) = \widetilde{P}(\phi_g) \times \widetilde{P}(\phi_s)$ (or $\widehat{P}_\Delta(\phi_g,\phi_s) = \widehat{P}_\Delta(\phi_g) \times \widehat{P}_\Delta(\phi_s)$). However, this "uncorrelated" formulation was found to underestimate significantly the measured soot volume fraction in both RANS, Brookes

and Moss (1999), and LES, Yang et al. (2019). These discrepancies are due to a strong overestimation of the soot oxidation and their origins were explained by Kronenburg et al. (2000).

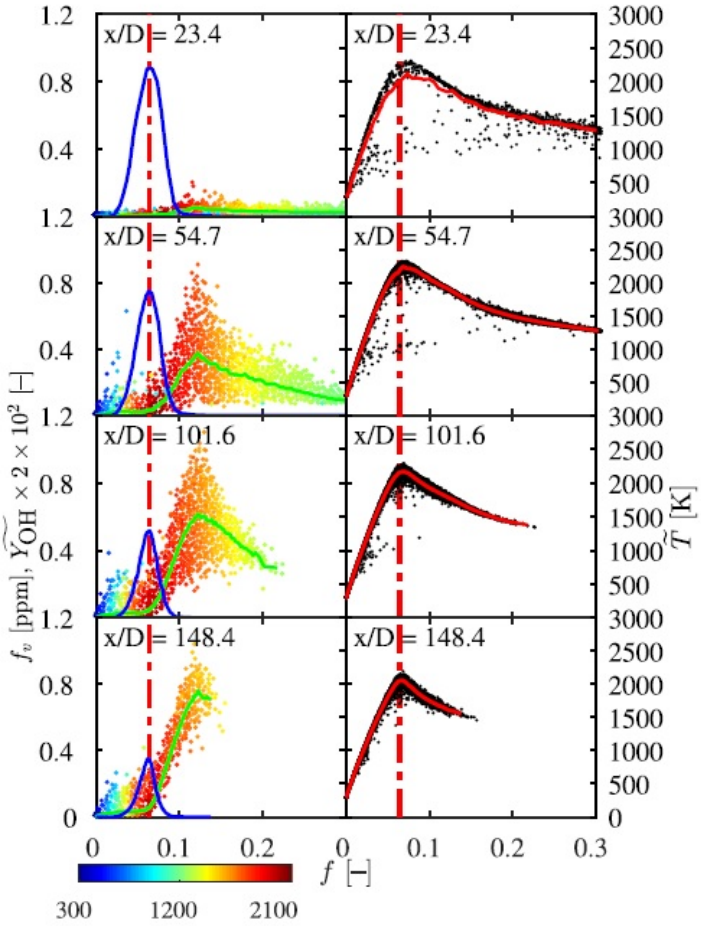

Figure 1.7 – Scatter plots of soot volume fraction, f_v, coloured by particle T (considered as the gas temperature) (left) and T (right) along with conditional means of f_v (green line), OH mass fraction (left) (blue line) and T (right) (red line) at different axial locations. The vertical line represents the stoichiometric mixture fraction, $Z_{st} = 0.064$. Taken from Tian et al. (2021) (with permission).

This is illustrated in Figure 1.7 which represents the scatter plots of soot volume fraction and temperature along with conditional means of soot volume fraction, OH mass fraction and temperature. This figure shows that, owing to fast oxidation, there is little overlap between oxidizer species and soot profiles in mixture fraction space which suggests limited coexistence of oxidizer and soot. Therefore, soot quantities are strongly correlated with oxidative species and the previous equalities do not hold.

Transported PDF and hybrid flamelet/transported PDF methods give direct access

to the joint PDF or FDF and provide an exact closure of the soot formation and oxidation rates, e.g.Lindstedt and Louloudi (2005), Mehta et al. (2010), Schiener and Lindstedt (2019), Tian et al. (2021), Consalvi et al. (2016), Consalvi and Nmira (2016). In particular, the RANS/flamelet/transported PDF model, developed at EDF R&D in collaboration with Aix-Marseille Université, was found to provide soot volume fraction within a factor of two for turbulent jet flames covering wide ranges of Reynolds number and fuel sooting propensities, Consalvi et al. (2016), Consalvi et al. (2013). However, the extension of this approach to LES of fire plumes can require prohibitive computation resources. On the other hand, flamelet presumed FDF approaches were developed in the context of LES, Mueller and Pitsch (2011), Mueller and Pitsch (2012), Yang et al. (2019). The joint presumed FDF was re-expressed as $\widetilde{P}(\phi_g,\phi_s) = \widetilde{P}(\phi_s|\phi_g)\widetilde{P}(\phi_g)$ (or $\widehat{P}_\Delta(\phi_g,\phi_s) = \widehat{P}_\Delta(\phi_s|\phi_g)\widehat{P}_\Delta(\phi_g)$). A first modelling strategy assumed that the conditional FDF can simply be modelled. The marginal FDF of soot quantities was designed to account for the very high spatial intermittency by introducing a sooting and a non-sooting mode Mueller and Pitsch (2011), e.g for LES :

$$\widehat{P}_\Delta(\phi_s|\phi_g) = \omega\delta(\phi_s) + (1-\omega)\delta(\phi_s - \phi_s^*) \tag{1.11}$$

However, equation 1.11 neglects the correlation between mixture fraction and soot quantities which leads to an overestimation of soot oxidation as discussed previously (see also Yang et al. (2019) for a detailed analysis). In order to limit the overlap between soot quantities and oxidative species and improve the prediction of the soot oxidation rates, Yang et al. (2019) updated equation 1.11 by introducing a threshold on mixture fraction :

$$\widehat{P}_\Delta(\phi_s|\phi_g) = \left[\omega\delta(\phi_s) + (1-\omega)\delta(\phi_s - \phi_s^*)\right] H(Z - Z_s) \tag{1.12}$$

Yang et al. (2019) determined Z_s as the location in the mixture fraction space where soot oxidation becomes faster than surface growth. This new subgrid-scale soot production model was found to improve the predictions as compared to equation 1.11. Berger et al. (2021) have further updated equation 1.12 by introducing a log-normal distribution to model the sooting mode instead of a δ-Dirac function. This modification was assessed in an *a priori* analysis based on DNS data and was found to improve model predictions for the coagulation source term.

1.5 Organisation of the present manuscript

The present manuscript is organised as follow.

- Chapter 2 is devoted to the description of the mathematical model, with a special emphasis on the combustion, soot and radiation modelling used in the present study.
- Chapter 3 presents the LES of well-documented ethylene lab-scale ethylene buoyant diffusion flames. A special emphasis will be put on the analysis of the soot subgrid scale modelling and its effects on both soot production and radiative heat transfer. These investigation will be made with the acetylene soot production models for ease of simplicity and the remaining of the thesis will be devoted to the development and validation of a PAH-based soot production model in view of application to aromatic fuels.
- Chapter 4 describes the PAH-based model, the related choices that were made and its assessment on well-documented ethylene laminar coflow diffusion flames.
- Chapter 5 extends the assessment of the PAH-based model on mixtures of common surrogate primary fuels for gasoline in laminar coflow diffusion flames.
- Finally, conclusions drawn from the present study are presented and perspectives for future works and developments will be outlined in chapter 6.

2 Mathematical formulation

The objective of this chapter is to provide the mathematical framework that is employed and common in the following chapters. The deviation and specificities are then provided in respective chapters.

Table of contents

2.1 Reactive flow governing equations

The Navier-stokes (NS) equations in low-Mach number formulation supplemented with transport equations for the species mass fractions, $(Y_\alpha)_{\alpha=1,N_s}$, total enthalpy, h, and the equation of state are expressed below. It can be assumed that the species diffusion and heat conduction follow the Fick and the Fourier laws, respectively.

Mass :

$$\frac{\partial \rho}{\partial t} + \frac{\partial \rho u_i}{\partial x_i} = 0 \tag{2.1}$$

Momentum :

$$\frac{\partial \rho u_j}{\partial t} + \frac{\partial \rho u_i u_j}{\partial x_i} = -\frac{\partial p}{\partial x_j} + \frac{\tau_{ij}}{\partial x_i} + (\rho - \rho_\infty) g_j \tag{2.2}$$

Species :

$$\frac{\partial \rho Y_\alpha}{\partial t} + \frac{\partial \rho u_i Y_\alpha}{\partial x_i} = \frac{\partial}{\partial x_i}\left(\rho D_\alpha \frac{\partial Y_\alpha}{\partial x_i}\right) + \dot{\omega}_\alpha \quad \text{with } \alpha = 1, ..., N_s \tag{2.3}$$

Energy :

$$\frac{\partial \rho h}{\partial t} + \frac{\partial \rho u_i h}{\partial x_i} = -\frac{\partial q_i}{\partial x_i} - \nabla \cdot \dot{q}''_R \tag{2.4}$$

Equation of state :

$$p = \rho \sum_{\alpha=1}^{N_s} \frac{Y_\alpha}{W_\alpha} RT \tag{2.5}$$

where ρ is the local density and $u_i = (u, v, w)$ is the flow velocity, p is the pressure. $(\tau_{ij})_{i,j=1,3}$ is the viscous stress defined as :

$$\tau_{ij} = \mu\left(\frac{\partial u_i}{\partial x_j} + \frac{\partial u_j}{\partial x_i}\right) + \frac{2}{3}\delta_{ij}\mu\frac{\partial u_k}{\partial x_k} \tag{2.6}$$

with μ the dynamic viscosity, $(D_\alpha)_{\alpha=1,N_s}$ are the species diffusion coefficients, N_s is the number of species and $\dot{\omega}_\alpha$ are the species reaction rates, which verifies $\sum_{\alpha=1}^{N_s} \dot{\omega}_\alpha = 0$. h is the total enthalpy defined as :

$$h = \sum_{\alpha=1}^{N_s} Y_\alpha h_\alpha(T) = \sum_{\alpha=1}^{N_s} Y_\alpha \left(h^0_{f,\alpha} + \int_{T_0}^{T} C_{p\alpha}(T')dT'\right) \tag{2.7}$$

where $h^0_{f,\alpha}$ is the formation enthalpy at the reference temperature, T_0, and $C_{p\alpha}$ the heat capacity at constant pressure of species α, $(q_i)_{i=1,3}$. The heat flux is modelled by the Fourier law :

$$q_i = -\lambda \frac{\partial T}{\partial x_i} \tag{2.8}$$

where λ is the heat conductivity, and $\nabla \cdot \dot{q}''_R$ is the radiative source term. T, R and W_α are the temperature, the universal gas constant and the molecular weight of species α, respectively.

Note that the system 2.1-2.5 can be transformed into a reduced dimension system in which scalar transport equations are solved for three quantities : the mixture fraction, Z, scalar dissipation, χ, and total enthalpy h. All other thermochemical quantities are obtained from a property database as a function of these scalars.

2.2 Combustion modelling

The transport of a whole set of species mass fraction is a computational impediment. As a consequence, a flamelet approach is considered to model combustion of non-premixed flames. Firstly, the mixture fraction is introduced. Secondly, the steady laminar flamelet (SLF) model is presented. Finally, the incorporation of radiative loss in the SLF model is explained.

2.2.1 The mixture fraction

Non-premixed flames are a specific class of combustion problems where fuel and oxidizer are initially separated and have to mix prior to combustion, Poinsot and Veynante (2005). A proper description of the mixing process is then a natural prerequisite to the modelling of theses flames.

In general, the structure of non-premixed flames can be described by means of a conserved scalar. This variable is the mixture fraction, Z, Peters (1984), defined between 0 and 1. Z is a conserved scalar that accounts for the level of mixing between the oxidizer and the fuel and changes because of diffusion and convection, but not due to chemical process since elements are conserved in chemical reactions. In the present study, following the formalism introduced by Pitsch and Peters (1998), the mixture fraction is defined from its transport equation :

$$\frac{\partial \rho Z}{\partial t} + \frac{\partial \rho u_i Z}{\partial x_i} = \frac{\partial}{\partial x_i}\left(\rho D \frac{\partial Z}{\partial x_i}\right) \tag{2.9}$$

where D is the diffusion coefficient for mixture fraction and is modeled using the thermal diffusion as recommended by Pitsch and Peters (1998).

2.2.2 Steady laminar flamelet model (SLF)

A flame can be viewed as an ensemble of thin locally one-dimensional structures embedded within the flow field. Each element of the flame front can then be viewed as a small laminar flame also called flamelet, Peters (1984), Poinsot and Veynante (2005). Physically, the flame structure is considered locally one-dimensional and only depends on time and the coordinate normal to the flame front. A coordinate system attached to the surface of stoichiometric mixture fraction can be introduced and the flamelet equations can be derived, Peters (1984). A transformation from the physical spatial-temporal space ($\mathbf{x}$, t) to the mixture fraction-temporal space (Z, τ) can be applied to the governing equations of species and enthalpy. It is assumed that through the flame front, the combustion behaviour is one-dimensional. Terms corresponding to the gradients along the tangent directions to the flame front are neglected in comparison to those normal to the flame front. In the mixture fraction space, unity Lewis is often

adopted, it implies that all chemical species and enthalpy have the same diffusivity. The following description employs the unity Lewis assumption for the sake of clarity but a more general derivation with non-unity Lewis numbers is possible and given by Pitsch and Peters (1998). The coordinate transformation results in the flamelet equations :

$$\rho \frac{\partial Y_\alpha}{\partial \tau} = \frac{1}{2}\rho\chi\frac{\partial^2 Y_\alpha}{\partial Z^2} + \dot{\omega}_\alpha \tag{2.10}$$

$$\rho \frac{\partial h}{\partial \tau} = \frac{1}{2}\rho\chi\frac{\partial^2 h}{\partial Z^2} - \nabla\cdot\dot{q}''_R \tag{2.11}$$

χ is the scalar dissipation rate and has the unit of the inverse of a time and characterizes typical diffusion times in the flamelet, Poinsot and Veynante (2005). It is defined as :

$$\chi = 2D\left(\frac{\partial Z}{\partial x_i}\frac{\partial Z}{\partial x_i}\right) \tag{2.12}$$

At sufficiently high Damköhler number or sufficiently high activation energy, the reaction zone is thinner than the surrounding turbulence eddies. In this regime, turbulent structures can deform and stretch the flame sheet, but are unable to penetrate the reaction zone and modify its structure. The combustion chemistry reaches a quasi-steady state and immediately adjusts to local flow-field conditions. The temporal terms in Equations 2.10-2.11 thus vanish:

$$\frac{1}{2}\rho\chi\frac{\partial^2 Y_\alpha}{\partial Z^2} = -\dot{\omega}_\alpha \tag{2.13}$$

$$\frac{1}{2}\rho\chi\frac{\partial^2 h}{\partial Z^2} = \nabla\cdot\dot{q}''_R \tag{2.14}$$

In order to solve this set of equations, a distribution of $\chi(Z)$ should be determined. The 1D flame structure is generally assumed to be represented by a counterflow diffusion flame. Peters (1984) obtained an analytic expression for $\chi(Z)$ based on the laminar counterflow configuration. Once this analytical expression of $\chi(Z)$ and an appropriate chemical mechanism are considered, Equations 2.13 and 2.14 can be solved as a function of a single parameter, χ_{st}, that represent the scalar dissipation rate at stoichiometric conditions. All thermochemical state variables, ϕ, consisting for instance of temperature, density, molecular viscosity and diffusivity, and species mass fractions can then be expressed in terms of Z and χ_{st}, Peters (1984) :

$$\phi = \phi^{slf}(Z,\chi_{st}) \tag{2.15}$$

It should be pointed out that, alternatively, these state relationships can be also obtained by solving all the transport equations (i.e. Equations 2.1-2.5 and 2.9) in the physical space for a laminar counterflow configuration. The thermochemical variables are subsequently mapped into the mixture fraction space and the profile of scalar dissipation rate, $\chi(Z)$, is directly obtained from its definition (Equation 2.12).

In the present study, the flamelet library is generated in physical space. Given a chemical mechanism, flamelet equations are solved by gradually increasing the strain rate from near equilibrium to conditions of local extinction. Solutions are parametrized by the mixture fraction and its dissipation rate at stoichiometric mixture fraction. The thermochemical states of the flamelet are then represented by a two-dimensional manifold, $\phi = \phi^{slf}(Z, \chi_{st})$. By introducing a table inversion to eliminate χ_{st} in favour of χ, the thermochemical states are finally expressed as :

$$\phi = \phi^{slf}(Z, \chi) \tag{2.16}$$

Figure 2.1 illustrates the evolution of temperature with respect of the mixture fraction for different values of χ_{st} for the ethylene-air flame

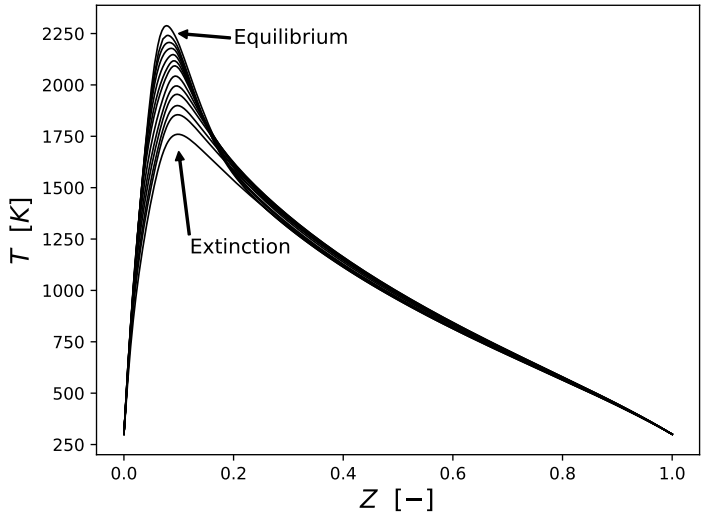

Figure 2.1 – Temperature profiles as a function of the mixture fraction for different values of χ_{st} for the C_2H_4/Air flame.

2.2.3 Extended non-adiabatic flamelet model

Thermal radiation is an important phenomenon, especially for buoyant diffusion flames. Heat is released to the surroundings leading to additional interaction at the level of the flame structure. The SLF model relies on the underlying assumption that

the thermochemical state of a particular flamelet relaxes to the steady-state solution on a sufficiently fast time-scale. However, radiative heat-loss processes evolve on time-scale that are slow compared to other processes in typical combustion applications, Ihme and Pitsch (2008). Based on this observation, several extensions of the SLF model have been proposed e.g Ihme and Pitsch (2008), Carbonell et al. (2009). In the present study, the methodology described by Carbonell et al. (2009) was used to incorporate the radiative loss in the flamelet library. It consists in generating flamelet profiles for each strain rate with different degrees of heat losses. A volumetric radiative heat sink term based on the optically-thin approximation was introduced in the flamelet energy Equation 2.11 and was multiplied by a constant δ to allow variation in the degrees of radiative loss. For each strain rate, the flamelet temperature and species equations were solved for a set of prescribed factors ranging from 0 (adiabatic) to the maximum value which was adjusted to be near quenching conditions. Figure 2.2 illustrates this procedure at the strain rate of 5 s^{-1} in the case of the ethylene/air flame which reaches quenching for a heat-loss of almost 80%.

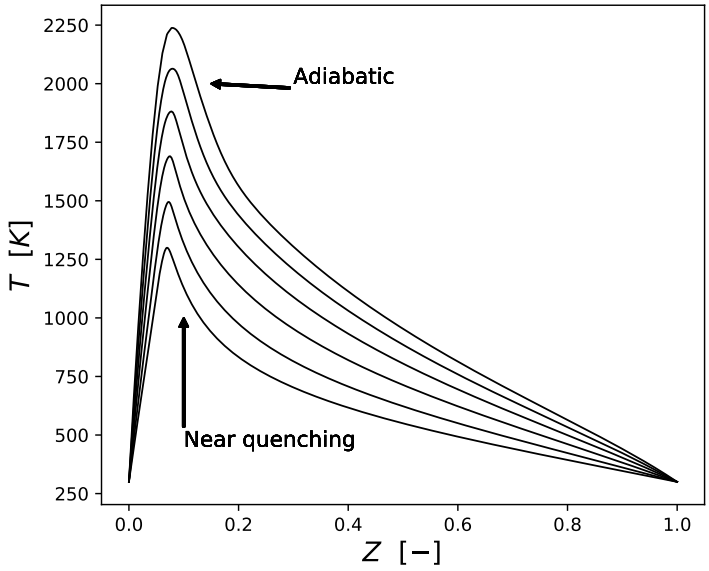

Figure 2.2 – Temperature profiles as a function of the mixture fraction for different heat-losses at $a = 5$ 1/s and $\chi_{st} = 0.27$ 1/s for the C_2H_4/Air flame.

As the total enthalpy is no longer conserved in a non-adiabatic flame, a new parameter characterizing the degree of heat loss has to be introduced to generate the flamelet library. In the present study, the enthalpy defect, X_R, defined as the difference between the actual non-adiabatic enthalpy and the adiabatic enthalpy, is considered :

$$X_R(Z) = h(Z) - h_{ad}(Z) \tag{2.17}$$

Finally, the thermochemical states with the extended non-adiabatic flamelet model are represented by the three-manifold Equation 2.18.

$$\phi = \phi^{slf}(Z, \chi, X_R) \tag{2.18}$$

2.3 Soot particle dynamics modelling

Soot production is a slow process and, as such, it cannot be fully incorporated in the flamelet generation. Moreover, as discussed in the introduction chapter 1, soot is a significant contributor to radiation. Assuming that soot radiates in the Rayleigh regime, modeling the radiative properties of soot only requires knowledge of its volume fraction. Consequently, obtaining a detailed description of the particle size distribution, which is a crucial issue in regard of soot pollution, is of secondary importance in the context of fires, except when addressing the issue of deposition.

2.3.1 The three-equation formulation

Soot particles are assumed to be fractal aggregates of fractal dimension D_f, volume v, and composed of n_p spherical primary particles of diameter d_p. The soot population is described by bivariate NDF, $n(v, n_p; \mathbf{x}, t)$, where $\mathbf{x}$ and t represent the position and time respectively, expressed in terms of soot particle volume and number of primary particles per aggregate, Xing et al. (2022). The distribution is assumed to be locally monodispersed, leading to, Franzelli et al. (2019) :

$$n(v, n_p; \mathbf{x}, t) = [\rho N_s(\mathbf{x}, t)]\delta[v - v_s(\mathbf{x}, t)]\delta[n_p - n_{ps}(\mathbf{x}, t)] \tag{2.19}$$

where $[\rho N_s]$ is the number density of soot aggregates, v_s and n_{ps} are the local mean values of the soot aggregate volume and the number of primary particles per aggregate, respectively. Based on this assumption, the local mean soot aggregate properties can be deduced from the three first moments of the distribution, namely the number density of soot aggregates, the number density of primary particles, $[\rho N_{ps}]$, and the soot volume fraction, $f_{vs} = \rho Y_s / \rho_s$, where ρ_s and Y_s are the soot density and the soot mass fraction, respectively :

$$[\rho N_s] = \int\int n(v, n_p; \mathbf{x}, t) dv dn_p \tag{2.20}$$

$$[\rho N_{ps}] = \int\int n_p \cdot n(v, n_p; \mathbf{x}, t) dv dn_p = [\rho N_s] n_{ps} \tag{2.21}$$

$$f_{vs} = \int\int v \cdot n(v, n_p; \mathbf{x}, t) dv dn_p = [\rho N_s] v_s \tag{2.22}$$

The mean primary particle diameter is related to the mean soot volume by $v_s = n_{ps}\frac{\pi}{6}d_{ps}^3$ where $d_{ps} = 6Y_s/(\pi\rho_s N_{ps})$. The soot specific surface area, A_s, and the fractal aggregate collision diameter, D_c, are then computed as :

$$A_s = [\rho N_s] n_{ps} \pi d_{ps}^2 \tag{2.23}$$

$$D_c = d_{ps}(n_{ps})^{1/D_f} \tag{2.24}$$

where D_f is the fractal dimension equal to 1.8. As a consequence, the three first moments, $\phi_s = \{N_s, N_{ps}, Y_s\}$, are governed by the following transport equations :

$$\frac{\partial \rho N_s}{\partial t} + \frac{\partial \rho(u_i + u_{th,i})N_s}{\partial x_i} = \dot{\omega}_{nucl}^{N_s} - \dot{\omega}_{C/A}^{N_s} \tag{2.25}$$

$$\frac{\partial \rho N_{ps}}{\partial t} + \frac{\partial \rho(u_i + u_{th,i})N_{ps}}{\partial x_i} = \dot{\omega}_{nucl}^{N_{ps}} - \dot{\omega}_{C}^{N_{ps}} \tag{2.26}$$

$$\frac{\partial \rho Y_s}{\partial t} + \frac{\partial \rho(u_i + u_{th,i})Y_s}{\partial x_i} = \dot{\omega}_{nucl}^{Y_s} + \dot{\omega}_{G}^{Y_s} - \dot{\omega}_{Ox}^{Y_s} \tag{2.27}$$

where the subscripts *nucl*, *G*, *C/A*, *Ox*, refer to the processes of nucleation, coalescence/aggregation, growth and oxidation, respectively. As two soot production models have been employed in the present work, the inception, growth and oxidation terms will be detailed in subsequent chapters. The soot molecular diffusion and thermophoresis are neglected.

Particle-particle interactions are assumed to transit from the coalescence regime, where collision of liquid-like nascent soot particles leads to complete merging of the colliding particles into a spherical particle, to the aggregation regime, where the collision process leads to the creation of chain-like structures (Tian et al. (2021), Schiener and Lindstedt (2018), Smooke et al. (2005), Veshkini et al. (2016), Sun et al. (2021)). Consistently with the aforementioned references, this transition is assumed to occur for a critical primary particle diameter, $d_{p,\text{crit}}$, at which the particles experience phase change and transfer from a liquid-like state into a solid state. Several values of $d_{p,\text{crit}}$ were proposed in the literature. Smooke et al. (2005) assumed 25 nm, Lindstedt and coworkers (Tian et al. (2021), Schiener and Lindstedt (2018)) selected 27.5 nm based on the works of Kazakov and Frenklach (1998) whereas Veshkini et al. (2016) considered 20 nm. Based on these assumptions, $\dot{\omega}_{C/A}^{N_s}$ and $\dot{\omega}_{C}^{N_{ps}}$ are given by :

$$\dot{\omega}_{C}^{N_{ps}} = \begin{cases} \frac{1}{2}\beta_C[\rho N_{ps}]^2 & \text{if } d_p < d_{p,\text{crit}}. \\ 0 & \text{if } d_p \geq d_{p,\text{crit}} \end{cases} \tag{2.28}$$

$$\dot{\omega}_{C/A}^{N_s} = \begin{cases} \dot{\omega}_C^{N_{ps}} & \text{if } d_p < d_{p,\text{crit}}. \\ \frac{1}{2}\beta_A[\rho N_s]^2 & \text{if } d_p \geq d_{p,\text{crit}} \end{cases} \tag{2.29}$$

The collision frequencies in both coalescence and aggregation regimes are computed as the harmonic average of the collision frequencies in the limits of the free molecular and continuum regimes :

$$\beta_C = \frac{\beta_C^f \beta_C^c}{\beta_C^f + \beta_C^c}; \qquad \beta_C^f = 4 \times C_A \left(\frac{6k_bT}{\rho_s}\right)^{1/2} d_{ps}^{1/2}; \qquad \beta_C^c = \frac{8k_bT}{3\mu_L} C_u \tag{2.30}$$

$$\beta_A = \frac{\beta_A^f \beta_A^c}{\beta_A^f + \beta_A^c}; \qquad \beta_A^f = 4 \times C_A (\pi k_b T)^{1/2} \frac{D_c^2}{m_A^{1/2}}; \qquad \beta_A^c = \frac{8k_bT}{3\mu_L} C_u \tag{2.31}$$

where $C_u = 1 + 1.257K_n$ is the Cunningham slip correction factor, $K_n = 2\lambda/d$ the Knudsen number with λ and d being the gas mean free path and the particle diameter, respectively. C_A is the coagulation rate constant equal to 2.2. μ_L is the gas dynamic viscosity and m_A is the aggregate mass defined by $m_A = Y_s/N_s$, Schiener and Lindstedt (2018).

2.3.2 The two-equation formulation

Soot particles are assumed to be spherical primary particles of diameter d_p and volume v. The soot population is described by a univariate NDF, $n(v;\mathbf{x},t)$, Leung et al. (1991). The distribution is assumed to be locally monodispersed, leading to :

$$n(v;\mathbf{x},t) = [\rho N_{ps}(\mathbf{x},t)]\delta[v - v_p(\mathbf{x},t)] \tag{2.32}$$

where v_p is the mean primary particle diameter. The local mean soot properties are here only deduced from the first two moments of the distribution, namely the number density of primary particles, $[\rho N_{ps}]$, and the soot volume fraction, f_{vs}.

$$[\rho N_{ps}] = \int n(v;\mathbf{x},t)\,dv \tag{2.33}$$

$$f_{vs} = \int v \cdot n(v;\mathbf{x},t)\,dv = [\rho N_{ps}]\,v_p \tag{2.34}$$

The soot specific surface area, A_s, and the collision diameter are then computed as :

$$A_s = [\rho N_{ps}]\pi d_{ps}^2 \tag{2.35}$$

$$d_{ps} = \left(\frac{6 f_{vs}}{\pi \rho_s N_{ps}}\right)^{1/3} \tag{2.36}$$

As a consequence, the two first moments $\phi_s = \{N_{ps}, Y_s\}$:

$$\frac{\partial \rho N_{ps}}{\partial t} + \frac{\partial \rho (u_i + u_{th,i}) N_{ps}}{\partial x_i} = \dot{\omega}_{nucl}^{N_{ps}} - \dot{\omega}_C^{N_{ps}} \tag{2.37}$$

$$\frac{\partial \rho Y_s}{\partial t} + \frac{\partial \rho (u_i + u_{th,i}) Y_s}{\partial x_i} = \dot{\omega}_{nucl}^{Y_s} + \dot{\omega}_G^{Y_s} - \dot{\omega}_{Ox}^{Y_s} \tag{2.38}$$

Particle-particle interactions are here regarded as being within the coalescence regime only i.e the collision of two particles leads the complete merging into a spherical particle. The collision frequency is calculated in the free molecular regime :

$$\dot{\omega}_C^{N_{ps}} = \frac{1}{2}\beta_C^f [\rho N_{ps}]^2 \quad \text{with} \quad \beta_C^f = 4 \times C_A \left(\frac{6 k_b T}{\rho_s}\right)^{1/2} d_{ps}^{1/2} \tag{2.39}$$

In comparison with the three-equation formulation, the two-equation formulation overlooks the agglomeration process and, as such, can be considered as a subdivision of the three equation formulation. Overall, the simulations showed that these two formulation provide equivalent predictions.

2.4 Radiation modelling

The spectral coverage range considered in the present study is 0-25000 cm^{-1}. The radiatively participating species considered are CO_2, H_2O, and soot. Soot particles were assumed to be spherical and small as compared with the wavelength and Rayleigh's theory was then applied to obtain the soot absorption coefficient, Modest (2013) :

$$\kappa_{s,\eta} = C_\eta f_{vs} \eta \quad \text{with} \quad C_\eta = \frac{36\pi n_s k_s}{(n_s^2 + k_s^2 - 2)^2 + 4 n_s^2 k_s^2} \tag{2.40}$$

The refractive and absorptive indexes of the soot, n_s and k_s, were determined using the correlations of Chang and Charalampopoulos (1990).

Two gas radiative property models are considered in this work to deal with the latter characteristics, namely the RCFSK and the non-grey WSGG. In both cases, the RTE can be written in a generic form, Modest (2013).

$$\frac{dI_i}{ds} + \underbrace{\kappa_i I_i}_{\text{Absorption}} = \underbrace{\kappa_i a_i I_b(T)}_{\text{Emission}} \qquad i = 1, N_g \tag{2.41}$$

where I_i is the radiative intensity, κ_i the absorption coefficient and $I_b(T)$ the blackbody intensity. N_g and a_i are the number of quadrature points and the stretching function for the RCFSK or the number of grey gases and the weight factor for the non-grey WSGG, respectively. The RTE is solved using the FVM.

2.4.1 The RCFSK model

The RCFSK belongs to the family of the global k-distribution-based radiation models. It preserves the total emission and does not require any specification of a reference state, Solovjov et al. (2018). In configuration relevant for combustion applications, the RCFSK was found to provide an overall very good agreement with reference LBL or narrow band calculations in both emission and absorption dominated problems, Solovjov et al. (2018), Liu et al. (2020), Consalvi et al. (2020). Consequently, it will be used as reference in the present study.

Full spectrum (FS) cumulative k-g distribution function is defined as:

$$g(k, \varphi, T_p) = \frac{1}{I_b(T_p)} \int_0^{\infty} H\left[k - \kappa_\eta(\varphi)\right] I_{b,\eta}(T_p) d\eta \tag{2.42}$$

where $\varphi = \{x_{CO_2}, x_{H_2O}, f_{vs}, T\}$ is an array of thermodynamic variables affecting the spectral absorption coefficient, κ_η, at the wavenumber η. H is the Heaviside function, k a given value of the absorption coefficient, and $I_{b,\eta}(T_p)$ the spectral blackbody intensity at the Planck temperature T_p. In the present study, mixed FS k-g distributions (for mixtures of CO_2, H_2O and soot) are constructed from HITEMP 2010, Rothman et al. (2010) by using the procedure proposed by Modest and Riazzi (2005), and a 10-point Gauss-Legendre quadrature scheme ($N_g = 10$) is used. For each quadrature point, g_i, the RCFSK scheme determines the absorption coefficient, κ_i, and the stretching function, $a_i(T)$, by solving (Solovjov et al. (2018)) :

$$g(\kappa_i, \phi, T_P) = g_i \tag{2.43}$$

$$a_i(T) = \frac{g(\kappa_i, \phi, T) - g(\kappa_{i-1}, \phi, T)}{\Delta g}, \quad \Delta g = g_i - g_{i-1} \tag{2.44}$$

The divergence of the radiative heat flux is then computed from the following equation :

$$\nabla \cdot \dot{q}''_R = \sum_{i=1}^{N_g} 4\pi\kappa_i a_i I_b \Delta g - \sum_{i=1}^{N_g} \kappa_i G_i \Delta g \tag{2.45}$$

where $G_i = \int_0^{4\pi} I_i d\Omega$ with Ω being the solid angle. As expected, predictions were found insensitive to the choice of T_p. In the present simulations, T_p was set equal to 1500 K.

2.4.2 The non-grey WSGG model

The WSGG assumes that the total emissivity, ϵ, can be computed as follows, Modest and Haworth (2016):

$$\epsilon = \sum_{i=1}^{N_g} a_i(T)[1 - \exp(-\kappa_i L)] \tag{2.46}$$

with

$$\kappa_i = (x_{CO_2} + x_{H_2O}) p_0 \kappa_{p,i} + \kappa_s \quad and \quad a_i = \sum_{k=0}^{K} b_{i,k} T^k \tag{2.47}$$

where L is the mean path length. In the present study, $p_0 = 1$ atm, $N_g = 5$ and $K = 5$. The constant WSGG parameters, $\kappa_{p,i}$ and $b_{i,k}$, derived from Modest and Haworth (2016) with $x_{H_2O}/x_{CO_2} = 1$. These parameters were optimized to fit total emissivities determined from HITEMP 2010, Rothman et al. (2010), for a set of specified temperatures and optical path lengths.

The divergence of the radiative flux is then determined as :

$$\nabla \cdot \dot{q}''_R = \sum_{i=1}^{N_g} 4\pi\kappa_i a_i I_b - \sum_{i=1}^{N_g} \kappa_i G_i \tag{2.48}$$

3 Large-eddy simulation of lab-scale ethylene buoyant diffusion flames

Table of contents

3.1 Introduction

The aim of this chapter is two-fold. The first objective is to extend the LES/presumed FDF model, developed and widely-validated for non-sooting flames (Ma et al. (2019), Ma et al. (2020), Nmira et al. (2020), Ma et al. (2021), Nmira et al. (2021), Ma et al. (2022)), to sooting flames. As chemical reactions, soot formation/oxidation processes occur at the unresolved subgrid-scales and has to be completely modelled, which introduces modelling issues related to the SGS TSI. In addition, soot production is a

kinetically-controlled process and, as such, its prediction in radiating fire plumes is expected to be sensitive to the modelling of thermal radiation, Modest and Haworth (2016). The second objective is thus to quantify the sensitivity of soot production and resulting radiative heat transfer to the modelling of SGS TSI and radiative models. To this end, the well-documented 15-kW buoyant ethylene turbulent diffusion flames, investigated experimentally at FM Global, Zeng et al. (2019), Ren et al. (2021), Xiong et al. (2021) are simulated.

3.2 Large Eddy Simulation modelling details

3.2.1 Turbulent governing equations

A LES approach is employed to simulate buoyancy controlled diffusion flames. For this particular flame configuration, LES is more accurate and general than RANS, since at least some of the fluctuations (the largest, most energetic ones) are captured explicitly and only the (presumably) more universal small-scale dynamics require modelling. LES is also expected to capture phenomena that are difficult to accommodate in RANS, such as large-scale unsteadiness as observed in fire plumes, Wang et al. (2011). The separation of scales is introduced by a Reynolds filtering operation which decomposes the velocity and scalar fields into a resolved (filtered) part, $\overline{\phi}$, and an unresolved (subgrid-scale) part, ϕ'. In addition, for variable density flow, the resolved quantities are density weighted (Favre filtered) as defined by:

$$\overline{\rho}\widetilde{\phi} = \overline{\rho\phi} \tag{3.1}$$

The numerical model solves, in a low Mach number formulation, the filtered transport equations of mass, momentum, enthalpy and mixture fraction.

Mass :

$$\frac{\partial \overline{\rho}}{\partial t} + \frac{\partial \overline{\rho}\widetilde{u}_i}{\partial x_i} = 0 \tag{3.2}$$

Momentum :

$$\frac{\partial \overline{\rho}\widetilde{u}_j}{\partial t} + \frac{\partial \overline{\rho}\widetilde{u}_i\widetilde{u}_j}{\partial x_i} = -\frac{\partial \overline{p}}{\partial x_j} + \frac{\partial}{\partial x_i}\left(2\widetilde{\mu}\widetilde{S}_{ij}\right) + \frac{\partial \tau^{sgs}_{u_i u_j}}{\partial x_i} + (\overline{\rho} - \rho_0)g_i \tag{3.3}$$

Energy :

$$\frac{\partial \overline{\rho}\widetilde{h}}{\partial t} + \frac{\partial \overline{\rho}\widetilde{u}_i\widetilde{h}}{\partial x_i} = \frac{\partial}{\partial x_i}\left(\overline{\rho}\widetilde{D}\frac{\partial \widetilde{h}}{\partial x_i}\right) + \frac{\partial \tau^{sgs}_{u_i h}}{\partial x_i} - \nabla \cdot \overline{\dot{q}}''_R \tag{3.4}$$

Mixture fraction :

$$\frac{\partial \bar{\rho}\widetilde{Z}}{\partial t} + \frac{\partial \bar{\rho}\widetilde{u}_i\widetilde{Z}}{\partial x_i} = \frac{\partial}{\partial x_i}\left(\bar{\rho}\widetilde{D}\frac{\partial \widetilde{Z}}{\partial x_i}\right) + \frac{\partial \tau^{sgs}_{u_i Z}}{\partial x_i} \tag{3.5}$$

The subgrid-scale terms, namely the subgrid-scale stress, $\tau^{sgs}_{u_i u_j} = -\bar{\rho}\left(\widetilde{u_i u_j} - \widetilde{u_i}\widetilde{u_j}\right)$, the subgrid-scale scalar fluxes, $\tau^{sgs}_{u_i h} = -\bar{\rho}\left(\widetilde{u_i h} - \widetilde{u_i}\widetilde{h}\right)$, and $\tau^{sgs}_{u_i Z} = -\bar{\rho}\left(\widetilde{u_i Z} - \widetilde{u_i}\widetilde{Z}\right)$ are computed using a dynamic Smagorinsky model and a dynamic eddy diffusivity model (DEDM), respectively, Moin et al. (1991). For further information on these models, see Ma (2020).

3.2.2 Subgrid-scale turbulence/chemistry interaction (SGS TCI)

In LES of non-premixed combustion, many important mixing and reaction processes occur at scales that are unresolved on the computational grid. Combustion-related variables such as the mixture fraction fluctuating quantities and their statistical distribution need to be considered. Subgrid fluctuations of the combustion variables can have an important impact on the filtered properties due to the sensitivity and non-linearity of combustion processes. To account for subgrid fluctuations in the combustion variables, filtered combustion variables are obtained by integrating the state equation over the joint FDF, Poinsot and Veynante (2005), Mueller and Pitsch (2012) :

$$\widetilde{\phi} = \int \phi^{fl}(Z,\chi,X_R)\widetilde{P}(Z,\chi,X_R)dZd\chi dX_R \tag{3.6}$$

Z, χ and X_R are assumed to be statistically independent and the marginal FDF of Z are modelled with a β-distribution and the conditional dissipation rate and conditional enthalpy defect are modeled by a "single flamelet closure" with δ-distribution around the corresponding filtered value, Mueller and Pitsch (2012).

$$\widetilde{P}(Z,\chi,X_R) = \beta(Z;\widetilde{Z},V_Z)\delta(\chi-\widetilde{\chi})\delta(X_R-\widetilde{X_R}) \tag{3.7}$$

where V_Z is the subgrid mixture fraction variance, defined as :

$$V_Z = \widetilde{Z^2} - \widetilde{Z}^2 \tag{3.8}$$

V_Z is determined through its definition and by solving the transport equation of the second moment of the mixture fraction $\widetilde{Z^2}$, Ma et al. (2021). The filtered scalar

dissipation rate, $\widetilde{\chi}$, is computed by the model proposed by Jiménez et al. (2001), with the constant involved in the model determined by a dynamic approach.

3.2.3 Soot production modeling

The two equation formulation is adopted. The soot production is modeled with the acetylene/benzene based model, proposed by Lindstedt (1994), called the Lindstedt model. It should be pointed out that the constant of the model are the same as used in our team previous studies of laminar and turbulent diffusion flames, Nmira et al. (2015), Consalvi and Nmira (2016), Consalvi et al. (2016).

$$\frac{\partial \overline{\rho}\widetilde{N_{ps}}}{\partial t} + \frac{\partial \overline{\rho}\widetilde{u}_i\widetilde{N_{ps}}}{\partial x_i} = \frac{\partial \tau^{sgs}_{u_i N_{ps}}}{\partial x_i} + \overline{\dot{\omega}^{N_{ps}}_{nucl}} - \overline{\dot{\omega}^{N_{ps}}_{coag}} \tag{3.9}$$

$$\frac{\partial \overline{\rho}\widetilde{Y_s}}{\partial t} + \frac{\partial \overline{\rho}\widetilde{u}_i\widetilde{Y_s}}{\partial x_i} = \frac{\partial \tau^{sgs}_{u_i Y_s}}{\partial x_i} + \overline{\dot{\omega}^{Y_s}_{nucl}} + \overline{\dot{\omega}^{Y_s}_{sg}} - \overline{\dot{\omega}^{Y_s}_{ox,O_2}} - \overline{\dot{\omega}^{Y_s}_{ox,OH}} \tag{3.10}$$

where the subscript *sg* refers to the surface growth process. The subgrid-scale scalar fluxes, $\tau^{sgs}_{u_i N_s}$ and $\tau^{sgs}_{u_i Y_s}$ are closed using the DEDM as for the other scalars.

$$\tau^{sgs}_{u_i N_{ps}} = -\overline{\rho}\left(\widetilde{u_i N_{ps}} - \widetilde{u_i}\widetilde{N_{ps}}\right) \approx \overline{\rho} D_t \frac{\partial \widetilde{N_{ps}}}{\partial x_i} \tag{3.11}$$

$$\tau^{sgs}_{u_i Y_s} = -\overline{\rho}\left(\widetilde{u_i Y_s} - \widetilde{u_i}\widetilde{Y_s}\right) \approx \overline{\rho} D_t \frac{\partial \widetilde{Y_s}}{\partial x_i} \tag{3.12}$$

The source terms of equations 3.9-3.10 also requires closures. The subgrid-scale soot production/turbulence interaction is dealt using a presumed filtered density function, see section 3.2.4.

3.2.3.1 Nucleation

The Lindstedt model models soot inception with a correlation based on acetylene, C_2H_2, and benzene, C_6H_6 :

$$\left.\begin{array}{l} C_2H_2 \rightarrow 2C_S + H_2 \\ C_6H_6 \rightarrow 2C_S + H_2 \end{array}\right\} \quad \text{with} \quad \dot{\omega}_{nucl} = 2k_1(T)[C_2H_2] + 6k_2(T)[C_6H_6] \tag{3.13}$$

where the $[C_i]$ represents the molar concentration of species i, the reactions kinetic coefficients are :

$$k_1(T) = 0.63 \times 10^4 e^{-21000/T} \tag{3.14}$$

$$k_2(T) = 0.75 \times 10^5 e^{-21000/T} \tag{3.15}$$

The nucleation rates are then expresses as :

$$\dot{\omega}_{nucl}^{N_{ps}} = \frac{N_{av}}{N_{C,min}} \dot{\omega}_{nucl} \tag{3.16}$$

$$\dot{\omega}_{nucl}^{Y_s} = W_s \times \dot{\omega}_{nucl} \tag{3.17}$$

where N_{av}, $N_{C,min} = 60$ and $W_s = 12.011$ kg/kmol are the Avogadro number, the number of carbon atoms in a soot nuclei and the carbon molecular weight, respectively.

3.2.3.2 Surface growth and oxidation

Acetylene, C_2H_2, is assumed to control the surface growth and the soot surface growth rate :

$$nC_S + C_2H_2 \rightarrow (n+2)C_S + H_2 \qquad \text{with} \qquad \dot{\omega}_{sg}^{Y_s} = 2M_c k_3(T) A_s [C_2H_2] \tag{3.18}$$

where $k_3(T) = 0.4 \times e^{-12100/T}$.

The rate of oxidation by O_2 was computed following Nagle and Strickland-Constable (1962), while the oxidation rate for OH was based on the work of Fenimore and Jones (1967) with a collision efficiency factor was set equal to 0.1.

3.2.4 Subgrid-scale turbulence/soot production interaction (SGS TSI)

As chemical reactions, soot formation/oxidation occur in the unresolved subgrid-scales. The turbulence/soot production interaction, represented by the filtered source terms of equations 3.9-3.10, is thus entirely modelled. The soot production rates, $\dot{\omega}$, can be decomposed into a gas-phase related part, $\dot{\omega}_g$, that depends on gas-phase thermo-chemical variables, $\phi_g = \{Z, \chi, X_R\}$, and a soot-related part, $\dot{\omega}_s$, that depends on soot variables, $\phi_s = \{Y_s, N_{ps}\}$:

$$\dot{\omega}(\phi_g, \phi_s) = \dot{\omega}_g(\phi_g)\dot{\omega}_s(\phi_s) \tag{3.19}$$

$\dot{\omega}_g$ was stored in the flamelet library while $\dot{\omega}_s$ was computed on the flight during the

sequence of calculations. This approach does not considered explicitly the consumption of benzene, acetylene, radical hydroxyl and oxygen, involved in the soot model as soot precursors or oxidative species. However, this modelling, in conjunction with the set of model parameters and kept unchanged in the present study, was found to predict soot volume fraction within the experimental uncertainties in both laminar and turbulent jet diffusion flames fueled by C_1-C_3 hydrocarbons, Nmira et al. (2015), Consalvi et al. (2016), Consalvi and Nmira (2016).

The filtered source terms for the soot production processes can be closed through convolution with a density-weighted joint FDF, $\widetilde{P}(\phi_g,\phi_s)$:

$$\overline{\dot{\omega}} = \overline{\rho} \iint \frac{\dot{\omega}(\phi_g,\phi_s)}{\rho^{fl}(\phi_g)} \widetilde{P}(\phi_g,\phi_s) d\phi_g d\phi_s \tag{3.20}$$

A presumed FDF approach is used to determine $\widetilde{P}(\phi_g,\phi_s)$, Mueller and Pitsch (2012), Yang et al. (2019). Let us first apply the Bayles theorem to equation 3.20 :

$$\overline{\dot{\omega}} = \overline{\rho} \iint \frac{\dot{\omega}(\phi_g,\phi_s)}{\rho^{fl}(\phi_g)} P(\phi_s|\phi_g) \widetilde{P}(\phi_g) d\phi_g d\phi_s \tag{3.21}$$

where the FDF associated to the gas-phase is presumed as previously discussed $\widetilde{P}(\phi_g) = \beta(Z;\widetilde{Z},V_Z)\delta(\chi-\widetilde{\chi})\delta(X_R-\widetilde{X_R})$, see section 3.7. Following Yang et al. (2019), the soot FDF conditioned by the gas-phase, $P(\phi_s|\phi_g)$, is presumed with two presumed conditional FDF, built to account for two main features of soot production process at the subgrid-scale. The first model, referred to as S_1 hereafter, considers the high spatial intermittent nature of soot by introducing a bimodal distribution with the parameter α determining the relative weight between the non-sooting and sooting modes, Mueller and Pitsch (2012), Yang et al. (2019).

$$S_1 : \quad P(\phi_s|\phi_g) = (1-\alpha)\delta(\phi_s) + \alpha\delta(\phi_s-\phi_s^*) \tag{3.22}$$

ϕ_s^* is a prescribed value to recover the filtered values of the soot scalars $\widetilde{\phi_s}$ upon convolution against $\widetilde{P}(\phi_g,\phi_s)$. α can be interpreted as the probability to have soot at a given location.

The second feature is that soot oxidation occurs extremely fast, Mueller and Pitsch (2012), Brookes and Moss (1999), Kronenburg et al. (2000). A consequence is that, in the mixture fraction space, soot particles do not exist over the entire region where soot oxidation can occur, leading to a strong correlation between soot quantities and mixture fraction, Mueller and Pitsch (2012), Brookes and Moss (1999), Kronenburg et al. (2000). In order to take this process into account, the model S_2 extends S_1, by introducing a Heaviside function, $H(Z-Z_s)$, where Z_s indicates the location in the mixture fraction space at which soot is completely burnt. In the present study, we assume that soot does not exist as soon as it ceases to be produced and, consistently

with the proposed production model, Z_s correspond to the location where acetylene is completely consumed and, then the gas-phase related part of the surface growth rate, $\dot{\omega}_{g,SG}$, becomes equal to zero.

$$S_2: \quad P(\phi_s|\phi_g) = \left[(1-\alpha)\delta(\phi_s) + \alpha\delta(\phi_s - \phi_s^*)\right] H(Z - Z_s) \tag{3.23}$$

From this definition, Z_s can be entirely determined from the gas-phase chemistry (flamelet library) and depends on both stoichiometric scalar dissipation rate and enthalpy defect, $Z_s \equiv Z_s(\chi_{st}, X_{R,st})$. The procedure to determine Z_s is illustrated in Figure 3.1.

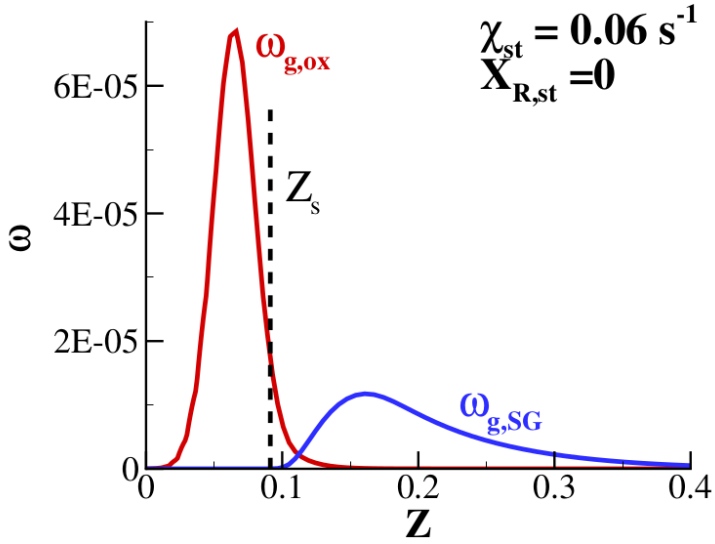

Figure 3.1 – Determination of Z_s for an adiabatic flamelet with $\chi_{st} = 0.06\ s^{-1}$. The red and blue lines correspond to the gas-phase related part of the soot oxidation rate, $\dot{\omega}_{g,Ox}$, and surface growth rate, $\dot{\omega}_{g,sg}$, respectively. Z_s corresponds to the location on the fuel lean region where $\dot{\omega}_{g,sg}$ is equal to zero.

α and ϕ_s^* are obtained from Yang et al. (2019) :

$$\alpha = \frac{\widetilde{N_{ps}}^2}{\widetilde{N_{ps}^2}}; \quad \phi_s^* = \frac{\widetilde{\phi_s}}{\alpha} \quad \text{for } S_1 \tag{3.24}$$

$$\alpha = \frac{\widetilde{N_{ps}}^2}{\widetilde{N_{ps}^2} H_{\text{int}}}; \quad \phi_s^* = \frac{\widetilde{\phi_s}}{\alpha H_{\text{int}}} \quad \text{for } S_2 \tag{3.25}$$

with $H_{\text{int}} = \int_0^1 H(Z - Z_s)\widetilde{\beta}(Z)dZ$. $\widetilde{N_{ps}^2}$ is the second moment of the soot number

density of primaries, its transport equation 3.26 is added to the set of solved transport equations. Its subgrid-scale scalar flux is solved similarly to the other soot subgrid-scale scalar fluxes.

$$\frac{\partial \overline{\rho}\widetilde{N_{ps}^2}}{\partial t} + \frac{\partial \overline{\rho}\widetilde{u}_i\widetilde{N_{ps}^2}}{\partial x_i} = \frac{\partial}{\partial x_i}\left(\overline{\rho}D_t\frac{\partial \widetilde{N_{ps}^2}}{\partial x_i}\right) + 2\overline{N_{ps}\dot{\omega}_{nucl}^{N_{ps}}} - 2\overline{N_{ps}\dot{\omega}_{coag}^{N_{ps}}} \tag{3.26}$$

The filtered source terms can be expressed for S_2 as:

$$\overline{\dot{\omega}} = \alpha\dot{\omega}_s(\phi_s^*) \times \overline{\rho}\int_{Z_s}^1 \frac{\dot{\omega}_g^{fl}(\phi_g)}{\rho^{fl}(\phi_g)}\widetilde{\beta}(Z)dZ \tag{3.27}$$

For S_1 the integration in equation 3.27 starts from 0 instead of Z_s.

3.2.5 Subgrid-scale turbulence/radiation interaction (SGS TRI)

The sensitivity of the flame structure to the radiative property models of soot and gas is investigated based on the RCFSK and non-grey WSGG. The generic filtered RTE can be written :

$$\frac{d\overline{I_i}}{ds} + \overline{\kappa_i I_i} = \overline{\kappa_i a_i I_b(T)} \qquad i = 1, N_g \tag{3.28}$$

Two different closures for the filtered absorption and emission terms in equation 3.28 are investigated in order to quantify the effects of subgrid-scale emission turbulence/radiation interaction (SGS emission TRI). In both models, the SGS absorption TRI is dealt with the optically thin fluctuation approximation (OTFA), which neglects the SGS absorption TRI, based on the work of Gupta et al. (2013), leading to :

$$\overline{\kappa_i I_i} = \overline{\kappa_i}\overline{I_i} + \overline{\kappa_i' I_i'} \approx \overline{\kappa_i}\overline{I_i} \tag{3.29}$$

The **first closure** takes the SGS emission TRI into account by computing $\overline{\kappa_i}$ and $\overline{\kappa_i a_i I_b(T)}$ by convolution with the presumed FDF :

$$\overline{\kappa_i} = \overline{\rho}\int \frac{\kappa_i(Z,\widetilde{\chi},\widetilde{X_R},\widetilde{f_{vs}})}{\rho(Z,\widetilde{\chi},\widetilde{X_R})}\beta(Z;\widetilde{Z},V_Z)dZ \tag{3.30}$$

$$\overline{\kappa_i a_i I_b} = \overline{\rho}\int \frac{\kappa_i a_i I_b(Z,\widetilde{\chi},\widetilde{X_R},\widetilde{f_{vs}})}{\rho(Z,\widetilde{\chi},\widetilde{X_R})}\beta(Z;\widetilde{Z},V_Z)dZ \tag{3.31}$$

The absorption coefficient and the emission term depend on mole fractions of CO_2 and H_2O, temperature and soot volume fraction, $\phi = \{x_{CO_2}, x_{H_2O}, T, f_{vs}\}$.

The **second closure** neglects SGS emission TRI by evaluating the filtered absorption coefficient directly from the filtered scalars :

$$\overline{\kappa_i} = \kappa_i(\widetilde{\phi}) \tag{3.32}$$

$$\overline{\kappa_i a_i I_b} = \kappa_i(\widetilde{\phi}) a_i(\widetilde{\phi}) I_b(\widetilde{\phi}) \tag{3.33}$$

3.3 Results and discussions

3.3.1 Experimental details

The well-document 15 kW buoyant ethylene turbulent diffusion flames, investigated experimentally at FM Global, Xiong et al. (2021), Ren et al. (2021), Zeng et al. (2019) and generated from water-cooled porous burner with an outer diameter, D, of 15.2 cm (inner diameter of 13.7 cm), was simulated. These experiments were performed under different controlled O_2/N_2 oxidizers with oxygen concentration, X_{O_2}, of 0.209, 0.168 and 0.152, see Figure 3.2. The measurements include soot volume fraction statistics from a laser induced incandescence (LII) technique, Xiong et al. (2021), temperature measurements for $X_{O_2} = 0.209$ from a dual thermocouple technique, Ren et al. (2021), and radiation characteristics, Zeng et al. (2019).

Figure 3.2 – Real view of the three experimented flames, with decreasing X_{O_2} from left to right, Zeng et al. (2019).

3.3.2 Computational details

Simulations were performed in a computational domain of $3 \times 3 \times 1.5$ m^3. Consistently with the experimental configuration, Zeng et al. (2019), the burner exit stands at 25.4 cm above the floor. A structured mesh with 3.6×10^6 cells is considered. A cell size of 2.5 mm^3 is applied in a box of $0.22 \times 0.22 \times 0.15$ m^3 centered around the burner. The cell size is progressively stretched toward the sides. In the vertical direction, Δz is stretched progressively between $z = 0.15$ m and $z = 0.30$ m to reach 5 mm. A uniform $\Delta z = 5$ mm is then applied up to $z = 0.60$ m. Above $z = 0.60$ m, Δz is stretched progressively.

The flamelet library was generated using the full chemical kinetic scheme developed by Qin et al. (2000). It consists of 70 species and 463 reactions and is dedicated to the oxidation of C_1-C_3 hydrocarbon species.

The present LES were performed on the supercomputer Gaia of EDF R&D over 700 cores. Processors are Intel Xeon Gold 6140 CPU 2.30 GHz. Throughout all simulations, a time-step of 5×10^{-4} s was set. The physical time of simulations was 50 s and the time-averaged mean and root mean square values were collected after the first 15 seconds, once a statistically stationary flow was established.

Concerning the boundary conditions, an inlet velocity was imposed at the burner to ensure the specified heat release rate (HRR). Fixed values of fuel mass flow rate and enthalpy flow rate are maintained according to the specified HRR. Both convective and diffusive mass and enthalpy fluxes are accounted for at the inlet. Typical entrainment boundary conditions are used for lateral sides. At the domain exit, a convective condition was used:

$$\frac{\partial \widetilde{\phi}}{\partial t} + u_c \frac{\partial \widetilde{\phi}}{\partial \mathbf{n}} = 0 \tag{3.34}$$

where $\phi = \left\{ u_j, Z, Z^2, V_Z, h, Y_s, N_{ps}, N_{ps}^2 \right\}$. Following Craske and van Reeuwijk (2013), the convective velocity u_c is given by a Gaussian profile, $u_c = u_0^{out} \exp(-r^2/b^2)$. The mean axial velocity on the plume centerline, u_0^{out}, and the radius, b, at the exit height where obtained from the Heskestad correlations (Heskestad (1984)). Homogeneous Neumann condition is used for the pressure. In the rest domain, the classical wall boundary condition is imposed.

Six different modelling approaches were considered to investigate the sensitivity of the predictions to either SGS TSI model or the radiative property models. The characteristics of these simulations are summarized in Table 3.1.

The model M_1 is the most complete model and will be considered as the baseline model. M_2 neglects the soot fast oxidation feature, M_3 considers soot as grey, M_4 employs the WSGG instead of the RCFSK and M_5 neglects the SGS emission TRI by computing the absorption coefficient and the emission term directly from the filtered

	SGS TSI	Gas radiation	Non-grey soot	SGS TRI	CPU(s)
M_1	S_2	RCFSK	Yes	Yes	5.34
M_2	S_1	RCFSK	Yes	Yes	5.02
M_3	S_2	RCFSK	No	Yes	5.15
M_4	S_2	WSGG	No	Yes	4.10
M_5	S_2	RCFSK	Yes	No	5.16

Table 3.1 – SGS TSI and radiative models with CPU time per iteration in the right hand side column.

scalars. Table 3.1 also provides the CPU times for all the models in one time step. All the models have similar iteration time except model M_4 that uses the WSGG and requires then to solve 4 radiative transfer equations instead of 10 for the RCFSK.

3.3.3 Quality of LES and grid sensitivity

The ratio of resolved temperature variance, $\langle T'^2\rangle_{ReS} = \langle \widetilde{T}^2\rangle - \langle \widetilde{T}\rangle^2$, to the total temperature variance, $\langle T'^2\rangle = \langle \widetilde{T^2}\rangle - \langle \widetilde{T}\rangle^2$, where the brackets denote the time-averaged values, is considered to assess the quality of the present LES. Figure 3.3 shows the evolution of the resolved part of temperature variance along the flame axis. It can be observed that the present LES resolves on the whole more than 80% of the temperature variance.

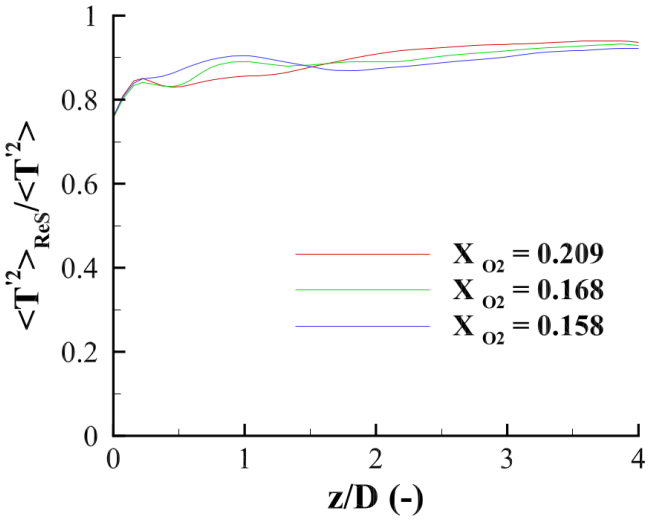

Figure 3.3 – Resolved-part of temperature variance as a function of the normalized height.

The grid independence of the LES solutions was checked by simulating the flame burning under $X_{O_2} = 0.209$ with M_1 on a refined mesh with a minimum grid size of

1.25 mm. This grid independence study is illustrated in Figure 3.4 and shows that the 2.5-mm cell size is appropriate.

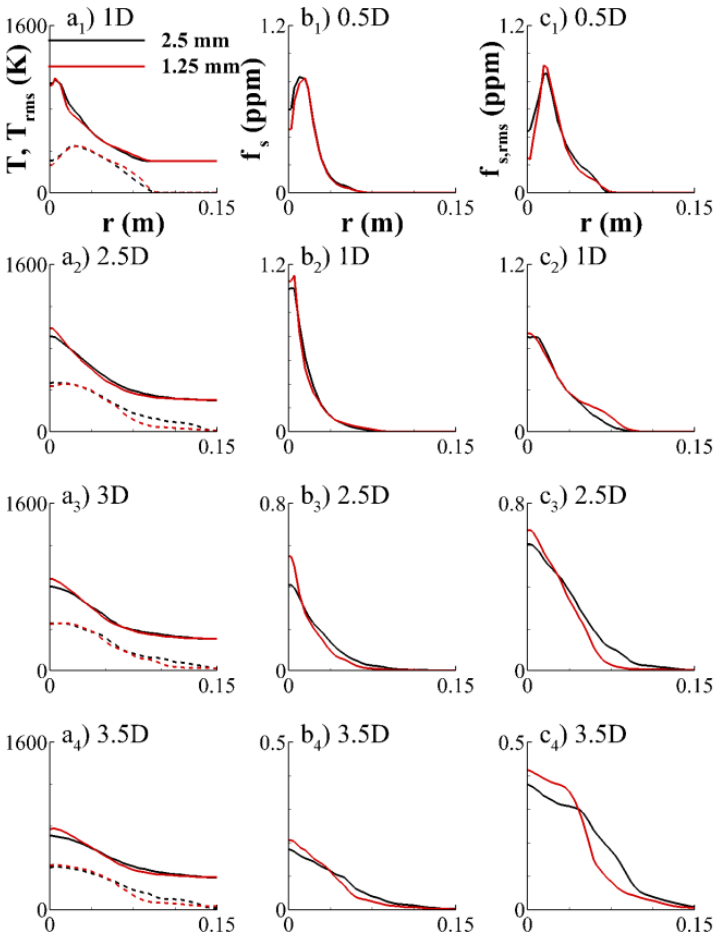

Figure 3.4 – Grid sensitivity study on the flame burning with $X_{O_2} = 0.209$ with model M_1.

3.3.4 Comparison with experiments

3.3.4.1 Comparison of temperature and soot characteristics with experiments

Model predictions with M_1 are compared with the available experiments in Figures 3.5-3.6-3.7 for the different X_{O_2}. This comparison concerns the radial distributions of mean and rms temperature, mean and rms SVF and the soot intermittency index at different heights. The soot intermittency index represents the fraction of time where soot is present at a given location and, consistently with the experiments, Xiong et al. (2021), is computed as the fraction of the time during which the SVF is higher than 0.09

ppm. The experimental uncertainties on instantaneous temperature measurements is ±41 K, Ren et al. (2021), whereas those on SVF were estimated to be about 17% based on a detailed analysis of SVF measurements, Xiong et al. (2021).

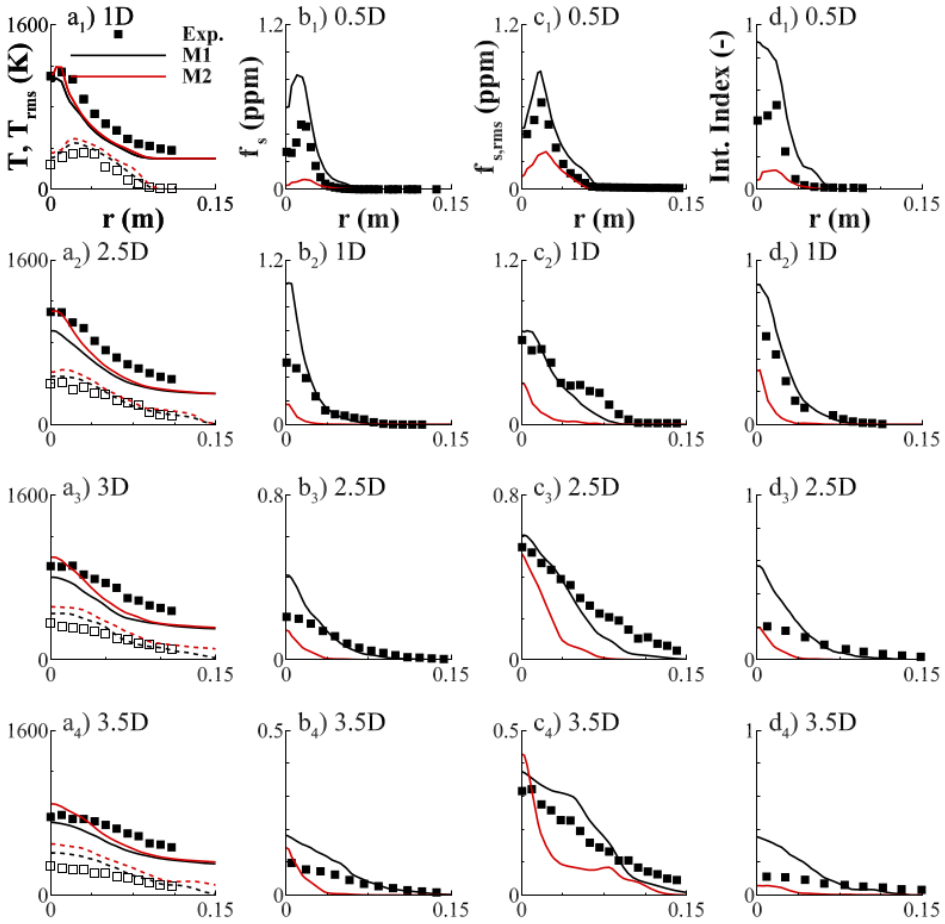

Figure 3.5 – Radial profiles of a) mean (solid lines and black squares) and fluctuations (dashed lines and open squares) of temperature, b) mean SVF, c) fluctuations of SVF, and d) soot intermittency index at different heights for $X_{O_2} = 0.209$.

The strong unsteady behaviour of these buoyant flames is illustrated by SVF fluctuations locally higher than the corresponding mean values. The measurements also highlight the strong intermittent nature of the soot at all locations in the flames with a soot intermittency index always lower than 0.6 and decreasing as the height above the burner increases for the three flames. The experimental results show also that decreasing X_{O_2} reduces the soot production with lower mean and rms SVF at a given height. The simulations performed with M_1 reproduce quantitatively all these features although, for $X_{O_2} = 0.209$, the mean temperature is underpredicted throughout the

entire flame (see Figure 3.5-(a)) and the mean SVF and soot intermittency index are overpredicted at vicinity of the flame axis.

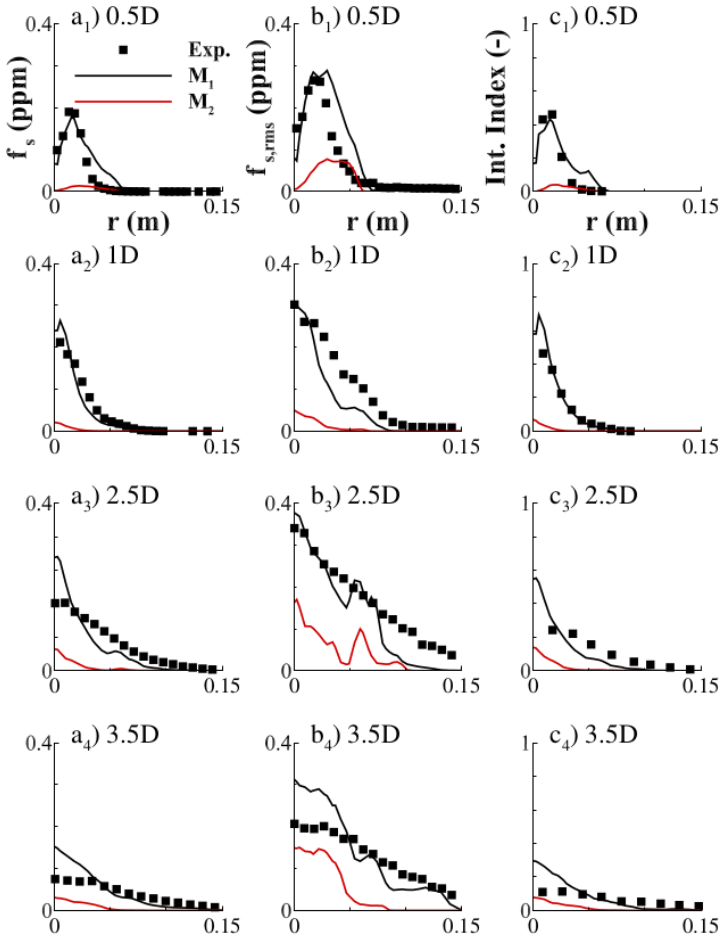

Figure 3.6 – Radial profiles of a) mean soot volume fraction, b) rms values of SVF fluctuations, and c) soot intermittency index at different heights for X_{O_2} = 0.168.

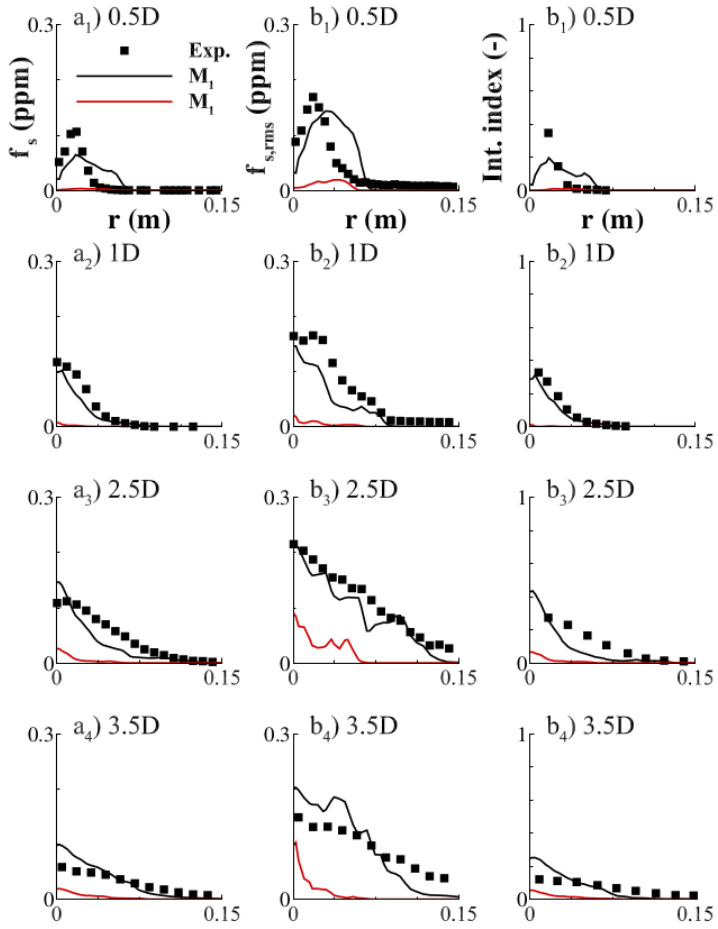

Figure 3.7 – Radial profiles of a) mean soot volume fraction, b) rms values of SVF fluctuations, and c) soot intermittency index at different heights for $X_{O_2} = 0.152$.

3.3.4.2 Influence of the SGS TSI

Predictions obtained with M_2, i.e. by neglecting the correlation between soot quantities and mixture fraction, are also plotted in Figures 3.5-3.6-3.7. The model M_2 leads to a severe underprediction of SVF, especially along the flame wings, which can be attributed to an overestimation of the soot oxidation rate. The origin of this overestimation was elucidated by Kronenburg et al. (2000). Oxidizer species and soot profiles little overlap in the mixture fraction space due to fast soot oxidation. A consequence is that soot quantities are strongly correlated with oxidative species and, in turn, mixture fraction in the soot oxidation region which cannot be captured by the uncorrelated M_2 model.

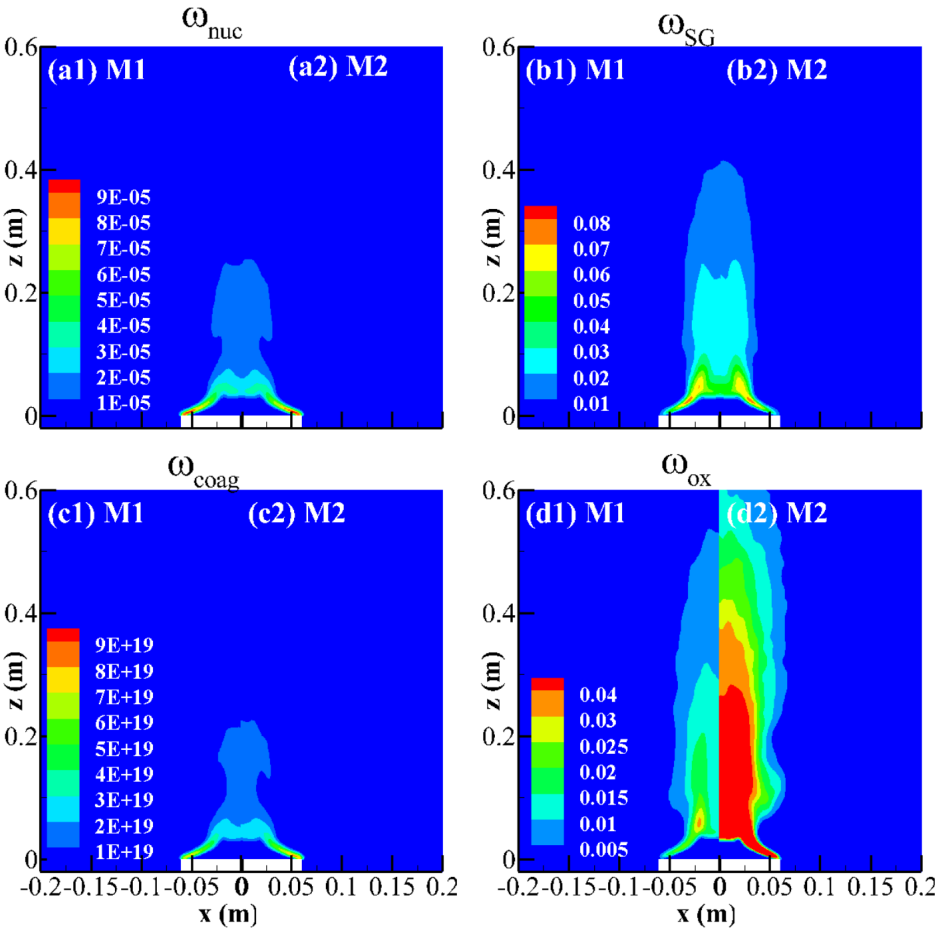

Figure 3.8 – Effects of SGS TSI model on the fields of soot production rates for $X_{O_2} = 0.209$: a) mass nucleation (kg/m^3/s), b) surface growth (kg/m^3/s), c) coagulation (part/m^3/s), and d) oxidation (kg/m^3/s). The left-side is computed with M_1 and the right-side with M_2.

Figure 3.8 compares the fields of the soot production rates evaluated with M_1 and M_2 for $X_{O_2} = 0.209$. Modifying the SGS TSI model in coupled flow/turbulence/soot/-combustion/radiation computations affects the prediction of soot quantities and, in turn, the mean soot production rates, which can lead to misleading interpretation on the role of SGS TSI. In order to avoid these difficulties, the mean soot production rates, reported in Figure 3.8 were computed for both M_1 and M_2 from instantaneous data obtained from the M_1 baseline calculations once a statistically steady state is reached. Figure 3.8 confirms that, contrary to the other soot processes, soot oxidation is strongly affected by the SGS TSI model and is one order of magnitude higher when computed with M_2. A consequence is that the contribution of soot to radiation becomes negligible when M_2 is considered. This leads, on the one hand, to higher temperature especially at vicinity of the flame axis as observed in Figure 3.5-(a) and,

X_{O_2}	Model	$\dot{Q}_{em}$ (kW)	$\dot{Q}_{em,s}$ (kW)	$\dot{Q}_{em,g}$ (kW)	$\dot{Q}_{abs}$ (kW)	$\frac{\dot{Q}_{em,s}}{\dot{Q}_{em}}$	$\frac{\dot{Q}_{abs}}{\dot{Q}_{em}}$	χ_R
Flame radiative structures								
20.9	M_1	7.89	3.91	3.98	2.06	0.496	0.261	0.389
16.8	M_1	5.37	1.99	3.38	1.54	0.370	0.286	0.255
15.2	M_1	4.25	1.14	3.12	1.37	0.267	0.322	0.192

Table 3.2 – Integrated flame radiative properties. Measured radiant fractions are 0.34, 0.30 and 0.22 for X_{O_2} = 0.209, 0.168, 0.152, respectively, Zeng et al. (2019).

on the other hand, to a substantial underestimation of the radiant fractions which reduced to 0.219, 0.159 and 0.138 for X_{O_2} = 0.209, 0.168 and 0.152, respectively.

3.3.4.3 Comparison of radiative characteristics with experiments

Table 3.2 compares predicted and measured radiant fractions. For the simulations, the radiant fractions are determined as :

$$\chi_R = \frac{\dot{Q}_{em} - \dot{Q}_{abs}}{\dot{Q}} \tag{3.35}$$

where $\dot{Q}_{em}$ and $\dot{Q}_{abs}$ are the total (integrated over the computational domain volume) emission and absorption, respectively, and $\dot{Q}$ is the heat release rate. On the other hand, experiment radiant fractions were obtained by integrating the radiant power distribution, obtained from slit radiometer measurements, along the flame height, Ren et al. (2021). Measured radiant fractions are 0.34, 0.30 and 0.22 for X_{O_2} = 0.209, 0.168, 0.152, respectively. Both measured and computed radiant fractions decrease with reducing X_{O_2} owing to a conjugated reduction in temperature and SVF. This produces a decrease in both soot, $\dot{Q}_{em,s}$, and gas, $\dot{Q}_{em,g}$, emission, as illustrated in the 4^{th} and 5^{th} columns of Table 3.2. Predicted χ_R are within about 15% of the experiments. The 7^{th} column of Table 3.2 shows the ratio between soot emission and total emission which is a metric to evaluate the contribution of soot to radiation. Model results show that gas and soot contributions are similar for X_{O_2} = 0.209 and gas radiation becomes increasingly dominant as X_{O_2} is reduced due to a decrease in SVF throughout the overall flame. For X_{O_2} = 0.152, the soot contribution to total emission remains only of 26.7%. The penultimate column of Table 3.2 shows the part of total emission reabsorbed within the flame that can be interpreted as a measure of the flame optical thickness. Model results show that $\dot{Q}_{abs}/\dot{Q}_{em}$ ranges between 0.261 and 0.322. Radiatively participating gases have a stronger non-gray behaviour as compared to soot particles and, consequently, are comparatively less transparent, Wu et al. (2020), Mehta et al. (2009). A consequence is that the flame becomes optically thicker as the contribution of gas radiation is enhanced, as illustrated by the increase in $\dot{Q}_{abs}/\dot{Q}_{em}$ with decreasing X_{O_2}.

X_{O_2}	Model	$\dot{Q}_{em}$ (kW)	$\dot{Q}_{em,s}$ (kW)	$\dot{Q}_{em,g}$ (kW)	$\dot{Q}_{abs}$ (kW)	$\frac{\dot{Q}_{em,s}}{\dot{Q}_{em}}$	$\frac{\dot{Q}_{abs}}{\dot{Q}_{em}}$	χ_R
Effects of radiation models								
20.9	M_1	7.89	3.91	3.98	2.06	0.496	0.261	0.389
20.9	M_3	7.65(-3.1)	3.91(0.0)	3.74(-6.0)	1.83(-11.1)	0.511(+3.0)	0.239	0.388
20.9	M_4	8.32(+5.4)	3.80(-2.8)	4.52(+13.5)	2.34(+14.0)	0.457(-7.8)	0.282	0.398
20.9	M_5	7.77(-1.6)	4.50(+15.1)	3.27(-17.9)	1.98(-3.5)	0.579(+16.9)	0.255	0.386

Table 3.3 – Integrated flame radiative properties obtained for the variant radiative models. The value in parenthesis represents the relative error in percent as compared to M_1.

3.3.4.4 Influence of the radiative models

Figure 3.9 and Table 3.3 illustrate the effects of the different radiative models for $X_{O_2} = 0.209$. The conclusions drawn for the other X_{O_2} are quantitatively similar and, consequently, are not shown. The model M_3 considers soot as grey. As expected this approximation leads to an underprediction of soot absorption and, in turn, of $\dot{Q}_{abs}$ by 11% (see the 6^{th} column of Table 3.3). Nevertheless, the present flames have moderate optical thicknesses and these discrepancies have almost no influence on χ_R (see the last column of 3.3) and on mean and rms temperature and SVF (see Figure 3.9). The WSGG (model M_4) overestimates significantly both gas emission and absorption (see the 5^{th} and 6^{th} columns of Table 3.3). Nevertheless, these two effects balance on the whole, leading to only slight overprediction of χ_R (see Table 3.3). The model M_5 neglects SGS emission TRI. As discussed by Nmira et al. (2021) in the case of non-sooting pool fires and illustrated in the 5^{th} column of Table 3.3, this reduces significantly gas emission, leading to higher instantaneous gas temperature when soot forms and growths and, consequently, to a higher soot production. This is clearly observed Figure 3.9-(c) and d where the model M_5 overestimates both mean and rms of SVF by a factor of about 2. This produces, in turn, an overprediction of soot emission as shown in the 4^{th} column of Table 3.3, leading to a reduction of the instantaneous temperature during the intermittent passage of the soot structures. Table 3.3 shows that the underpediction of $\dot{Q}_{em,g}$ balances the overprediction of $\dot{Q}_{em,s}$, resulting in minor effects on χ_R (see Table 3.3) and temperature statistics (see Figure 3.9-(a) and (b)).

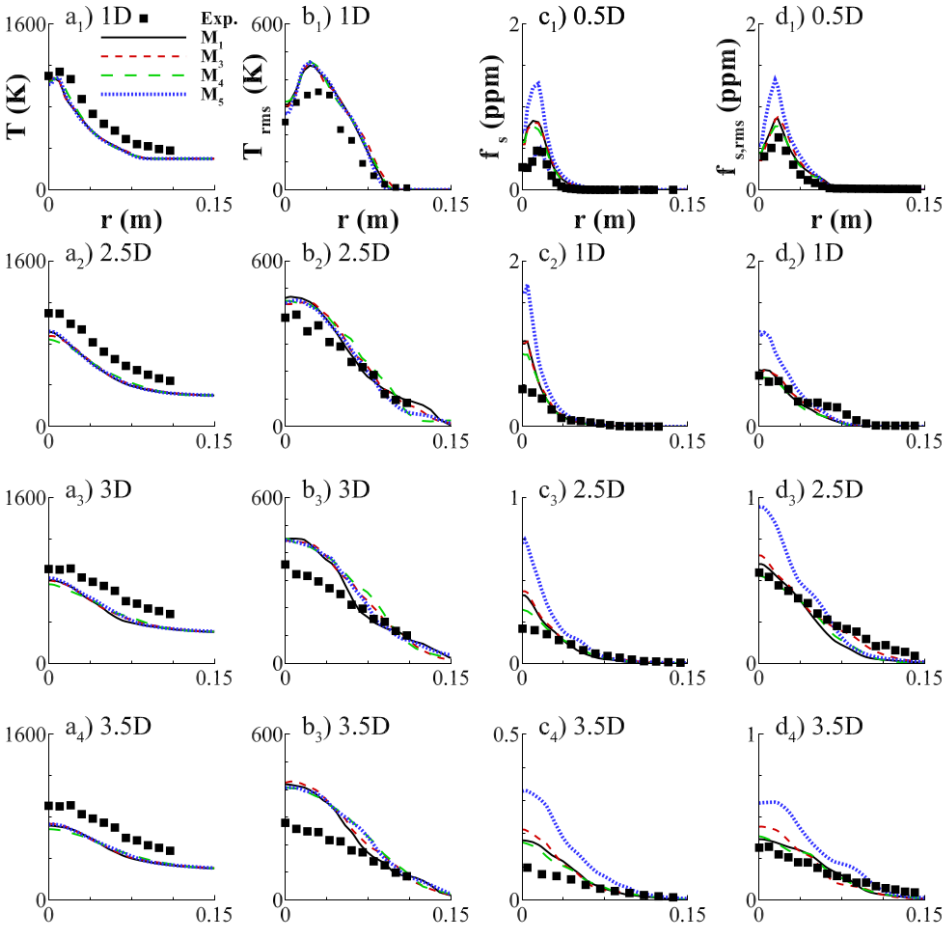

Figure 3.9 – Effects of radiation models. Radial profiles of a) mean temperature, b) fluctuations of temperature, c) mean soot volume fraction, and d) fluctuations of soot volume fraction at different heights for $X_{O_2} = 0.209$.

3.4 Chapter conclusions and perspectives

LES of lab-scale ethylene buoyant diffusion flames burning at normal and reduced-oxygen conditions are performed by using a flamelet/presumed FDF combustion model, an acetylene/benzene-based soot production model and non-grey gas radiative models. The baseline simulation considers the coupling between soot quantities and mixture fraction, the SGS emission TRI and the RCFSK with non-grey soot. The sensitivity of the solutions to SGS TSI and approximate radiative models is investigated. The following conclusions can be drawn :

- The baseline calculation reproduces with fidelity the flame structure, the soot production dynamics, and the radiative loss at both normal and under-oxygenated

conditions.

- The contributions of gas and soot to radiation are similar for the flame burning under air whereas gas radiation becomes increasingly dominant with decreasing X_{O_2}.
- Disregarding the correlation between soot quantities and mixture fraction leads to a substantial underestimation in the soot production.
- The grey-soot approximation is valid in these flames characterized by a low soot optical thickness and the non-grey WSGG can be used for these peculiar flames. However, the readers have to keep in mind that this model does not predict accurately the emission and absorption terms, and the final acceptable results is due to compensation of errors.
- For the present LES that resolves more than 80% of temperature variance, disregarding SGS emission TRI induces a severe overprediction in the soot production.

The main result obtained in the present chapter is that presumed FDF can be designed to account for spatial intermittency and correlation between soot quantities and mixture fraction. This approach represents an alternative to transported FDF models to capture subgrid soot production/turbulence interaction at a significantly lower cost. The simulated flames were fuelled by ethylene and the exhaustively-validated acetylene/benzene model, proposed by Lindstedt (1994), was considered. Due to its inherent formulation, this soot production model is limited to non-aromatic fuels and, in order to introduce a more general approach, PAH-based soot models will be developed and assessed in the next chapters. Fuels involving aromatic components, such as those encountered in transport activities (gasoline, diesel, jet fuels, kerosene), are of particular interest for fire applications.

4 Calibration and validation of a PAH-based soot production model in ethylene coflow diffusion flames

Table of contents

4.1 Introduction

The previous chapter has reinforced conclusions drawn by Nmira et al. (2015), Consalvi et al. (2016), Consalvi and Nmira (2016) that the acetylene/benzene-based model, proposed by Lindstedt (1994), is a good candidate for fire applications involving non-aromatic fuels. As fuels containing aromatics components are involved, the inherent assumptions behind the model formulation are no longer valid and, an alternative

has to be developed. The presence of aromatics implies that PAHs have to be directly selected as soot precursors. The first objective of this chapter is to develop and calibrate a PAH-based soot model. This task will be made by considering the laminar ethylene coflow diffusion flames investigated experimentally by Sun et al. (2021), burning under oxygen concentration in the oxidizer down to 16.8% and characterized by a constant volumetric stoichiometric air to fuel ratio to keep the residence time unchanged. A consequence is that the reduction in oxygen is the only mechanism responsible for the mitigation of soot production in these flames. The second objective is then naturally to provide insights on the processes governing the reduction in soot production while decreasing X_{O_2}. This model will then be used to model liquid fuels containing aromatic components in the next Chapter.

4.2 PAH-based soot production model

The three equation formulation is adopted and hereafter called PAH-based model. The transport equations of the number density of soot aggregate, the number density of primary particles and the soot mass fraction express as :

$$\frac{\partial \rho N_s}{\partial t} + \frac{\partial \rho (u_i + u_{th,i}) N_s}{\partial x_i} = \dot{\omega}^{N_s}_{nucl} - \dot{\omega}^{N_s}_{C/A} \tag{4.1}$$

$$\frac{\partial \rho N_{ps}}{\partial t} + \frac{\partial \rho (u_i + u_{th,i}) N_{ps}}{\partial x_i} = \dot{\omega}^{N_{ps}}_{nucl} - \dot{\omega}^{N_{ps}}_{C} \tag{4.2}$$

$$\frac{\partial \rho Y_s}{\partial t} + \frac{\partial \rho (u_i + u_{th,i}) Y_s}{\partial x_i} = \dot{\omega}^{Y_s}_{nucl} + \dot{\omega}^{Y_s}_{cond} + \dot{\omega}^{Y_s}_{sg} - \dot{\omega}^{Y_s}_{Ox} \tag{4.3}$$

where $u_{th,i} = -0.55 \frac{\mu}{\rho T} \frac{\partial T}{\partial x_i}$ is the thermophoretic velocity in the direction i,

4.2.1 Soot production processes

4.2.1.1 Nucleation

Nascent soot particles are presumed to nucleate through the dimerization of two PAH species, Frenklach and Wang (1994), Appel et al. (2000) :

$$PAH + PAH \rightarrow soot \tag{4.4}$$

The corresponding reaction rates can be expressed from the gas theory, Frenklach and Wang (1994), Blanquart and Pitsch (2009b) :

$$\dot{\omega}_{nucl}^{N_s} = \dot{\omega}_{nucl}^{N_{ps}} = 2.2\gamma_{nucl}\left(\frac{4\pi k_B T}{N_{c,PAH} m_c}\right)^{1/2} [PAH]^2 N_{av}^2 d_{PAH}^2 \tag{4.5}$$

$$\dot{\omega}_{nucl}^{Y_s} = 2N_{c,PAH} m_c \dot{\omega}_{nucl}^{N_s} \tag{4.6}$$

where N_{av}, $[PAH]$, k_B, $N_{c,PAH}$, are the Avogadro number, the molar concentration of PAH, the Boltzmann constant, and the number of carbon atoms in the PAH, respectively. m_c is the mass of carbon atom ($m_c = 12 \times AMU$, $AMU = 1.67 \cdot 10^{-24}$ g). d_{PAH} is the collision diameter of the PAH, and is assumed to be related to the content of carbon atom following Frenklach and Wang (1994) :

$$d_{PAH} = D_A\sqrt{2N_{c,PAH}/3} \quad \text{with} \quad D_A = 1.395\sqrt{3}\text{Å} \tag{4.7}$$

The nucleation collision efficiency, γ_{nucl}, was calibrated to 10^{-3}, further discussion on its calibration is carried out in section 4.2.4.

4.2.1.2 Soot surface growth and oxidation

The soot surface growth and oxidation are assumed to follow the H-abstraction and acetylene addiction (HACA) reaction sequence proposed by Appel et al. (2000) and are depicted in Table 4.1. These specific reactions include the surface activation and deactivation (R_1, R_2, R_3). Surface growth occurs via two alternate reactions, R_{4a} and R_{4b}, that differ in the assumption whether the radical site on the soot surface is preserved after the reaction. According to Wang et al. (1996), reaction R_{4a} is more adequate at the high-temperature, high H atom concentration region of the soot window whereas reaction R_{4b} is needed in order to sustain surface growth toward the low temperature. The two reaction models represent the two limiting cases. In the present study, it is assumed that the role of surface radicals in the generation of soot lies within these extremes such that $k_{ss} = \xi k_{ss,cons} + (1-\xi) k_{ss,dep}$ with ξ being adjusted to 0.7 while the indexes *dep.* and *cons.* represents depleted and conserved reactive sites, respectively (Kalbhor and van Oijen (2022)).

No.	Reaction	A ($cm^3/mol/s$)	n	E ($kcal/mol$)
R_1	$C_{(s)} - H + H \rightleftharpoons C_{(s)}^{\bullet} + H_2$	4.2×10^{13}	-	13.0
R_2	$C_{(s)} - H + OH \rightleftharpoons C_{(s)}^{\bullet} + H_2O$	1.0×10^{10}	0.734	1.43
R_3	$C_{(s)}^{\bullet} + H \rightarrow C_{(s)} - H$	2.0×10^{13}	-	-
R_{4a}	$C_{(s)}^{\bullet} + C_2H_2 \rightarrow C_{(s)} - H + H$	8.0×10^{7}	1.56	3.8
R_{4b}	$C_{(s)}^{\bullet} + C_2H_2 \rightarrow C_{(s)}^{\bullet} + H$	8.0×10^{7}	1.56	3.8
R_5	$C_{(s)}^{\bullet} + O_2 \rightarrow 2CO + \text{products}$	2.2×10^{12}	-	7.5
R_6	$C_{(s)} - H + OH \rightarrow CO + \text{products}$	φ_{OH}		

Table 4.1 – Heterogeneous soot-gas surface reaction mechanism. $C_{(s)}$ represents the saturated sites with n carbon atoms and $C^{\bullet}_{(s)}$ the number of active sites present on the soot surface.

$$k_{ss,dep} = \frac{\{k_{f_1}[H] + k_{f_2}[OH]\}}{\{k_{r_1}[H_2] + k_{r_2}[H_2O] + k_{f_3}[H] + k_{f_4}[C_2H_2] + k_{f_5}[O_2]\}} \tag{4.8}$$

$$k_{ss,cons} = \frac{\{k_{f_1}[H] + k_{f_2}[OH]\}}{\{k_{r_1}[H_2] + k_{r_2}[H_2O] + k_{f_3}[H] + k_{f_5}[O_2]\}} \tag{4.9}$$

The number density of radical sites on the soot surface is then expressed as $\chi_{C^{\bullet}_{(s)}} = k_{ss}\chi_{C_{(s)}-H}$ where $\chi_{C_{(s)}-H} = 2.3\times10^{15}$sites/$m^2$ is the number of sites per particle surface area and the HACA reaction rates are then computed as :

$$\dot{\omega}^{Y_s}_{sg} = 2m_c\alpha k_{f_4}[C_2H_2]\chi_{C^{\bullet}_{(s)}}A_s \tag{4.10}$$

where α is the steric factor. Different formalism for α have been used in the literature : constant values 0.1-0.6 to functions that dependent on temperature alone (Xu et al. (1997), Guo et al. (2006)) or on temperature and mean particle diameter (Appel et al. (2000)). In the present work, an constant value set equal to 0.2 is assumed.

Similarly, the oxidation rate by O_2 is given by :

$$\dot{\omega}^{Y_s}_{ox,O_2} = 2m_c\alpha k_{f_5}[O_2]\chi_{C^{\bullet}_{(s)}}A_s \tag{4.11}$$

Soot oxidation by OH is based on the formulation of Fenimore and Jones (1967). The collision efficiency for OH oxidation is set to the value 0.06, Guo et al. (2006).

$$\dot{\omega}^{Y_s}_{ox,OH} = 1.27\times10^{-2}\times\varphi_{OH}\frac{P_{OH}}{\sqrt{T}}A_s \tag{4.12}$$

4.2.1.3 Condensation of PAH on soot particles

The condensation of PAH on soot particle is considered and modeled as the collision of a PAH molecule with a soot particle :

$$PAH + soot \rightarrow soot \tag{4.13}$$

The condensation rate is calculated with :

$$\dot{\omega}_{cond}^{Y_s} = 2.2 N_{c,PAH} \times m_c \times N_{av}[PAH] \sqrt{\frac{\pi k_B T}{2 N_{c,PAH} m_c}} (d_{PAH} + D_c)^2 (\rho N_s) \tag{4.14}$$

4.2.2 PAH model

The soot production model relies on prediction of PAH species. The modelling of combustion with the SLF model is maintained to keep the PAH-based model evaluation tractable for LES of fire scenarios. The difficulty is that PAHs are governed by a slow chemistry i.e PAH species requires a longer time to respond to rapid changes in the flow field. The slower time scales of PAH formation often violate the fast chemistry assumption of flamelet-based models. To model the unsteady effects, an additional transport equation is solved for PAH species, Mueller and Pitsch (2012).

$$\frac{\partial \rho Y_{PAH}}{\partial t} + \frac{\rho u_i Y_{PAH}}{\partial x_i} = \frac{\partial}{\partial x_i} \left(\rho D_{PAH} \frac{\partial Y_{PAH}}{\partial x_i} \right) + S_{PAH} \tag{4.15}$$

where D_{PAH} is the molecular diffusivity of the PAH. S_{PAH} is the source term of the mass fraction of PAH :

$$S_{PAH} = \dot{\omega}_{PAH}^{+,fl} + \left(\frac{\dot{\omega}_{PAH}^{-,fl}}{Y_{PAH}^{fl}} \right) Y_{PAH} - \dot{\omega}_{nucl}^{Y_s} - \dot{\omega}_{cond}^{Y_s} \tag{4.16}$$

$\dot{\omega}_{PAH}^{+,fl}$, $\dot{\omega}_{PAH}^{-,fl}$ represent the production and consumption rates of the PAH. Assuming that all other species are in steady state, the chemical production rate is a constant $\dot{\omega}_{PAH}^{+} \propto$ const, and the chemical consumption rate is linearly dependent on the PAH mass fraction i.e $\dot{\omega}_{PAH}^{-} \propto Y_{PAH}$. Therefore, $\dot{\omega}_{PAH}^{+,fl}$ and $\dot{\omega}_{PAH}^{-,fl}$, can be tabulated *a priori* into the flamelet library only using only steady state flamelet solutions.

4.2.3 Choice of the PAH for nucleation and condensation

Several PAHs have been used as precursors in the literature, illustrating the lack of consensus :

- Naphthalene (A_2), Wen et al. (2005), Bhatt and Lindstedt (2009), Xuan and Blanquart (2015),
- Pyrene (A_4), Appel et al. (2000), Guo et al. (2006), Zhang (2010), Dworkin et al. (2011a), Saffaripour et al. (2011), Roy (2014), Liu et al. (2014), Aubagnac-Karkar et al. (2015),

- 8 PAHs from naphtalene (A_2) to cyclo[cd]pentapyrene (A_5), Blanquart (2008), Mueller et al. (2009b), Mueller et al. (2009a), Mueller and Pitsch (2011), Mueller and Pitsch (2012),
- 3 five-ring PAHs (A_5), Escudero (2019), Torres (2021),
- 7 PAHs from pyrene (A_4) up to coronene (A_7), Rodrigues et al. (2018).

In the present study, pyrene (A_4) is used as PAH for inception and condensation.

4.2.4 Calibration of the PAH-based soot production model

The PAH-based soot production model was calibrated by simulating the well documented laminar coflow ethylene/air diffusion flame designed by Santoro et al. (1983), using the experimental data on number density of soot aggregates, Santoro et al. (1987), Puri et al. (1993), the number density of primary particles, Puri et al. (1993), Megaridis and Dobbins (1989), and the average number of primary particles per aggregate, Puri et al. (1993), Iyer et al. (2007). This calibration is consistent as the fuel burner dimension and injection velocity considered by Sun et al. (2020) are very similar to those considered in the flame designed by Santoro et al. (1983). The sticking factor for nucleation, γ_{nucl}, and the surface growth parameters, α and ξ, were adjusted to match the experimental number densities of aggregates and primary particles, and the radial soot volume fraction profiles along the height, respectively. On the other hand, the critical primary particle diameter, $d_{p,\text{crit}}$, was adjusted to reproduce at best the primary particle diameter. These parameters were kept constant for all the simulations.

4.3 Validation of the PAH-based model on laminar coflow ethylene flames under normal and oxygen-reduced conditions

This section carries on the comprehensive validation of the soot PAH-based model in the laminar coflow diffusion flame under normal and oxygen-reduced conditions. The laminar regime is chosen so as to prevent any interaction with turbulence. Figure 4.1-(a) schematizes a laminar coflow normal diffusion flames, two concentric cylinder inject fuel and oxidizer separately at fixed velocities that enable the establishment of a laminar and stable flame. Figure 4.1-(b) schematizes the spatial regions where soot particles undergo its life processes : fuel pyrolysis, nucleation, growth and oxidation.

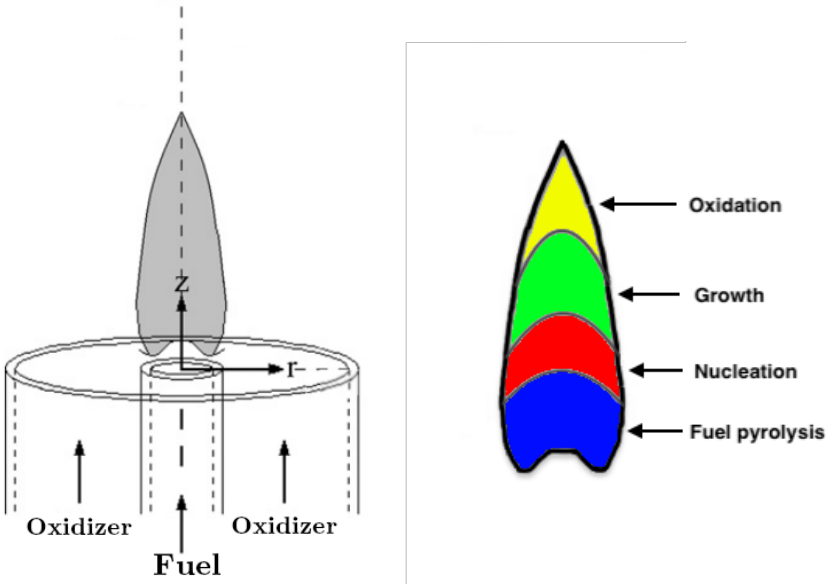

(a) (b)

Figure 4.1 – Schematic representation of a normal coflow diffusion flame.

4.3.1 Numerical model

The overall Navier-Stokes equations in a low Mach-number formulation and transport equations for the mixture fraction, Z, total enthalpy, h, and soot quantities were solved in axisymmetric cylindrical coordinates Nmira et al. (2015). The non-adiabatic SLF is used to obtain the local thermochemical state relationship as a function of (Z, χ, X_R). The flamelet library was generated using the KM2 mechanism developed by Wang et al. (2013). It models C_1-C_4 oxidation and the growth of PAH up to coronene with 202 species and 2438 reactions. The RCFSK is used for radiative property modelling.

4.3.2 Experimental and computational details

Three well-documented axisymmetric ethylene laminar flames, investigated experimentally by Sun et al. (2020), were simulated. Coflow diffusion flames were produced by a Santoro-type concentric-tube burner, consisting of a 10.5-mm inner diameter fuel tube, with a 1.0-mm wall thickness, centered in a 97.7-mm inner diameter laminar oxidizer coflow. Ethylene and the oxidizer were released with velocities of 3.98 cm/s and 24.0 cm/s respectively. The total volumetric flow rates were kept constant for both the fuel and oxidizer streams to maintain a constant ratio of exit flow velocities as $U_{fuel}/U_{ox} = 1/6$. These experiments were performed under different controlled O_2/N_2 oxidizers with X_{O_2} of 0.21, 0.189 and 0.168 in which both the fuel and oxidant were simultaneously diluted with nitrogen to maintain a constant volumetric oxidizer

to fuel ratio for stoichiometric combustion equal to 14.3, see Table 4.2. This procedure allows to maintain similar flame heights and, in turn, residence times, for the three oxidizers.

Soot volume fraction was measured using Laser-Induced Incandescence (LII) and a dimensionless extinction coefficient of $K_e = 4.9$ was used for the calibration. The time-resolved laser-induced incandescence (TiRe-LII) technique was applied simultaneously with LII to measure the diameter of primary soot particles. The experimenters estimated the precision of the soot volume fraction to be ±10%. Temperature was measured by using the nonlinear excitation regime two-line atomic fluorescence (NTLAF) technique whose scope is $T > 800$K and precision within 100K.

Fuel	Oxidizer
100%C_2H_4	21%O_2, 79% N_2
90%C_2H_4, 10% N_2	18.9%O_2, 81.1% N_2
80%C_2H_4, 20% N_2	16.8%O_2, 83.2% N_2

Table 4.2 – Composition of the three simulated coflow diffusion flames of Sun et al. (2020), (%vol).

Simulations are performed in a computational domain (r,z) of 45×150 mm^2. Non-uniform meshes were used with a constant cell size of 0.1875×0.375 mm^2 in the flaming zone. In all cases the fuel and oxidizer are injected at ambient temperature (300 K), with the effects of preheating being disregarded. Fuel is injected a with parabolic inflow velocity profile whereas oxidizer with a flat inflow velocity profile. Pressure is set at 1 atm.

4.3.3 Validation against experiments

4.3.3.1 Results for temperature, soot volume fraction and soot primary particle diameter

Model predictions of the temperature, soot volume fraction and primary particle diameters have been compared with the available experimental data. Figure 4.2 shows the axial and radial distributions of temperature at different heights above the burner. As expected, the predicted temperature is overall lower as X_{O_2} decreases. The differences in the region between 3 cm and 7 cm at vicinity of the axis are less pronounced than in the remaining flame. This can be attributed to a balance between, on the one hand, a reduction in temperature due to stoichiometric effects and, on the other hand, a reduction in radiative loss owing to the simultaneous decrease in both temperature and soot volume fraction.

The experimental data are noisy which prevents a detailed comparison, especially along the flame axis. The flame at 21% is the same as one of the target flames designed

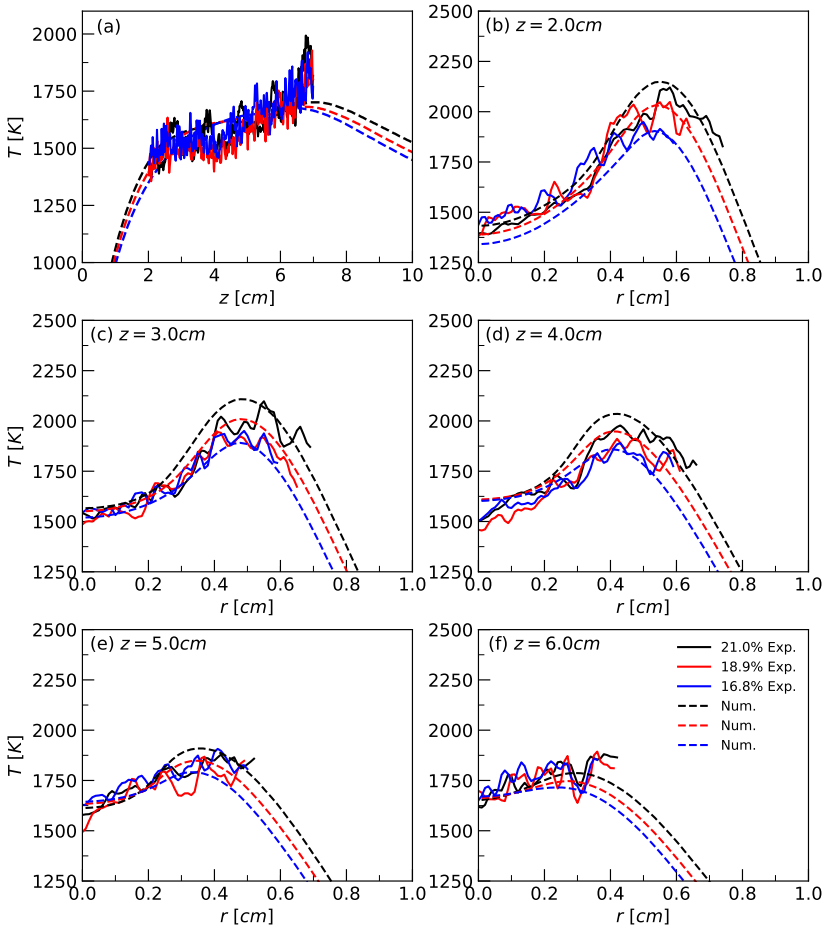

Figure 4.2 – Modeled axial and radial profiles of temperature compared against experiment, Sun et al. (2021).

by Santoro et al. (1983) and temperature measurements from thermocouples for this peculiar flame have been also considered to refine the comparison, see Figure 4.3. Predicted temperatures along the flame axis, Figures 4.2-(a) and 4.3, increase rapidly up to 2 cm, reach a plateau between 2 cm and 5 cm, increase again to reach a maximum a about 6 cm before decreasing. The axial predictions agree quantitatively with the measurements of Santoro et al. (1983), although the temperature in the plateau is overpredicted. In addition, 4.2.b to f show that the prediction of the radial peak location, their magnitude as well as the progressive transition from a M-shaped profile to a bell-shaped profile are in reasonable agreement with the experimental behavior.

Figure 4.4 displays both axial and radial profiles of soot volume fraction at different heights. The experimental axial profiles (Figure 4.4-(a)) are similar for the three oxidizers with a sharp increase in soot volume fraction followed by a region of almost constant soot volume fraction and finally a rapid decrease due to oxidation. In ad-

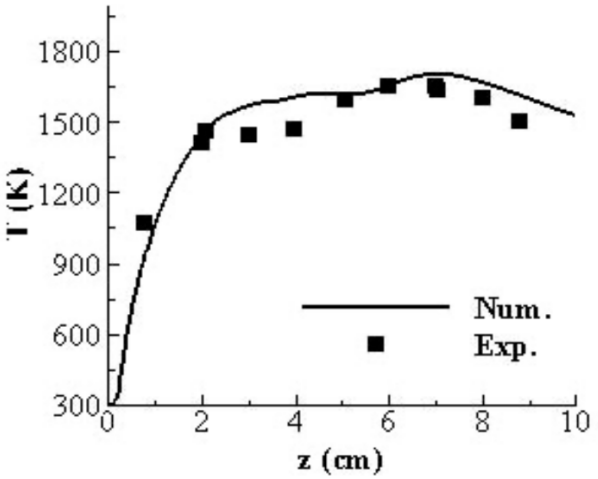

Figure 4.3 – Axial evolution of temperature for the flame at $X_{O_2} = 21\%$. The measurements are taken from Santoro et al. (1983).

dition, the experimental profiles show that a decrease in X_{O_2} delays the appearance of soot in the lower part of the flame, leads to a reduction in the axial peak of soot volume fraction and an early occurrence of soot oxidation. However, the rates of increase and decrease in soot volume fraction observed, respectively, at the early stage of soot formation and in the soot oxidation region are similar for the three oxidizers. Whatever X_{O_2}, the predicted soot volume fraction appears systematically upstream and increases with z much more gradually toward the peak than in the experiments. A part of these discrepancies can be attributed to the LII technique, Michelsen (2017). To be detectable by LII, soot particles must be sufficiently mature and graphitic and the minimum particle size for detection is often estimated to be around 10 nm, Michelsen (2017), Conturso et al. (2016). The present results indicate that soot particles have diameters lower than this limit up to about 2 cm (see Figure 4.5-(b)), which may explain the differences in soot profiles between the model and the experiments in the lower part of the flame. On the other hand, the computed profiles exhibit a peak rather than a region of almost constant soot volume fraction as observed experimentally. In addition, the maximum value is systematically underpredicted and its rate of decrease with decreasing X_{O_2} is overestimated by the model. The computed peak of soot volume fraction is reduced by 32.5% and 38% as X_{O_2} decreases from 21% to 18.9% and from 18.9% to 16%, respectively, whereas the corresponding experimental reductions are only of 13.8% and 18.8%. These discrepancies can be attributed to (i) the PAH growth mechanisms and (ii) soot production processes, Martin et al. (2022).

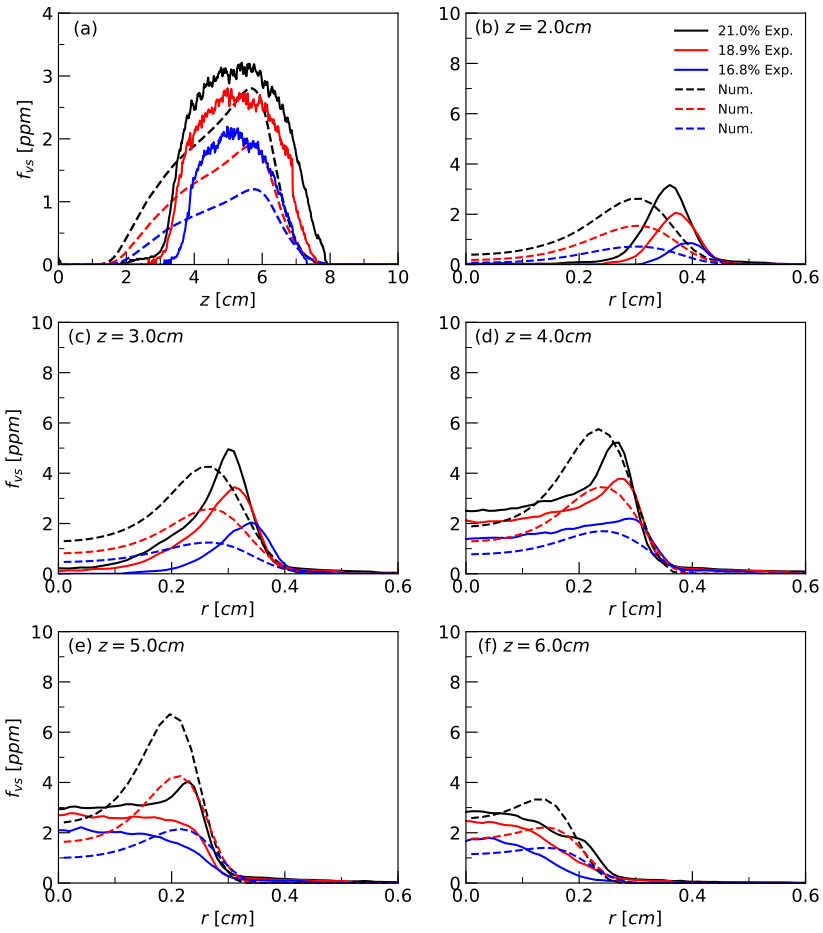

Figure 4.4 – Modeled axial and radial profiles of soot volume fraction compared against experiment, Sun et al. (2021).

The radial profiles are reasonably reproduced by the model (see Figures 4.4-(b) to (e)). The peak location as well as its magnitude along the wings are consistent with the experimental data in the formation region and the transition from a M-shaped profile to a bell-shaped profile in the oxidation region is reasonably captured, although the model still predicts a M-shaped profile at $z = 6$ cm whereas a bell-shaped is observed experimentally. The effects induced by decreasing X_{O_2} are also reasonably well predicted by the model. More specifically, at each height, the reduction in the peak of soot volume fraction is consistent with the experimental one as well as the tendency of the radial profiles to become flatter.

The radially integrated soot volume fraction, defined as :

$$f_{vs,int} = 2\pi \int_0^\infty r f_{vs}(r,z) dr \tag{4.17}$$

$f_{vs,int}$ is directly related to the soot yield and, such as, is a measure of the total carbon in the fuel converted to soot at a given height. Figure 4.5-(a) shows that, $f_{vs,int}$ is also reasonable well predicted by the model. This figure illustrates the capability of the model to reproduce the overall soot production. Figures 4.5-(b) to (d) show the axial and radial profiles of soot primary particle diameter. Measured diameters are within 30-40 nm in almost the overall domain, except along the wings at $z = 4$ cm where diameters of about 50 nm are observed. In addition, the experimental data suggest a slight reduction in the primary particle diameter with decreasing X_{O_2}. The model reproduces reasonably these trends although the experimental data are systematically underestimated, with predictions around 30 nm in the overall fuel rich region.

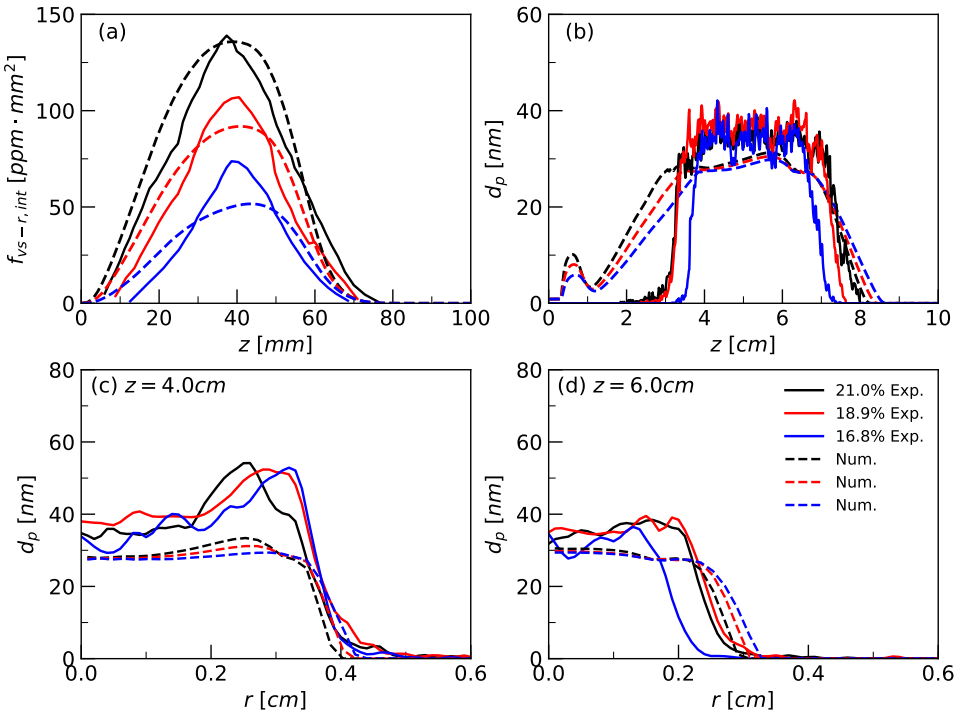

Figure 4.5 – (a) Predicted axial evolution of the radially integrated soot volume fraction, (b) axial and (c-d) radial profiles of soot primary particle diameter compared against experiment, Sun et al. (2021).

As discussed by Sun et al. (2020), the TiRe-LII measurements are biased toward measurement of soot with relatively large primary diameter, which may explain at least partially this underestimation. As mentioned previously, the flame at X_{O_2}21% is one of the target flames designed by Santoro et al. (1983) and *in situ* measurements of soot primary diameters based on thermophoretic sampling and transmission electron microscopic measurements were reported along the flame axis and path of maximum soot volume fraction, Dobbins et al. (1998), Köylü et al. (1997). Model predictions are compared with these data Figure 4.6, showing a better agreement.

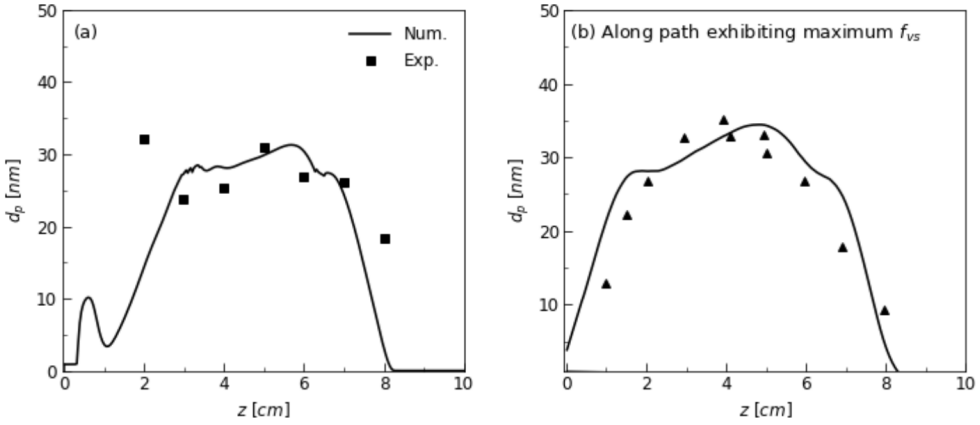

Figure 4.6 – Evolution of the soot primary particle diameter for the flame at $X_{O_2} = 21\%$ along (a) the flame axis and (b) the path of maximum soot volume fraction. The experimental data are taken from Santoro et al. (1983) (diagram (a)) and Dobbins et al. (1998) (diagram (b)).

4.3.3.2 Effects of oxygen depletion on soot production rates

The objective of this section is to quantify how a reduction in the oxygen concentration in the oxidizer affects the different mechanisms responsible for soot inception, surface growth and oxidation. Figure 4.7 shows the production rates as a function of the residence times, defined as :

$$t_{res} = \int_0^z \frac{dz}{u_z(r=0,z)} \tag{4.18}$$

where $u_z(r=0,z)$ refers to the axial component of the velocity vector along the flame axis. It should be noticed that in all the diagrams of Figure 4.7, the scale related to the soot nucleation rate differs from that related to the other processes. The mass generated by soot nucleation is significantly lower that produced or oxidized by the other processes, although the nucleation mechanism is the bottleneck of soot production. The diagrams (a) to (c) represent soot production rates along the flame centerline. The diagrams (d) to (f) display the same rates along the path of maximum soot volume fraction and, finally, the radially integrated rates are given in diagrams (g) to (i). The radially integrated rates are defined as :

$$\dot{\omega}'_{-r,int} = 2\pi \int_0^\infty \dot{\omega}''' r dr \tag{4.19}$$

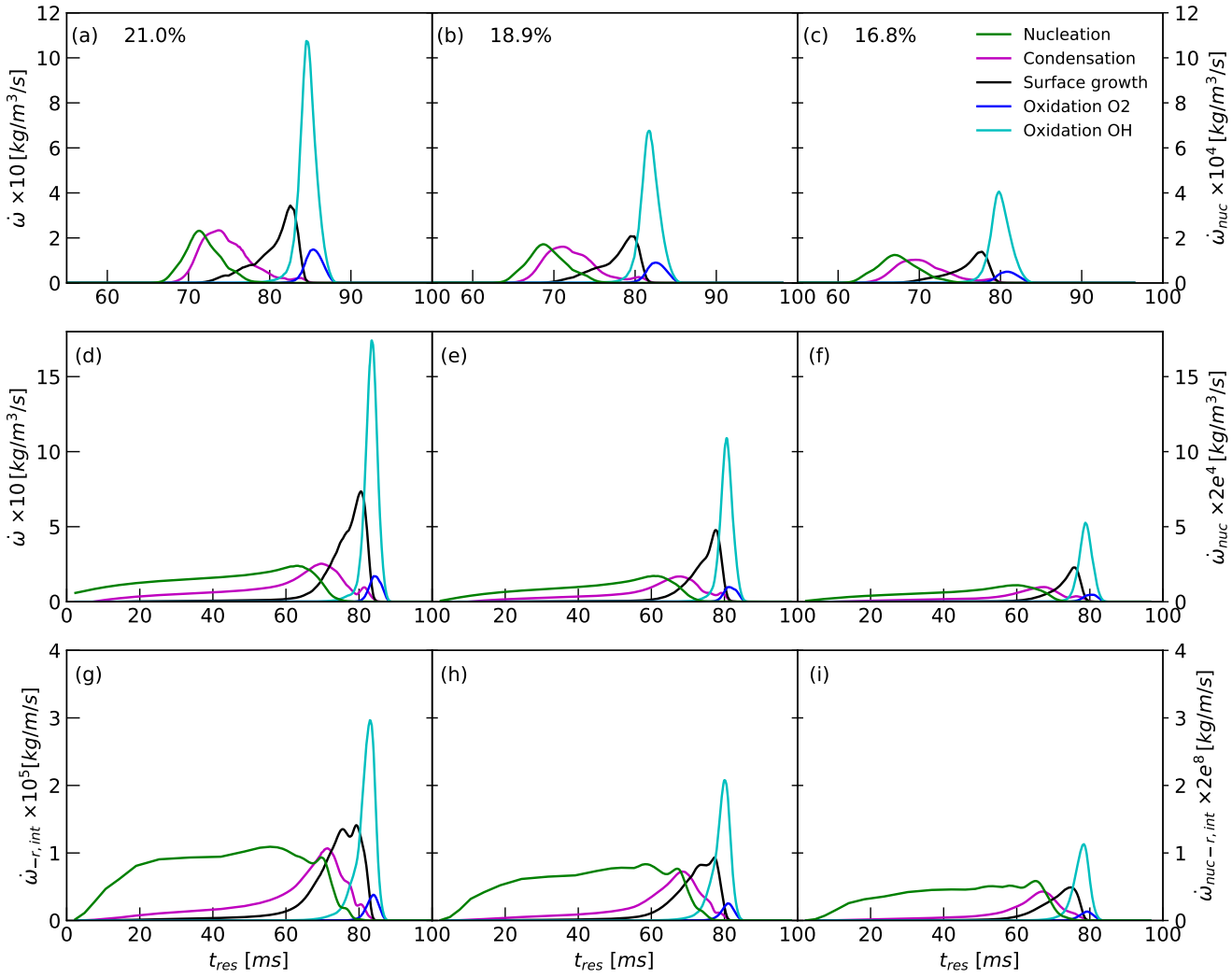

Figure 4.7 – Effects of oxygen oxidizer on the soot production rates as a function of the residence time : (a)-(c) along the flame axis, (b)-(f) along the flame wings, and (g)-(i) radially integrated profiles.

Soot nucleation and PAH condensation are PAH-based processes and are limited by the slow chemistry associated to PAH. These processes take longer time to start along the flame axis than along the path of maximum soot volume fraction due to the lower temperature encountered at the centerline which inhibits the formation of soot precursors. They are followed by surface growth by HACA as the soot spread towards the flame stoichiometry where H and, in less extent, OH atoms become present to activate sites on the soot surface. Figure 4.7 shows that the HACA is a quite rapid process as compared to nucleation and PAH condensation. Finally, the soot oxidation is a fast process that occurs as soot spreads further toward the stoichiometry where OH and O_2 particle are encountered. This sequence of processes remains the same as

O_2 (% vol)	Ω_{nucl} ($\times 10^{10}$) (kg/m)	Ω_{HACA} ($\times 10^{7}$) (kg/m)	Ω_{cond} ($\times 10^{7}$) (kg/m)	$\Omega_{ox,OH}$ ($\times 10^{7}$) (kg/m)	Ω_{ox,O_2} ($\times 10^{7}$) (kg/m)	χ_R (-)
21.0	2.86	2.13	1.98	1.53	0.15	0.22
18.9	1.99 (-31%)	1.33 (-38%)	1.14 (-42%)	1.03 (-33%)	0.11 (-31%)	0.15 (-29%)
16.8	1.25 (-56%)	0.69 (-68%)	0.53 (-73%)	0.57 (-63%)	0.06 (-60%)	0.11 (-48%)

Table 4.3 – Effects of oxygen on soot production processes and radiant fraction, χ_R. The value in parenthesis quantifies the change in percent as compared to the reference flame burning in 21%.

decreasing X_{O_2} but all the rates are reduced.

Table 4.3 summarizes the mass per unit length produced by each process obtained by integrating :

$$\Omega_{int} = \int_0^{\infty} \dot{\omega}'_{-r,int} dt \tag{4.20}$$

These results show that Ω_{nucl} is reduced by about 31% and 56% as the oxygen content in the oxidizer is decreased to 18.9% and 16.8%, respectively. For all the flames, the mass of soot produced by both the HACA and PAH condensation is very similar although the HACA process is dominant. HACA surface growth and PAH condensation have a similar sensitivity to a reduction in X_{O_2}, their rates being reduced by about 40% and 70% when X_{O_2} decreases down to 18.9% and 16.8%, respectively. The OH oxidation widely dominates the oxidation process with $\Omega_{ox,OH}$ being one order of magnitude higher than Ω_{ox,O_2}. Both oxidation processes exhibit a similar sensitivity to oxygen depletion and are less sensitive than the mass growth related processes.

4.3.3.3 Effects of oxygen depletion on radiative loss

Figure 4.8 shows the evolution along the flame height of the radially-integrated net volumetric radiative power defined as :

$$\text{divqT}(z) = 2\pi \int_0^{\infty} \nabla \cdot \dot{q}''_R(r,z) r dr \tag{4.21}$$

where $\nabla \cdot \dot{q}''_R$ is the divergence of the radiative flux. The profiles are similar whatever X_{O_2}. They increase up to a maximum located at $z \approx 3-4$ cm, that corresponds approximately to the location of the peaks of radially integrated soot volume fraction (see Figure 4.5-(a)), before decreasing. Reducing X_{O_2} reduces significantly divqT due to the conjugated effects of a decrease in temperature and soot volume fraction. It can be also observed that the peak of divqT is slightly shifted toward z as X_{O_2} decreases.

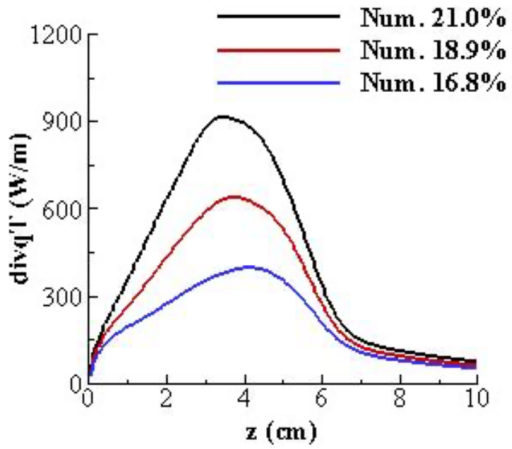

Figure 4.8 – Effects of oxygen oxidizer on the radially-integrated net volumetric radiative power profiles.

The last column of Table 4.3 shows the radiant fractions. The radiant fraction is 0.22 for $X_{O_2} = 21\%$ and is reduced by about 29% and 48% as X_{O_2} decreases down to 18.9% and 16.8%, respectively.

4.4 Chapter conclusions

Simulations of laminar ethylene coflow diffusion flames burning under normal and reduced oxygen concentrations were performed by using a three-equation pyrene-based soot production model. Both fuel and oxidizer have been simultaneously diluted by nitrogen in order to keep the volumetric stoichiometric oxidizer to fuel ratio and, in turn, the flame height and residence time constant. The following conclusions can be drawn:

- The model predicts reasonably the experimental data in terms of temperature, soot volume fraction, primary particle diameter and soot number densities.
- The influence of the reduction of oxygen in the oxidizer is quantitatively reproduced.
- Whatever the oxidizer, both HACA and PAH condensation contribute significantly to the soot mass growth, with the HACA slightly dominating the overall process. On the other hand, the soot oxidation by OH is on the whole one order of magnitude higher than the oxidation by O_2.
- The decrease in oxygen concentration affects similarly the production process.

This soot model, with the same set of parameters, will be applied to laminar coflow diffusion flames fuelled by mixtures of n-heptane/iso-octane/toluene mixtures. These

three components are surrogate fuels for gasoline with toluene representing the aromatic component.

5 Extension of the PAH-based soot production model to gasoline surrogate fuels

Table of contents

5.1 Introduction

In the previous chapter, the PAH model proved its ability to offer reasonable soot predictions for ethylene while using pyrene as the precursor. For this aliphatic fuel, pyrene showed to be an appropriate precursor for soot in regard of the kinetic uncertainty of PAHs. Now, the model is applied with the same set of parameters to a more complex fuel, namely gasoline, of great interest for fire applications. The additional difficulty of modelling soot production from gasoline arises from the initial

composition that contains aromatics. Pitz et al. (2007) recommended the surrogate of gasoline to be composed of n-heptane, iso-octane, and toluene, with the proportion of aromatics being about 35 %. The objective of this chapter is thus to extend the validation and investigation of the PAH-based model to mixtures of these primary fuels. As the kinetic uncertainty of PAHs are reported to increase with the complexity of fuel, the PAH model may become to be less predictive. If that so, the objective is also to propose an alternate solution.

5.2 Experimental and numerical details

5.2.1 Experimental details

The availability of complete experimental data on soot produced by liquid fuels is very limited in the literature. The methane flames doped with mixtures of n-heptane, iso-octane and toluene, experimentally investigated by Kashif et al. (2014) and Kashif et al. (2015), were selected. Methane CH_4 has a small sooting propensity and, as such, can be considered to play a marginal role in soot production. Two sets of flames were simulated:

- **First set, Set1**, Kashif et al. (2014): Two methane flames, doped with pure n-heptane or iso-octane. The mole fraction of the doping blend is 6.14%.
- **Second set, Set2**, Kashif et al. (2015) : Four nitrogen diluted methane flames, doped with blends of n-heptane/toluene and iso-octane/toluene. The mole fraction of the doping blend is 2.47%.

The burner used to produce the coflow diffusion flames is the Santoro-type described in previous chapter 4. The fuel and the oxidizer were released with velocities of 5.20 cm/s and 12.32 cm/s for the first set and 10.30 cm/s and 12.32 cm/s in the second set, respectively. The fuel stream is initially composed of a carrier gas, made of methane and also nitrogen if diluted. Vapors of the doping blend are then mixed with the carrier gas and the whole is maintained at 423 K above the evaporation temperature. The oxidizer stream is composed of air and injected at ambient temperature. The studied fuel compositions are summarized in Table 5.1. As the proportions of aromatics in real transportation fuels typically range from 20% and 40%, Violi (2019), the analysis was restricted to toluene proportion of 20% and 40%.

Soot volume fraction (SVF) was measured with a Light Extinction Measurement (LEM) technique in both experiments. The detection threshold of the methodology was estimated to be 0.15 ppm (Kashif et al. (2014)). Experiments involving pure n-heptane and iso-octane dopings were conducted in both Set1 and Set2. However, the measured SVF for the pure n-heptane doped flame in Set2 falls within the limit of the measurement technique which questions its reliability. As a consequence, the experimental measurements of Set1 Kashif et al. (2014), that involve higher doping and then SVF, will be preferred for the analysis of pure n-heptane and iso-octane blends.

	Carrier gas		Doping blend		
Set	CH_4	N_2	C_7H_{16}	C_8H_{18}	C_7H_8
1	100%	–	100%	–	–
2	50%	50%	80%	–	20%
2	50%	50%	60%	–	40%
1	100%	–	–	100%	–
2	50%	50%	–	80%	20%
2	50%	50%	–	60%	40%

Table 5.1 – Composition of the six methane coflow diffusion flames doped with n-heptane, C_7H_{16}, iso-octane, C_8H_{18} and toluene, C_7H_8, (% vol).

5.2.2 Numerical details and chemical mechanism

The numerical model is the same as the one presented in the previous chapter for the validation of the PAH-based model on ethylene, see section 4.3. In particular, the PAH-based model parameters are kept identical. The flamelet library is here generated using the KM1 mechanism, developed by Raj et al. (2012). It is a toluene reference fuel (TRF) mechanism that models the oxidation of n-heptane, iso-octane and toluene and includes the growth of PAH up to coronene A_7 with 231 species and 2159 reactions (forward and backward reactions counted separately). The reactions for PAH production, larger than benzene A_1, are the same as in the KM2 mechanism with only marginal modifications. Raj and coworkers validated qualitatively the prediction of PAH with available data on these three fuels and a particular attention was paid on the ability of the mechanism to predict the synergistic effect observed by Choi et al. (2011) for PAHs in counterflow diffusion flames fuelled by n-heptane/toluene and iso-octane/toluene mixtures. A synergistic effect occur when PAH formation is enhanced for mixture of fuels as compared to respective pure fuels.

5.3 Pyrene-based model soot prediction compared against experience

Model predictions of the SVF have been compared with the available experimental data for the six blend mixtures.

5.3.1 Predictions for n-heptane and iso-octane

Figure 5.1 shows the axial and radial SVF profiles at different heights above the burner for the pure n-heptane and iso-octane blendings. Iso-octane has a higher sooting propensity than n-heptane as illustrated by its lower laminar smoke point height of 11.0 cm compared to 12.3 cm for n-heptane.

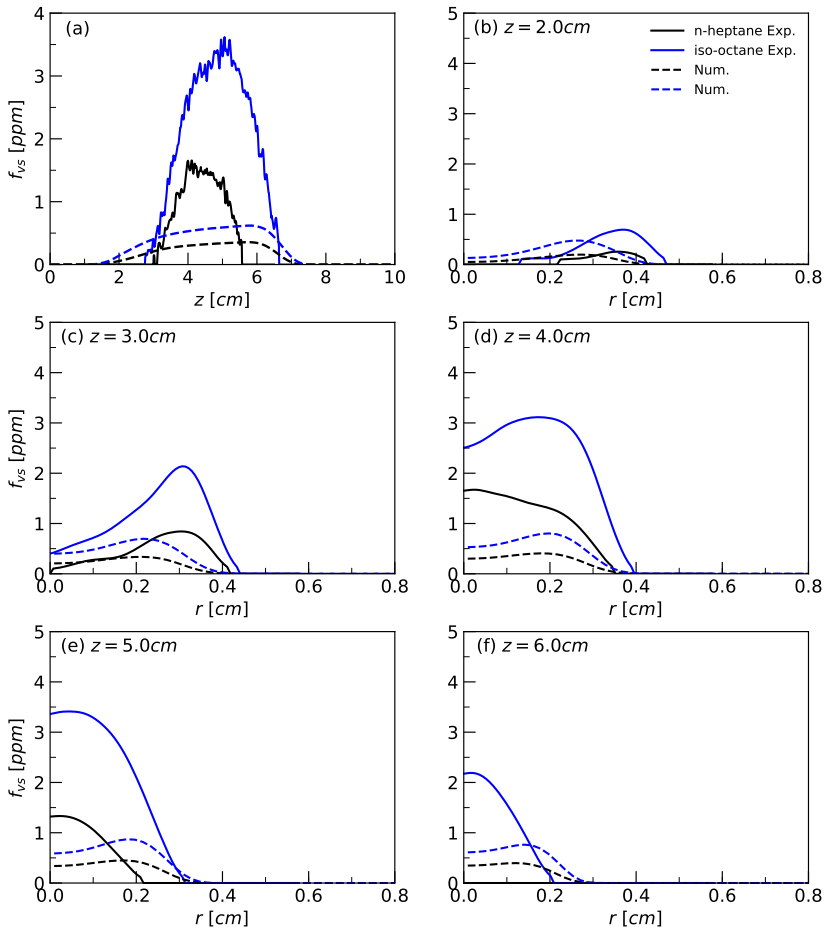

Figure 5.1 – Modeled axial and radial profiles of SVF compared against experiment, Kashif et al. (2014), for the pure n-heptane and iso-octane dopants.

Transitioning from n-heptane to iso-octane experimentally increases SVF by a factor 2. A comparable increase rate is obtained for the predictions. However, the magnitudes of soot prediction are significantly underestimated for both n-heptane and iso-octane doped flames. The departure is about a factor 4, at 0.46 ppm and 0.89 ppm, compared to the measurements at 1.68 ppm and 3.66 ppm for n-heptane and iso-octane, respectively. The experimental axial profiles, Figure 5.1-(a), show a rapid increase of SVF before reaching a peak, and then subsequent decrease due to oxidation. Experimental profiles demonstrate that transitioning from n-heptane doped flame to iso-octane doped flame slightly accelerates the appearance of soot and delays its complete oxidation, as observed in the diagrams (a), (b) and (f). However, increase and decrease rates of SVF are not significantly affected. Figures 5.1-(b) and (c) show that both experimental and numerical soot distribution reasonably concur in the lower part of the flame for both blends. In this region, SVF features a M-shaped profile. As the height above the burner increases toward the region between 4.0 cm and 6.0 cm, the predicted distribution departs from the experience. The experimental maximum

soot shifts toward the flame axis, forming a bell-shaped profile (see Figures 5.1-(d) to (f)), whereas prediction maintains a M-shaped profile until the very tip of the sooting region. More precisely, the predicted profiles have a weakly pronounced M-shape with almost constant SVF values. The shape transition is slightly delayed for the iso-octane doped flame, see Figure 5.1-(d) but the discrepancy is similar for both flames. The profiles of Figure 5.1 are completed with the contour plots of SVF fields in Figure 5.2, (a) for the pure n-heptane and (b) for the pure iso-octane doped flame. They show that the location of the predicted soot tip is found remarkably downstream compared to the experience for the n-heptane doped flame, although its location is in reasonable agreement for the pure iso-octane doped flame, see also Figure 5.1-(a).

5.3.2 Predictions for n-heptane/toluene and iso-octane/toluene mixtures

In Figure 5.3, modeled axial and radial SVF profiles are compared against experience for the flames doped with 80% and 60% n-heptane (H) with 20% and 40% toluene (T), respectively. Similarly, Figure 5.4 gives modeled and experimental profiles when n-heptane is substituted by iso-octane (I). Toluene has a larger sooting propensity than both n-heptane and iso-octane, as a consequence, the addition of toluene to n-heptane or iso-octane significantly enhances soot production. Here, the increase by 20% of toluene slightly accelerates experimental soot appearance and delays its oxidation, see Figures 5.3-(a) and 5.4-(a). Similar observations can be carried out for both n-heptane/toluene and iso-octane/toluene doped flames. Contour fields in Figure 5.2 also shows SVF fields for the present flames, (c)-(d) for the flames doped with H80%/T20% and H60%/T40%, respectively, and (e)-(f) for the flames doped with I80%/T20% and I60%/T40%, respectively.

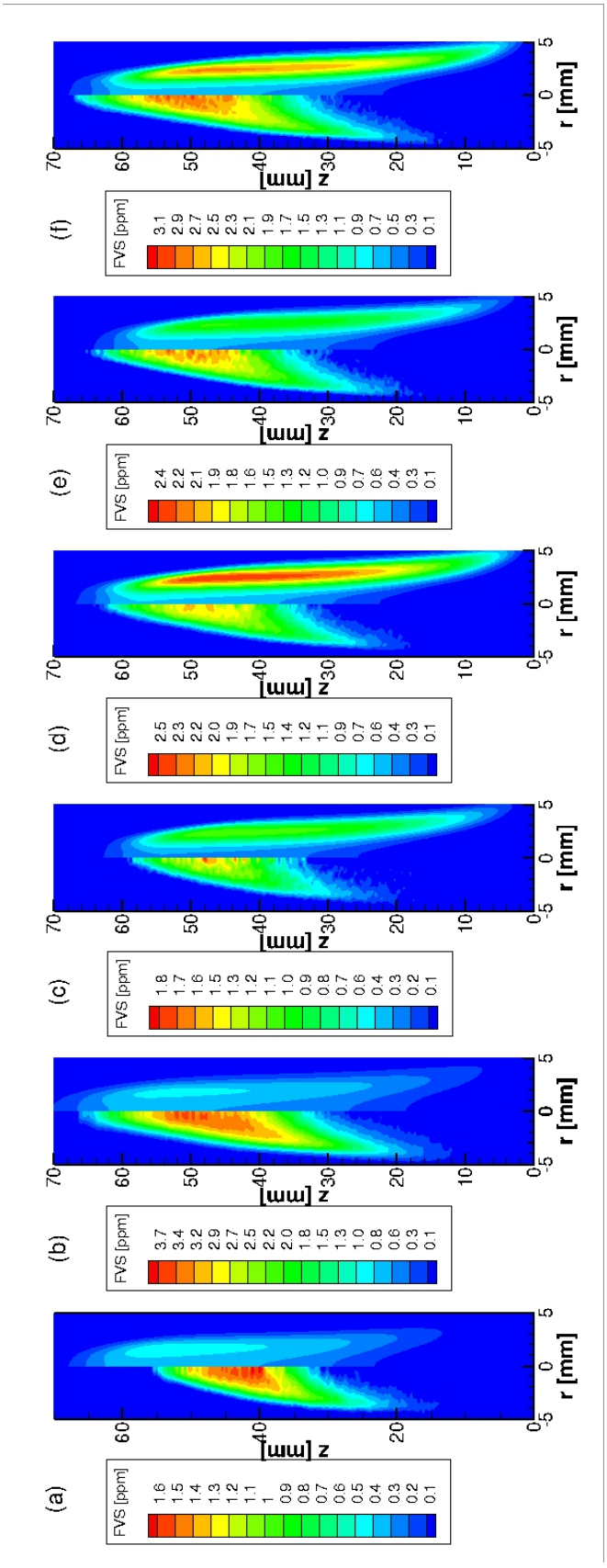

Figure 5.2 – Predicted fields of soot volume fraction using pyrene as precursor (right) compared against experiments (left), Kashif et al. (2014), Kashif et al. (2015), for (a) pure n-heptane doped flame, (b) pure iso-octane doped flame, (c)-(d) diluted 80%n-heptane/20%toluene and 60%n-heptane/40%toluene doped flames, and (e)-(f) diluted 80%iso-octane/20%toluene and 60%iso-octane/40%toluene doped flames.

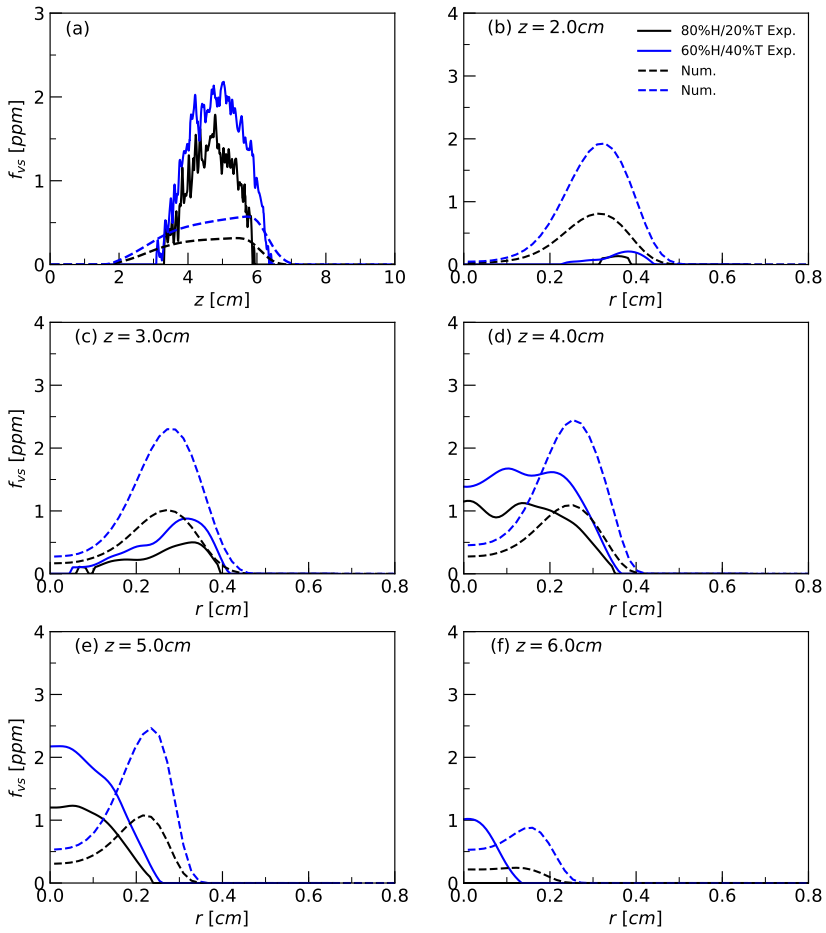

Figure 5.3 – Modeled axial and radial profiles of SVF compared against experiment, Kashif et al. (2015), for the n-heptane/toluene doping mixtures.

The PAH model does not capture the position of the soot peak : it is experimentally located on the flame wings in the region below 4.0 cm, and it shifts to the flame axis in the region above 4.0 cm forming a bell-shaped profile whereas, numerically, it remains on the flame wings forming a well pronounced M-shaped profiles throughout the flame until the soot oxidation region. Moreover, predicted SVF profiles, Figures 5.3-(b) and (c) and 5.4-(b) and (c), show that soot already has a high magnitude between 2.0 and 3.0 cm on the flame wings, revealing the early formation of soot with the PAH model compared to experience in the presence of toluene. The early formation of soot is confined to the flame wings, as axial profiles indicate the presence of soot at reasonably similar heights along z, see Figures 5.3-(a) and 5.4-(a).

Predicted radial SVF profiles in Figures 5.3-(d) to (f) and 5.4-(d) to (f) show a reasonable agreement in terms of peak of SVF compared to the experiments. Indeed, the measured peaks are at 1.81 ppm and 2.36 ppm for the n-heptane and iso-octane with 20% of toluene, respectively, whereas the model predicts the SVF peaks at 1.12 ppm and 1.35 ppm, respectively, which is less than the experimental uncertainty estimated

to a factor 2. Moreover, the increase rate related to the transition from 20% to 40% toluene is reasonably captured as the predictions remain within the 2 factor. They range at 2.48 ppm and 2.77 ppm for the n-heptane and iso-octane mixed with 40% toluene, respectively, against the 2.19 ppm and 3.11 ppm for the experience. Finally, Figures 5.3-(f) and 5.4-(f) show that soot oxidation occurs at concurring rates and heights as all soot is oxidized above the region between 6.0 and 7.0 cm, see also Figure 5.2.

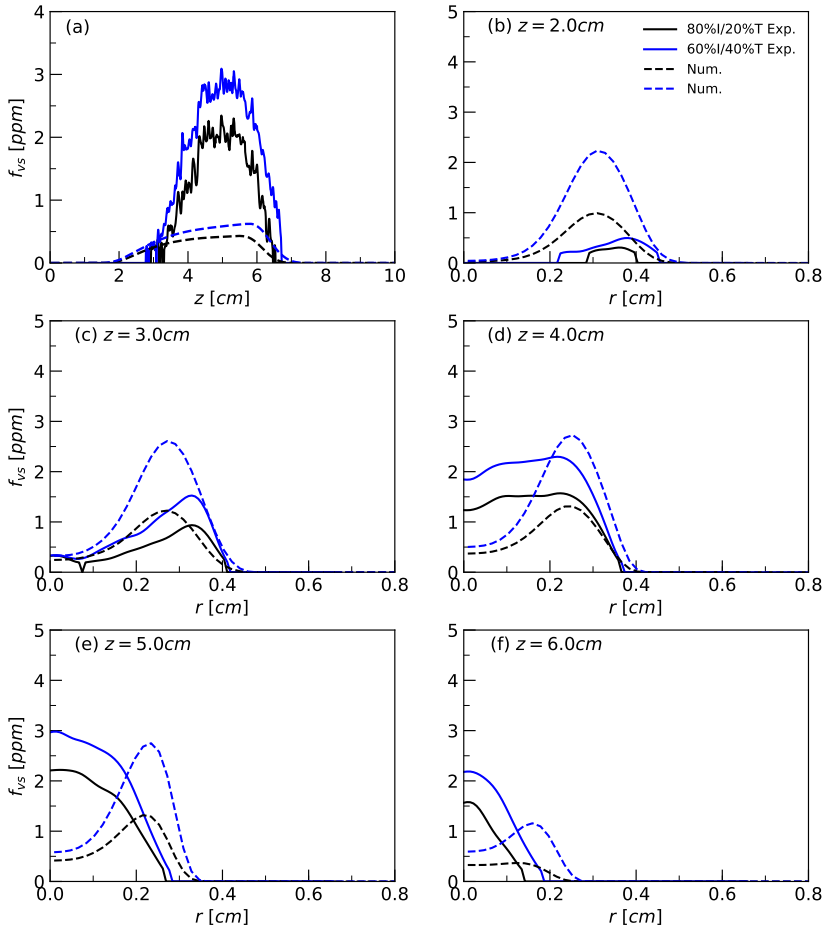

Figure 5.4 – Modeled axial and radial profiles of SVF compared against experiment, Kashif et al. (2015), for the iso-octane/toluene dopant mixtures.

Figure 5.5 show the radially integrated SVF, $f_{vs,r-int}$, for the n-heptane/toluene flames (a) and the iso-octane/toluene flames (b). The four radially integrated SVF profiles are in reasonable agreement with the experimental profiles in the region between 3.0 and 6.0 cm where the experimental soot peak is met. However, the radially integrated SVF profiles stress out the early formation of soot in the upstream region below 4.0 cm, in particular the predicted peaks are reached about 0.5 cm before the experimental peaks. The profiles also confirm that oxidation rates are in good agreement with experience as they show similar decrease rate trends.

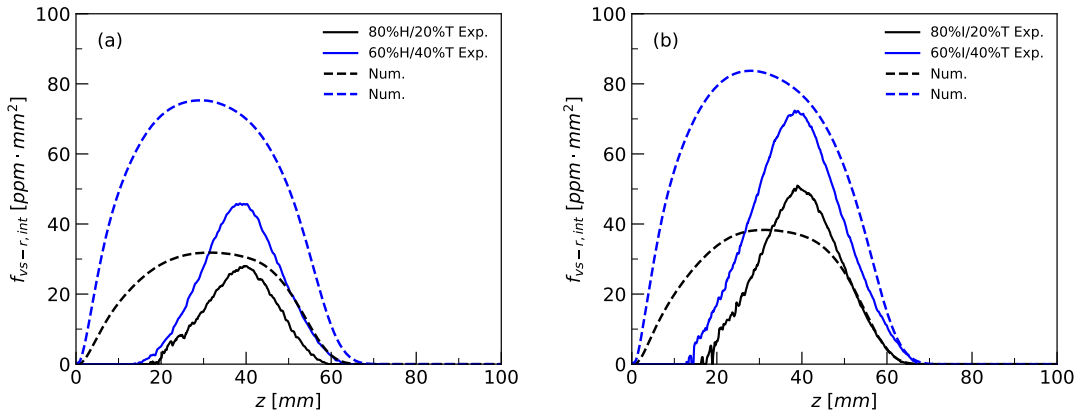

Figure 5.5 – Predicted radially integrated SVF compared against experiment, Kashif et al. (2015), for the n-heptane/toluene (a) and iso-octane/toluene (b) dopant mixtures.

The pyrene-based soot model captures the magnitude of the peak of SVF and integrated SVF in n-heptane/toluene and iso-octane/toluene blends representative of gasoline. These results suggest that it can be considered as an engineering model to predict soot production in gasoline surrogates. However, it suffers of a significant amount of issues : (i) it significantly underestimates soot formation in the case of n-heptane and iso-octane fuels, (ii) it abnormally favors the formation of soot in the lower part of the flame when toluene is added. The objective of the following part of the chapter is to investigate if another PAH can be substituted to pyrene in order to correct these issues.

5.4 Origins of the pyrene-based model discrepancies

5.4.1 Sensitivity of the pyrene-based model to its parameters and the precursor concentration

The objective of the present section is to investigate the effects of the most influential processes of the PAH model on SVF. Consequently, attention is paid on the condensation collision efficiency as condensation contributes the most to the growth of soot and on the nucleation collision efficiency as nucleation is the bottleneck of soot production.

Figure 5.6 compares the axial (a) and radial (b) to (f) SVF profiles obtained for the pure n-heptane doped flames with simulations obtained by multiplying and dividing the condensation efficiency by a factor 10. The results show that increasing the condensa-

tion efficiency have a minor impact on the SVF peak that rises by only 23%. On the other hand, decreasing the condensation efficiency reduces more significantly the SVF peak by 92% and enhances the underestimation as compared to the experimental values. Two observations on soot distribution can be drawn when the condensation efficiency is modified. First, the axial increase rate of soot is either reduced or increased (Figure 5.6-(a)). As a result, the axial SVF profile then features a plateau or heads towards a higher peak in the region between 3 and 6 cm. Second, the radial expansion of the soot region is either reduced or widened throughout the flame and the weakly pronounced M-shaped profile transits toward a flatter profile or a more pronounced M-shaped profile (Figures 5.6-(b) to (f)).

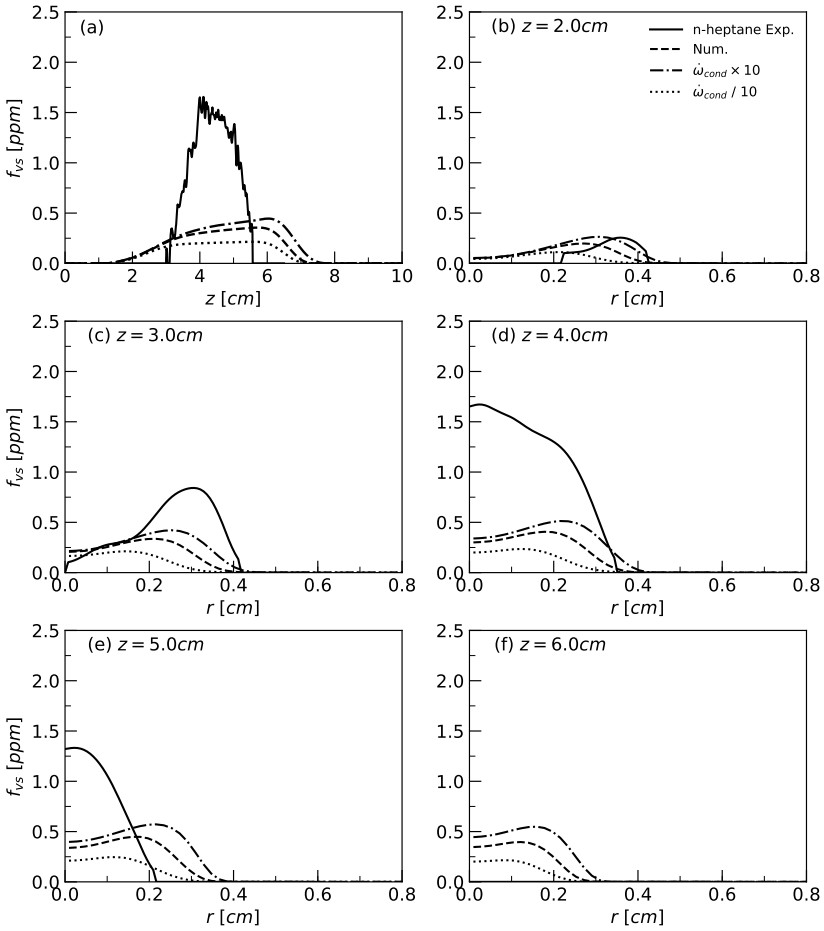

Figure 5.6 – Modeled axial and radial profiles of SVF for 3 condensation collision efficiency values, compared against experiment, Kashif et al. (2014), for the pure n-heptane doped flame.

Table 5.2 gives the mass per unit length produced by each process obtained by temporal and radial integration of process source terms :

Case	Ω_{nucl} ($\times 10^{11}$) (kg/m)	Ω_{HACA} ($\times 10^{8}$) (kg/m)	Ω_{cond} ($\times 10^{8}$) (kg/m)	$\Omega_{ox,OH}$ ($\times 10^{8}$) (kg/m)	Ω_{ox,O_2} ($\times 10^{8}$) (kg/m)
Effect of condensation collision efficiency					
×10	0.52 (-1137)	0.63 (24)	3.46 (47)	1.75 (42)	0.09 (66)
/10	51.62 (88)	0.21 (-129)	0.62 (-195)	0.39 (-159)	0.01 (-200)
Effect of nucleation collision efficiency					
×10	3.43 (-87)	0.67 (28)	2.50 (27)	1.21 (30)	0.04 (25)
/10	11.58 (44)	0.35 (-37)	1.54 (-18)	0.85 (-16)	0.03 (0)
Effect of precursor formation enhancement					
×3	16.02 (60)	1.60 (87)	7.66 (76)	3.69 (72)	0.23 (86)

Table 5.2 – Effects of parameters in the PAH model on soot production processes and effect of a artificial enhancement of precursor production in the pure n-heptane doped flame. The value in parenthesis quantifies the change in percent as compared to the simulations of previous section.

$$\Omega_i = 2\pi \iint \dot{\omega}_i''' r dr dt_{res} \tag{5.1}$$

where $\dot{\omega}_i$ is the rate associated with the soot production process i (nucleation, HACA, PAH condensation,...) and $t_{res} = \int_0^z dz/u_z(r=0,z)$ is a Lagrangian time, where $u_z(r=0,z)$ is the axial velocity along the flame axis. Multiplying the condensation efficiency by 10 increases the condensation rate only by a factor of 3.42. This is due to the associated consumption of pyrene that reduces their availability, not only for PAH condensation but also for nucleation, explaining the observed reduction in the nucleation rate. A consequence is that fewer but heavier soot aggregates are predicted. Inversely, reducing the condensation efficiency by a factor of 10 results in an enhancement in soot nucleation, leading to a higher number of soot aggregates but of lower mass. In summary, a modification in the PAH condensation efficiency is inhibited by the scrubbing effects of soot production on pyrene. In both case, the mass change due to the HACA and oxidation processes is piloted by the variation of condensation as it is the dominant growth process and similar magnitude variations are observed.

Figure 5.7 shows similar investigation on the nucleation efficiency. The axial (a) and radial (b) to (f) SVF profiles, obtained for the pure n-heptane flame, are compared with SVF profiles computed after multiplying and dividing the nucleation efficiency by a factor 10. The nucleation efficiency has a negligible effect on SVF mainly due to the coupling between nucleation and condensation processes through the consumption of pyrene. Table 5.2 shows that when nucleation efficiency is enhanced, the mass gain from condensation increases slightly by 27% due to the rise of aggregate number density. The increase of condensation eventually reduces the quantity of precursors and leads to the diminution of nucleation, by 87%. The enhancement of nucleation

efficiency also impacts positively the number density of primary particles, leading to the increase of soot surface available for chemical reactions, resulting in the increase of surface growth and OH and O_2 oxidation by 28%, 30% and 25%, respectively. Conversely, reducing the nucleation efficiency decreases both aggregate and primary number densities, leading on the one hand to the 18% decrease of condensation which, in turn, increases precursor concentration, resulting in 44% nucleation rise, and on the other hand reduces surface growth and OH oxidation by 37% and 16%, respectively.

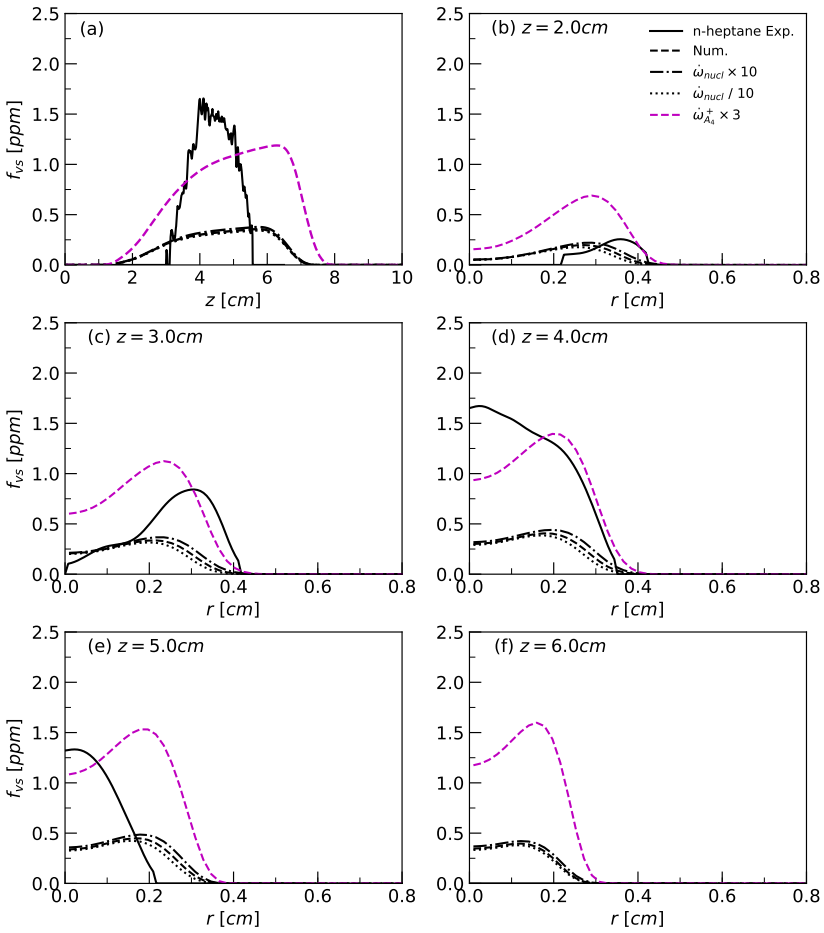

Figure 5.7 – Modeled axial and radial profiles of SVF for 3 nucleation collision efficiency values and when the pyrene production term is multiplied by 3, compared against experiment, Kashif et al. (2014), for the pure n-heptane doped flame.

Figure 5.7 also shows the outcome of enhancing the precursor formation after multiplying by a factor 3 the chemical production term of pyrene, $\dot{\omega}^{+}_{A_4}$. The SVF peak is positively impacted with a 71% increase, raising the peak at 1.61 ppm which bridges the discrepancy with the experimental value of 1.68 ppm. The axial (a) and radial

(b) to (f) SVF profiles shows that soot is increased throughout the flame and more particularly on the flame wings, indeed the plateau-shaped profile is turned into a M-shaped profile, in departure to the experience. Table 5.2 shows that the precursor enhancement positively increases all the processes. Nucleation and condensation rise following the increase of precursor concentration by 60% and 76%, respectively. Likewise, surface growth and OH and O_2 oxidation increase by 87%, 72% and 86%, respectively, due to the rise of particle diameter and soot number densities.

The latter investigations suggest that the predictions of the PAH model are largely insensitive to the model parameters and that the significant underestimation of the SVF, obtained for pure n-heptane and iso-octane, is due to a lack of pyrene. The lack of pyrene may be the result of the uncertainties related to PAH chemistry as pyrene mass fraction remains correlated to soot production when toluene is within the fuel.

5.4.2 Investigation of pyrene formation reactions

The objective of the present section is to investigate the reactions forming pyrene, in the present mechanism, in order to comprehend the underlying chemical processes leading to the early prediction of the pyrene-based model for toluene mixtures.

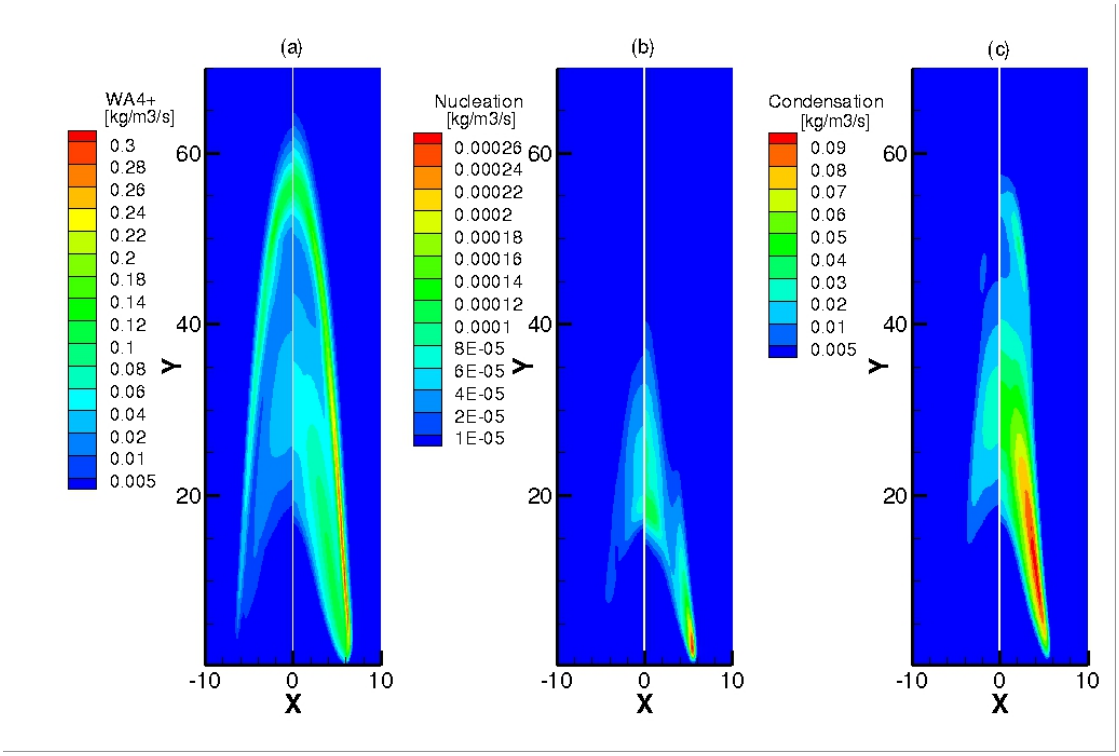

Figure 5.8 – Predicted fields of pyrene production rate (a), nucleation rate (b) and condensation rate (c) for the diluted pure n-heptane (left) and 80% n-heptane/20% toluene (right) doped flame.

Figure 5.8 shows the field of the pyrene chemical production rate (a), nucleation rate (b) and condensation rate (c), obtained for pure n-heptane (left) and 80% n-heptane/20% toluene (right). Here, the investigation is carried out in the configuration of the nitrogen diluted doped flames (Set2, see Table 5.1) for both fuels to achieve relevant chemical comparison. In Figure 5.8-(a), for pure n-heptane, pyrene forms favorably in a thin layer near the flame front in the fuel rich side and increasingly along the flame to reach a peak in the region between 5.0 and 6.0 cm. A region of pyrene formation is also located on the vicinity of the flame axis, near the 3.0-cm height, but at a lower magnitude. For the mixture of n-heptane/toluene, pyrene formation is initiated as early as the fuel injection, with a peak reached upstream in the region between the burner and 2.0 cm above it. A second region of lower magnitude can also be found in the region between the flame wing and the flame axis, and a third one in the region around 3.0 cm in the vicinity of the flame. Both flames have similar distribution pattern in the downstream part, the toluene addition mainly impacts the upstream part of pyrene formation.

Figure 5.8-(b) shows that soot inception is concentrated in the vicinity of the flame axis between 1.5 cm and 3.0 cm for the pure n-heptane doped flame whereas for the n-heptane/toluene flame soot inception is anchored on the burner edges. Figure 5.8-(c) shows that condensation has a similar distribution than nucleation but is elongated along the flame axis. The uniformed distribution of condensation in the vicinity of the flame axis explain the plateau-shaped radial SVF profile of the pure n-heptane doped flame. The M-shaped radial profile of pyrene production rate, nucleation rate and condensation rate explains the M-shaped radial profile of soot when toluene is present. Moreover, the anchoring of their peaks at the burner edges also explains the early occurrence of soot.

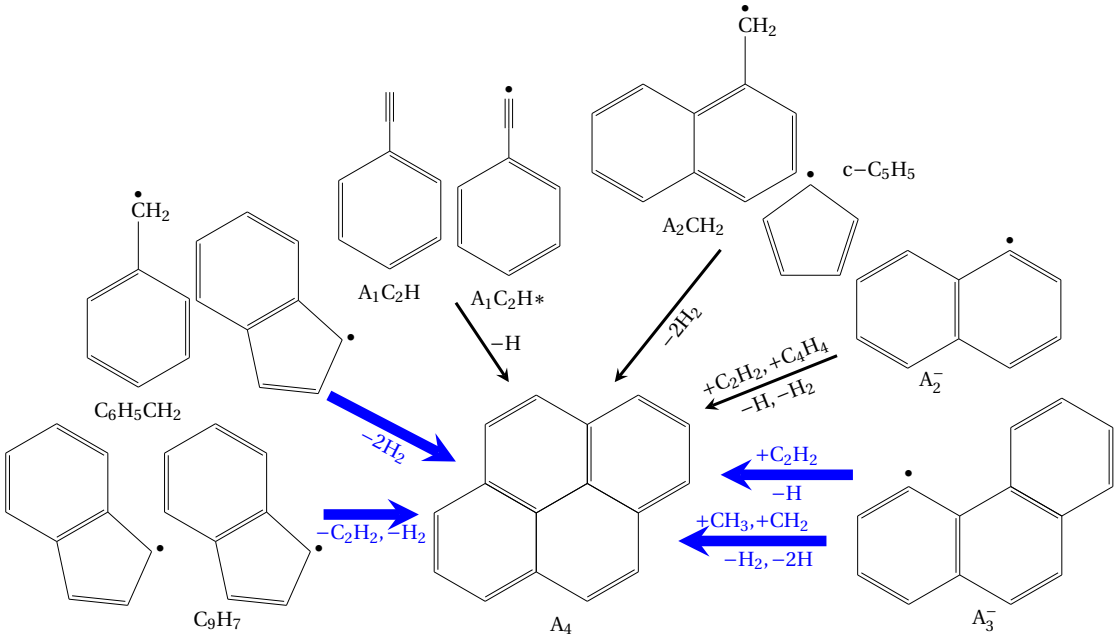

Figure 5.9 – Kinetic pathways of the KM1 and KM2 mechanisms leading to the formation of pyrene A_4.

Figure 5.9 summarized all the chemical paths leading to the formation of pyrene included in the KM1 mechanism : A_4 from A_3 reactions (HACA), reaction between benzyl $C_6H_5CH_2$ and indenyl C_9H_7, reaction between two indenyls, reaction between phenylacetylene A_1C_2H and its radical, reaction between A_2CH_3 and cyclopentadiene c-C_5H_5, reaction between naphthalene and C_4H_4. These chemical paths have different contributions to the pyrene formation, the reaction $R_{tol} : C_6H_5CH_2 + C_9H_7$, the HACA reactions $R_{HACA} : A_3^- + C_2H_2$ and reaction $R_{ind} : C_9H_7 + C_9H_7$ (blue arrows) are the three paths that have the highest contribution for the present flame configurations. The pathways included in this mechanism show that toluene contribute to PAHs larger than benzene, the formation and growth of PAHs beyond benzene has then become the rate-limiting step in the overall soot formation process.

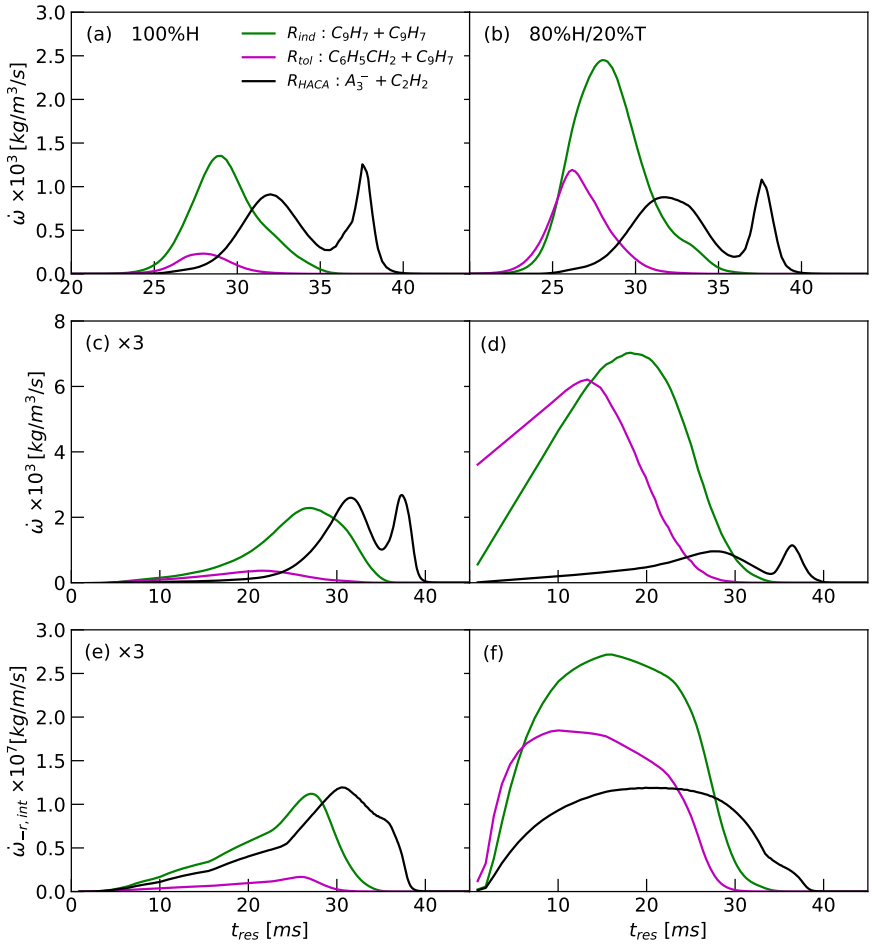

Figure 5.10 – Effect of toluene on the pyrene production reaction rates as a function of the residence time : (a)-(b) along the flame axis, (c)-(d) along the path of maximum SVF, and (e)-(f) give radially integrated profiles, for the nitrogen diluted pure n-heptane (left) and 80% n-heptane/20% toluene (right) doped flames.

Figure 5.10 shows the reaction rates of pyrene production that contribute the most to pyrene formation as a function of the residence times, t_{res}, obtained for nitrogen diluted methane flames doped with 100% n-heptane and 80%n-heptane/20%toluene (Set2, see Table 5.1). The diagrams (a) to (b) represent pyrene production reaction rates along the flame centerline. The diagrams (c) to (d) display reaction rates along the path of maximum SVF located at the vicinity of the flame wings and, finally, the radially integrated reaction rates are given in diagrams (e) to (f). The radially integrated rates are defined as $\dot{\omega}'_{-r,int} = 2\pi \int_0^\infty \dot{\omega}''' r dr$. It should be noted that pyrene formation reaction rates were multiplied by a factor 3 in the diagrams (c) and (e) related to pure n-heptane to enhance visibility. Similar results are obtained when n-heptane is substituted by iso-octane.

Figure 5.10 illustrates the slow chemistry of PAHs as the reactions occur over long residence times. Reactions R_{ind} and R_{tol} appear faster than the HACA sequence as they do not rely on the formation of A_3 to occur but on smaller species that have a smaller characteristic time-scales. Similarly, reaction R_{tol} slightly reaches its peak before R_{ind} as it relies on $C_6H_5CH_2$, radical of toluene, smaller than C_9H_7.

Figures 5.10-(a),(c) and (e) show that, for the pure n-heptane flame, the reactions R_{ind} and R_{HACA} equally contribute to the formation of pyrene, both along the flame axis and along the path of maximum SVF, followed by R_{tol} at a lower magnitude. Figures 5.10-(b), (d) and (f) show this balance disrupted by substituting 20% of n-heptane by 20% of toluene :

- The reaction rates are significantly increased in the flame by 83%, 97% and 64% for R_{ind}, R_{tol} and R_{HACA}, respectively. The increase is more pronounced for reactions R_{ind} and R_{tol} as the radical of toluene is among the reactants and as toluene contribute to the formation of indenyl through reaction $C_6H_5CH_2 + C_2H_2$.
- Reactions R_{ind} and R_{tol} now contribute to pyrene formation in majority, especially on the path of maximum SVF where their peaks are reached (see Figure 5.10-(d)).
- Their peaks are shifted upstream on the flame wings and they depict significant magnitude only a few milliseconds after the burner exit.

Consequently, the early appearance of pyrene and subsequent soot can be attributed to these two reactions and more particularly to reaction R_{tol} as its contribution is higher than R_{ind} in the vicinity of the burner edges (see Figure 5.10-(d)). Figure 5.10-(f) shows that the occurrence of the HACA sequence is also accelerated as toluene also participates to the formation of A_3 (i) by forming both indenyl and c-C_5H_5 that react together and (ii) by benzyl addition $C_6H_5CH_2 + C_6H_5CH_2$.

Raj et al. (2012) considered reaction R_{tol}, in combination with the HACA sequence, to explain synergistic effects of toluene on pyrene. In the present study, reaction R_{tol} emerges as a crucial reaction influencing pyrene production when toluene is within the fuel. However, the recent study of Sinha et al. (2017) found that the rate constant assumed for reaction R_{tol} was more than an order of magnitude higher than the rate determined through calculations, and the reaction preferably formed fluoranthene, an isomer of pyrene, instead of pyrene. This indicates that toluene contributes to the formation of 4-ring PAHs, but the predicted quantity of pyrene may be overestimated with the present mechanism. The entirety of the pathways leading to pyrene is not yet known as their discovery remains the subject of ongoing research, Raj et al. (2014), Raj (2022). Similarly, Sinha and Raj (2016) found that the reverse reaction of the benzyl addition, $C_6H_5CH_2 + C_6H_5CH_2$, was underestimated and as a result, A_3 predictions were overestimated. These findings question the accuracy of the chemical pathways leading to the formation of A_3 and A_4 (pyrene) and may explain

the observed discrepancies when transitioning from ethylene to gasoline surrogate fuels.

The results raise the question of whether it is possible to have a PAH that allows better describing the soot production for gasoline surrogate fuels. The use of pyrene as a precursor leads to (i) a significant underestimation for liquid aliphatic fuels, and (ii) an early soot appearance for fuels containing toluene. As toluene directly contributes to the formation of PAHs up to pyrene, an intuitive solution to address the second issue is to use larger PAHs as soot precursors. Choosing a larger PAH as precursor is consistent with experimental studies on the composition of nascent particles suggesting that soot formation occurs from PAHs beyond pyrene, as discussed in the introduction chapter. The objective of the following section is to investigate the large PAHs provided by the chemical mechanism in order to select a more suitable precursor than pyrene.

5.5 A six-ring PAH-based model for gasoline surrogate fuels

5.5.1 Selection of the PAH precursor

A suitable PAH precursor should respect two specific properties related to soot :

(i) its production rate must be closely correlated to soot production i.e the PAH precursor must not form excessively ahead of soot nor excessively delayed, and

(ii) the PAH precursor must reach a sufficient level of concentration to, on the one hand, nucleate sufficient soot particles, and, on the other hand, to add sufficient mass through the condensation process.

The nature of the PAHs respecting these two properties depends on the chemical mechanism due to the variety of kinetics used for PAHs in the literature. The selection process considers the most relevant and abundant large PAH of the mechanism. These PAHs are the five-ring isomers benzo[a]pyrene (BAPYR) and benzo[e]pyrene (BEPYREN), the six-ring isomers benzo[ghi]perylene (BGHIPER) and anthanthrene (ANTHAN) and the seven-ring coronene (CORONEN), this latter being the largest PAH of the mechanism. Intermediary and radical PAHs were disregarded as potential candidate for soot precursor. In the present mechanism, PAHs larger than pyrene are formed following the HACA sequence from smaller PAHs. A consequence is that their chemical characteristic time is proportional to their ring number. Figure 5.11 schematizes their chemical pathways. Pyrene serves as the starting point in two major independent pathways, highlighted by the blue curved arrows in Figure 5.11 :

- **Pathway 1** : $A_4 \rightarrow$ BAPYR $\rightarrow$ ANTHAN
- **Pathway 2** : $A_4 \rightarrow$ BEPYREN $\rightarrow$ BGHIPER $\rightarrow$ CORONEN

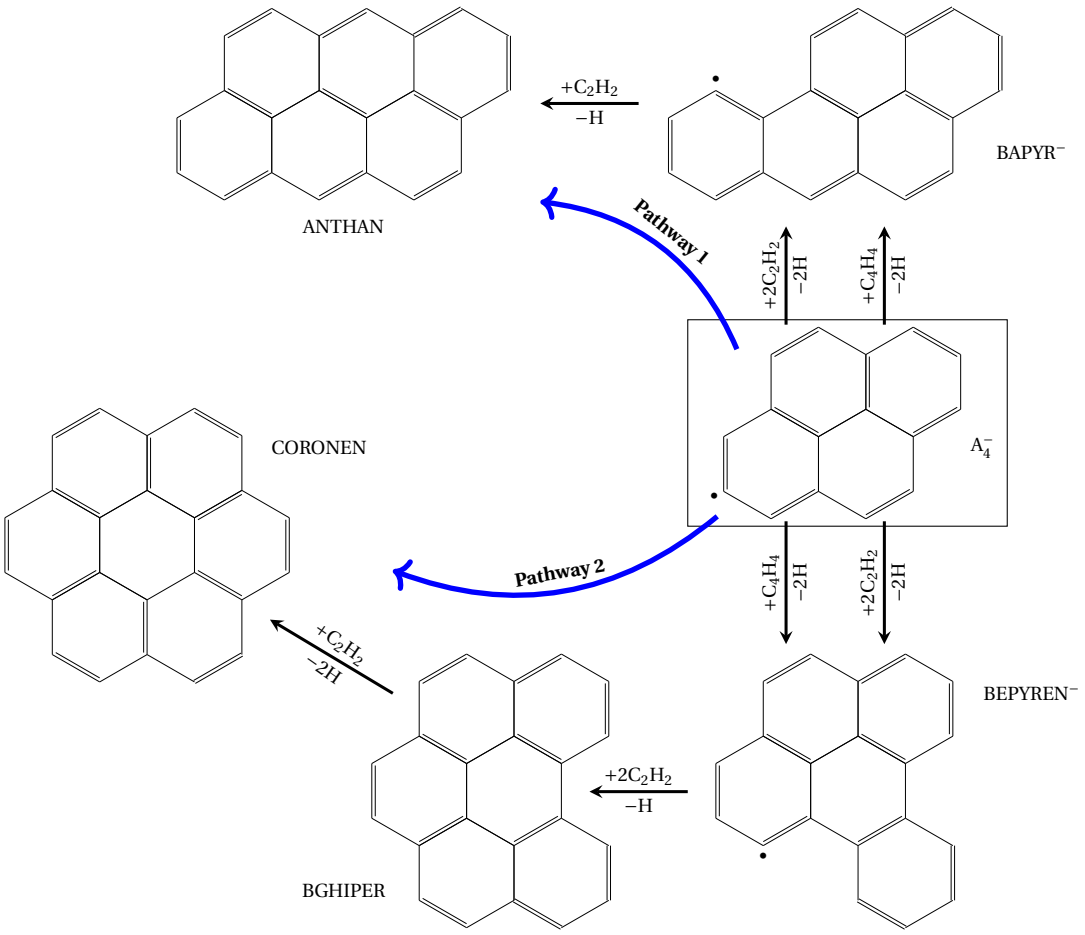

Figure 5.11 – Major kinetic pathways of the chemical mechanism leading to the formation of large PAH. For simplicity, the isomers of some radical species are not shown.

The mass fraction transport equation of the selected PAHs were solved on-the-fly in a passive manner, i.e. by neglecting the consumption due to soot production. Figure 5.12 shows the evolution of their radially integrated mass fraction, $Y_{-r,int}$, as a function of the residence time for the pure n-heptane doped flame, (a) and (c), and the diluted 80%n-heptane/20%toluene doped flame, (b) and (d). The radially integrated mass fractions are normalised by the maximum values in graphs (a) and (b) and compared with the experimental radially integrated SVF to demonstrate propriety (i) and Graphs (c) and (d) illustrate propriety (ii).

Normalized profiles show asymmetric shapes expressing that a longer time is need for their formation than for their oxidation, consistently with previous investigations. Figure 5.12-(a) and (b) show that large PAHs appear after pyrene with the following chronological order : pyrene, BEPYREN, BAPYR, BGHIPER, ANTHAN and CORONEN. Given that each of the isomers of pathway 2 appear before the isomers of pathway 1, it can be concluded that pathway 2 is the fastest. It should be pointed out that

CORONEN is the largest PAH in the mechanism and, as such, is neither consumed nor oxidized. This explains why its peak is found upstream the soot region and that CORONEN escapes the flame.

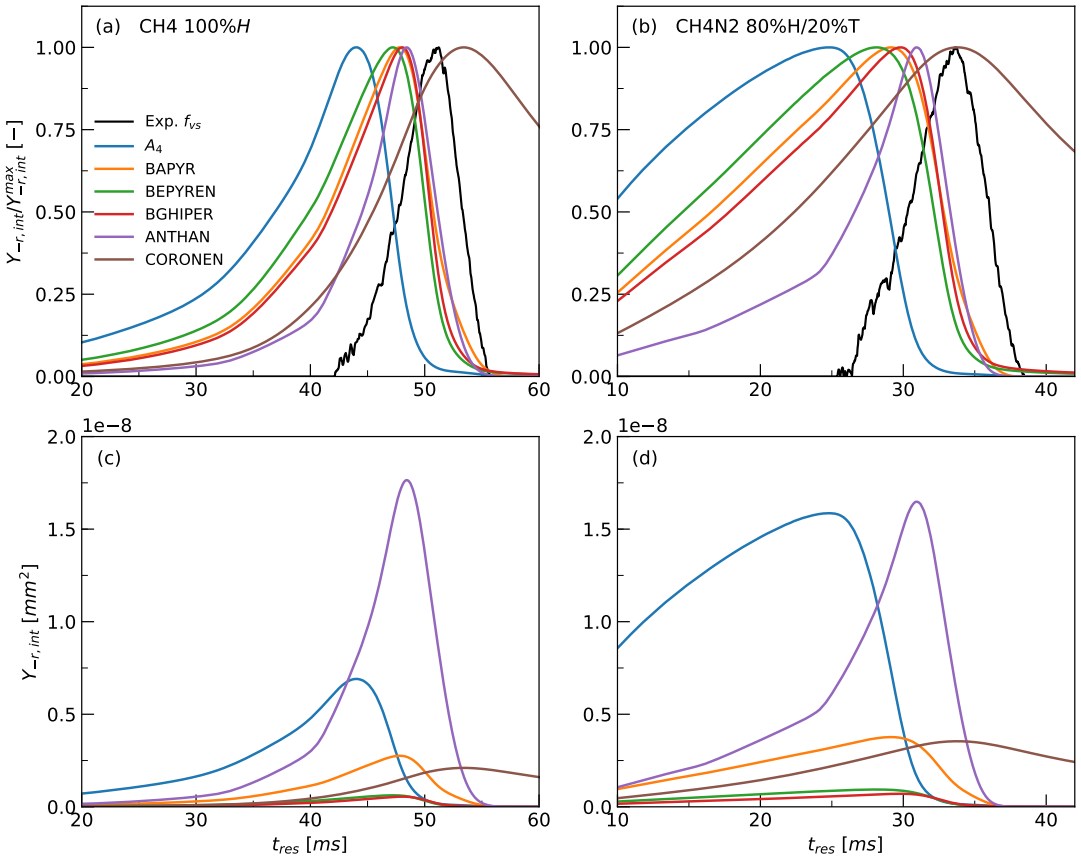

Figure 5.12 – Evolution of radially integrated mass fraction of PAH species over the residence time for the n-heptane doped flame, (a) and (c), and the diluted 80%n-heptane/20%toluene doped flame, (b) and (d).

Although the time at which the mass fraction peak is reached cannot be compared between the two flames due to the difference in configuration, their time occurrence with respect to the soot peak can be used for comparison. In the pure n-heptane flame, the peaks of pyrene, BEPYREN, BAPYR, BGHIPER and ANTHAN are reached approximately 7, 4, 3, 3, 3 ms before the soot peak, respectively. This chronological order is maintained when toluene is added and the peaks of pyrene, BEPYREN, BAPYR, BGHIPER and ANTHAN are reached about 9, 6, 5, 4, 3 ms before the soot peak. These results show that the PAHs closest to pyrene in size appear faster in the n-heptane/toluene flame. Moreover, 50% of their maximum amplitude is reached at a much earlier stage due to the influence of toluene on pyrene formation, see 5.12-(b). The impact of toluene is gradually diffused through each larger PAH. Overall, ANTHAN is observed to be weakly impacted by toluene and is the only PAH that satisfies property (i) for both types of fuels.

Figure 5.12-(c) and (d) compares the amplitude of the radially integrated PAH mass fractions. Larger PAH mass fraction are significantly lower than pyrene mass fraction in both flames, except for ANTHAN : BEPYREN, BGHIPER and CORONEN are one order of magnitude lower than pyrene, BAPYR is of the same order but insufficiently concentrated. Overall, the mass flux through pathway 1 is favored compared to pathway 2. The mass fraction of ANTHAN is more than two time higher than the mass fraction of pyrene for pure n-heptane and present similar mass fraction for n-heptane/toluene, which makes it a good candidate in term of mass. Similar results were obtained for iso-octane.

This *a priori* investigation shows that ANTHAN is the only PAH that respects both properties (i) and (ii) for the present mechanism. Consequently, it will be used as soot precursor in the next section.

5.5.2 ANTHAN-based soot prediction

In this section, the six methane doped flames are simulated by using ANTHAN instead of pyrene as soot precursor while keeping the same model parameters than those used in the previous simulations.

5.5.2.1 Predictions for n-heptane and iso-octane

Figure 5.13 shows the axial and radial SVF profiles for the pure n-heptane and iso-octane doping blends. These figures are completed with the fields of predicted SVF compared with experiments in Figure 5.16-(a) and (b) for the pure n-heptane and iso-octane flames, respectively. SVF predictions are significantly improved compared to the pyrene-base PAH model. The SVF amplitude is reasonably predicted as it is within a factor 2 throughout the flame. Numerical peaks are observed at 2.14 ppm and 2.50 ppm, against the experimental peaks at 1.68 ppm and 3.66 ppm for the pure n-heptane and iso-octane doped flames, respectively. However, the deviation from the experimental results is more pronounced for iso-octane. Moreover the experimental increase by a factor of 2 as n-heptane is replaced by iso-octane is not captured. This is illustrated in the region of highest soot concentration, see the axial profile in Figure 5.13-(a) and radial profiles in Figure 5.13-(d) to (e).

Predicted axial profiles in Figure 5.13-(a) have a shape close to the bell-shaped of the experience with soot production being initiated at acceptably similar position. However the overall profile is delayed downstream for both flame resulting in a more elongated soot distribution along the flame axis, which is more pronounced for the pure n-heptane doped flame, see Figure 5.16-(a) and (b). The predicted radial predictions are in good agreement in the upstream part of the flame below 3 cm, see Figure 5.13-(b) and (c), where numerical and experimental SVF have M-shaped profiles. In the downstream region of the flame, the modeled SVF maintains a M-shaped profile, in departure to the experimental observation.

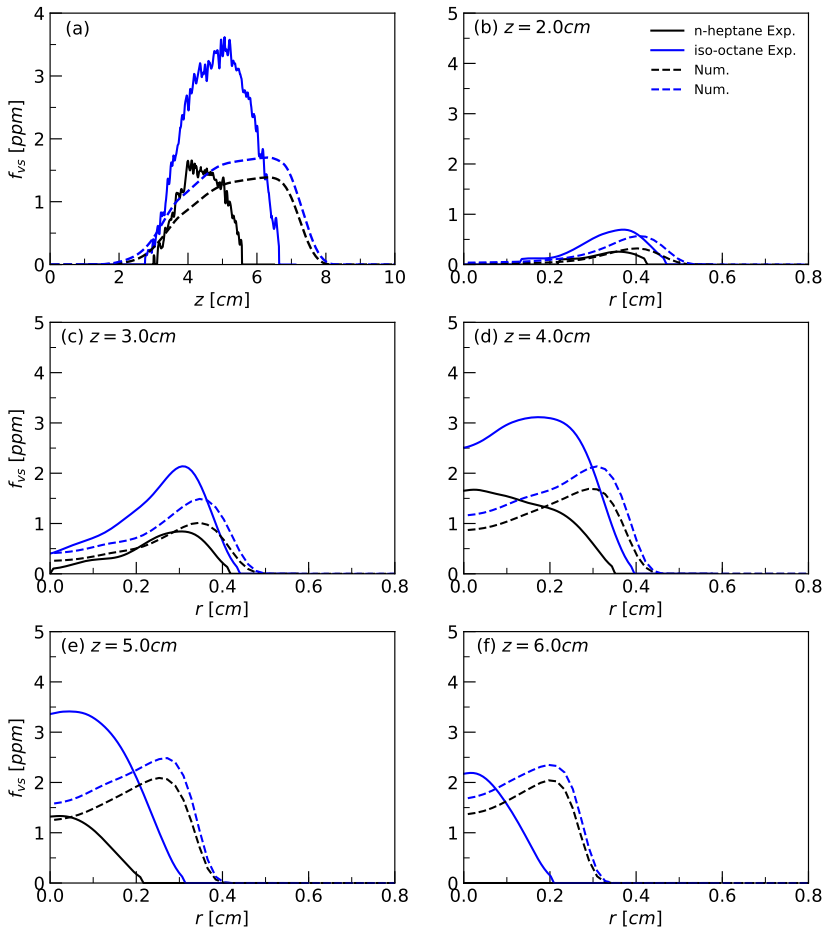

Figure 5.13 – Modeled axial and radial profiles of SVF obtained using ANTHAN as precursor compared against experiment, Kashif et al. (2014), for the pure n-heptane and iso-octane dopants.

Figure 5.14 shows the radially integrated SVF along the flame axis obtained with ANTHAN, it is compared with the result obtained using pyrene as precursor. Firstly, it confirms the more elongated feature of the predicted soot distribution. Secondly, it shows a clear improvement compared to the pyrene-based PAH model. Although a part of the discrepancy can attributed to the experimental technique as previously discussed, particularly for the pure n-heptane flame that have lower soot, another part can be attributed to the PAH model that seems to delay the soot growth step for both flame due to the position of ANTHAN as the majority of the growth stems from condensation. Indeed, toluene was observed to accelerate the PAH-based processes of soot production, and as we will see in the following paragraph, this seems to resolve the issue, as the departure is overridden when toluene is present.

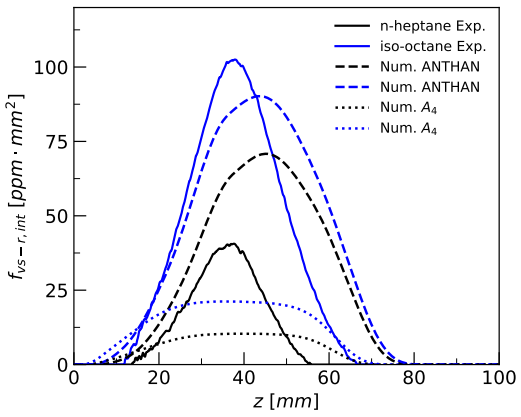

Figure 5.14 – Predicted radially integrated SVF obtained using ANTHAN as precursor compared against experiment, Kashif et al. (2014), for the pure n-heptane and iso-octane dopants.

5.5.2.2 Predictions for n-heptane/toluene and iso-octane/toluene mixtures

Figure 5.15 and Figure 5.17 show the axial and radial SVF predictions obtained for the mixtures of n-heptane/toluene (H/T) and iso-octane/toluene (I/T), respectively. They are completed with the contour plots of the SVF in Figure 5.16-(c) to (f). SVF predictions are in overall good agreement with the experiments in terms of magnitude with predicted peaks at 1.62 ppm, 2.38 ppm, 1.75 ppm and 2.36 ppm against 1.81 ppm, 2.19 ppm, 2.36 ppm and 3.11 ppm for the 80%H/20%T, 60%H/40%T, 80%I/20%T and 60%I/40%T doped flames, respectively.

Modeled axial profiles in Figure 5.15-(a) and Figure 5.17-(a) feature bell-shaped profiles tilted on the downstream side whereas experimental profiles shows clear bell-shaped profiles. The radial profiles in Figure 5.15-(b) to (e) and Figure 5.17-(b) to (e) show that the predicted profiles maintain a M-shaped profile through the flame in departure to the experiment which feature a bell-shape profile. Experimentally, the 20% increase of toluene content induces a 21% and 32% increase in soot for the n-heptane/toluene and iso-octane/toluene flames, respectively. Numerically, the increases are equal to 47% and 35% in soot for the n-heptane/toluene and iso-octane/toluene flames, respectively. Although, the increase rate is reasonable for iso-octane, it is overestimated for n-heptane and higher than for iso-octane which conveys that the influence of toluene is higher in the n-heptane flame than in the iso-octane flame. Moreover, SVF profiles show that the influence of toluene is restricted to the flame wings as the increase in soot is located along the flame wings. A consequence is that the increase in soot is negligible along the flame axis for n-heptane and low for iso-octane. The downstream part of the axial SVF profiles, Figure 5.15-(a) and Figure 5.17-(a), show that SVF is oxidized at similar rates than the experiment for both flames, inducing reasonable predictions in Figure 5.15-(f) and Figure 5.17-(f). Nevertheless, Figure 5.16 shows that global predicted soot distribution are slightly

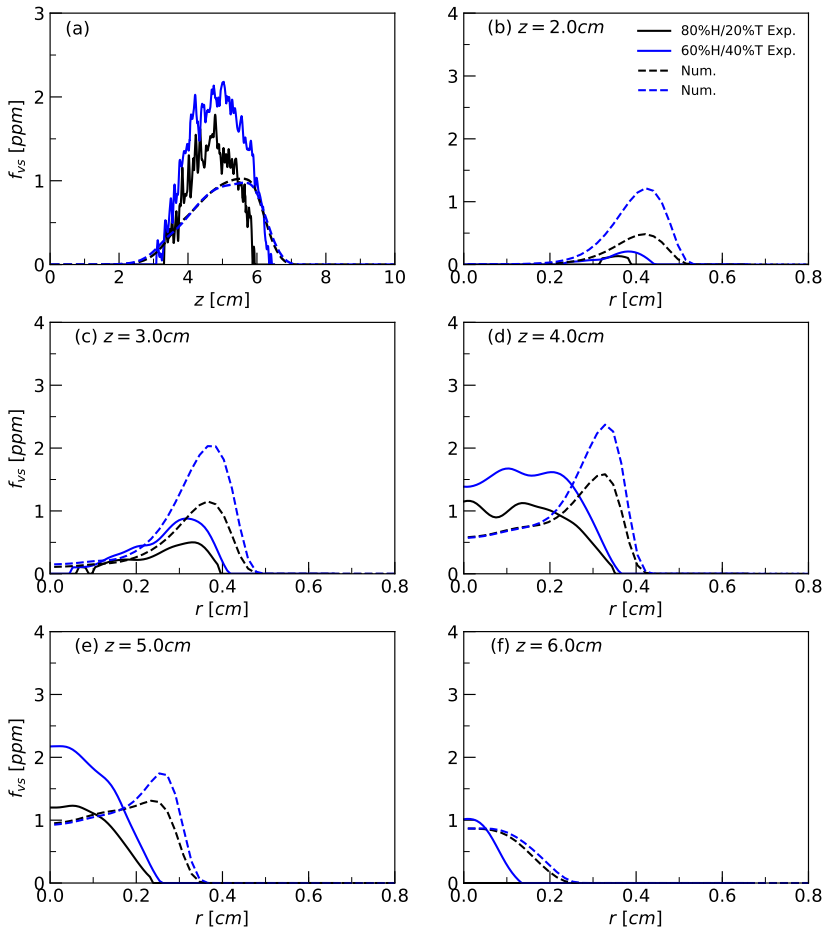

Figure 5.15 – Modeled axial and radial profiles of SVF obtained using ANTHAN as precursor compared against experiment, Kashif et al. (2015), for the n-heptane/toluene dopant mixtures.

offset along the flame axis with respect to the experience, the direction of offset varies according to the composition of the doping blends. The more toluene is present, the more upstream is the soot distribution. It echoes with the pure n-heptane and iso-octane doped flames which feature an offset in the downstream direction. As soot predictions are largely controlled by PAH-based processes, and in turn, to PAHs, these discrepancies can be attributed to the uncertainty related to PAH chemistry.

Figure 5.18 shows the radially integrated SVF along the flame axis obtained with ANTHAN and compared with previous result obtained using pyrene. It reveals the significant correction of the early appearance of soot while maintaining reasonable amplitude in comparison to the experience for both fuels.

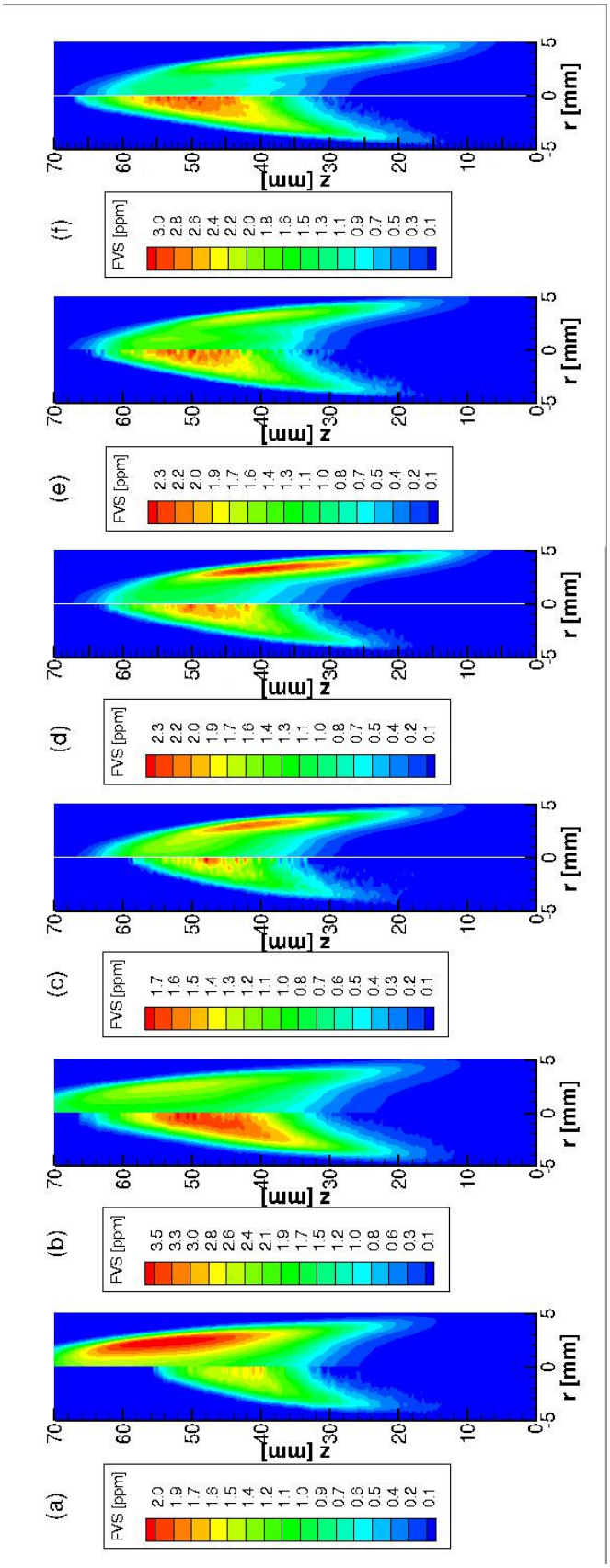

Figure 5.16 – Predicted fields of soot volume fraction using ANTHAN as precursor (right) compared against experiments (left), Kashif et al. (2014), Kashif et al. (2015), for (a) pure n-heptane doped flame, (b) pure iso-octane doped flame, (c)-(d) diluted 80%n-heptane/20%toluene and 60%n-heptane/40%toluene doped flames, and (e)-(f) diluted 80%iso-octane/20%toluene and 60%iso-octane/40%toluene doped flames.

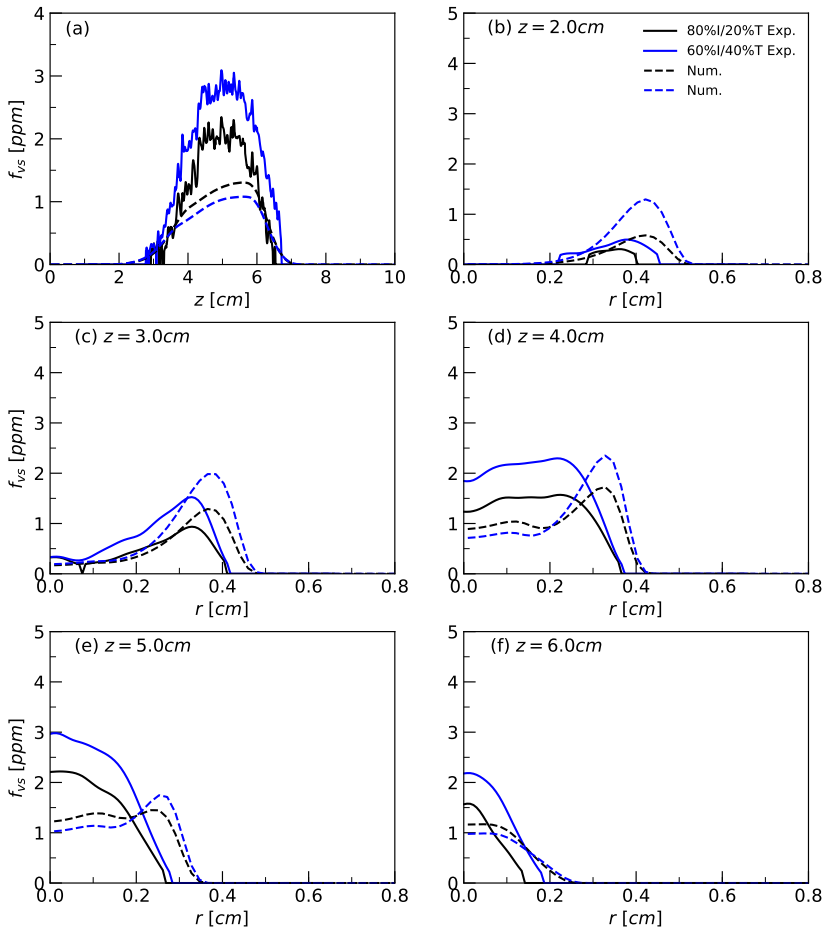

Figure 5.17 – Modeled axial and radial profiles of SVF obtained using ANTHAN as precursor compared against experiment, Kashif et al. (2015), for the iso-octane/toluene dopant mixtures.

Overall, the predictions of the ANTHAN-based PAH model show a quantitative agreement with the experimental results, significantly improving upon the pyrene-based PAH model. On the one hand, reasonable soot distribution is achieved for all fuel mixtures, on the other hand, soot predictions are within a factor of 2 compared to the experiments. Despite some discrepancies, the ANTHAN-based PAH model offer an acceptable trade-off for all the mixtures of n-heptane, iso-octane and toluene. These simulations demonstrate that despite the uncertainties surrounding the chemistry of PAHs, it is possible to find a large PAH that describes soot growth. Here, with the current chemical mechanism, it is the six-ring PAH anthanthrene. However the nature of this PAH depends on the chemical mechanism due to the different PAH kinetics employed in the literature. Consequently, the choice of the PAH should be meticulously achieved and adapted to the mechanism.

The predicted soot peak remains located on the flame wings, contrary to the experi-

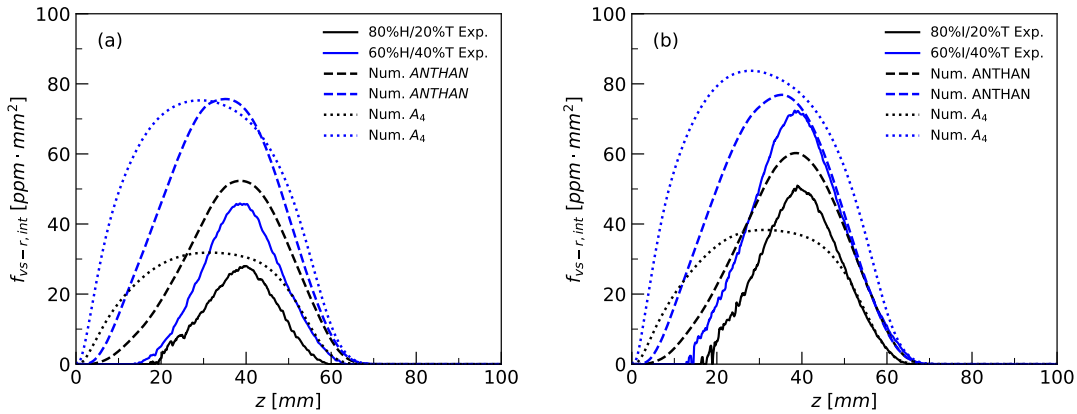

Figure 5.18 – Predicted radially integrated SVF obtained using ANTHAN as precursor compared against experiment, Kashif et al. (2015), for the n-heptane/toluene, (a), and iso-octane/toluene, (b), dopant mixtures.

ment, despite remarkable modeled soot magnitude on the flame centerline. To the author's best knowledge, no literature study has been successful in predicting the experimentally observed bell-shaped profile of radial SVF for these fuels in laminar coflow diffusion flames while utilizing various kinetic mechanisms and different soot production model. Certainly, a significant portion of this defect can be attributed to the uncertain chemistry of PAHs, as suggested by this study, however, it has been suggested that the thermal diffusion of PAHs may play a non-negligible role, Dworkin and Smooke (2009). Due to their substantial mass, PAHs would be drawn towards colder regions through thermal diffusion, leading to the displacement of the soot peak towards the center. However, the development of a well-established PAH kinetic mechanism is a prerequisite before moving towards more detailed and complex models.

5.5.3 Analysis of soot production processes

The objective of this section is to quantify the contribution of the different processes of soot production for gasoline surrogate fuels related to the soot predictions of the previous section. Figure 5.19 shows the production rates as a function of the residence time, defined as $t_{res} = \int_0^z dz/u_z(r=0,z)$ where $u_z(r=0,z)$ refers to the axial component of the velocity vector along the flame axis. It should be noticed that in all the diagrams of Figure 5.19, the scale related to the soot nucleation rate differs from that related to the other processes. The diagrams (a) to (c) represent soot production rates along the flame centerline. The diagrams (d) to (f) display the same rates along the path of maximum SVF and, finally, the radially integrated rates are given in diagrams (j) to (i). The radially integrated rates are defined as $\dot{\omega}'_{-r,int} = 2\pi \int_0^\infty \dot{\omega}''' r dr$. Similar results are obtained when iso-octane is used instead

of n-heptane and are thus not shown.

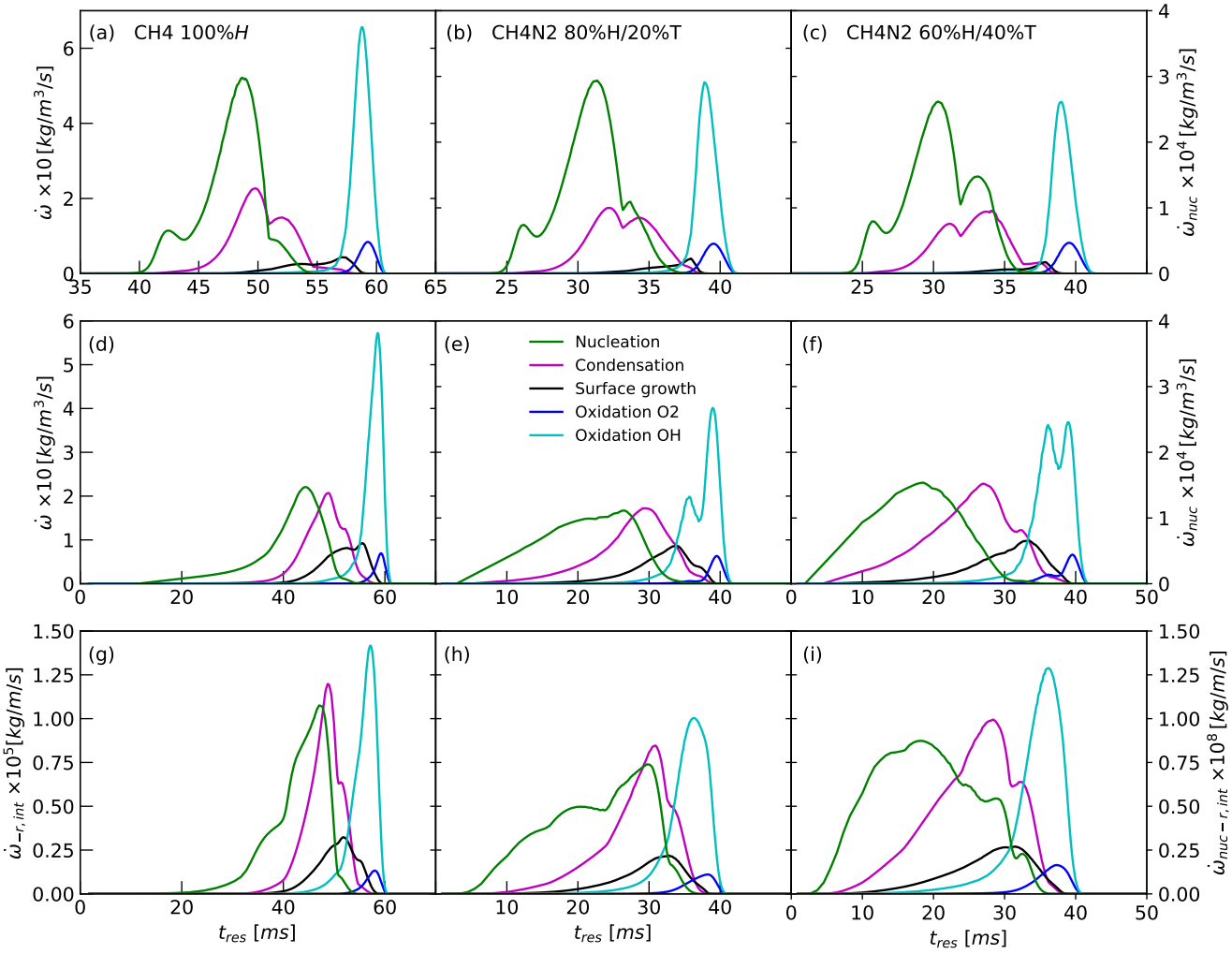

Figure 5.19 – Analyse of soot production processes as a function of the residence time: (a)-(c) along the flame centerline, (b)-(f) along the path of maximum SVF, and (g)-(i) radially integrated profiles.

Nucleation as the bottleneck of soot production is the first process to occur, it spans over a relatively long time and its initiation is accelerated by the presence of toluene. Soot nucleation is favored in the flame centerline for the three blends, see Figure 5.19-(a) to (c) and (d) to (f), nascent soot particles are thus more concentrated in the flame centerline region. A consequence is that the growth of particles is controlled by condensation for all the blends as PAH precursor is spread in the flame centerline region and on the inner part of the flame wings, whereas *H* atoms, required for the HACA process, are found on the outer part of the flame wings inducing a minor role of surface growth by HACA, see Figure 5.19-(g) to (i). More particularly, 76%, 80% and 80%

of the soot growth can be attributed to condensation for the pure n-heptane, diluted 80%H/20%T and diluted 60%H/40%T doped flames, respectively. The presence of 20% of toluene increases the contribution of condensation compared to the pure n-heptane doping blend, however the additional increase of toluene content by 20% maintains the contribution of condensation to 80%. Oxidation by OH widely dominates the oxidation process with $\omega_{Ox,OH}$ being one order of magnitude higher than ω_{Ox,O_2}, consistently with the observations carried out on ethylene.

As a reminder, the processes of condensation and surface growth played comparable roles in the ethylene flames of the previous chapter. This change of trend might explain why the experimental SVF features an overall bell-shaped profile for gasoline surrogate fuels and a M-shaped profile for ethylene. Moreover, the major role of PAH condensation reinforces the idea that the discrepancies of the prediction are mainly due to uncertainties related to the PAH chemistry.

5.6 Chapter conclusions

The extension of the PAH model to gasoline surrogate fuels was carried out by simulating laminar coflow diffusion flames fueled by n-heptane, iso-octane and toluene mixtures. The pyrene-based model captures the peak of SVF and integrated SVF in n-heptane/toluene and iso-octane/toluene mixtures representative of gasoline. However, it underestimates significantly the soot production for pure n-heptane and iso-octane and predicts significantly earlier the onset of soot production when toluene is added. Based on a chemical analysis, a PAH larger than pyrene, namely anthanthrene, was found to reduce these discrepancies and provides a more quantitative agreement for all the flames. The analysis of the soot production processes shows that PAH condensation contributes in large majority to the growth process compared to HACA surface growth, which marks a turning point compared to light gaseous fuels.

6 Conclusions and perspectives

6.1 Conclusions

The objective of this thesis was to extend a LES-based fire simulator including state-of-the-art sub-models for combustion and radiation to sooting well-ventilated and under-ventilated purely buoyant fire plumes.

Two challenging issues have to be addressed to achieve this objective. The first is related to the choice of the soot model. Previous works in the group have demonstrated that the acetylene/benzene based soot production model proposed by Lindstedt is well-suited to predict SVF and related radiative heat transfer in both laminar and turbulent non-premixed flames fuelled by aliphatics and, especially C_1-C_3 hydrocarbons. However, its extension to liquid fuels involved in the transportation sector, such as gasoline, diesel, kerosene, is challenging since these fuels contain PAHs in their initial composition. In this case, the formation of benzene is no-longer the bottleneck of PAH growth and the use of PAH-based soot production model appears to be a natural strategy. This strategy has been explored during the course of this thesis. A PAH-based model was developed using pyrene as the soot precursor. The analysis of this model focused on laminar coflow diffusion flames so as to avoid the complexities related to turbulence. As a first step, a PAH-based soot production model, based on pyrene as soot precursor, has been developed and calibrated in well and under-oxygenated laminar coflow diffusion flames. It was found to predict quantitatively the experimental data in terms of temperature, soot volume fraction, primary particle diameter and soot number densities. The influence of the reduction of oxygen in the oxidizer was also quantitatively reproduced. This model has been then applied without modifying the model parameters to laminar coflow diffusion flames fuelled by pure n-heptane, iso-octane and mixtures of n-heptane/toluene and iso-octane/toluene, these two latter being representative of gasoline. Model predictions showed that the pyrene-based model reproduces reasonably well the peak of SVF and integrated SVF in the mixtures representative of gasoline but overestimates significantly the onset of the soot production. In addition, it underpredicts significantly the soot production in pure n-heptane and iso-octane flames. A chemical analysis was performed to highlight the origin of these discrepancies and has revealed that a PAH larger than pyrene, namely anthanthrene, is better suited. Simulations performed by using anthanthrene as soot precursor were found to improve those performed with pyrene.

The second challenge is related to the modeling of the interaction between soot pro-

duction and turbulence (TSI). A flamelet/presumed filtered density function (FDF) combustion model was used, where the presumed FDF was built to account both the spatial intermittent behavior and the fast oxidation feature of soot. This implementation was utilized for simulating soot production and associated radiation produced by three well-documented 15-kW ethylene buoyant diffusion flames burning under normal and reduced oxygen. Model predictions reproduced with fidelity the flame structure, the soot production dynamics and the radiative loss for the three flames. The acetylene/benzene-based model was employed, drawn on the accumulated expertise from previous studies of our research team regarding soot production of C_1-C_3 fuels. Soot radiation was included and gas radiation was modeled with state-of-the-art rank-correlated full-spectrum k-distribution model (RCFSK). A particular attention was paid on the interaction between turbulence and radiation (TRI): subgrid-scale (SGS) absorption TRI is neglected whereas the filtered emission term is modelled from the presumed FDF approach.

Conclusions are the following :

- Model results showed that soot and radiating gas have a similar contribution to radiation for the flame burning in air and the contribution of radiating gas becomes increasingly dominant with reducing oxygen due to a decrease in soot volume fraction (SVF) throughout the overall flames. As a consequence, this study confirms the paramount influence of soot.
- A sensitivity study was performed on the influence of the modelling approach of SGS TSI and radiative heat transfer. Model predictions showed that neglecting the coupling between soot quantities and mixture fraction overestimates substantially soot oxidation, resulting in significantly lower soot production and radiative loss. The study suggests that the presumed FDF is capable to reproduce the SGS coupling between soot quantities and mixture fraction in the studied flames and that it is mainly due to the influence of oxidative species.
- The comparison of predictions obtained with variant radiative models showed that the approximation of grey soot is valid for these lab-scale flames characterized by moderate optical thicknesses and the use of a non-grey weighted-sum-of-grey-gases (WSGG) model coupled to the grey soot approximation represents an alternative to the full-spectrum k-distribution models.

6.2 Perspectives

This work is part of a development program of a LES-based fire simulator to model fire spread in nuclear plants. It represents the second step in these developments toward more realistic scenarios and, as such, is limited to the modelling a non-luminous fire plumes in non-confined environments although under-ventilated configurations were considered. As such, the perspectives of the work and the future developments are exhaustive. Among them, future works will include the coupling between gas

phase and condensed phase through the development of thermal degradation models, the inclusion of solid inert or flammable walls and the associated conjugated heat transfer, ... As a consequence, in order to avoid an exhaustive description of such new problems, the perspective will deal with improvements of the current fire model and the related physics :

- The PAH model now requires to be asserted on turbulent buoyant diffusion flames for fuel containing aromatics. Available comprehensive experimental data for these fuels are scarce in the literature, however measurements were recently carried out at EDF R&D and numerical simulations should soon follow. Moreover, the subgrid-scale model for the soot production turbulence interaction should be studied in the case of smoking flames.
- The dependence of the PAH model to chemical mechanism questions its feasibility for certain complex fire scenario for which chemical mechanism including the PAH production are not available. A smoke-point based model should be jointly developed to address these scenarios. However, they are not adequately designed in their current form and they should be reexamined to incorporate the fundamental principles of soot formation and oxidation processes.

During my PhD, I have also participated to different works of my research group that have led to an accepted publication in the *Combustion Theory and Modelling* about flamelet/transported PDF simulations of ethylene/air jet turbulent non-premixed flame using the three-equation PAH-based soot production model developed in Chapter 4, it is provided in the Annex.

Bibliography

J. Appel, H. Bockhorn, and M. Frenklach. Kinetic modeling of soot formation with detailed chemistry and physics: laminar premixed flames of c2 hydrocarbons. *Combustion and Flame*, 121(1):122–136, 2000. doi: https://doi.org/10.1016/S0010-2180(99)00135-2.

A. Attili, F. Bisetti, M. E. Mueller, and H. Pitsch. Formation, growth, and transport of soot in a three-dimensional turbulent non-premixed jet flame. *Combustion and Flame*, 161(7):1849–1865, 2014. doi: https://doi.org/10.1016/j.combustflame.2014.01.008.

A. Attili, F. Bisetti, M. E. Mueller, and H. Pitsch. Damköhler number effects on soot formation and growth in turbulent nonpremixed flames. *Proceedings of the Combustion Institute*, 35(2):1215–1223, 2015. doi: https://doi.org/10.1016/j.proci.2014.05.084.

D. Aubagnac-Karkar, J.-B. Michel, O. Colin, P. E. Vervisch-Kljakic, and N. Darabiha. Sectional soot model coupled to tabulated chemistry for Diesel RANS simulations. *Combustion and Flame*, 162(8):3081–3099, 2015. doi: 10.1016/j.combustflame.2015.03.005.

M. Balthasar and M. Kraft. A stochastic approach to calculate the particle size distribution function of soot particles in laminar premixed flames. *Combustion and Flame*, 133(3):289–298, 2003. doi: https://doi.org/10.1016/S0010-2180(03)00003-8.

T. Beji, J. P. Zhang, and M. Delichatsios. Determination of soot formation rate from laminar smoke point measurements. *Combustion Science and Technology*, 180(5):927–940, 2008. doi: 10.1080/00102200801894398.

L. Berger, A. Wick, A. Attili, M. Mueller, and H. Pitsch. Modeling subfilter soot-turbulence interactions in large eddy simulation: An a priori study. *Proceedings of the Combustion Institute*, 38(2):2783–2790, 2021. doi: 10.1016/j.proci.2020.06.386.

G. Bertin, J. Most, and M. Coutin. Wall fire behavior in an under-ventilated room. *Fire Safety Journal*, 37(7):615–630, 2002. doi: https://doi.org/10.1016/S0379-7112(02)00016-4.

J. Bhatt and R. Lindstedt. Analysis of the impact of agglomeration and surface chemistry models on soot formation and oxidation. *Proceedings of the Combustion Institute*, 32(1):713–720, 2009. doi: https://doi.org/10.1016/j.proci.2008.06.201.

F. Bisetti, G. Blanquart, M. E. Mueller, and H. Pitsch. On the formation and early evolution of soot in turbulent nonpremixed flames. *Combustion and Flame*, 159(1): 317–335, 2012. doi: https://doi.org/10.1016/j.combustflame.2011.05.021.

G. Blanquart. *Chemical and statistical soot modeling*. PhD thesis, Stanford University, 2008.

G. Blanquart and H. Pitsch. Analyzing the effects of temperature on soot formation with a joint volume-surface-hydrogen model. *Combustion and Flame*, 156(8):1614–1626, 2009a. doi: https://doi.org/10.1016/j.combustflame.2009.04.010.

G. Blanquart and H. Pitsch. A joint volume-surface-hydrogen multi-variate model for soot formation. In H. Bockhorn, A. D'Anna, A. F. Sarofim, and H. Wang, editors, *Combustion Generated Fine Carbonceous Particles*. Springer-Verlag, KIT Scientific Publishing, Karlsruhe, 2009b.

T. C. Bond, S. J. Doherty, D. W. Fahey, P. M. Forster, T. Berntsen, B. J. DeAngelo, M. G. Flanner, S. Ghan, B. Kärcher, D. Koch, S. Kinne, Y. Kondo, P. K. Quinn, M. C. Sarofim, M. G. Schultz, M. Schulz, C. Venkataraman, H. Zhang, S. Zhang, N. Bellouin, S. K. Guttikunda, P. K. Hopke, M. Z. Jacobson, J. W. Kaiser, Z. Klimont, U. Lohmann, J. P. Schwarz, D. Shindell, T. Storelvmo, S. G. Warren, and C. S. Zender. Bounding the role of black carbon in the climate system: A scientific assessment. *Journal of Geophysical Research: Atmospheres*, 118(11):5380–5552, 2013. doi: https://doi.org/10.1002/jgrd.50171.

S. Brookes and J. Moss. Predictions of soot and thermal radiation properties in confined turbulent jet diffusion flames. *Combustion and Flame*, 116(4):486–503, 1999. doi: https://doi.org/10.1016/S0010-2180(98)00056-X.

A. Brown, M. Bruns, M. Gollner, J. Hewson, G. Maragkos, A. Marshall, R. McDermott, B. Merci, T. Rogaume, S. Stoliarov, J. Torero, A. Trouvé, Y. Wang, and E. Weckman. Proceedings of the first workshop organized by the iafss working group on measurement and computation of fire phenomena (macfp). *Fire Safety Journal*, 101:1–17, 2018. doi: https://doi.org/10.1016/j.firesaf.2018.08.009.

D. Burot. *Transported probability density function for the numerical simulation of flames characteristic of fire*. PhD thesis, Aix-Marseille University, 2017.

J. P. Cain, P. L. Gassman, H. Wang, and A. Laskin. Micro-ftir study of soot chemical composition—evidence of aliphatic hydrocarbons on nascent soot surfaces. *Physical Chemistry Chemical Physics*, 12:5206–5218, 2010. doi: 10.1039/B924344E.

D. Carbonell, C.-D. Perez-Segarra, A. Oliva, and P.-J. Coelho. Flamelet mathematical models for non-premixed laminar combustion. *Combustion and Flame - COMBUST FLAME*, 156:334–347, 2009. doi: 10.1016/J.COMBUSTFLAME.2008.07.011.

B. M. Cetegen and T. A. Ahmed. Experiments on the periodic instability of buoyant plumes and pool fires. *Combustion and Flame*, 93(1):157–184, 1993. doi: https://doi.org/10.1016/0010-2180(93)90090-P.

H. Chang and T. T. Charalampopoulos. Determination of the wavelength dependence of refractive indices of flame soot. *Proceedings: Mathematical and Physical Sciences*, 430(1880):577–591, 1990.

P. Chatterjee, Y. Wang, K. V. Meredith, and S. B. Dorofeev. Application of a subgrid soot-radiation model in the numerical simulation of a heptane pool fire. *Proceedings of the Combustion Institute*, 35(3):2573–2580, 2015. doi: https://doi.org/10.1016/j.proci.2014.05.045.

Z. Chen, J. Wen, B. Xu, and S. Dembele. Extension of the eddy dissipation concept and smoke point soot model to the les frame for fire simulations. *Fire Safety Journal*, 64: 12–26, 2014. doi: https://doi.org/10.1016/j.firesaf.2014.01.001.

B. Choi, S. Choi, and S. Chung. Soot formation characteristics of gasoline surrogate fuels in counterflow diffusion flames. *Proceedings of the Combustion Institute*, 33(1): 609–616, 2011. doi: https://doi.org/10.1016/j.proci.2010.06.067.

M. Commodo, K. Kaiser, G. De Falco, P. Minutolo, F. Schulz, A. D'Anna, and L. Gross. On the early stages of soot formation: Molecular structure elucidation by high-resolution atomic force microscopy. *Combustion and Flame*, 205:154–164, 2019. doi: https://doi.org/10.1016/j.combustflame.2019.03.042.

J. Consalvi and F. Nmira. Transported scalar pdf modeling of oxygen-enriched turbulent jet diffusion flames: Soot production and radiative heat transfer. *Fuel*, 178: 37–48, 2016. doi: https://doi.org/10.1016/j.fuel.2016.03.035.

J. Consalvi, R. Demarco, A. Fuentes, S. Melis, and J. Vantelon. On the modeling of radiative heat transfer in laboratory-scale pool fires. *Fire Safety Journal*, 60:73–81, 2013. doi: https://doi.org/10.1016/j.firesaf.2012.10.010.

J. Consalvi, F. Nmira, and D. Burot. Simulations of sooting turbulent jet flames using a hybrid flamelet/stochastic eulerian field method. *Combustion Theory and Modelling*, 20(2):221–257, 2016. doi: 10.1080/13647830.2015.1125024.

J. Consalvi, F. Andre, F. Coelho, F. Franca, F. Nmira, M. Galtier, V. Solovjov, and B. Webb. Assessment of engineering gas radiative property models in high pressure turbulent jet diffusion flames. *Journal of Quantitative Spectroscopy and Radiative Transfer*, 253:107169, 2020. doi: https://doi.org/10.1016/j.jqsrt.2020.107169.

M. Conturso, M. Sirignano, and A. D'Anna. Effect of alkylated aromatics on particle formation in diffusion flames: An experimental study. *Experimental Thermal and Fluid Science*, 73:27–32, 2016. doi: https://doi.org/10.1016/j.expthermflusci.2015.08.020.

G. Cox. *Combustion fundamentals of fire*. Academic Press London, 1995.

J. Craske and M. van Reeuwijk. Robust and accurate open boundary conditions for incompressible turbulent jets and plumes. *Computers Fluids*, 86:284–297, 2013. doi: https://doi.org/10.1016/j.compfluid.2013.06.026.

G. Curtis. *The cave painters: Probing the mysteries of the world's first artists*. Anchor, 2007.

P. Dagaut and M. Cathonnet. The ignition, oxidation, and combustion of kerosene: A review of experimental and kinetic modeling. *Progress in Energy and Combustion Science*, 32(1):48–92, 2006. doi: https://doi.org/10.1016/j.pecs.2005.10.003.

J. de Ris. Fire radiation—a review. *Symposium (International) on Combustion*, 17(1): 1003–1016, 1979. doi: https://doi.org/10.1016/S0082-0784(79)80097-1.

B. D. Ditch, J. L. de Ris, T. K. Blanchat, M. Chaos, R. G. Bill, and S. B. Dorofeev. Pool fires – an empirical correlation. *Combustion and Flame*, 160(12):2964–2974, 2013. doi: https://doi.org/10.1016/j.combustflame.2013.06.020.

R. Dobbins, R. Fletcher, and H.-C. Chang. The evolution of soot precursor particles in a diffusion flame. *Combustion and Flame*, 115(3):285–298, 1998. doi: https://doi.org/10.1016/S0010-2180(98)00010-8.

K. Donaldson, L. Tran, L. A. Jimenez, R. Duffin, D. E. Newby, N. Mills, W. MacNee, and V. Stone. Combustion-derived nanoparticles: A review of their toxicology following inhalation exposure. *Particle and Fibre Toxicology*, 2(1):1743–8977, 2005. doi: 10.1186/1743-8977-2-10.

S. Dworkin and V. Smooke, M.D.and Giovangigli. The impact of detailed multicomponent transport and thermal diffusion effects on soot formation in ethylene/air flames. *Proceedings of the Combustion Institute*, 32(1):1165–1172, 2009. doi: https://doi.org/10.1016/j.proci.2008.05.061.

S. Dworkin, Q. Zhang, M. Thomson, N. Slavinskaya, and U. Riedel. Application of an enhanced pah growth model to soot formation in a laminar coflow ethylene/air diffusion flame. *Combustion and Flame*, 158:1682–1695, 2011a. doi: 10.1016/j.combustflame.2011.01.013.

S. B. Dworkin, Q. Zhang, M. J. Thomson, N. A. Slavinskaya, and U. Riedel. Application of an enhanced pah growth model to soot formation in a laminar coflow ethylene/air diffusion flame. *Combustion and Flame*, 158(9):1682–1695, 2011b. doi: https://doi.org/10.1016/j.combustflame.2011.01.013.

C. A. Echavarria, I. C. Jaramillo, A. F. Sarofim, and J. S. Lighty. Studies of soot oxidation and fragmentation in a two-stage burner under fuel-lean and fuel-rich conditions. *Proceedings of the Combustion Institute*, 33(1):659–666, 2011. doi: https://doi.org/10.1016/j.proci.2010.06.149.

EDF R&D. Code_saturne, 2023. URL https://www.code-saturne.org/cms/web/.

F. A. Escudero. *Experimental and numerical contributions to soot production in laminar axisymmetric diffusion flames*. PhD thesis, Aix-Marseille University, 2019.

C. P. Fenimore and G. W. Jones. Oxidation of soot by hydroxyl radicals. *The Journal of Physical Chemistry*, 71(3):593–597, 1967. doi: 10.1021/j100862a021.

B. Franzelli, A. Vié, and N. Darabiha. A three-equation model for the prediction of soot emissions in les of gas turbines. *Proceedings of the Combustion Institute*, 37(4): 5411–5419, 2019. doi: https://doi.org/10.1016/j.proci.2018.05.061.

M. Frenklach. Reaction mechanism of soot formation in flames. *Physical Chemistry Chemical Physics*, 4:2028–2037, 2002. doi: 10.1039/B110045A.

M. Frenklach and S. Harris. Aerosol dynamics modeling using the method of moments. *Journal of Colloid and Interface Science*, 118(1):252–261, 1987. doi: https://doi.org/10.1016/0021-9797(87)90454-1.

M. Frenklach and H. Wang. *Detailed Mechanism and Modeling of Soot Particle Formation*, pages 165–192. Springer Berlin Heidelberg, Berlin, Heidelberg, 1994. doi: 10.1007/978-3-642-85167-4_10.

M. Frenklach, D. W. Clary, W. C. Gardiner, and S. E. Stein. Detailed kinetic modeling of soot formation in shock-tube pyrolysis of acetylene. *Symposium (International) on Combustion*, 20(1):887–901, 1985. doi: https://doi.org/10.1016/S0082-0784(85)80578-6.

M. Frenklach, W. Gardiner, S. Stein, D. Clary, and T. Yuan. Mechanism of soot formation in acetylene-oxygen mixtures. *Combustion Science and Technology*, 50(1-3):79–115, 1986. doi: 10.1080/00102208608923927.

E. Georganta, R. K. Rahman, A. Raj, and S. Sinha. Growth of polycyclic aromatic hydrocarbons (pahs) by methyl radicals: Pyrene formation from phenanthrene. *Combustion and Flame*, 185:129–141, 2017. doi: https://doi.org/10.1016/j.combustflame.2017.07.011.

M. Gradziński, H. Hercman, M. Nowak, and P. Bella. Age of black coloured laminae within speleothems from domica cave and its significance for dating of prehistoric human settlement. *Geochronometria*, 28(1):39–45, 2007.

H. Guo, F. Liu, G. J. Smallwood, and L. Gülder. Numerical study on the influence of hydrogen addition on soot formation in a laminar ethylene–air diffusion flame. *Combustion and Flame*, 145(1):324–338, 2006. doi: https://doi.org/10.1016/j.combustflame.2005.10.016.

A. Gupta, D. Haworth, and M. Modest. Turbulence-radiation interactions in large-eddy simulations of luminous and nonluminous nonpremixed flames. *Proceedings of the Combustion Institute*, 34(1):1281–1288, 2013. doi: https://doi.org/10.1016/j.proci.2012.05.052.

A. Hamins, S. J. Fischer, T. Kashiwagi, M. E. Klassen, and J. P. Gore. Heat feedback to the fuel surface in pool fires. *Combustion Science and Technology*, 97(1-3):37–62, 1994. doi: 10.1080/00102209408935367.

G. Heskestad. Engineering relations for fire plumes. *Fire Safety Journal*, 7(1):25–32, 1984. doi: https://doi.org/10.1016/0379-7112(84)90005-5.

J. Hwang and S. Chung. Growth of soot particles in counterflow diffusion flames of ethylene. *Combustion and Flame*, 125(1):752–762, 2001. doi: https://doi.org/10.1016/S0010-2180(00)00234-0.

M. Ihme and H. Pitsch. Modeling of radiation and nitric oxide formation in turbulent nonpremixed flames using a flamelet/progress variable formulation. *Physics of Fluids*, 20(5):055110, 2008. doi: 10.1063/1.2911047.

S. S. Iyer, T. A. Litzinger, S.-Y. Lee, and R. J. Santoro. Determination of soot scattering coefficient from extinction and three-angle scattering in a laminar diffusion flame. *Combustion and Flame*, 149(1):206–216, 2007. doi: https://doi.org/10.1016/j.combustflame.2006.11.009.

M. Z. Jacobson. Control of fossil-fuel particulate black carbon and organic matter, possibly the most effective method of slowing global warming. *Journal of Geophysical Research: Atmospheres*, 107(D19):ACH 16–1–ACH 16–22, 2002. doi: https://doi.org/10.1029/2001JD001376.

A. Jain and Y. Xuan. Effects of large aromatic precursors on soot formation in turbulent non-premixed sooting jet flames. *Combustion Theory and Modelling*, 23(3):439–466, 2019. doi: 10.1080/13647830.2018.1549751.

C. Jiménez, F. Ducros, B. Cuenot, and B. Bédat. Subgrid scale variance and dissipation of a scalar field in large eddy simulations. *Physics of Fluids*, 13(6):1748–1754, 2001. doi: 10.1063/1.1366668.

K. O. Johansson, T. Dillstrom, P. Elvati, M. F. Campbell, P. E. Schrader, D. M. Popolan-Vaida, N. K. Richards-Henderson, K. R. Wilson, A. Violi, and H. A. Michelsen. Radical–radical reactions, pyrene nucleation, and incipient soot formation in combustion. *Proceedings of the Combustion Institute*, 36(1):799–806, 2017. doi: https://doi.org/10.1016/j.proci.2016.07.130.

A. Kalbhor and J. van Oijen. Effects of curvature on soot formation in steady and unsteady counterflow diffusion flames. *Combustion and Flame*, 241:112108, 2022. doi: https://doi.org/10.1016/j.combustflame.2022.112108.

B. Karlsson and J. Quintiere. *Enclosure fire dynamics*. CRC Press, 1999. doi: https://doi.org/10.1201/9781420050219.

M. Kashif, P. Guibert, J. Bonnety, and G. Legros. Sooting tendencies of primary reference fuels in atmospheric laminar diffusion flames burning into vitiated air. *Combustion and Flame*, 161(6):1575–1586, 2014. doi: https://doi.org/10.1016/j.combustflame.2013.12.009.

M. Kashif, J. Bonnety, A. Matynia, P. Da Costa, and G. Legros. Sooting propensities of some gasoline surrogate fuels: Combined effects of fuel blending and air vitiation. *Combustion and Flame*, 162(5):1840–1847, 2015. doi: https://doi.org/10.1016/j.combustflame.2014.12.005.

A. Kazakov and M. Frenklach. Dynamic modeling of soot particle coagulation and aggregation: Implementation with the method of moments and application to high-pressure laminar premixed flames. *Combustion and Flame*, 114(3):484–501, 1998. doi: https://doi.org/10.1016/S0010-2180(97)00322-2.

I. M. Kennedy. Models of soot formation and oxidation. *Progress in Energy and Combustion Science*, 23(2):95–132, 1997. doi: https://doi.org/10.1016/S0360-1285(97)00007-5.

V. V. Kislov, A. I. Sadovnikov, and A. M. Mebel. Formation mechanism of polycyclic aromatic hydrocarbons beyond the second aromatic ring. *The Journal of Physical Chemistry A*, 117(23):4794–4816, 2013. doi: 10.1021/jp402481y.

A. Kronenburg, R. Bilger, and J. Kent. Modeling soot formation in turbulent methane–air jet diffusion flames. *Combustion and Flame*, 121(1):24–40, 2000. doi: https://doi.org/10.1016/S0010-2180(99)00146-7.

S. Kruse, A. Wick, P. Medwell, A. Attili, J. Beeckmann, and H. Pitsch. Experimental and numerical study of soot formation in counterflow diffusion flames of gasoline surrogate components. *Combustion and Flame*, 210:159–171, 2019a.

S. Kruse, J. Ye, Z. Sun, A. Attili, B. Dally, P. Medwell, and H. Pitsch. Experimental investigation of soot evolution in a turbulent non-premixed prevaporized toluene flame. *Proceedings of the Combustion Institute*, 37(1):849–857, 2019b. doi: https://doi.org/10.1016/j.proci.2018.05.075.

Köylü and G. Faeth. Structure of overfire soot in buoyant turbulent diffusion flames at long residence times. *Combustion and Flame*, 89(2):140–156, 1992. doi: https://doi.org/10.1016/0010-2180(92)90024-J.

Köylü, C. McEnally, D. Rosner, and L. Pfefferle. Simultaneous measurements of soot volume fraction and particle size / microstructure in flames using a thermophoretic sampling technique. *Combustion and Flame*, 110(4):494–507, 1997. doi: https://doi.org/10.1016/S0010-2180(97)00089-8.

A. Landera, A. M. Mebel, and R. I. Kaiser. Addition of one and two units of csub 2h to styrene: A theoretical study of the csub 10hsub 9 and csub 12hsub 9 systems and implications toward growth of polycyclic aromatic hydrocarbons at low temperatures. *Journal of Chemical Physics*, 134(2), 2011. doi: 10.1063/1.3526957.

C. W. Lautenberger, J. L. de Ris, N. A. Dembsey, J. R. Barnett, and H. R. Baum. A simplified model for soot formation and oxidation in cfd simulation of non-premixed hydrocarbon flames. *Fire Safety Journal*, 40(2):141–176, 2005. doi: https://doi.org/10.1016/j.firesaf.2004.10.002.

S.-Y. Lee, S. R. Turns, and R. J. Santoro. Measurements of soot, oh, and pah concentrations in turbulent ethylene/air jet flames. *Combustion and Flame*, 156(12): 2264–2275, 2009. doi: https://doi.org/10.1016/j.combustflame.2009.09.005.

K. Leung, R. Lindstedt, and W. Jones. A simplified reaction mechanism for soot formation in nonpremixed flames. *Combustion and Flame*, 87(3):289–305, 1991. doi: https://doi.org/10.1016/0010-2180(91)90114-Q.

A. Lifshitz, C. Tamburu, and F. Dubnikova. Reactions of 1-naphthyl radicals with ethylene. single pulse shock tube experiments, quantum chemical, transition state theory, and multiwell calculations. *The Journal of Physical Chemistry A*, 112(5): 925–933, 2008. doi: 10.1021/jp077289s.

D. O. Lignell, J. H. Chen, P. J. Smith, T. Lu, and C. K. Law. The effect of flame structure on soot formation and transport in turbulent nonpremixed flames using direct numerical simulation. *Combustion and Flame*, 151(1):2–28, 2007. doi: https://doi.org/10.1016/j.combustflame.2007.05.013.

P. R. Lindstedt. *Simplified Soot Nucleation and Surface Growth Steps for Non-Premixed Flames*, pages 417–441. Springer Berlin Heidelberg, Berlin, Heidelberg, 1994. doi: 10.1007/978-3-642-85167-4_24.

R. Lindstedt and S. Louloudi. Joint-scalar transported pdf modeling of soot formation and oxidation. *Proceedings of the Combustion Institute*, 30(1):775–783, 2005. doi: https://doi.org/10.1016/j.proci.2004.08.080.

R. Lindstedt and B. Waldheim. Modeling of soot particle size distributions in premixed stagnation flow flames. *Proceedings of the Combustion Institute*, 34(1):1861–1868, 2013. doi: https://doi.org/10.1016/j.proci.2012.05.047.

F. Liu, J. Consalvi, and A. Fuentes. Effects of water vapor addition to the air stream on soot formation and flame properties in a laminar coflow ethylene/air diffusion flame. *Combustion and Flame*, 161(7):1724–1734, 2014. doi: https://doi.org/10.1016/j.combustflame.2013.12.017.

F. Liu, J. Consalvi, and F. Nmira. The importance of accurately modelling soot and radiation coupling in laminar and laboratory-scale turbulent diffusion flames. *Combustion and Flame*, page 112573, 2022. doi: https://doi.org/10.1016/j.combustflame.2022.112573.

P. Liu, H. Lin, Y. Yang, C. Shao, B. Guan, and Z. Huang. Investigating the role of ch2 radicals in the haca mechanism. *The Journal of Physical Chemistry A*, 119(13): 3261–3268, 2015. doi: 10.1021/jp5124162.

P. Liu, Y. Zhang, Z. Li, A. Bennett, H. Lin, S. M. Sarathy, and W. L. Roberts. Computational study of polycyclic aromatic hydrocarbons growth by vinylacetylene addition. *Combustion and Flame*, 202:276–291, 2019. doi: https://doi.org/10.1016/j.combustflame.2019.01.023.

Y. Liu, G. Liu, F. Liu, and J. Consalvi. Effects of the k-value solution schemes on radiation heat transfer modelling in oxy-fuel flames using the full-spectrum correlated k-distribution method. *Applied Thermal Engineering*, 170:114986, 2020. doi: https://doi.org/10.1016/j.applthermaleng.2020.114986.

L. Ma. *Large-eddy simulation of purely buoyant diffusion flames*. PhD thesis, Aix-Marseille University, 2020.

L. Ma, F. Nmira, and J. L. Consalvi. Verification and validation of a variable–density solver for fire safety applications. *Numerical Heat Transfer, Part B: Fundamentals*, 76(3):107–129, 2019. doi: 10.1080/10407790.2019.1647721.

L. Ma, F. Nmira, and J. Consalvi. Large eddy simulation of medium-scale methanol pool fires - effects of pool boundary conditions. *Combustion and Flame*, 222:336–354, 2020. doi: https://doi.org/10.1016/j.combustflame.2020.09.007.

L. Ma, F. Nmira, and J.-L. Consalvi. Exploring subgrid-scale variance models in les of lab-scale methane fire plumes. *Combustion Theory and Modelling*, 25(1):44–72, 2021. doi: 10.1080/13647830.2020.1831078.

L. Ma, F. Nmira, and J.-L. Consalvi. Modelling extinction/re-ignition processes in fire plumes under oxygen-diluted conditions using flamelet tabulation approaches. *Combustion Theory and Modelling*, 26(4):613–636, 2022. doi: 10.1080/13647830.2022.2036373.

S. Mahmoud, G. Nathan, P. Medwell, B. Dally, and Z. Alwahabi. Simultaneous planar measurements of temperature and soot volume fraction in a turbulent non-premixed jet flame. *Proceedings of the Combustion Institute*, 35(2):1931–1938, 2015. doi: https://doi.org/10.1016/j.proci.2014.06.122.

D. L. Marchisio and R. O. Fox. Solution of population balance equations using the direct quadrature method of moments. *Journal of Aerosol Science*, 36(1):43–73, 2005. doi: https://doi.org/10.1016/j.jaerosci.2004.07.009.

J. W. Martin, S. Maurin, and K. Markus. Soot inception: Carbonaceous nanoparticle formation in flames. *Progress in Energy and Combustion Science*, 88:100956, 2022. doi: https://doi.org/10.1016/j.pecs.2021.100956.

B. J. McCaffrey. Purely buoyant diffusion flames: Some experimental results. NBSIR 79-1910, 1979.

C. Megaridis and R. Dobbins. Comparison of soot growth and oxidation in smoking and non–smoking ethylene diffusion flames. *Combustion Science and Technology*, 66(1-3):1–16, 1989. doi: 10.1080/00102208908947136.

R. Mehta, D. Haworth, and M. Modest. Composition pdf/photon monte carlo modeling of moderately sooting turbulent jet flames. *Combustion and Flame*, 157(5): 982–994, 2010. doi: https://doi.org/10.1016/j.combustflame.2009.11.009.

R. S. Mehta, M. F. Modest, and D. C. Haworth. Radiation characteristics and turbulence-radiation interactions in sooting turbulent jet flames. volume 1 of *Heat Transfer Summer Conference*, pages 77–91, 2009. doi: 10.1115/HT2009-88078.

H. Michelsen. Probing soot formation, chemical and physical evolution, and oxidation: A review of in situ diagnostic techniques and needs. *Proceedings of the Combustion Institute*, 36(1):717–735, 2017. doi: https://doi.org/10.1016/j.proci.2016.08.027.

P. Mitchell and M. Frenklach. Monte carlo simulation of soot aggregation with simultaneous surface growth-why primary particles appear spherical. *Symposium (International) on Combustion*, 27(1):1507–1514, 1998. doi: https://doi.org/10.1016/S0082-0784(98)80558-4.

M. Modest and D. Haworth. *Radiative Heat Transfer in Turbulent Combustion Systems*. 2016. doi: 10.1007/978-3-319-27291-7.

M. Modest and R. Riazzi. Assembly of full-spectrum k-distributions from a narrow-band database; effects of mixing gases, gases and nongray absorbing particles, and mixtures with nongray scatterers in nongray enclosures. *Journal of Quantitative Spectroscopy and Radiative Transfer*, 90(2):169–189, 2005. doi: https://doi.org/10.1016/j.jqsrt.2004.03.007.

M. F. Modest. *Radiative Heat Transfer, 3rd ed.; Academic Press: New York, NY, USA*. 2013.

P. Moin, K. Squires, W. Cabot, and S. Lee. A dynamic subgrid-scale model for compressible turbulence and scalar transport. *Physics of Fluids A: Fluid Dynamics*, 3(11): 2746–2757, 1991.

M. Mueller and H. Pitsch. Large eddy simulation subfilter modeling of soot-turbulence interactions. *Physics of Fluids*, 23(11):115104, 2011. doi: 10.1063/1.3657826.

M. Mueller and H. Pitsch. Les model for sooting turbulent nonpremixed flames. *Combustion and Flame*, 159:2166–2180, 2012. doi: 10.1016/j.combustflame.2012.02.001.

M. Mueller, G. Blanquart, and H. Pitsch. Modeling the oxidation-induced fragmentation of soot aggregates in laminar flames. *Proceedings of the Combustion Institute*, 33(1):667–674, 2011. doi: https://doi.org/10.1016/j.proci.2010.06.036.

M. E. Mueller, G. Blanquart, and H. Pitsch. Hybrid method of moments for modeling soot formation and growth. *Combustion and Flame*, 156(6):1143–1155, 2009a. doi: https://doi.org/10.1016/j.combustflame.2009.01.025.

M. E. Mueller, G. Blanquart, and H. Pitsch. A joint volume-surface model of soot aggregation with the method of moments. *Proceedings of the Combustion Institute*, 32(1):785–792, 2009b. doi: https://doi.org/10.1016/j.proci.2008.06.207.

J. Nagle and R. F. Strickland-Constable. Oxidation of carbon between 1000–2000 c. In *Proceedings of the fifth conference on carbon*, pages 154–164. Elsevier, 1962.

K. Netzell, H. Lehtiniemi, and F. Mauss. Calculating the soot particle size distribution function in turbulent diffusion flames using a sectional method. *Proceedings of the Combustion Institute*, 31:667–674, 2007. doi: 10.1016/j.proci.2006.08.081.

F. Nmira, J. Consalvi, R. Demarco, and L. Gay. Assessment of semi-empirical soot production models in c1–c3 axisymmetric laminar diffusion flames. *Fire Safety Journal*, 73:76–90, 2015. doi: https://doi.org/10.1016/j.firesaf.2015.03.005.

F. Nmira, L. Ma, and J. Consalvi. Influence of gas radiative property models on large eddy simulation of 1 m methanol pool fires. *Combustion and Flame*, 221:352–363, 2020. doi: https://doi.org/10.1016/j.combustflame.2020.08.005.

F. Nmira, L. Ma, and J. Consalvi. Assessment of subfilter-scale turbulence-radiation interaction in non-luminous pool fires. *Proceedings of the Combustion Institute*, 38 (3):4927–4934, 2021. doi: https://doi.org/10.1016/j.proci.2020.06.271.

M. Pabst, I. Letofsky-Papst, E. Bock, M. Moser, L. Dorfer, E. Egarter-Vigl, and F. Hofer. The tattoos of the tyrolean iceman: a light microscopical, ultrastructural and element analytical study. *Journal of Archaeological Science*, 36(10):2335–2341, 2009. doi: https://doi.org/10.1016/j.jas.2009.06.016.

J. Park, G. J. Nam, I. V. Tokmakov, and M. C. Lin. Experimental and theoretical studies of the phenyl radical reaction with propene. *The Journal of Physical Chemistry A*, 110(28):8729–8735, 2006. doi: 10.1021/jp062413d.

J. Park, I. V. Tokmakov, and M. C. Lin. Experimental and computational studies of the phenyl radical reaction with allene. *The Journal of Physical Chemistry A*, 111(29): 6881–6889, 2007. doi: 10.1021/jp0708502.

O. Park, R. A. Burns, O. R. Buxton, and N. T. Clemens. Mixture fraction, soot volume fraction, and velocity imaging in the soot-inception region of a turbulent non-premixed jet flame. *Proceedings of the Combustion Institute*, 36(1):899–907, 2017. doi: https://doi.org/10.1016/j.proci.2016.08.048.

N. Peters. Laminar diffusion flamelet models in non-premixed turbulent combustion. *Progress in Energy and Combustion Science*, 10(3):319–339, 1984. doi: https://doi.org/10.1016/0360-1285(84)90114-X.

H. Pitsch and N. Peters. A consistent flamelet formulation for non-premixed combustion considering differential diffusion effects. *Combustion and Flame*, 114(1):26–40, 1998. doi: https://doi.org/10.1016/S0010-2180(97)00278-2.

W. J. Pitz, N. P. Cernansky, F. L. Dryer, F. N. Egolfopoulos, J. T. Farrell, D. G. Friend, and H. Pitsch. Development of an experimental database and chemical kinetic models for surrogate gasoline fuels. In *SAE World Congress Exhibition*. SAE International, 2007. doi: https://doi.org/10.4271/2007-01-0175.

T. Poinsot and D. Veynante. *Theoretical and Numerical Combustion*. R.T. Edwards Inc., 2005.

D. P. Porfiriev, V. N. Azyazov, and A. M. Mebel. Conversion of acenaphthalene to phenalene via methylation: A theoretical study. *Combustion and Flame*, 213:302–313, 2020. doi: https://doi.org/10.1016/j.combustflame.2019.11.038.

R. Puri, T. Richardson, R. Santoro, and R. Dobbins. Aerosol dynamic processes of soot aggregates in a laminar ethene diffusion flame. *Combustion and Flame*, 92(3):320–333, 1993. doi: https://doi.org/10.1016/0010-2180(93)90043-3.

Z. Qin, V. V. Lissianski, H. Yang, W. C. Gardiner, S. G. Davis, and H. Wang. Combustion chemistry of propane: A case study of detailed reaction mechanism optimization. *Proceedings of the Combustion Institute*, 28(2):1663–1669, 2000. doi: https://doi.org/10.1016/S0082-0784(00)80565-2.

A. Raj. Pah growth assisted by five-membered ring: pyrene formation from acenaphthylene. *Combustion Theory and Modelling*, 26(1):91–109, 2022. doi: 10.1080/13647830.2021.1991596.

A. Raj, I. D. Prada, A. A. Amer, and S. H. Chung. A reaction mechanism for gasoline surrogate fuels for large polycyclic aromatic hydrocarbons. *Combustion and Flame*, 159(2):500–515, 2012. doi: https://doi.org/10.1016/j.combustflame.2011.08.011.

A. Raj, M. J. Al-Rashidi, S. H. Chung, and S. M. Sarathy. Pah growth initiated by propargyl addition: Mechanism development and computational kinetics. *The Journal of Physical Chemistry A*, 118(16):2865–2885, 2014. doi: 10.1021/jp410704b.

N. Ren, D. Zeng, K. V. Meredith, Y. Wang, and S. B. Dorofeev. Modeling of flame extinction/re-ignition in oxygen-reduced environments. *Proceedings of the Combustion Institute*, 37(3):3951–3958, 2019. doi: https://doi.org/10.1016/j.proci.2018.06.076.

X. Ren, D. Zeng, Y. Wang, G. Xiong, G. Agarwal, and M. Gollner. Temperature measurement of a turbulent buoyant ethylene diffusion flame using a dual-thermocouple technique. *Fire Safety Journal*, 120:103061, 2021. doi: https://doi.org/10.1016/j.firesaf.2020.103061.

H. Richter and J. B. Howard. Formation of polycyclic aromatic hydrocarbons and their growth to soot—a review of chemical reaction pathways. *Progress in Energy and Combustion Science*, 26(4):565–608, 2000. doi: https://doi.org/10.1016/S0360-1285(00)00009-5.

J. L. D. Ris, P. K. Wu, and G. Heskestad. Radiation fire modeling. *Proceedings of the Combustion Institute*, 28:2751–2759, 2000.

P. Rodrigues, B. Franzelli, R. Vicquelin, O. Gicquel, and N. Darabiha. Coupling an les approach and a soot sectional model for the study of sooting turbulent non-premixed flames. *Combustion and Flame*, 190:477–499, 2018. doi: https://doi.org/10.1016/j.combustflame.2017.12.009.

L. Rothman, I. Gordon, R. Barber, H. Dothe, R. Gamache, A. Goldman, V. Perevalov, S. Tashkun, and J. Tennyson. Hitemp, the high-temperature molecular spectroscopic database. *Journal of Quantitative Spectroscopy and Radiative Transfer*, 111(15):2139–2150, 2010. doi: https://doi.org/10.1016/j.jqsrt.2010.05.001.

S. Roy. *Aerosol-dynamics-based soot modeling of flames*. PhD thesis, Pennsylvania State University, 2014.

K. Rummel and P. Veh. Die strahlung leuchtender flammen. erster teil: Schrifttumsgrundlagen, arbeitshypothesen und vorversuche. *Archiv für das Eisenhüttenwesen*, 14(10):489–499, 1941.

H. Sabbah, M. Commodo, F. Picca, G. De Falco, P. Minutolo, A. D'Anna, and C. Joblin. Molecular content of nascent soot: Family characterization using two-step laser desorption laser ionization mass spectrometry. *Proceedings of the Combustion Institute*, 38(1):1241–1248, 2021. doi: https://doi.org/10.1016/j.proci.2020.09.022.

M. Saffaripour, P. Zabeti, S. Dworkin, Q. Zhang, H. Guo, F. Liu, G. Smallwood, and M. Thomson. A numerical and experimental study of a laminar sooting coflow jet-a1 diffusion flame. *Proceedings of the Combustion Institute*, 33(1):601–608, 2011. doi: https://doi.org/10.1016/j.proci.2010.06.068.

S. Salenbauch, A. Cuoci, A. Frassoldati, C. Saggese, T. Faravelli, and C. Hasse. Modeling soot formation in premixed flames using an extended conditional quadrature method of moments. *Combustion and Flame*, 162(6):2529–2543, 2015. doi: https://doi.org/10.1016/j.combustflame.2015.03.002.

G. Santo and M. Delichatsios. Effects of vitiated air on radiation and completeness of combustion in propane pool fires. *Fire Safety Journal*, 7(2):159–164, 1984. doi: https://doi.org/10.1016/0379-7112(84)90036-5.

G. Santo and F. Tamanini. Influence of oxygen depletion on the radiative properties of pmma flames. *Symposium (International) on Combustion*, 18(1):619–631, 1981. doi: https://doi.org/10.1016/S0082-0784(81)80067-7.

R. Santoro, H. Semerjian, and R. Dobbins. Soot particle measurements in diffusion flames. *Combustion and Flame*, 51:203–218, 1983. doi: https://doi.org/10.1016/0010-2180(83)90099-8.

R. J. Santoro, T. T. Yeh, J. J. Horvath, and H. G. Semerjian. The transport and growth of soot particles in laminar diffusion flames. *Combustion Science and Technology*, 53 (2-3):89–115, 1987. doi: 10.1080/00102208708947022.

M. Schiener and R. Lindstedt. Transported probability density function based modelling of soot particle size distributions in non-premixed turbulent jet flames. *Proceedings of the Combustion Institute*, 37(1):1049–1056, 2019. doi: https://doi.org/10.1016/j.proci.2018.06.088.

M. A. Schiener and R. P. Lindstedt. Joint-scalar transported pdf modelling of soot in a turbulent non-premixed natural gas flame. *Combustion Theory and Modelling*, 22 (6):1134–1175, 2018. doi: 10.1080/13647830.2018.1472391.

F. Schulz, M. Commodo, K. Kaiser, G. De Falco, P. Minutolo, G. Meyer, A. D'Anna, and L. Gross. Insights into incipient soot formation by atomic force microscopy. *Proceedings of the Combustion Institute*, 37(1):885–892, 2019. doi: https://doi.org/10.1016/j.proci.2018.06.100.

B. Shukla, A. Miyoshi, and M. Koshi. Role of methyl radicals in the growth of pahs. *Journal of the American Society for Mass Spectrometry*, 21(4):534–544, 2010. doi: https://doi.org/10.1016/j.jasms.2009.12.019.

K. Siegmann, H. Hepp, and K. Sattler. Reactive dimerization: A new pah growth mechanism in flames. *Combustion Science and Technology*, 109(1-6):165–181, 1995. doi: 10.1080/00102209508951900.

S. Sinha and A. Raj. Polycyclic aromatic hydrocarbon (pah) formation from benzyl radicals: a reaction kinetics study. *Physical Chemistry Chemical Physics*, 18:8120–8131, 2016. doi: 10.1039/C5CP06465A.

S. Sinha, R. K. Rahman, and A. Raj. On the role of resonantly stabilized radicals in polycyclic aromatic hydrocarbon (pah) formation: pyrene and fluoranthene formation from benzyl–indenyl addition. *Physical Chemistry Chemical Physics*, 19: 19262–19278, 2017. doi: 10.1039/C7CP02539D.

M. Smooke, C. McEnally, L. Pfefferle, R. Hall, and M. Colket. Computational and experimental study of soot formation in a coflow, laminar diffusion flame. *Combustion and Flame*, 117(1):117–139, 1999. doi: https://doi.org/10.1016/S0010-2180(98)00096-0.

M. Smooke, M. Long, B. Connelly, M. Colket, and R. Hall. Soot formation in laminar diffusion flames. *Combustion and Flame*, 143(4):613–628, 2005. doi: https://doi.org/10.1016/j.combustflame.2005.08.028.

V. P. Solovjov, B. W. Webb, and F. Andre. The rank correlated fsk model for prediction of gas radiation in non-uniform media, and its relationship to the rank correlated slw model. *Journal of Quantitative Spectroscopy and Radiative Transfer*, 214:120–132, 2018. doi: https://doi.org/10.1016/j.jqsrt.2018.04.026.

B. Sun, S. Rigopoulos, and A. Liu. Modelling of soot coalescence and aggregation with a two-population balance equation model and a conservative finite volume method. *Combustion and Flame*, 229:111382, 2021. doi: https://doi.org/10.1016/j.combustflame.2021.02.028.

Z. Sun, B. Dally, Z. Alwahabi, and G. Nathan. The effect of oxygen concentration in the co-flow of laminar ethylene diffusion flames. *Combustion and Flame*, 211:96–111, 2020. doi: https://doi.org/10.1016/j.combustflame.2019.09.023.

A. Tewarson. *Prediction of fire properties of materials. part 1: aliphatic and aromatic hydrocarbons and related polymers.* U.S. Department of Commerce, National Institute of Standards and Technology, 1986.

Thomson Lab. Soot formation in a laminar coflow diffusion flame, different processes involved in soot formation modeling, coflow flame and the computational domain, 2016. URL https://thomsonlab.mie.utoronto.ca/detailed-and-fundamental-modeling-of-soot-formation/.

L. Tian, M. Schiener, and R. Lindstedt. Fully coupled sectional modelling of soot particle dynamics in a turbulent diffusion flame. *Proceedings of the Combustion Institute*, 38(1):1365–1373, 2021. doi: https://doi.org/10.1016/j.proci.2020.06.093.

R. S. Tieszen, H. Pitsch, G. Blanquart, and S. Abarzhi. Toward the development of a les-sgs closure model for buoyant plumes. *Center for Turbulence Research Proceedings of the Summer Program 2004*, 2004. URL https://www.osti.gov/biblio/1144113.

S. R. Tieszen and L. A. Gritzo. Transport phenomena that affect heat transfer in fully turbulent fires. *Transport Phenonema in Fires*, page 25, 2008.

I. V. Tokmakov and M. C. Lin. Combined quantum chemical/rrkm-me computational study of the phenyl + ethylene, vinyl + benzene, and h + styrene reactions. *The Journal of Physical Chemistry A*, 108(45):9697–9714, 2004. doi: 10.1021/jp049950n.

I. V. Tokmakov, J. Park, and M. C. Lin. Experimental and computational studies of the phenyl radical reaction with propyne. *ChemPhysChem*, 6(10):2075–2085, 2005. doi: https://doi.org/10.1002/cphc.200500088.

K. Torres. *Numerical simulation and thermal radiation analysis in sooted flames : impact of radiative properties description*. Phd thesis, Paris-Saclay University, 2021.

U.S. Environmental Protection Agency. Setting and reviewing standards to control particulate matter (pm) pollution, 2023. URL https://www.epa.gov/pm-pollution/setting-and-reviewing-standards-control-particulate-matter-pm-pollution#standards.

S. Vandevelde, J. Brochier, B. Desachy, C. Petit, and L. Slimak. Sooted concretions: A new micro-chronological tool for high temporal resolution archaeology. *Quaternary International*, 474:103–118, 2018. doi: https://doi.org/10.1016/j.quaint.2017.10.031.

A. Veshkini, S. B. Dworkin, and M. J. Thomson. Understanding soot particle size evolution in laminar ethylene/air diffusion flames using novel soot coalescence models. *Combustion Theory and Modelling*, 20(4):707–734, 2016. doi: 10.1080/13647830.2016.1169319.

A. M. Vincitore and S. M. Senkan. Polycyclic aromatic hydrocarbon formation in opposed flow diffusion flames of ethane. *Combustion and Flame*, 114(1):259–266, 1998. doi: https://doi.org/10.1016/S0010-2180(97)00274-5.

A. Violi. Computational methods for soot formation, 2019. URL https://cefrc.princeton.edu/sites/g/files/toruqf1071/files/summerschool_slides_violi_v.pdf.

H. Wang. Formation of nascent soot and other condensed-phase materials in flames. *Proceedings of the Combustion Institute*, 33(1):41–67, 2011. doi: https://doi.org/10.1016/j.proci.2010.09.009.

H. Wang, D. Du, C. Sung, and C. Law. Experiments and numerical simulation on soot formation in opposed-jet ethylene diffusion flames. *Symposium (International) on Combustion*, 26(2):2359–2368, 1996. doi: https://doi.org/10.1016/S0082-0784(96)80065-8.

Y. Wang and S. Chung. Soot formation in laminar counterflow flames. *Progress in Energy and Combustion Science*, 74:152–238, 2019. doi: https://doi.org/10.1016/j.pecs.2019.05.003.

Y. Wang, P. Chatterjee, and J. L. de Ris. Large eddy simulation of fire plumes. *Proceedings of the Combustion Institute*, 33(2):2473–2480, 2011. doi: https://doi.org/10.1016/j.proci.2010.07.031.

Y. Wang, A. Raj, and S. Chung. A pah growth mechanism and synergistic effect on pah formation in counterflow diffusion flames. *Combustion and Flame*, 160:1667–1676, 2013. doi: 10.1016/j.combustflame.2013.03.013.

A. Y. Watson and P. A. Valberg. Carbon black and soot: Two different substances. *American Industrial Hygiene Association*, 62(2):218–228, 2001. doi: 10.1080/15298660108984625.

M. Wei, T. Zhang, S. Li, G. Guo, and D. Zhang. Naphthalene formation pathways from phenyl radical via vinyl radical (c2h3) and vinylacetylene (c4h4): computational studies on reaction mechanisms and kinetics. *Canadian Journal of Chemistry*, 95(8):816–823, 2017. doi: 10.1139/cjc-2017-0090.

J. Z. Wen, M. Thomson, S. Park, S. Rogak, and M. Lightstone. Study of soot growth in a plug flow reactor using a moving sectional model. *Proceedings of the Combustion Institute*, 30(1):1477–1484, 2005. doi: https://doi.org/10.1016/j.proci.2004.08.178.

J. White, E. Link, A. Trouvé, P. Sunderland, A. Marshall, J. Sheffel, M. Corn, M. Colket, M. Chaos, and H.-Z. Yu. Radiative emissions measurements from a buoyant, turbulent line flame under oxidizer-dilution quenching conditions. *Fire Safety J.*, 76:74–84, 2015.

J. White, E. Link, A. Trouvé, P. Sunderland, and A. Marshall. A general calorimetry framework for measurement of combustion efficiency in a suppressed turbulent line fire. *Fire Safety J.*, 92:164–170, 2017.

B. Wu, S. Roy, and X. Zhao. Detailed modeling of a small-scale turbulent pool fire. *Combustion and Flame*, 214:224–237, 2020. doi: https://doi.org/10.1016/j.combustflame.2019.12.034.

J. Y. Xing, C. P. T. Groth, and J. T. C. Hu. On the use of fractional-order quadrature-based moment closures for predicting soot formation in laminar flames. *Combustion Science and Technology*, 194(1):22–44, 2022. doi: 10.1080/00102202.2019.1678375.

G. Xiong, D. Zeng, P. P. Panda, and Y. Wang. Laser induced incandescence measurement of soot in ethylene buoyant turbulent diffusion flames under normal and reduced oxygen concentrations. *Combustion and Flame*, 230:111456, 2021. doi: https://doi.org/10.1016/j.combustflame.2021.111456.

F. Xu, P. Sunderland, and G. Faeth. Soot formation in laminar premixed ethylene/air flames at atmospheric pressure. *Combustion and Flame*, 108(4):471–493, 1997. doi: https://doi.org/10.1016/S0010-2180(96)00200-3.

F. Xu, A. El-Leathy, C. Kim, and G. Faeth. Soot surface oxidation in hydrocarbon/air diffusion flames at atmospheric pressure. *Combustion and Flame*, 132(1):43–57, 2003. doi: https://doi.org/10.1016/S0010-2180(02)00459-5.

Y. Xuan and G. Blanquart. A flamelet-based a priori analysis on the chemistry tabulation of polycyclic aromatic hydrocarbons in non-premixed flames. *Combustion and Flame*, 161(6):1516–1525, 2014. doi: https://doi.org/10.1016/j.combustflame.2013.11.022.

Y. Xuan and G. Blanquart. Effects of aromatic chemistry-turbulence interactions on soot formation in a turbulent non-premixed flame. *Proceedings of the Combustion Institute*, 35(2):1911–1919, 2015. doi: https://doi.org/10.1016/j.proci.2014.06.138.

S. Yang, J. K. Lew, and M. Mueller. Large eddy simulation of soot evolution in turbulent reacting flows: Presumed subfilter pdf model for soot–turbulence–chemistry interactions. *Combustion and Flame*, 209:200–213, 2019. doi: https://doi.org/10.1016/j.combustflame.2019.07.040.

D. Zeng and Y. Wang. Dependence of limiting oxygen index of buoyant turbulent non-premixed flame on fuel. In *26th Int. Colloquium on the Dynamics of Explosions and Reactive Systems, Boston*, 2017.

D. Zeng, P. Chatterjee, and Y. Wang. The effect of oxygen depletion on soot and thermal radiation in buoyant turbulent diffusion flames. *Proceedings of the Combustion Institute*, 37(1):825–832, 2019. doi: https://doi.org/10.1016/j.proci.2018.05.139.

H.-B. Zhang, D. Hou, C. K. Law, and X. You. Role of carbon-addition and hydrogen-migration reactions in soot surface growth. *The Journal of Physical Chemistry A*, 120(5):683–689, 2016. doi: 10.1021/acs.jpca.5b10306.

Q. Zhang. *Detailed Modeling of Soot Formation/Oxidation in Laminar Coflow Diffusion Flames*. PhD thesis, University of Toronto, 2010.

B. Öktem, M. P. Tolocka, B. Zhao, H. Wang, and M. V. Johnston. Chemical species associated with the early stage of soot growth in a laminar premixed ethylene–oxygen–argon flame. *Combustion and Flame*, 142(4):364–373, 2005. doi: https://doi.org/10.1016/j.combustflame.2005.03.016.

Annex

Article published in *Combustion Theory and Modelling*

Taylor & Francis
Taylor & Francis Group

Combustion Theory and Modelling

ISSN: (Print) (Online) Journal homepage: https://www.tandfonline.com/loi/tctm20

Flamelet/transported PDF simulations of ethylene/air jet turbulent non-premixed flame using a three-equation PAH-based soot production model

Fatiha Nmira, Antoine Bouffard & Jean-Louis Consalvi

To cite this article: Fatiha Nmira, Antoine Bouffard & Jean-Louis Consalvi (2023) Flamelet/transported PDF simulations of ethylene/air jet turbulent non-premixed flame using a three-equation PAH-based soot production model, Combustion Theory and Modelling, 27:6, 820-851, DOI: 10.1080/13647830.2023.2224755

To link to this article: https://doi.org/10.1080/13647830.2023.2224755

Combustion Theory and Modelling, 2023
Vol. 27, No. 6, 820–851, https://doi.org/10.1080/13647830.2023.2224755

Flamelet/transported PDF simulations of ethylene/air jet turbulent non-premixed flame using a three-equation PAH-based soot production model

Fatiha Nmira[a], Antoine Bouffard[a,b] and Jean-Louis Consalvi[b*]

[a]*Direction R&D EDF, Chatou Cedex, France* [b]*Aix-Marseille University, IUSTI UMR 7343, Marseille, France*

(*Received 2 December 2022; accepted 13 May 2023*)

This article reports flamelet/transported PDF (TPDF) simulations of the well-documented ethylene/air turbulent non-premixed jet flame investigated experimentally at Sandia. The transported PDF equation is solved with the Stochastic Eulerian Field method. The soot production is modelled by a validated three equation PAH-based soot model that predicts the mean soot aggregate properties at low computational time and includes a detailed description of the soot production processes. Gas and soot radiation is modelled using the rank-correlated full-spectrum k model. The turbulence/chemistry/soot production/radiation interactions are taken into account by means of the PDF method. Simulations are run by considering or not soot differential mixing. Based on recent conclusions drawn from Direct Numerical Simulations (Zhou et al., Proc. Combsut. Inst. 38 (2021) 2731–2739), soot differential mixing is modelled by neglecting soot mixing owing to sufficiently large mixing timescales. When soot differential mixing is considered, model predictions reproduce reasonably well the exhaustive set of experimental data, including flame structure, soot statistics and radiative outputs without adjusting parameters. In particular, the predictions demonstrate for the first time the capability of RANS/TPDF models to capture the soot intermittency. On the other hand, neglecting the soot differential mixing produces notable reductions in mean and fluctuating soot volume fraction and soot intermittency. Scatter plot analysis shows that the effects of soot differential mixing are more pronounced in regions of the mixture fraction space where soot surface growth and soot oxidation dominate the soot production, affecting these processes in a non-negligible manner. In an opposite way, soot nucleation and PAH condensation are much less significantly affected. Model results show also that disregarding soot differential mixing reduces the mean soot emission as well the soot emission turbulence/radiation interaction.

Keywords: Flamelet/transported PDF; three-equation soot model; soot differential mixing; radiative heat transfer; soot intermittency

Nomenclature

a	Stretching factor
A_s	Soot-specific surface area
C_u	Cunningham slip correction factor
D	Diffusivity or nozzle diameter
D_c	Fractal aggregate diameter
D_f	Soot aggregate fractal dimension

*Corresponding author. Email: jean-louis.consalvi@univ-amu.fr

d_p	Primary particle diameter
$d_{p,crit}$	Primary particle diameter delimiting the transition between coalescence and aggregation
f_s	Soot volume fraction
g	Full-spectrum k − g distribution
g_0	Quadrature point
G	Incident radiation
h	Enthalpy
I	Radiative intensity
Int	Soot intermittency index
J_j^α	Diffusive flux of the αth scalar in direction j
k	Turbulent kinetic energy or absorption coefficient variable
k_b	Boltzmann constant
K_e	Dimensionless extinction coefficient
K_n	Knudsen number
k_s	Soot absorptive index
m_c	Mass of a carbon atom
n	Number density function
N_{av}	Avogadro number
$N_{c,PAH}$	Number of carbon atom in the PAH
N_F	Number of Eulerian fields
n_p	Number of primary particles per aggregate
$N_{p,s}$	Number density of primary particle per unit mass mixture
n_s	Soot refractive index
N_s	Number density of soot aggregate per unit mass mixture
N_α	Number of scalars
p	Pressure
$\widetilde{P}_\phi$	Density-weighted probability density function
$\dot{q}_R''$	Radiative flux
r	Radial coordinate
T	Temperature
t	Time
u_i	*ith* velocity component
v	Soot aggregate volume
W_i	Molecular weights of species i
$\mathbf{x}$	Position vector
X_R	Enthalpy defect
Y_{PAH}	PAH mass fraction
Y_s	Soot mass fraction
Z	Mixture fraction
z	Axial coordinate
Z_{st}	Stoichiometric mixture fraction
$\widetilde{Z''^2}$	Mixture fraction variance

Greek symbols

α	Steric factor
β	Particle collision rate

χ	Scalar dissipation rate
χ_R	Radiant fraction
χ_{C_s}	Number of sites per particle surface
$\chi^{\star}_{C_s}$	Number of active sites per particle surface
ϵ	Dissipation of turbulent kinetic energy
η	Wavenumber
κ	Absorption coefficient
λ	Gas-mean free path
μ_t	Apparent turbulent viscosity
$\dot{\omega}$	Reaction rate
Ω	Solid angle
ϕ	Set of composition scalar
ψ	Sample-space variable corresponding to ϕ
ρ	Density
σ	Stefan–Boltzmann constant
σ_t	Apparent turbulent Prandtl or Schmidt number
τ_ϕ	Time-scale of scalar ϕ
φ	Set of variables affecting the absorption coefficient

Subscripts

A	Aggregation
b	Blackbody
C	Coalescence
$cond$	Condensation
$nucl$	nucleation
O_2	Oxidation by O_2
OH	Oxidation by OH
p	Planck
SG	Surface growth
p	Gas
s	Soot
R	Radiative
t	Turbulent
η	At wavenumber η

Superscripts

c	Continuum regime
f	Free molecular regime
fl	Flamelet
n	nth Eulerian field
$'$	Fluctuation about mean value
$''$	Fluctuation about density-weighted mean or filtered value

Operators

$\langle\phi\rangle$	Averaged value of ϕ
$\langle\underline{\phi}\|Z\rangle$	Conditional mean of ϕ at given Z
$\widetilde{\phi}$	Favre averaged value of ϕ Averaged value of ϕ

1. Introduction

The accurate prediction of soot is of great practical importance since soot is associated with strong radiative heat transfer in industrial processes or in fire hazard and also because soot emissions from combustion devices induce health and environmental issues. Soot formation is a complex not-fully understood process [1] whose modelling requires a gas-phase kinetic mechanism to predict soot precursors and oxidisers, a soot kinetic mechanism to account for the interactions between soot particles and surrounding gas and a soot particle dynamic model to describe the interactions between soot particles and predicts the soot aggregate properties. The prediction of soot formation and associated radiative heat transfer in turbulent reacting flows introduces additional difficulties related to turbulence/chemistry/soot formation/radiation interactions [2]. Direct Numerical Simulation (DNS) [3–6] showed that turbulence/chemistry/soot interactions are mainly due to, on the one hand, the very low diffusivity of soot, that is then transported differentially as compared to gaseous species, and, on the other hand, the slow soot (but also polycyclic aromatic hydrocarbon, PAH) chemistry that results in time scales significantly longer than those of typical combustion processes. The simulations of sooting turbulent flames have then to address several modelling issues related to the soot production model, the interactions between turbulence, chemistry and soot production and the modelling of radiation and its interaction with turbulence. The subsequent literature review will be restricted to the modelling of well-documented canonical laboratory-scale turbulent flames, as those investigated in the ISF workshop [7], in which most of the modelling efforts have been assessed.

A significant amount of modelling studies of turbulent flames is considered semi-empirical two equation soot production models based on acetylene as soot precursor [8–11]. Detailed PAH-based soot kinetics [12–21] were also considered coupled to either methods of moments or sectional methods for solving the population balance equation. In methods of moments [14–17], a finite number of moments of the number density function (NDF) are transported, introducing a closure problem as their source terms usually depend on some untransported moments. In addition, the method of moments do not give access to the NDF. On the other hand, sectional methods solve directly for the NDF and do not suffer from closure problems. Although sectional methods are highly CPU-time demanding and require the development of specific solution methods, it was demonstrated that they can be applied to the simulations of turbulent flames [18–24]. Alternatively, in view of industrial applications, Franzelli et al. [25] introduced a three-equation model that provides information on the local properties of soot aggregates at low computational times.

Simulations of turbulent non-premixed flames were mainly based on flamelet/presumed PDF approaches [14,16–18,26,27] or transported PDF methods [10,11,13,15,20–24,28–31] in both Large Eddy Simulation (LES) or Reynolds-Averaged Navier–Stokes simulation (RANS). Although LES provides advantages when large-scale motions are complex, soot production occurs at the unresolved scale and has to be completely modelled in both methods. Flamelet/presumed PDF modelling requires the design of a joint PDF of gas-phase parameters and soot-related quantities, which is a complex task owing to the subtle turbulence/chemistry/soot production interactions. DNS provided guidance to design such presumed PDF but these modelling efforts are still under development [14,16,17]. On the other hand, TPDF or hybrid flamelet/TPDF method provides a rigorous closure for the soot production rates [2,32] but requires the modelling of the unclosed micro-mixing due to molecular diffusion. In particular, the mixing timescales of gas-phase quantities and soot

moments may exhibit large difference, leading to differential mixing. Soot differential mixing was disregarded in a significant amount of studies by considering that soot moments are mixed as gas phase-related quantities such as chemical species or enthalpy [20–22,29,30]. In other modelling efforts [10,13,23,33], soot differential mixing was introduced in a simplified manner based on the argument that the mixing timescales of soot moments are sufficiently large to fully neglect soot mixing. Recent DNS confirmed the validity of this modelling approach [34]. A more sophisticated approach was applied by Tian et al. [24,31] by considering the modified Curl's model with differential diffusion, proposed by Zhou et al. [35], with mixing time scales being function of the soot mass. Very few studies have investigated the effects of soot differential mixing on the predictions of sooting flames. Fernandez et al. [33] used RANS/TPDF to investigate soot production and radiative heat transfer in a high-pressure turbulent spray flame by using a two-equation acetylene-based soot model and a photon Monte Carlo line-by-line model for spectral radiation. Their simulations showed a great impact of the differential soot mixing on the total soot mass in the vessel. Tian et al. [23,24,31] simulated atmospheric and high-pressure ethylene turbulent jet non-premixed flames with acetylene-based soot models coupled to a sectional method. Neglecting soot differential mixing was found to reduce significantly the fluctuations of soot volume fraction with more modest effects on the mean soot volume fraction.

Like other combustion-generated pollutants, the soot related processes, namely inception, surface growth, and oxidation, are kinetically controlled and highly sensitive to temperature and, in turn, to the modelling of radiative heat transfer. Detailed analysis of lab-scale non-premixed turbulent jet flames demonstrated that considering the commonly-used optically-thin approximation is not valid, inducing large discrepancies on mean and fluctuation of temperature as well as on soot volume fraction statistics [10,26,36]. The turbulence/radiation interaction (TRI) was also found to have a significant impact on predictions of lab-scale sooting turbulent non-premixed jet flames [13,26,28,37]. In particular, TRI was found to affect the mean radiative source term through competitive mechanisms, with enhancement mechanisms resulting from gas emission TRI and temperature self-correlation effects on soot emission and inhibiting mechanisms resulting from the negative correlation between soot volume fraction and temperature [26,37–39]. This negative correlation, first evidenced experimentally in the 90s by the group around Sivathanu and Gore [40,41], was found to play an important role on the prediction of mean soot emission [26,37] and to result from two physical mechanisms [38]. The first was dominant and related to the structure of non-premixed flame whereas the second was less important and related to the fuel sooting propensity.

The objective of this study is to twofold: (i) to assess the predictive capability of an RANS/flamelet/TPDF approach coupled to three-equation PAH-based soot model and an advanced radiation model and (ii) to provide a better understanding of the effects of soot differential mixing on soot production and radiative heat transfer. The well-documented ethylene turbulent non-premixed jet flame, investigated experimentally at Sandia [7,42], is used as target flame. The proposed three-equation model accounts for soot fractality at a low computational cost. As such, it represents a good candidate for engineering applications. The rank-correlated full-spectrum k-distribution (RCFSK) model [43] is considered as gas radiative property model and emission TRI is considered rigorously through the transported PDF. On the other hand, absorption TRI is neglected based on previous conclusions [36,44].

This article is organised as follows. The second section presents the numerical model whereas model predictions are compared with experimental measurements in Section 2.

Section 2 includes also an analysis of the effects of soot differential diffusion. The conclusions drawn in this work are then summarised in Section 3.

2. Numerical model

The computations reported here are carried out using an in-house CFD code based on the finite volume method. The mean continuity and momentum for a chemically reacting ideal-gas mixture are solved coupled to the standard $k-\epsilon$ model in cylindrical coordinates using a staggered grid. Following conventional practice (e.g. [45]), the value of $C_{\epsilon 1}$ has been increased from its standard value of 1.44–1.55 to obtain a more satisfactory spreading rate for the axisymmetric jet flames. The local thermochemical properties of the reactive flows are determined by a set of scalar variables, namely the mixture fraction, Z, the enthalpy defect, $X_R = h - h_{ad}$, the scalar dissipation rate, χ, the PAH mass fraction, Y_{PAH}, and the soot moments, ϕ_s. In sooting flames, the mixture fraction is no longer a conserved scalar as it is reduced due to soot formation and increased due to soot oxidation [46–48]. Mueller et al. introduced a source term in continuity, mixture fraction and energy equations to account for the PAH removal from the gas phase to form soot and modified the flamelet equations accordingly [14–17]. On the other hand, a significant amount of previous studies [10,11,18,49–51] have kept the conserved scalar formulation. This latter approach is considered in this study. The scalar dissipation rate is assumed to be statistically independent of the other scalars and its PDF is modelled by a Dirac function [10]. The corresponding one-point one-time composition joint PDF can be then expressed as $P(\psi, \chi; x, t) = P_\phi(\psi; x, t)\delta(\chi - \widetilde{\chi})$ where $\phi = \{Z, X_R, Y_{PAH}, \phi_s\}$ is the set of composition variable and $\widetilde{\chi} = C_\phi k/\epsilon \widetilde{Z''^2}$ with $C_\phi = 2$.

The submodels for gas-phase chemistry, soot production, radiation and turbulence/chemistry/soot/radiation interactions are detailed below and are summarised in Table 1.

2.1. *Flamelet model*

The non-adiabatic steady laminar flamelet model is used to obtain state relationships for density, species mass fraction, viscosity, diffusion coefficients, temperature, PAH production rates and gas-phase related part of soot production rates as unique functions of Z, χ and X_R, respectively. The flamelet library was generated by solving the governing equations of counterflow diffusion flames in the physical space at a series of specified strain rates using the FlameMaster code [52] and the KM2 mechanism [53] composed of 203 species and 1346 reactions. The radiative loss is introduced in the flamelet library using the methodology described by Carbonell et al. [54]. A specific transport equation is solved for the PAH mass fraction (see Section 2.2.3) [14]. It should be pointed out that the flamelet library was generated without including the effects of soot production through the consumption of PAH, acetylene, radical hydroxyl and oxygen. The errors induced by this approximation can be quantified from the work of Kalbhor and van Oijen [55] in ethylene counterflow diffusion flames at different strain rates. These authors compared different flamelet strategies with direct calculations. They considered explicitly the flamelet strategy used in the present work, i.e. disregarding the coupling between gas phase and soot in the flamelet library and considering it partially through the transport equation of the lumped PAH (see Section 2.2.3). They showed that this strategy leads to an overprediction of the peak of soot volume fraction by about 40 %. This error is significantly lower than that induced by the

Table 1. Summary of submodels and corresponding parameters used in the current study.

Quantity	Model	Parameters	References
Turbulent Reynolds stress	$k-\epsilon$	$C_\mu = 0.09$; $C_{\epsilon 1} = 1.55$ $\sigma_k = 1$; $\sigma_\epsilon = 1.3$	
Turbulent scalar fluxes	Gradient diffusion $+k-\epsilon$	$\sigma_t = 0.7$	standard
Gas-phase chemistry	KM2	none	[53]
Turbulence/chemistry Interaction	Flamelet/Transported PDF	Mixing model IEM, $C_\phi = 2$	standard
Soot Model			
Nucl.	A_4-based	$\gamma_{nucl} = 0.001$	Adjusted from lam. flames
SG and Ox. O_2	HACA	$\alpha = 0.2$; $\xi = 0.7$	Adjusted from lam. flames
Ox. OH		η_{OH} =0.1	[63]
PAH cond.	A_4-based	None	
Coagulation	$d_{p,crit}$	20 nm	Adjusted from lam. flames
Radiation Model			
Gas-phase rad. properties	RCFSK/HITEMP 2010	None	[43,76]
Soot rad. properties	Rayleigh theory Negligible scattering	soot index of refraction	[74]
Turbulence/soot Interaction	Transported PDF	No Soot mixing	[34]
Turbulence/rad. Interaction	Transported PDF	OTFA	

sensitivity of soot prediction to chemical mechanisms (cf. Refs. [16,56] for example) and than the uncertainties on soot measurements (see Section S2 of the supplementary materials), justifying its consideration. In addition, the parameters of the present soot production model have been adjusted from simulations of laminar coflow diffusion flames by considering this approximation (see Section 2.2.4) and were kept unchanged in the turbulent flame simulations.

2.2. *Soot production model*

2.2.1. *The three-equation formulation*

Soot particles are assumed to be fractal aggregates of fractal dimension D_f, volume v, and composed of n_p spherical primary particles of diameter d_p. The soot population is described by a bivariate number density function, $n(v, n_p; \mathbf{x}, t)$, expressed in terms of soot particle volume and number of primary particles per aggregate [57]. The distribution is assumed to be locally monodisperse, leading to [25]

$$n(v, n_p; \mathbf{x}, t) = [\rho N_s(\mathbf{x}, t)]\, \delta\,[v - v_s(\mathbf{x}, t)]\, \delta\left[n_p - n_{ps}(\mathbf{x}, t)\right] \tag{1}$$

where $[\rho N_s]$ is the number density of soot aggregate (kg/m^3) and v_s and n_{ps} are the local mean values of the soot aggregate volume and the number of primary particles per aggregate, respectively. Based on this assumption, the local mean soot aggregate properties can be deduced from the three first moments of the distribution, namely the number density

Table 2. Heterogeneous soot-gas surface reaction mechanism. $C_{s,n}$ represents the saturated sites with n carbon atoms and $C^{\star}_{s,n}$ the number of active sites present on the soot surface.

Reaction number	Reaction
R_1	$C_{s,n} + H \leftrightarrow C^{\star}_{s,n} + H_2$
R_2	$C_{s,n} + OH \leftrightarrow C^{\star}_{s,n} + H_2O$
R_3	$C^{\star}_{s,n} + H \rightarrow C_{s,n}$
$R_{4,a}$	$C^{\star}_{s,n} + C_2H_2 \rightarrow C_{s,n+2} + H$
$R_{4,b}$	$C^{\star}_{s,n} + C_2H_2 \rightarrow C^{\star}_{s,n+2} + \mathrm{H}$
R_5	$C^{\star}_{c,n} + O_2 \rightarrow 2CO + \text{products}$
R_6	$C_{s,n} + OH \rightarrow CO + \text{products}$

of soot aggregates, the number density of primary particles, $[\rho N_{ps}]$ (kg/m^3), and the soot volume fraction, $f_s = \rho Y_s/\rho_s$, where ρ, ρ_s and Y_s are the gas-phase density, the soot density and the soot mass fraction, respectively:

$$[\rho N_s] = \iint n(v, n_p; \mathbf{x}, t)\, \mathrm{d}v\, \mathrm{d}n_p \tag{2}$$

$$\left[\rho N_{ps}\right] = \iint n_p \cdot n(v, n_p; \mathbf{x}, t)\, \mathrm{d}v\, \mathrm{d}n_p = [\rho N_s]\, n_{ps} \tag{3}$$

$$f_s = \iint v \cdot n(v, n_p; \mathbf{x}, t)\, \mathrm{d}v\, \mathrm{d}n_p = [\rho N_s]\, v_s \tag{4}$$

The mean primary particle diameter is related to the mean soot volume by $v_s = n_{ps}\frac{\pi}{6}d_{ps}^3$. The soot-specific surface area, A_s, and the fractal aggregate collision diameter are then computed as

$$A_s = [\rho N_s]\, n_{ps} \pi d_{ps}^2 \tag{5}$$

$$D_c = d_{ps}\left(n_{ps}\right)^{1/D_f} \tag{6}$$

As a consequence, the three first moments, $\phi_s = \{N_s, N_{ps}, Y_s\}$, are governed by the following transport equations:

$$\rho\frac{DN_s}{Dt} = \dot{\omega}^{N_s} = \dot{\omega}^{N_s}_{nucl} - \dot{\omega}^{N_s}_{C/A} \tag{7}$$

$$\rho\frac{DN_{ps}}{Dt} = \dot{\omega}^{N_{ps}} = \dot{\omega}^{N_{ps}}_{nucl} - \dot{\omega}^{N_{ps}}_{C} \tag{8}$$

$$\rho\frac{DY_s}{Dt} = \dot{\omega}^{Y_s} = \dot{\omega}^{Y_s}_{nucl} + \dot{\omega}^{Y_s}_{SG} + \dot{\omega}^{Y_s}_{cond} - \dot{\omega}^{Y_s}_{OH} - \dot{\omega}^{Y_s}_{O_2} \tag{9}$$

where the subscripts *nucl*, *C/A*, *SG*, *cond*, *OH* and O_2 refer to the processes of nucleation, coalescence/aggregation, surface growth, condensation and oxidation by OH and O_2, respectively. It should be pointed out that soot molecular diffusion and thermophoresis are neglected.

2.2.2. *Soot kinetic model*

- *Nucleation*
  Nascent soot particles are presumed to nucleate through the dimerisation of two PAH species:

$$\mathrm{PAH} + \mathrm{PAH} \longrightarrow soot \tag{10}$$

  In this study, pyrene (A_4) is assumed to be the PAH species for soot inception [58,59] and the corresponding reaction rates can be computed from the gas kinetic theory [58,60]:

$$\dot{\omega}_{nucl}^{N_s} = \dot{\omega}_{nucl}^{N_{ps}} = 2.2\gamma_{nucl}\sqrt{\frac{4k_b\pi T}{N_{c,PAH}\cdot m_c}}\,[PAH]^2\,N_{av}^2 d_{PAH}^2 \tag{11}$$

$$\dot{\omega}_{nucl}^{Y_s} = 2N_{c,PAH}\cdot m_c\cdot\dot{\omega}_{nucl}^{N_s} \tag{12}$$

  The PAH diameter is given by $d_{PAH} = D_A\sqrt{2N_{c,PAH}/3}$ with $D_A = 1.395\sqrt{3}$Å.
- Surface growth and oxidation
  The surface growth and oxidation are assumed to follow the H-abstraction and acetylene addition (HACA) reaction sequence given by Appel et al. [59] and summarised in Table 2. These specific reactions include the surface activation and deactivation (R_1, R_2 and R_3). Surface growth occurs via two alternate reactions, R_{4a} and R_{4b}, that differ in the assumption whether the radical site on the soot surface is preserved after the reaction. According to Wang et al. [61], reaction R_{4a} is more adequate at the high temperature, high H atom concentration region of the soot window whereas reaction R_{4b} is needed to sustain surface growth toward the low temperature. The two reaction models represent the two limiting cases. In the present study, it is assumed that the role of surface radicals in the generation of soot lies within these extremes such that $k_{ss} = \xi k_{ss,cons} + (1-\xi)k_{ss,dep}$, with the indexes dep. and cons. representing depleted and conserved reactive sites, respectively [55]:

$$k_{ss,dep} = \frac{k_{1,f}[H] + k_{2,f}[OH]}{k_{1,r}[H_2] + k_{2,r}[H_2O] + k_{3,f}[H] + k_{4,f}[C_2H_2] + k_{5,f}[O_2]} \tag{13}$$

$$k_{ss,cons} = \frac{k_{1,f}[H] + k_{2,f}[OH]}{k_{1,r}[H_2] + k_{2,r}[H_2O] + k_{3,f}[H] + k_{5,f}[O_2]} \tag{14}$$

  The number density of radical sites on the soot surface is then expressed as $\chi_{C_s^\bullet} = k_{ss}\chi_{C_s}$ where $\chi_{C_s} = 2.3\cdot 10^{15}$ site/cm^2 is the number of sites per particle surface area and the HACA reaction rate is then computed as

$$\dot{\omega}_{SG}^{Y_s} = 2m_c\cdot\alpha\cdot k_{4,f}\cdot\chi_{C_s^\bullet}\cdot A_s \tag{15}$$

  where α is the steric factor. Similarly, the oxidation rate by O_2 is given by (see Table 2):

$$\dot{\omega}_{O_2}^{Y_s} = 2m_c\cdot\alpha\cdot k_{5,f}\cdot\chi_{C_s^\bullet}\cdot A_s \tag{16}$$

  The oxidation rate by OH is given by the model of Fenimore and Jones [62,63]:

$$\dot{\omega}_{OH}^{Y_s} = 1.27\cdot 10^3\frac{\eta_{OH}p_{OH}}{\sqrt{T}}A_s \tag{17}$$

- PAH condensation
  The source term due to PAH condensation is modelled as [59]

$$\dot{\omega}_{cond}^{Y_s} = 2.2 N_{c,PAH} \cdot m_c \cdot N_{av} \cdot [PAH] \sqrt{\frac{\pi k_b T}{2 N_{c,PAH} m_c}} \left(d_{PAH} + D_c\right)^2 [\rho N_s] \tag{18}$$

  where pyrene (A_4) is assumed to be the PAH associated with condensation.
- Coalescence/aggregation
  Particle–particle interactions are assumed to transit from the coalescence regime, where collision of liquid-like nascent soot particles leads to complete merging of the colliding particles into a spherical particle, to the aggregation regime, where the collision process leads to the creation of chain-like structures [23,29,64–66]. Consistently with Refs. [23,29,64–66], this transition is assumed to occur for a critical primary particle diameter, $d_{p,crit}$, at which the particles experience phase change and transfer from a liquid-like state into a solid state [23,29,64–66]. Several values of $d_{p,crit}$ were proposed in the literature. Smooke et al. [64] assumed 25 nm, Lindstedt et al. [23,29] selected 27.5 nm based on the works of Kazakov and Frenklach [67] whereas Veshkini et al. [65] considered 20 nm. Based on these assumptions, $\dot{\omega}_{C/A}^{N_s}$ and $\dot{\omega}_{C}^{N_{ps}}$ are given by

$$\dot{\omega}_{C}^{N_{ps}} = \begin{cases} \frac{1}{2}\beta_C \left[\rho N_{ps}\right]^2 & \text{if } d_p < d_{p,crit} \\ 0 & \text{if } d_p \geq d_{p,crit} \end{cases} \tag{19}$$

$$\dot{\omega}_{C/A}^{N_s} = \begin{cases} \dot{\omega}_{C}^{N_{ps}} & \text{if } d_p < d_{p,crit} \\ \frac{1}{2}\beta_A \left[\rho N_s\right]^2 & \text{if } d_p \geq d_{p,crit} \end{cases} \tag{20}$$

  The collision frequencies in both coalescence and aggregation regimes are computed as the harmonic average of the collision frequencies in the limits of the free molecular and continuum regimes:

$$\beta_C = \frac{\beta_C^f \beta_C^c}{\beta_C^f + \beta_C^c}; \quad \beta_C^f = 4 \times 2.2 \left(\frac{6 k_b T}{\rho_s}\right)^{1/2} d_p^{1/2}; \quad \beta_C^c = \frac{8 k_b T}{3 \mu_L} C_u \tag{21}$$

$$\beta_A = \frac{\beta_A^f \beta_A^c}{\beta_A^f + \beta_A^c}; \quad \beta_A^f = 4 \times 2.2 \left(\pi k_b T\right)^{1/2} \frac{D_c^2}{m_A^{1/2}}; \quad \beta_A^c = \frac{8 k_b T}{3 \mu_L} C_u \tag{22}$$

  where $C_u = 1 + 1.257 K_n$ is the Cunningham slip correction factor, $K_n = 2\lambda/d$ the Knudsen number with λ and d being the gas mean free path and the particle diameter, respectively, and m_A is the aggregate mass defined by $m_A = Y_s/N_s$ [29].

2.2.3. *PAH transport equation*

As PAHs are governed by a slow chemistry, a longer time is needed to respond to rapid changes in the flow field. As a result, the slower time scales of PAH formation compared to other gas-phase species often violate the fast chemistry assumption in flamelet-based models. To model the unsteady effects, an additional transport equation is solved for PAH

species [14]:

$$\rho \frac{DY_{PAH}}{Dt} = \frac{\partial}{\partial x_j}\left(\rho D_{PAH} \frac{\partial Y_{PAH}}{\partial x_j}\right) + \dot{\omega}_{PAH} \tag{23}$$

where D_{PAH} is the molecular diffusivity of the PAH species. The chemical source term is expressed as [14]

$$\dot{\omega}_{PAH} = \dot{\omega}_{PAH}^{fl,+} + \left(\frac{\dot{\omega}_{PAH}^{fl,-}}{Y_{PAH}^{fl}}\right) Y_{PAH} - \dot{\omega}_{nucl}^{Y_s} - \dot{\omega}_{cond}^{Y_s} \tag{24}$$

where $\dot{\omega}_{PAH}^{fl,+}$, $\dot{\omega}_{PAH}^{fl,-}$ represent the production and consumption rates of the PAH species. Assuming that all other species are in steady state, the chemical production rate is a constant $\dot{\omega}_{PAH}^{fl,+} \propto const$, and the chemical consumption rate is linearly dependent on $\dot{\omega}_{PAH}^{fl,-} \propto Y_{PAH}$. Therefore, $\dot{\omega}_{PAH}^{fl,+}$, $\dot{\omega}_{PAH}^{fl,-}$ can be tabulated a priori into the flamelet library using only steady-state flamelet solutions.

2.2.4. *Validation in laminar coflow ethylene flames*

The previously-described soot model is validated by simulating the well-documented laminar coflow ethylene diffusion flames, burning under air and oxygen-reduced conditions, investigated experimentally by Sun et al. [68]. The coflow diffusion flames were produced by a Santoro burner with a 10.5-mm diameter for the central fuel tube and ethylene was released with velocities of 3.98 cm/s. Soot volume fraction was measured using Laser-Induced Incandescence (LII) and a dimensionless extinction coefficient of $K_e = 4.9$ was used for the calibration. In addition, time-resolved laser-induced incandescence (TiRe-LII) technique was applied simultaneously with LII to measure the diameter of primary soot particles. The fuel burner dimension and injection velocity considered by Sun et al. [68] were very similar to those considered in the target ethylene/air non-premixed flame designed by Santoro et al. [69], allowing to complete this set of data by the number density of soot aggregate [70,71], the number density of primary particles [71,72], and the average number of primary particles per aggregate [71,73]. The model parameters were calibrated on the ethylene/air flame and were assessed on the flames burning in oxygen-reduced conditions. The sticking factor for nucleation, γ_{nucl}, and the surface growth parameters, α and ξ, were adjusted to match the experimental number densities of aggregates and primary particles and the radial soot volume fraction profiles along the height, respectively. On the other hand, the critical primary particle diameter, $d_{p,crit}$, was adjusted to reproduce at best the number of primary particles per aggregates as well as the primary particle diameter. The validation is reported in Section S1 of the Supplementary Materials and the values of the parameters are listed in Table 1.

2.3. *Radiation model*

The spectral coverage range considered in the present study is 50–25,000 cm^{-1}. Water vapour, carbon dioxide and soot are considered as the radiative participating species. Our investigation showed that the contributions of CO and C_2H_4 are negligible in the present flame. The soot absorption coefficient is computed from the Rayleigh theory with the correlations of Chang and Charalampopoulos [74] for the spectral refractive, n_s, and absorptive

indexes, k_s:

$$\kappa_{s,\eta} = C_\eta f_s \eta \quad \text{with } C_\eta = \frac{36\pi n_s k_s}{\left(n_s^2 + k_s^2 - 2\right)^2 + 4n_s^2 k_s^2} \tag{25}$$

The RCFSK model is used as gas radiative property model [43]. The full spectrum (FS) cumulative $k-g$ distribution function is defined as [2,75]

$$g\left(k, \varphi, T_p\right) = \frac{1}{I_b(T_p)} \int_0^\infty \mathrm{H}\left[k - \kappa_\eta\left(\varphi\right)\right] I_{b,\eta}(T)\, \mathrm{d}\eta \tag{26}$$

where $\varphi = \{x_{CO_2}, x_{H_2O}, f_s, T\}$ is an array of variables affecting the spectral absorption coefficient, κ_η. H is the Heaviside function, k a given value of the absorption coefficient, and $I_{b,\eta}(T_p)$ the spectral blackbody intensity at the Planck temperature T_p. Mixed FS $k-g$ distributions (for mixtures of H_2O, CO_2 and soot) are constructed from HITEMP 2010 [76] by using the procedure proposed by Modest and Riazzi [77]. The FS RTE is written as [2,75]

$$\frac{\mathrm{d}I_{g_0}}{\mathrm{d}s} = -k^\star\left(g_0\right) I_{g_0} + k^\star\left(g_0\right) a\left(g_0\right) I_b(T) \tag{27}$$

where g_0 corresponds to a quadrature-point of a 10-point Gauss–Legendre quadrature scheme and I_{g_0} is the radiative intensity at this quadrature point. $k^\star(g_0)$ and $a(g_0)$ are determined from the RCFSK scheme [43]:

$$g\left(k^\star, \varphi, T_p\right) = g_0 \tag{28}$$

$$a\left(g_0\right) = \frac{\partial g\left[k\left(g_0, \varphi, T_p\right), \varphi, T\right]}{\partial g_0} \tag{29}$$

The RCFSK preserves the total emission and, as such, is weakly dependent on T_p [43,78], which was set equal to 1500 K. The total radiative intensity, I, and the total incident radiation, G, are computed as $I = \int_0^1 I_{g_0}\, \mathrm{d}g_0$ and $G = \int_{4\pi} I\, \mathrm{d}\Omega$, respectively. The radiative source term is then calculated from the following equation:

$$\dot{Q}_R = -\nabla \cdot \dot{\mathbf{q}}''_{\mathbf{R}} = \int_0^1 k^\star G\, \mathrm{d}g_0 - \int_0^1 4\pi k^\star a I_b\, \mathrm{d}g_0 \tag{30}$$

The time-averaged FS RTE and divergence of the radiative flux are expressed as

$$\frac{\mathrm{d}\langle I_{g_0}\rangle}{\mathrm{d}s} = -\langle k^\star I_{g_0}\rangle + \langle k^\star a I_b(T)\rangle \tag{31}$$

$$\langle \dot{Q}_R\rangle = -\nabla \cdot \langle \dot{\mathbf{q}}''_{\mathbf{R}}\rangle = \int_0^1 \langle k^\star G\rangle\, \mathrm{d}g_0 - \int_0^1 4\pi \langle k^\star a I_b\rangle\, \mathrm{d}g_0 \tag{32}$$

The optically-thin fluctuation approximation (OTFA) is considered, assuming a weak correlation between the absorption coefficient and radiative intensity [2,75]. This approximation implies that $\langle k^\star I_{g_0}\rangle \approx \langle k^\star\rangle\langle I_{g_0}\rangle$ and $\langle k^\star G\rangle \approx \langle k^\star\rangle\langle G\rangle$. Previous studies showed that this approximation is valid for sooting flames at atmospheric pressure such as that considered in this study [13,44].

The RTE is solved by using the finite volume method [79] with an angular mesh with 12×16 control angles. A sensitivity analysis was performed during the course of Ref.

[10] where RANS/TPDF simulations of similar labs-scale sooting flames were reported, showing that this angular discretisation is sufficiently fine. Based on this analysis, this angular mesh was adopted in our subsequent modelling studies of lab-scale turbulent jet flames [11,37–39].

2.4. *Turbulence/chemistry/soot production/radiation interactions*

By using a gradient diffusion approach to model the turbulent transport, the density-weighted joint composition PDF transport equation can be written as follows [2,32]:

$$\frac{\partial\langle\rho\rangle\widetilde{P_\phi}}{\partial t}+\frac{\partial\langle\rho\rangle\widetilde{u_j}\widetilde{P_\phi}}{\partial x_j}=\frac{\partial}{\partial x_j}\left[\frac{\mu_t}{\sigma_t}\frac{\partial\widetilde{P_\phi}}{\partial x_j}\right]+\frac{\partial}{\partial\psi_\alpha}\left[\left\langle\frac{1}{\rho}\frac{\partial J_j^\alpha}{\partial x_j}\middle|\psi\right\rangle\langle\rho\rangle\widetilde{P_\phi}\right]$$
$$-\frac{\partial}{\partial\psi_\alpha}\left[\frac{\langle\rho\rangle\dot{\omega}_\alpha(\psi)\widetilde{P_\phi}}{\rho(\psi)}\right]-\delta_{\alpha(X_R)}\frac{\partial}{\partial\psi_\alpha}\left[\langle\rho\rangle\left\langle\frac{\dot{Q}_R}{\rho}\middle|\psi\right\rangle\widetilde{P_\phi}\right] \quad (33)$$

where $J_j^\alpha=-\rho D_\alpha(\partial\phi_\alpha/\partial x_j)$ is the diffusive flux of the αth scalars. $\delta_{\alpha(X_R)}$ indicates that the radiative source term appears only in the enthalpy defect equation. The emission term depends only on local scalars and, as such, can be closed 'exactly' whereas the OTFA is introduced to close the absorption term [10,32].

Two aspects of molecular diffusion have to be considered: the first is the spatial transport, which appears as gradient diffusion of the PDF in physical space, and the second is the micro-mixing process, which appears as transport in scalar space in the PDF [32]. This latter is modelled by the interaction by exchange with the mean (IEM) [32]:

$$\left\langle\frac{1}{\rho}\frac{\partial J_j^\alpha}{\partial x_j}\middle|\psi\right\rangle=\widetilde{\frac{1}{\rho}\frac{\partial J_j^\alpha}{\partial x_j}}+\left\langle\left(\frac{1}{\rho}\frac{\partial J_j^\alpha}{\partial x_j}\right)''\middle|\psi\right\rangle=\frac{1}{\langle\rho\rangle}\frac{\partial\langle J_j^\alpha\rangle}{\partial x_j}+\frac{1}{2}\frac{\left(\psi_\alpha-\widetilde{\phi_\alpha}\right)}{\tau_\phi} \quad (34)$$

where $\langle J_j^\alpha\rangle\approx\langle\rho\rangle\widetilde{D_\alpha}(\partial\widetilde{\phi_\alpha}/\partial x_j)$. The corresponding diffusion coefficient, D_α, is taken equal to the thermal diffusion coefficient for mixture fraction and enthalpy defect and to the diffusion coefficient of A_4 for Y_{PAH}. $\tau_\phi=k/(C_\phi\epsilon)$ is the mixing time-scale of ϕ with $C_\phi=2$ for Z, X_R, and Y_{PAH}. Soot particles are characterised by a much lower diffusivity as compared to gas-phase species and differential mixing for soot moments may be an important feature of turbulence/soot interactions. The differential mixing between soot and gas-phase related quantities can be quantified through the ratio of the mixing time scales, that scale with the square root of the ratio of molecular weights [24,31]:

$$\frac{\tau_g}{\tau_s}\propto\frac{D_s}{D_g}\propto\sqrt{\frac{W_g}{W_s}} \quad (35)$$

Recently, Tian et al. [24,31] considered the mass-based modified Curl's model with differential diffusion, developed in Ref. [34], in connection with a soot sectional model. In this model, Equation (35) was considered to determine the mixing time scale for each soot section. On the other hand, the molecular weight of soot particles is expected to be significantly higher than that of gas-phase species. This has led a significant number of authors [10,13,15,33] to consider the limit $W_s\to\infty$ (and then $\tau_s\to\infty$) that corresponds to neglect soot micro-mixing. The zero micro-mixing assumption was supported by DNS [34] and by recent RANS/TPDF simulations [31], confirming that differential mixing for

soot moments can be accurately incorporated by neglecting soot mixing. This approach is used in the present study by setting $C_\phi = 0$ for soot moments and the corresponding baseline simulations will be referred to as SDM (Soot Differential Mixing), hereafter. To quantify the impact of soot differential mixing on predictions, simulations have been also performed by considering that soot moments are mixed as gas-phase quantities ($C_\phi = 2$ for soot moments) and will be denoted to as No SDM (No Soot Differential Mixing), hereafter.

The Stochastic Eulerian Field method is used to solve the composition PDF transport equation [80,81] and details on implementation can be found in Ref. [10].

3. Results and discussion

3.1. *Experimental configuration and computational details*

The well-documented pure ethylene/air turbulent jet non-premixed flame investigated experimentally at Sandia [42] is simulated. Ethylene is injected at a velocity of 54.7 m/s through a tube with an inner diameter of 3.2 mm (D) and an outer diameter of 4.6 mm, leading to a Reynolds number of 20,000, a heat release rate of about 24 kW, and a visible flame length of about 0.83 m. The fuel injection tube is surrounded by another tube with an inner diameter 15.2 mm and an outer diameter 19.1 mm. A pilot plate, consisting of premixed ethylene/air flames at an equivalence ratio of 0.9, is situated in the annulus between the two tubes. The flow rate of the pilot mixture is adjusted to provide a heat release rate corresponding to 2% of that of the fuel jet. Finally, a coflow of air, injected at 0.6 m/s, surrounds the pilot flames. The exhaustive measurements included temperature from CARS [82], soot volume fraction from LII [7,83], OH and PAH signals from PLIF [7,83] and radiative intensity from radiometer measurements [7,83].

The computational domain was 0.1 m in the r-direction and 1.2 m in the z-direction. A non-uniform mesh of 128 (r) $\times$ 230(z) was considered. The number of stochastic fields was set to $N_F = 60$, consistently with previous studies [10,11]. The 64 pilot flames were modelled with a single concentric flow at temperature of 2296 K (corresponding to the experimental equivalence ratio) with a uniform mass flow rate adjusted to represent 2% of the flame heat release rate.

3.2. *Comparison of SDM simulations with experimental data*

Let us first compare the baseline simulation (SDM) with the experimental data in terms of flame structure, soot statistics and radiative intensity. Figure 1 shows that the model reproduces well the radial profiles of temperature and its fluctuations at different heights. Nevertheless, temperature fluctuations at the flame wings tend to be underpredicted, especially at $z = 0.42$ m. Similar discrepancies were reported in other studies [18,20,23].

Figures 2 and 3 display the predicted radial profiles of mean OH and PAH mole fractions, respectively, as well as the PLIF signals of these two species at different heights. The experimental data being non-quantitative, experimental and numerical results are here normalised by their respective maximum values for each height above the burner. Overall, a satisfactory agreement is observed, suggesting that the position of the oxidative species and PAH regions is well captured by the model. However, the predicted profile of PAH is wider than the measured one in the lower part of the flame (see Figure 3a). Similar discrepancies were reported by Sun and Rigopoulos [20] while using an LES/Population Balance Equation/TPDF formalism with the chemical mechanism of Blanquart et al. [84].

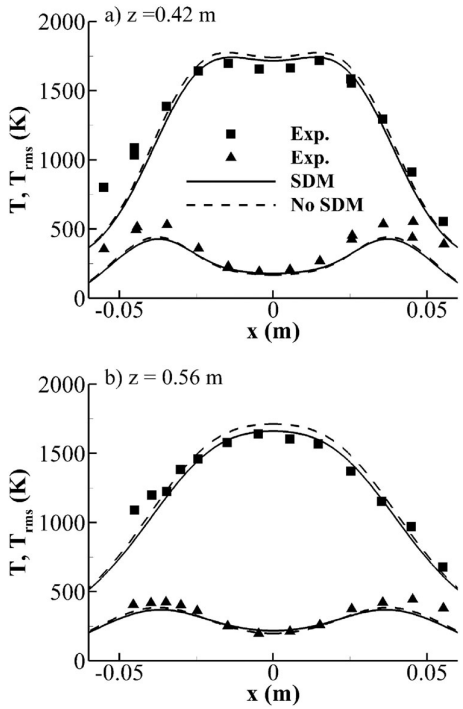

Figure 1. Radial profiles of mean and rms temperature at (a) $z = 0.42$ m and (b) $z = 0.56$ m. The experimental data are taken from Ref. [82].

Figures 4–6 show the axial and radial profiles of mean and rms soot volume fraction (SVF). LII signals are calibrated from extinction measurements. A consequence is that the SVF retrieved from these measurements is inversely proportional to the soot dimensionless extinction coefficient, K_e, used to interpret the extinction data [85]. As discussed in Section S2 of the supplementary materials, the values of K_e used in soot measurement studies exhibit a large scatter, which affects significantly the retrieved SVF. As an example, the present soot production model was calibrated from LII measurements in laminar coflow diffusion flames with $K_e = 4.9$ [68] (see Section 2.2.4) whereas the LII measurements for the Sandia flame were performed with $K_e = 9.3$ [83,85]. To account for these differences and provide a consistent comparison with the experimental data, the computed SVF reported for the Sandia flame was scaled by a factor of 4.9/9.3. Further discussion about the scaling is given in Section S2 of the supplementary materials. The raw computed data (without the scaling) for the SDM case are denoted as SDM in Figure 4 whereas the scaled data are denoted as SDM cor. The scaled mean and rms SVF reproduce reasonably well the experimental axial distributions, especially the feature that the fluctuations peak at a higher value than the mean (see Figure 4). In addition, the rates of increase and decrease of the axial mean and rms SVF in the soot growth and soot oxidation regions are consistent with the experiments. Nevertheless, mean and rms SVF are overestimated in the soot oxidation region, as also illustrated in Figures 5 and 6. Moreover the soot formation process is

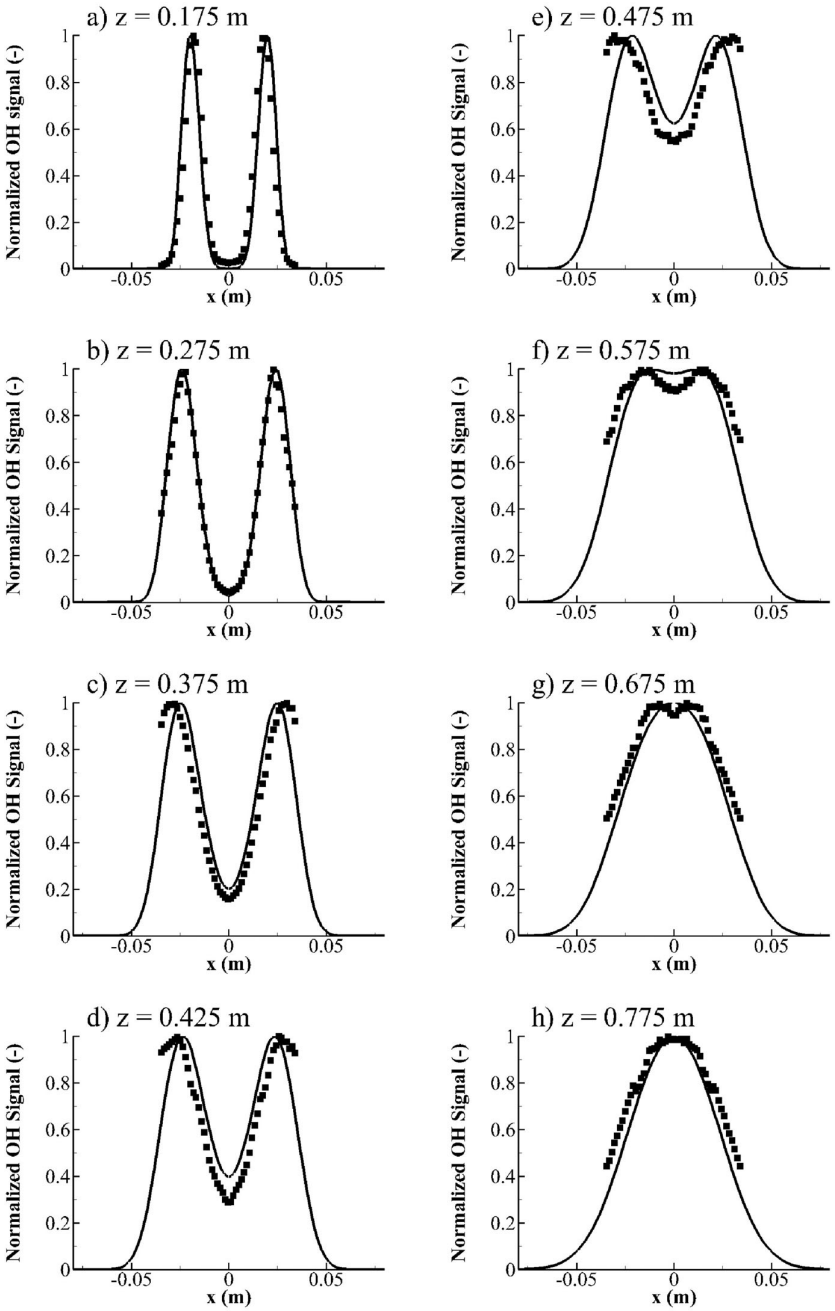

Figure 2. Radial profiles of OH normalised signals at different heights. The black line represents the SDM simulations whereas the black squares the experimental data taken from Refs. [7,83].

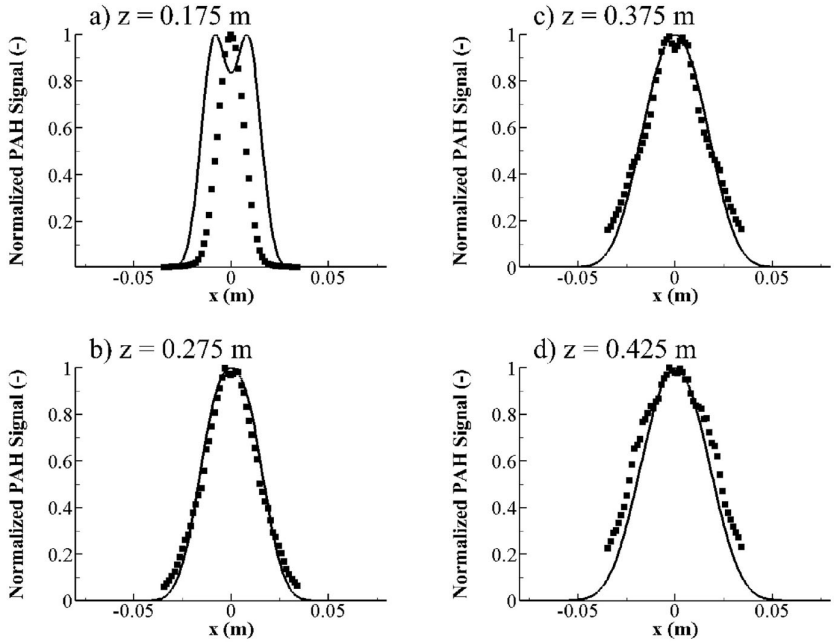

Figure 3. Radial profiles of PAH normalised signals at different heights. The black line represents the SDM simulations whereas the black squares the experimental data taken from Refs. [7,83].

predicted to start earlier as compared to the experiments, which may be attributed, at least partially, to the limit of detection of LII [21].

Figure 7 represents the evolution of the soot intermittency along the flame axis. The soot intermittency was defined experimentally as the probability at a given location to have SVF lower than a given threshold taken equal to 0.03 ppm [83]. The experimental soot intermittency remains approximately equal to 1 up to $z = 0.15$ m before decreasing to reach a minimum of 0.2 at $z = 0.4$ m, this location corresponding roughly to the axial peak of soot volume fraction (see Figure 4). Beyond the minimum the soot intermittency increases sharply to reach about 0.9 at $z = 0.7$ m. As discussed above and also in the Section S2 of the supplementary materials, the predicted intermittency was determined as the probability to have SVF lower than $f_{s,lim} = 0.03 \times 9.3/4.9$ ppm:

$$Int\,(r=0,z) = \lim_{T\to\infty} \frac{1}{T} \int_t^{t+T} \frac{N_P\left(r=0,z,t'\right)}{N_F}\,\mathrm{d}t' \tag{36}$$

where N_P is the number of stochastic fields for which $f_s^n(r=0,z,t) < f_{s,lim}$. The comparison reported in Figure 7 shows that the model predicts a more rapid decrease in intermittency in the soot growth region than the experiments, indicating a lower probability to find soot below the threshold. In addition, the minimum is predicted at $z = 0.25$ m, notably earlier than in the experiments. As pointed out by Huo et al. [21], a part of these discrepancies maybe attributed to the limit of detection of LII. A much better agreement between the model and the experiments is observed in the soot oxidation region

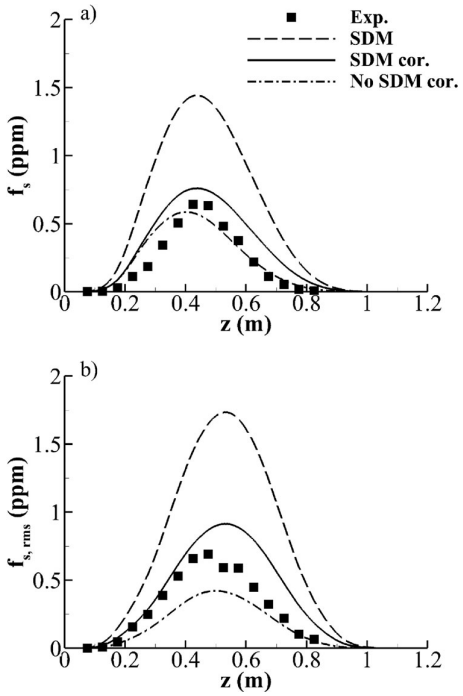

Figure 4. Axial profiles of mean and rms soot volume fraction. The experimental data are taken from Refs. [7,83].

($z \geq 0.4$ m). To the authors' best knowledge, this comparison demonstrates for the first time the capability of RANS/transported PDF approach to capture the soot intermittency.

Finally, Figure 8 shows the radial profiles of radiative intensity at different heights. Overall, model results agree reasonably well with the experiments. Predicted peaks of radiative intensities are on the whole within 20% of the experiments. A very good agreement is observed at $z = 0.16$ m and 0.72 m where the soot volume fractions is very low (see Figure 5). At the other heights, the overpredictions are consistent with those observed for SVF (see Figure 5).

3.3. *Effects of soot differential mixing*

Figures 4–8 show also the role of the soot differential mixing. Neglecting soot differential mixing reduces both mean and rms SVF, with the effects being more pronounced on rms. The experimental observation that fluctuations peak at a higher value than its mean is no longer verified. As a consequence, the lower SVF induces lower radiative loss, as illustrated in Figure 8. The overall reduction in radiative loss can be quantified through the radiant fraction, χ_R, that represents the part of the heat release rate radiated away from the flame. χ_R is equal to about 0.26 for the SDM simulation compared to about 0.23 for the No SDM simulation, explaining the higher mean temperature observed in the No SDM case, especially at $z = 0.56$ m (see Figure 1). In addition, Figure 7 shows that the No SDM

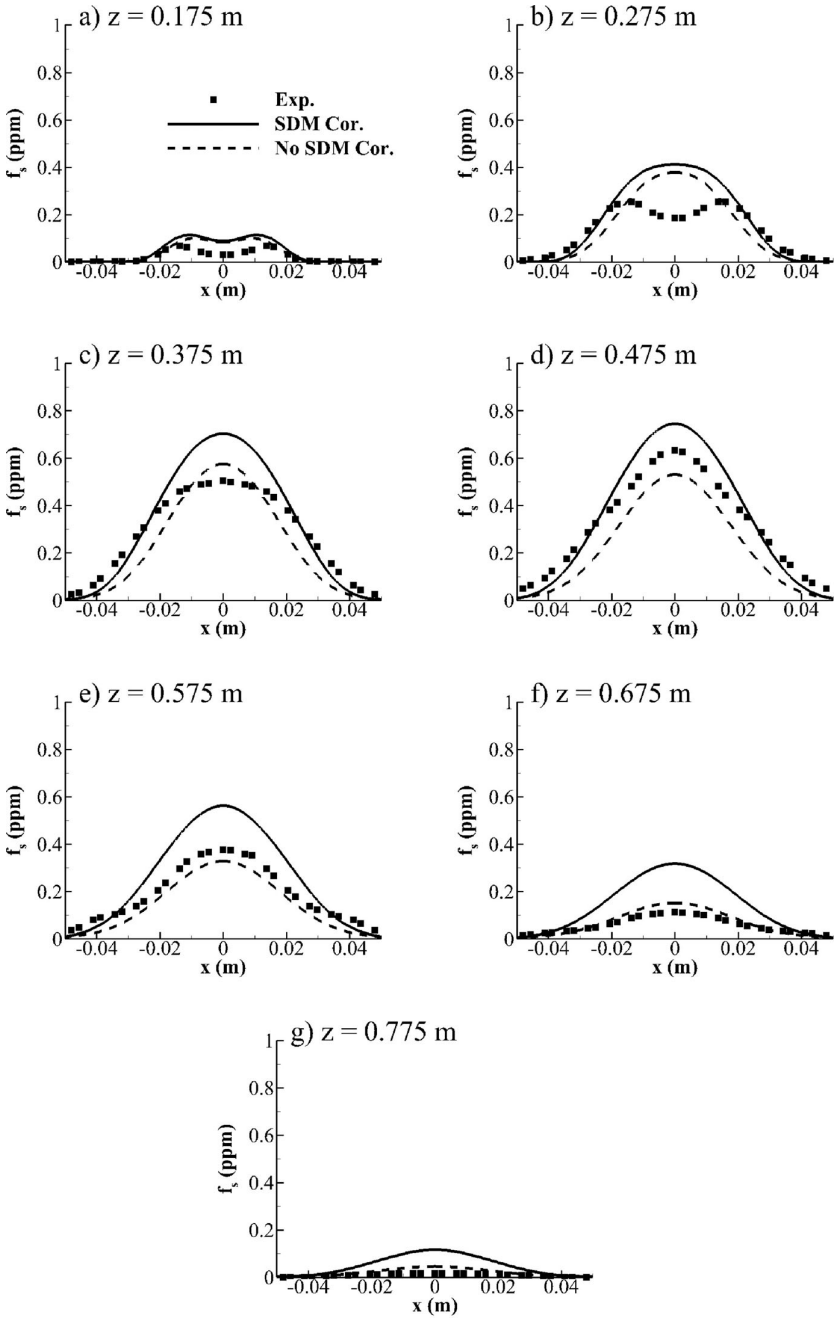

Figure 5. Radial profiles of mean soot volume fraction at different heights. The experimental data are taken from Refs. [7,83].

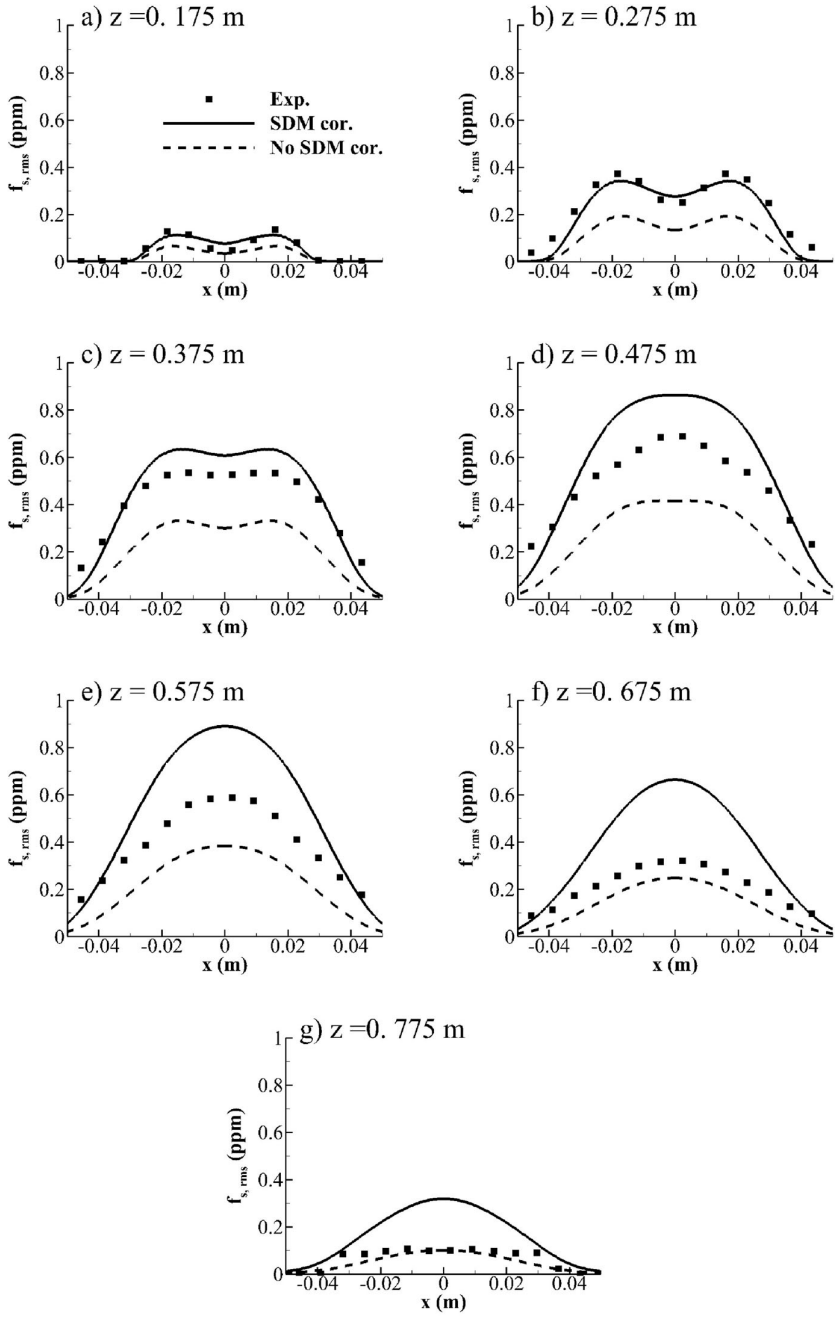

Figure 6. Radial profiles of rms soot volume fraction at different heights. The experimental data are taken from Refs. [7,83].

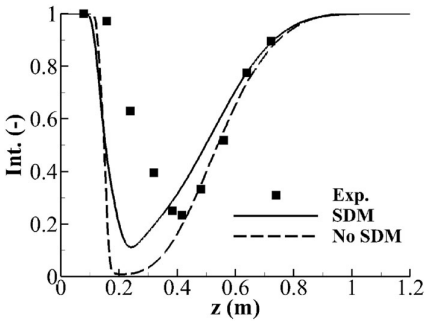

Figure 7. Axial profile of soot intermittency. The experimental data are taken from Ref. [83].

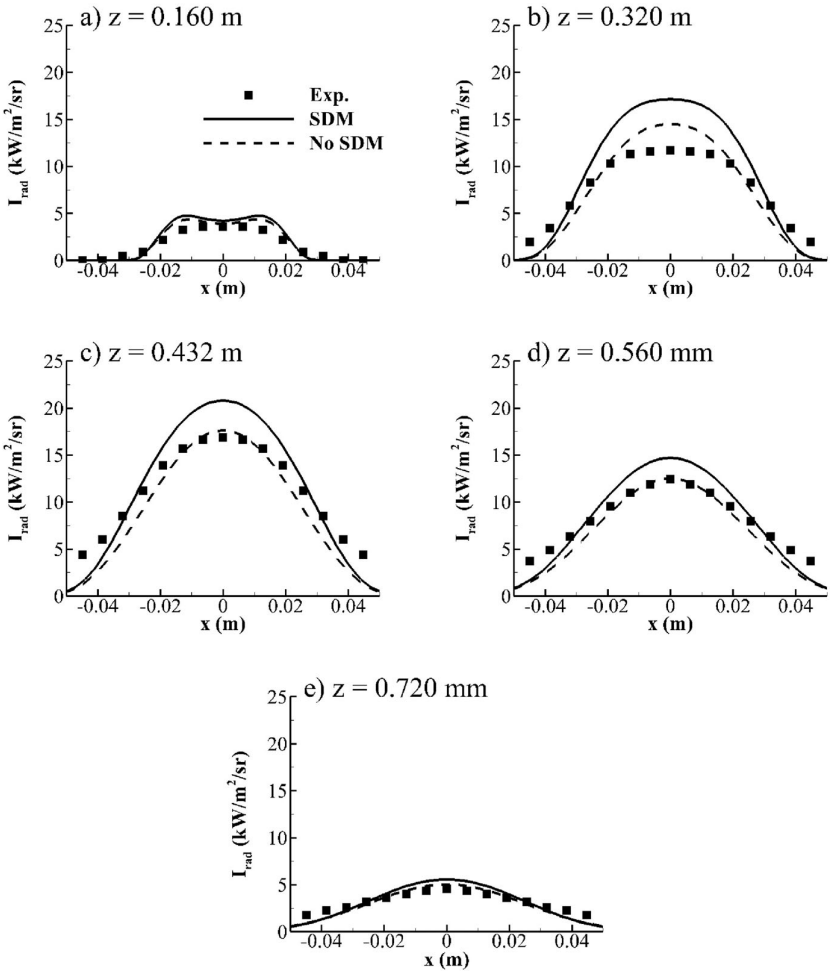

Figure 8. Radial profiles of radiative intensity at different heights. The experimental data are taken from Refs. [7,83].

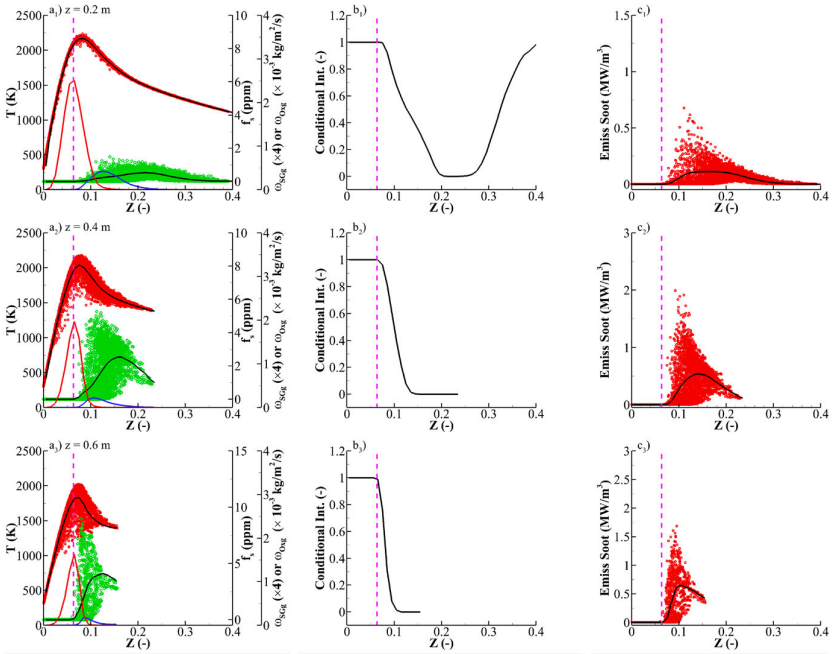

Figure 9. Mixture fraction-space analysis for the SDM case: (a) scatter plot of the temperature (red symbols) and soot volume fraction (green circles) in the mixture fraction space at different heights. The blue and red lines represent the conditional means of the gas-phase related part of soot surface growth and oxidation by OH, respectively. (b) Conditional mean of soot intermittency as a function of the mixture fraction. (c) Scatter plot of the soot emission term in the mixture fraction space. In all diagrams, the vertical pink dashed line represent the stoichiometric mixture fraction.

model predicts a lower soot intermittency over the entire sooting region, with more pronounced differences in the soot formation region ($z < 0.4$ m). The intermittency is defined as the possibility of finding particles below a given threshold. In the No SDM model, the sample-space soot volume fraction is allowed to relax toward its mean value. This reduces the probability to find stochastic fields below the threshold, thus leading to lower intermittency.

The origin of the differences between the SDM and No SDM simulations is analysed in the following sections from analysis of scatter plot in the mixture fraction space and soot production rates.

3.3.1. *Analysis in the mixture fraction space*

Figure 9 is the relative to the SDM case. The diagram (a) shows the scatter plot of temperature and SVF in the mixture fraction space along with the conditional mean of temperature, SVF and gas-phase related part of surface growth and soot oxidation rates at different heights. These two latter conditional means indicate the region of the mixture fraction space where the H/OH radical pool is located. For all the heights, the conditional mean of SVF follows the same trend as the mixture fraction decreases from the fuel richest region: it grows up a peak and, then, decreases to zero around the stoichiometric mixture fraction

($Z_{st} = 0.0635$) as soot particles are fully oxidised. The peak of conditional mean of SVF occurs at $Z \approx 0.24$ at $z = 0.2$ m and drifts toward Z_{st} as the height increases. A large scatter of SFV with respect to the conditional mean is observed with the level of dispersion increasing with the height. In addition, at all the heights, the level of dispersion increases as the mixture fraction evolves from the fuel richest mixtures to Z_{st}, being higher in the region where high level of H/OH radicals are encountered. The diagram (b) shows the conditional soot intermittency as a function of the mixture fraction. The presence of an intermittent behaviour in the fuel richest mixture fractions is observed only at $z = 0.2$ m. In an opposite way, for the higher heights, instantaneous SVF are always higher than the threshold down to region where the presence of H/OH radicals starts to become important. Below this location, the conditional intermittency increases to reach 1 around the stoichiometry. As discussed above, soot particles do not cross the stoichiometric mixture fraction as they are fully oxidised before and, as a consequence, no soot is observed below Z_{st}. The diagram (c) displays the scatter plots of the soot radiative emission term in the mixture fraction space. The soot radiative emission is defined as $S_{emi} = \kappa_{p,s} I_b(T)$ where $\kappa_{p,s}$ is the Planck mean soot absorption coefficient. S_{emi} increases linearly with f_s and with the temperature at an exponent of about 5 ($S_{emi} \propto f_s T^5$) [75]. As a consequence, the high instantaneous values of soot emission are mainly located in the region between the peak of the conditional mean of SVF and Z_{st} where the highest temperatures are encountered. The large scatter in SVF induces a large scatter in the soot emission term. This results, in turn, in lower instantaneous temperature owing to radiative loss, as observed in Figure 9(a).

Figure 10 shows the same results as Figure 9 for the No SDM case and the comparison of these two figures highlights the effects induced by neglecting soot differential mixing. These differences explain those observed in Figures 4– 7:

- The comparison of the diagrams (a) shows clearly that the scatter of SVF with respect to the conditional mean is significantly lower when soot differential mixing is neglected. This becomes more and more pronounced as the mixture fraction decreases from fuel richest mixtures down to Z_{st} and as the height above the burner increases. In addition, a detailed examination of the profiles shows that the conditional mean of SVF is on the whole lower in the No SDM calculation at all heights.
- The comparison of diagrams (a) shows also that, contrary to the SDM simulation, soot is observed in the fuel lean side of the flame from $z = 0.4$ m when soot differential mixing is neglected. Figure 10 suggests that the non-oxidised soot remains in fuel lean mixtures downstream (e.g. at $z = 0.6$ m). A careful observation of the scatter plots reported by Tian et al. [31] for the Sandia ethylene flame shows that, although they predict the presence of non-oxidised soot in the fuel lean side of the flame for both SDM and no SDM cases, the quantity of non-oxidised soot is significantly higher in the No SDM case. These results support the present observation that disregarding soot differential mixing favours the soot emission.
- The comparison of diagrams (b) shows that the conditional soot intermittency is lower in the No SDM case. In this latter case, it remains equal to zero down to the H/OH radical region even at $z = 0.2$ m and the transition to 1 is on the whole more abrupt than in the SDM case.
- The comparison of diagrams (c) shows that, consistently with the lower dispersion of SVF around the conditional mean, the scatter plot of the soot emission term presents also a lower dispersion with respect to its conditional mean in the No SDM case.

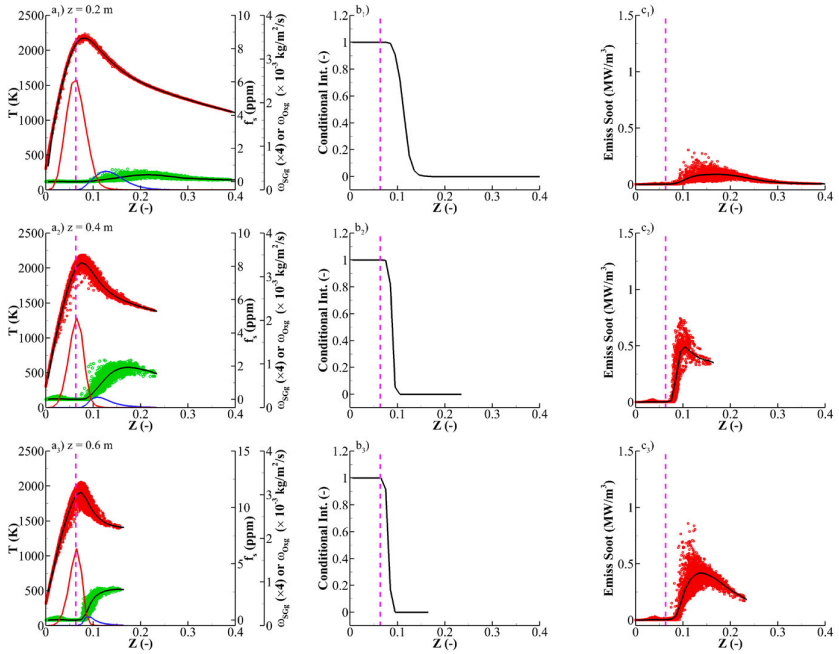

Figure 10. Mixture fraction-space analysis for the No SDM case: (a) scatter plot of the temperature (red symbols) and soot volume fraction (green circles) in the mixture fraction space at different heights. The blue and red lines represent the conditional means of the gas-phase related part of soot surface growth and oxidation by OH, respectively. The back lines represent the conditional means. The vertical pink dashed line represent the mixture fraction stoichiometry. (b) Conditional mean of soot intermittency as a function of the mixture fraction. (c) Scatter plot of the soot emission term in the mixture fraction space. In all diagrams, the vertical pink dashed line represents the stoichiometric mixture fraction.

3.3.2. *Soot production reaction rates*

Figure 11 shows the fields of soot mass production rates. This figure is completed by Figure 12 that displays the axial evolution of the radially-integrated soot mass production rates. Only the soot oxidation by OH is reported as the soot oxidation by O_2 was found to be significantly lower. Let us to discuss first the SDM results. Figure 12 shows that soot production is initiated by nucleation followed by PAH condensation and, finally, surface growth. As expected, the production of mass by nucleation is negligible. The formation rate of PAH condensation is locally significantly higher than that of surface growth (see Figure 11). However, the field of surface growth rate is wider with high values on the wings, which explains that the differences on the radially-integrated reaction rates are much less pronounced (see Figure 12).

As discussed in the previous section, neglecting soot differential mixing produces its most important effects in the region where surface growth and oxidation occur. As a consequence, contrary to nucleation and PAH condensation, soot surface growth and oxidation rates are affected in a non-negligible manner when neglecting soot differential mixing, with surface growth being reduced and soot oxidation being enhanced (see Figures 11

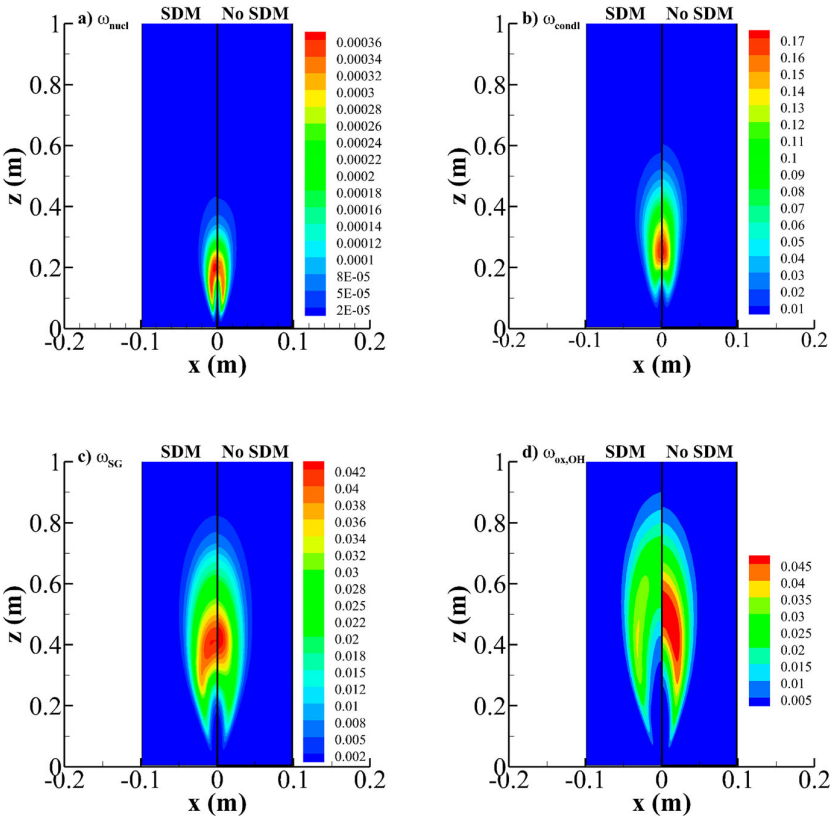

Figure 11. Fields of soot production rates in (kg/m^3/s) for: (a) nucleation, (b) PAH condensation, (c) surface growth and (d) oxidation by OH. On each diagram, the left panel refers to SDM simulation whereas the right panel refers to No SDM simulation.

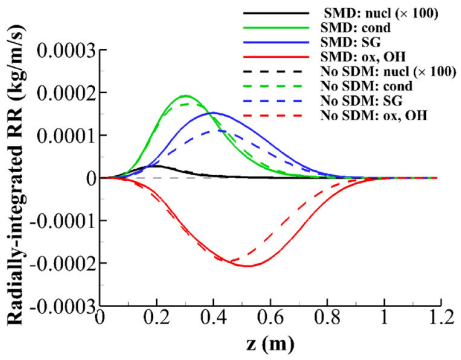

Figure 12. Effects of soot differential mixing on the radially-integrated soot reaction rates.

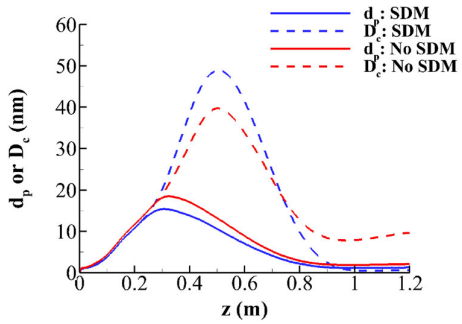

Figure 13. Effects of soot differential mixing on the axial distribution of primary particle diameters (d_p, sold lines) and fractal soot fractal aggregate diameters (D_c, dashed lines) for both SDM and No SDM simulations.

and 12). This explains the lower SVF observed in the No SDM case, especially along the flame wings and beyond $z = 0.4$ m where these processes dominate the soot production (see Figures 4 and 5). Figure 13 displays the axial evolution of the mean primary particle diameter (d_{ps}, solid lines) and the mean fractal aggregate diameter (D_c, dashed lines) for both SDM (blue lines) and No SDM (red lines) cases. It can be observed that in both SMD and No SDM simulations, d_{ps} increases first to reach a peak at about $z = 0.3$ m before decreasing beyond this location. Neglecting soot differential mixing increases noticeably d_{ps} for z ranging from about 0.25 m to 0.7 m. The largest differences are observed at the peaks that are of about 15.25 and 18.50 nm for the SDM and no SDM calculations, respectively. For both models, d_{ps} and D_c exhibit very close values for $z < 0.25$ m, showing that no notable aggregation occurs in this region. The aggregation process starts beyond $z = 0.25$ m and D_c reaches a peak at about $z = 0.5$ m, before decreasing. From Equation (6) and the lower value of d_{ps} observed in the SDM simulation, it can be deduced that the higher values of D_c for $z \in [0.25\,m, 0.7\,m]$ in this simulation results from an enhancement of the number of primary particles per aggregate, n_{ps}. It is also interesting to note that D_c exhibits a different behaviour at the flame tip in SDM and No SDM simulations. It tends toward zero in the SDM case, in line with the full oxidation of the soot particle in this case, whereas it reaches a plateau outside the flame in the No SDM case. This confirms that neglecting soot differential mixing favours the soot emission process.

3.3.3. *Mean soot radiative emission*

This section investigates the effects of soot differential mixing on the mean soot radiative emission that can be expressed as

$$\langle S_{emi} \rangle = 4\sigma \langle \kappa_{ps} I_b (T) \rangle \tag{37}$$

By introducing $\kappa_{ps} = 3.83 \frac{C_0 f_s T}{C_2}$, where C_2 is the second Planck constant [75], and $I_b(T) = \frac{\sigma T^4}{\pi}$ and considering only the lowest order terms in the truncation series, Equation (37)

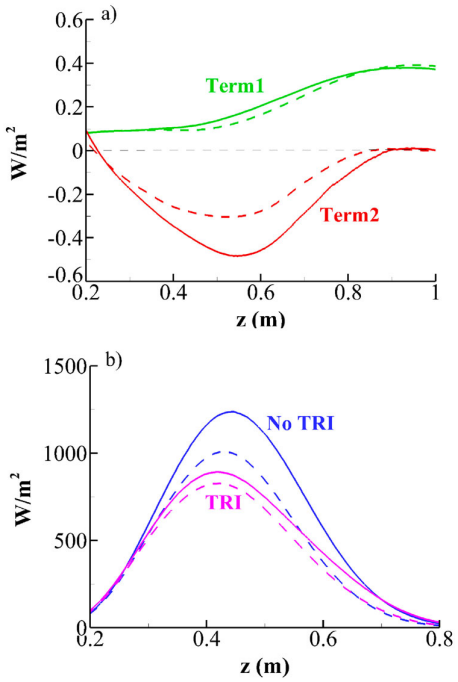

Figure 14. Axial evolution of the terms involved in the mean soot radiative emission. The solid and dashed lines refer to the SDM and No SDM simulations, respectively.

can be re-expressed as [26]

$$\langle S_{emi}\rangle \approx \underbrace{C\,\sigma\,\langle f_s\rangle\langle T^5\rangle}_{\text{NoTRI}}\underbrace{\left[1+\underbrace{10\frac{\langle T'^2\rangle}{\langle T\rangle^2}}_{\text{Term1}}+\underbrace{5\frac{\langle f_s'T'\rangle}{\langle T\rangle\langle f_s\rangle}}_{\text{Term2}}\right]}_{\text{Total}} \tag{38}$$

where $C=\frac{15.82C_0}{C_2}$. Term1 and Term2 represent the effects of TRI on the mean soot emission term. Term1 represents the effects of the temperature self-correlation and enhances mean soot emission. Term2 is directly related to the correlation between temperature and SVF that is strongly negative in the soot oxidation region where soot emission is the most important. A consequence is that this term balances Term1 and contributes to reduce mean soot emission. Figure 14(a) compares these two terms along the flame axis. It shows that Term2 dominates for both SDM and No SDM simulations, except in the upper part of the flame. On the other hand, neglecting soot differential mixing tends to decrease slightly Term1 due to the conjugated effects of lower temperature fluctuations and higher mean temperature (see Figure 1). This shows that neglecting soot differential mixing contributes to reduce the temperature-based turbulence intensity. In an apposite way, disregarding soot differential mixing increases significantly Term2.

Figure 14(b) shows the evolution of the No TRI and total terms of Equation (38) along the flame axis. The comparison of these two terms quantifies the effects of soot emission TRI. When TRI is neglected (blue line), the mean soot emission predicted by the SDM simulation is significantly higher than that predicted by the No SDM case owing to higher mean SVF. In both SDM and No SDM simulations, the total term is lower than the No TRI term, showing that soot emission TRI tends mainly to reduce mean soot emission as Term2 dominates over a significant part of the flame (see Figure 14a). This reduction is lower when soot differential mixing is neglected as Term2 is significantly less negative.

4. Conclusion

The Sandia ethylene turbulent non-premixed jet flame has been simulated by using an RANS/flamelet/transported PDF method coupled with a three-equation PAH-based soot production model previously validated in laminar coflow diffusion flames and a state-of-the art radiation model. Simulations have been run with and without considering soot differential mixing. Model predictions have been compared with the complete set of experimental data including mean and rms temperature, OH and PAH PLIF signals, mean and rms soot volume fraction, soot intermittency and radiative intensity. The following conclusions can be drawn:

- Model predictions when considering soot differential mixing reproduce reasonably well the experimental data without adjusting parameters of the soot model. In particular, it reproduces the experimental observation that soot fluctuations are higher than mean values.
- The simulations demonstrate for the first time the capability of RANS/transported PDF approaches to capture the soot intermittency.
- Consistently with the conclusions drawn by Tian et al. [23,24,31], considering soot differential mixing enhances the rms of soot volume fraction. This is found to affect also the soot intermittency, the mean soot volume fraction and soot particle sizes. Scatter plot analysis in the mixture fraction space shows that these effects are much more pronounced in regions where soot surface growth and soot oxidation dominate the soot production, affecting these processes in a non-negligible manner. In an opposite way, the effects on soot inception and PAH condensation are less important.
- Disregarding soot differential mixing was also found to reduce mean soot emission as well as the effects of turbulence on mean soot emission.

Acknowledgments

JLC wishes to express his gratitude to Electricité de France (EDF) for financial supports.

Disclosure statement

No potential conflict of interest was reported by the author(s).

Supplemental data

Supplemental data for this article can be accessed online at http://dx.doi.org/10.1080/13647830.2023.2224755.

References

[1] J.W. Martin, M. Salamanca, and M. Kraft, *Soot inception: carbonaceous nanoparticle formation in flames*, Prog. Ener. Combust. Sci. 88 (2022), p. 100956.

[2] M.F. Modest and D.C. Haworth, *Radiative Heat Transfer in Turbulent Combustion Systems*, Springer, Heidelberg, 2016.

[3] D.O. Lignell, J.H. Chen, and P.J. Smith, *Three-dimensional direct numerical simulation of soot formation and transport in a temporally evolving nonpremixed ethylene jet flame*, Combust. Flame 155 (2008), pp. 316–333.

[4] F. Bisetti, G. Blanquart, M.E. Mueller, and H. Pitsch, *On the formation and early evolution of soot in turbulent nonpremixed flames*, Combust. Flame 159 (2012), pp. 317–335.

[5] A. Attili, F. Bisetti, M.E. Mueller, and H. Pitsch, *Formation, growth, and transport of soot in a three-dimensional turbulent non-premixed jet flame*, Combust. Flame 161 (2014), pp. 1849–1865.

[6] A. Attili, F. Bisetti, M.E. Mueller, and H. Pitsch, *Damkholer number effects on soot formation and growth in turbulent nonpremixed flames*, Proc. Combust. Inst. 35 (2015), pp. 1215–1223.

[7] *International Sooting Flame (ISF) Workshop*, 2018, available at https://www.adelaide.edu.au/cet/isfworkshop.

[8] Yunardi, R.M. Woolley, and M. Fairweather, *Conditional moment closure prediction of soot formation in turbulent, nonpremixed ethylene flames*, Combust. Flame 152 (2008), pp. 360–376.

[9] S. Navarro-Martinez and S. Rigopoulos, *Differential diffusion modelling in les with rcce-reduced chemistry*, Flow Turbul. Combust 89 (2012), pp. 311–328.

[10] J.L. Consalvi, F. Nmira, and D. Burot, *Simulations of sooting turbulent jet flames using a hybrid flamelet/stochastic eulerian field method*, Combust. Theor. Model. 20 (2016), pp. 221–257.

[11] J.L. Consalvi and F. Nmira, *Transported scalar pdf modelling of oxygen-enriched turbulent jet diffusion flames: soot production and radiative heat transfer*, Fuel 178 (2016), pp. 37–48.

[12] R.P. Lindstedt and S.A. Louloudi, *Joint-scalar transported pdf modeling of soot formation and oxidation*, Proc. Combust. Inst. 30 (2005), pp. 775–783.

[13] R.S. Mehta, D.C. Haworth, and M.F. Modest, *Composition pdf/photon monte carlo modeling of moderately sooting turbulent jet flames*, Combust. Flame 157 (2010), pp. 982–994.

[14] M.E. Mueller and H. Pitsch, *Les model for sooting turbulent nonpremixed flames*, Combust. Flame 159 (2012), pp. 2166–2180.

[15] P. Donde, V. Raman, M.E. Mueller, and H. Pitsch, *Les/pdf based modeling of soot–turbulence interactions in turbulent flames*, Proc. Combust. Inst. 34 (2013), pp. 1183–1192.

[16] S. Yang, J.K. Lew, and M.E. Mueller, *Large eddy simulation of soot evolution in turbulent reacting flows: presumed subfilter pdf model for soot–turbulence–chemistry interactions*, Combust. Flame 209 (2019), pp. 200–213.

[17] P.P. Duvvuri, H.M. Colman, and M.E. Mueller, *Relative influence of soot oxidation kinetics and subfilter soot-turbulence interactions on soot evolution in turbulent nonpremixed flames, available online*, Proc. Combust. Inst. 39 (2022), pp. 1–9.

[18] P. Rodrigues, B. Franzelli, R. Vicquelin, O. Gicquel, and N. Darabiha, *Coupling an les approach and a soot sectional model for the study of sooting turbulent non-premixed flames*, Combust. Flame 190 (2018), pp. 477–499.

[19] M. Grader, C. Eberle, and P. Gerlinger, *Large-eddy simulation and analysis of a sooting lifted turbulent jet flame*, Combust. Flame 215 (2018), pp. 458–470.

[20] B. Sun and S. Rigopoulos, *Modelling of soot formation and aggregation in turbulent flows with the les-pbe-pdf approach and a conservative sectional method*, Combust. Flame 242 (2022), p. 12152.

[21] Z. Huo, M.J. Cleary, A.R. Masri, and M.E. Mueller, *A coupled mmc-les and sectional kinetic scheme for soot formation in a turbulent flame*, Combust. Flame 241 (2022), p. 112089.

[22] F. Sewerin and S. Rigopoulos, *An les-pbe-pdf approach for predicting the soot particle size distribution in turbulent flames*, Combust. Flame 189 (2018), pp. 62–76.

[23] L. Tian, M.A. Schiener, and R.P. Lindstedt, *Fully coupled sectional modelling of soot particle dynamics in a turbulent diffusion flame*, Proc. Combust. Inst. 38 (2021), pp. 1365–13735.

[24] L. Tian, W.R. Boyette, R.P. Lindstedt, T.F. Guiberti, and W.L. Roberts, *Transported JPDF modelling and measurements of soot at elevated pressures*, Proc. Combust. Inst. 39 (2022), pp. 1–9.

[25] B. Franzelli, A. Vié, and N. Darabiha, *A three-equation model for the prediction of soot emissions in les of gas turbines*, Proc. Combust. Inst. 37 (2019), pp. 5411–5419.
[26] P. Rodrigues, O. Gicquel, B. Franzelli, N. Darabiha, and R. Vicquelin, *Analysis of radiative transfer in a turbulent sooting jet flame using a monte carlo method coupled to large eddy simulation*, J. Quant. Spectrosc. Radiat. Transf. 235 (2019), pp. 187–203.
[27] F. Nmira, A. Bouffard, J.L. Consalvi, and Y. Wang, *Large-eddy simulation of lab-scale ethylene buoyant diffusion flames: effects of subgrid turbulence/soot production interaction and radiation models*, Proc. Combust. Inst. 39 (2022), pp. 1–9.
[28] A. Gupta, D.C. Haworth, and M.F. Modest, *Turbulence-radiation interactions in large-eddy simulations of luminous and nonluminous nonpremixed flames*, Proc. Combust. Inst. 34 (2013), pp. 1281–1288.
[29] M.A. Schiener and R.P. Lindstedt, *Joint-scalar transported pdf modelling of soot in a turbulent non-premixed natural gas flame*, Combust. Theor. Model. 22 (2018), pp. 1134–1175.
[30] M.A. Schiener and R.P. Lindstedt, *Transported probability density function based modelling of soot particle size distributions in non-premixed turbulent jet flames*, Proc. Combust. Inst. 37 (2019), pp. 1049–1056.
[31] L. Tian and R. Lindstedt, *On the impact of differential diffusion between soot and gas phase species in turbulent flames*, Combust. Flame 251 (2023), p. 112684.
[32] D.C. Haworth, *Progress in probability density function methods for turbulent reacting flows*, Prog. Ener. Combust. Sci. 157 (2010), pp. 982–994.
[33] S.F. Fernandez, C. Paul, A. Sircar, A. Imren, D.C. Haworth, S. Roy, and M.F. Modest, *Soot and spectral radiation modeling for high-pressure turbulent spray flames*, Combust. Flame 190 (2018), pp. 402–415.
[34] H. Zhou, Z. Li, T. Yang, E.R. Hawkes, Z. Ren, H. Wang, and A. Wehrfritz, *An evaluation of gas-phase micro-mixing models with differential mixing timescales in transported pdf simulations of sooting flame dns*, Proc. Combust. Inst. 38 (2021), pp. 2731–2739.
[35] T. Yang, H. Zhou, and Z. Ren, *A particle mass-based implementation for mixing models with differential diffusion*, Combust. Flame 214 (2020), pp. 116–120.
[36] R.S. Mehta, M.F. Modest, and D.C. Haworth, *Radiation characteristics and turbulence-radiation interactions in sooting turbulent jet flames*, Combust. Theory Model. 14 (2010), pp. 105–124.
[37] J.L. Consalvi and F. Nmira, *Effects of soot absorption coefficient–planck function correlation on radiative heat transfer in oxygen-enriched propane turbulent diffusion flame*, J. Quant. Rad. Heat Transf. 172 (2016), pp. 50–57.
[38] F. Nmira, D. Burot, and J.L. Consalvi, *Soot emission radiation–turbulence interactions in diffusion jet flames*, Combust. Sci. Technol. 191 (2019), pp. 126–136.
[39] F. Nmira, J.L. Consalvi, and M.A. Delichatsios, *Radiant fraction from sooting jet fires*, Combust. Flame 208 (2019), pp. 51–62.
[40] Y.R. Sivathanu, J.P. Gore, and J. Dolinar, *Simultaneous multiline emission absorption measurements in optically thick turbulent flames*, Combust. Sci. Technol. 76 (1991), pp. 45–66.
[41] Y.R. Sivathanu and J.P. Gore, *Transient structure and radiation properties of strongly radiant buoyant flames*, J. Heat Transf. 114 (1992), pp. 659–665.
[42] J. Zhang, C.R. Shaddix, and R.W. Schefer, *Design of 'model-friendly' turbulent non-premixed jet burners for c2 + hydrocarbon fuels*, Rev. Sci. Instrum. 82 (2011), p. 074101.
[43] V.P. Solovjov, B.W. Webb, and F. André, *The rank correlated fsk model for prediction of gas radiation in non-uniform media, and its relationship to the rank correlated slw model*, J. Quant. Spectrosc. Radiat. Transf. 214 (2018), pp. 120–132.
[44] J.L. Consalvi and F. Nmira, *Absorption turbulence-radiation interactions in sooting turbulent jet flames*, J. Quant. Spectrosc. Rad. Trans. 201 (2017), pp. 1–9.
[45] J. Jaishree and D.C. Haworth, *Comparisons of Lagrangian and Eulerian pdf methods in simulations of non-premixed turbulent jet flames with moderate-to-strong turbulence chemistry interactions*, Combust. Theory Model. 16 (2012), pp. 435–463.
[46] Y. Sivathanu and J. Gore, *Coupled radiation and soot kinetics calculations in laminar acetylene/air diffusion flames*, Combust. Flame 97 (1994), pp. 161–172.
[47] C. Lautenberger, J. de Ris, N. Dembsey, J. Barnett, and H. Baum, *A simplified model for soot formation and oxidation in cfd simulation of non-premixed hydrocarbon flames*, Fire Safety J. 40 (2005), pp. 141–176.

[48] F. Nmira, J. Consalvi, R. Demarco, and L. Gay, *Assessment of semi-empirical soot production models in c1–c3 axisymmetric laminar diffusion flames*, Fire Safety J. 73 (2015), pp. 76–90.
[49] X.S. Bai, M. Balthasar, F. Mauss, and L. Fuchs, *Detailed soot modeling in turbulent jet diffusion flames*, Proc. Combust. Inst. 27 (1998), pp. 1623–1630.
[50] H. Pitsch, E. Riesmeier, and N. Peters, *Unsteady flamelet modeling of soot formation in turbulent diffusion flames*, Combust. Sci. Technol. 158 (2000), pp. 389–406.
[51] F. Ferraro, S. Gierth, S. Salenbauch, W. Han, and C. Hasse, *Soot particle size distribution reconstruction in a turbulent sooting flame with the split-based extended quadrature method of moments*, Phys. Fluids 34 (2022), p. 075121.
[52] H. Pitsch, *Flamemaster: A c++ computer program for 0d combustion and 1d laminar flame calculations*, 1998.
[53] Y. Wang, A. Raj, and S. Chung, *A pah growth mechanism and synergistic effect on pah formation in counterflow diffusion flames*, Combust. Flame 160 (2013), pp. 1667–1676.
[54] D. Carbonell, C.D. Perez-Segarra, P.J. Coelho, and A. Oliva, *Flamelet mathematical models for non-premixed laminar combustion*, Combust. Flame 156 (2009), pp. 334–347.
[55] A. Kalbhor and J. van Oijen, *Effects of curvature on soot formation in steady and unsteady counterflow diffusion flames*, Combust. Flame 241 (2019), p. 112108.
[56] S. Yang, J.K. Lew, and M.E. Mueller, *Large eddy simulation of soot evolution in turbulent reacting flows: strain-sensitive transport approach for polycyclic aromatic hydrocarbons*, Combust. Flame 220 (2020), pp. 219–234.
[57] J.Y. Xing, C.P.T. Groth, and J.T.C. Hu, *On the use of fractional-order quadrature-based moment closures for predicting soot formation in laminar flames*, Combust. Sci. Technol. 194 (2022), pp. 22–44.
[58] M. Frenklach and H. Wang, *Detailed mechanism and modeling of soot particle formation*, in *Soot Formation in Combustion*, H. Bockhorn, ed., Springer series in chemical physics, Berlin Heidelberg, 1994.
[59] J. Appel, H. Bockhorn, and M. Frenklach, *Kinetic modeling of soot formation with detailed chemistry and physics: laminar premixed flames of c2 hydrocarbons*, Combust. Flame 121 (2000), pp. 122–136.
[60] G. Blanquart and H. Pitsch, *A joint volume-surface-hydrogen multi-variate model for soot formation*, in *Combustion Generated Fine Carbonceous Particles*, H. Bockhorn, A. D'Anna, A. F. Sarofim, H. Wang, eds., Springer-Verlag, KIT Scientific Publishing, Karlsruhe, 2009.
[61] H. Wang, D.X. Du, C.J. Sung, and C.K. Law, *Experiments and numerical simulations on soot formation in opposed jet ethylene diffusion flames*, Proc. Combust. Inst 26 (1996), pp. 2359–2368.
[62] C.P. Fenimore and G.W. Jones, *Oxidation of soot by hydroxyl radicals*, J. Phys. Chem. 71 (1967), pp. 593–597.
[63] H. Guo, P.M. Anderson, and P.B. Sunderland, *Optimized rate expressions for soot oxidation by oh and o_2*, Fuel 172 (2016), pp. 248–252.
[64] M.D. Smooke, M.B. Long, B.C. Connelly, M.B. Colket, and R.J. Hall, *Soot formation in laminar diffusion flames*, Combust. Flame 143 (2005), pp. 613–628.
[65] A. Veshkini, S.B. Dworkin, and M.J. Thomson, *Understanding soot particle size evolution in laminar ethylene/air diffusion flames using novel soot coalescence models*, Combust. Theor. Model. 20 (2016), pp. 707–734.
[66] B. Sun, S. Rigopoulos, and A. Liu, *Modelling of soot coalescence and aggregation with a two-population balance equation model and a conservative finite volume method*, Combust. Flame 229 (2021), p. 111382.
[67] A. Kazakov and M. Frenklach, *Dynamic modeling of soot particle coagulation and aggregation: implementation with the method of moments and application to high-pressure laminar premixed flames*, Combust. Flame 114 (1998), pp. 484–501.
[68] Z. Sun, B. Dally, Z. Alwahabi, and G. Nathan, *The effect of oxygen concentration in the co-flow of laminar ethylene diffusion flames*, Combust. Flame 211 (2020), pp. 96–111.
[69] R.J. Santoro, H.G. Semerjian, and R.A. Dobbins, *Soot particle measurements in diffusion flames*, Combust. Flame 51 (1983), pp. 203–218.
[70] R.J. Santoro, T.T. Yeh, J.J. Horvath, and H.G. Semerjian, *The transport and growth of soot particles in laminar diffusion flames*, Combust. Sci. Technol. 53 (1987), pp. 89–115.

[71] R. Puri, T.F. Richardson, R.J. Santoro, and R.A. Dobbins, *Aerosol dynamic processes of soot aggregates in a laminar ethene diffusion flame*, Combust. Flame 92 (1993), pp. 320–333.
[72] C.M. Megaridis and R.A. Dobbins, *Soot aerosol dynamics in a laminar ethylene diffusion flame*, Proc. Combust. Inst. 22 (1989), pp. 353–362.
[73] S.S. Iyer, T.A. Litzinger, S.Y. Lee, and R.J. Santoro, *Determination of soot scattering coefficient from extinction and three-angle scattering in a laminar diffusion flame*, Combust. Flame 149 (2007), pp. 206–216.
[74] H. Chang and T. Charalampopoulos, *Determination of the wavelength dependence of refractive indices of flame soot*, Proc. Royal Soc. 430 (1990), pp. 577–591.
[75] M.F. Modest and S. Mazumder, *Radiative Heat Transfer*, Academic Press, Cambridge, 2021.
[76] L.S. Rothman, I.E. Gordon, R.J. Barber, H. Dothe, R.R. Gamache, A. Goldman, V.I. Perevalov, S. Tashkun, and J. Tennyson, *Hitemp: the high-temperature molecular spectroscopic database*, J. Quant. Spectrosc. Radiat. Transf. 111 (2010), pp. 2139–2150.
[77] M.F. Modest and R.J. Riazzi, *Assembly of full-spectrum k-distributions from a narrow-band database; effects of mixing gases, gases and nongray absorbing particles, and mixtures with nongray scatterers in nongray enclosures*, J. Quant. Spectrosc. Radiat. Transf. 90 (2005), pp. 169–189.
[78] J.L. Consalvi, F. André, F.R. Coelho, F.H.R. França, F. Nmira, M. Galtier, V. Solovjov, and B.W. Webb, *Assessment of engineering gas radiative property models in high pressure turbulent jet diffusion flames*, J. Quant. Spectrosc. Radiat. Transf. 253 (2020), p. 107169.
[79] G.D. Raithby and E.H. Chui, *Finite-volume method for predicting a radiant heat transfer in enclosures with participating media*, J. Heat Transf. 112 (1990), pp. 415–423.
[80] L. Valino, *A field monte carlo formulation for calculating the probability density function of a single scalar in a turbulent flow*, Flow Turb. Combust. 60 (1998), pp. 157–172.
[81] L. Valino, R. Mustata, and K.B. Letaief, *Consistent behavior of Eulerian monte carlo fields at low Reynolds numbers*, Flow Turb. Combust. 96 (2016), pp. 503–512.
[82] S.P. Kearney, D.R. Guildenbecher, C. Winters, P.A. Farias, T.W. Grasser, and J.C. Hewson, *Temperature, oxygen, and soot-volume-fraction measurements in a turbulent c2h4-fueled jet flame*, Tech. Rep. SANDIA, SAND2015-7968, Albuquerque, New Mexico, USA, 2015.
[83] C.R. Shaddix, J. Zhang, R.W. Schefer, J. Doom, J.C. Oefelein, S. Kook, L.M. Pickett, and H. Wang, *Understanding and predicting soot generation in turbulent non-premixed jet flames*, Tech. Rep., SANDIA, SAND2010-7178, Livermore, California, USA, 2010.
[84] G. Blanquart, P. Pepiot-Desjardins, and H. Pitsch, *Chemical mechanism for high temperature combustion of engine relevant fuels with emphasis on soot precursors*, Combust. Flame 156 (2009), pp. 588–607.
[85] C.R. Shaddix, J. Zhang, and T.C. Williams, *Quantifying soot concentrations in turbulent non-premixed jet flames*, Tech. Rep. SANDIA, SAND2016-2072C, Livermore, CA, USA, 2010.